

EMISSION CHARACTERISTICS AND ELECTRON OPTICAL  
PROPERTIES OF THE ZrO/W POINT CATHODE

David William Tuggle  
B.S. Physics, Oregon State University, 1974  
M.S. Applied Physics, Oregon Graduate Center, 1981


A dissertation submitted to the faculty  
of the Oregon Graduate Center  
in partial fulfillment of the  
requirements for the degree  
Doctor of Philosophy  
in  
Applied Physics

June 1984


The dissertation "Emission Characteristics and Electron Optical Properties of the ZrO/W Point Cathode" by David William Tuggle, has been examined and approved by the following Examination Committee:

---

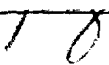
Lynwood W. Swanson, Thesis Advisor

---

Jonathan H. Orloff 

---

Douglas F. Barofsky 

---

Richard A. Elliott

## ACKNOWLEDGMENTS

I would like to thank my advisor, Professor Lynwood W. Swanson, not only for the benefit of his considerable expertise and experience, but also for being a personal example of dedication and integrity that, in my experience, is very rare. Thanks are also due to Professor Jon Orloff for many helpful discussions and encouragement during this work.

Mr. Noel Martin of FEI Co. constructed most of the precision experimental apparatus and his experience saved me many weeks of trial and error. Dale Larson contributed a great deal to the ease with which I was able to manipulate and graph large amounts of computer output and experimental data by creating a Graphics Editor on the computer at OGC. The SCWIM program was written by Nian-Kan Kang of Academia Sinica, Beijing, China, and this program has proven to be extremely useful, not only for the Zr/W emitter but for studying all sorts of point electron and ion sources. I am grateful to Nanometrics, Inc. for a one-year scholarship provided to me during this work.

I would like to thank Bev Kyler for typing most of the reports out of which this dissertation was constructed and also for her efficiency and speed (whatever she's being paid, it's not enough).

1

TABLE OF CONTENTS

	Page
ACKNOWLEDGEMENTS . . . . .	iii
LIST OF TABLES . . . . .	vi
LIST OF FIGURES . . . . .	vii
ABSTRACT . . . . .	xviii
CHAPTER	
1. INTRODUCTION . . . . .	1
References . . . . .	7
2. FIELD BUILD UP PROCESS . . . . .	8
References . . . . .	28
3. ANGULAR DISTRIBUTION CHARACTERISTICS . . . . .	29
A. Experimental Angular Distribution Studies . . . . .	29
B. Computer Studies of Surface Electric Field for the Faceted Emitter . . . . .	46
C. Computer Simulation of I-V Characteristics . . . . .	59
D. Computer Calculations of "Cold Electron" Trajectories . . . . .	73
E. Computer Simulation of Angular Intensity Distributions . . . . .	86
References . . . . .	104
4. CURRENT FLUCTUATION STUDY . . . . .	105
A. Experimental Current Fluctuation Results . . . . .	105
B. Thermal Fluctuations - Theoretical . . . . .	119

References . . . . . 125

5. ELECTRON OPTICAL CHARACTERISTICS . . . . . 126

    A. Electron Gun Transmission . . . . . 126

    B. Computer Studies of Backscattered Trajectories  
        in Gun . . . . . 134

    C. Virtual Source Size Calculation . . . . . 148

    D. Virtual Source - Experimental Consideration . . 164

    References . . . . . 168

6. SUMMARY AND CONCLUSIONS . . . . . 169

APPENDICES . . . . . 175

VITA . . . . . 227

1

LIST OF TABLES

TABLE	Page	
3-1	Summary of the values of $\beta_e$ and $\beta_c$ and the central emission field strengths $F_c$ and voltages $V$ required for 1 mA/sr for emitters of two different radii $r$ . The total current is $I_T$ and $T = 1800$ K.	45
3-2	$\beta$ ratio from Table 3-1 data.	53
3-3	Experimental $r$ and $f/r$ values.	56
3-4	Sensitivity of $\beta$ to geometry of gun and bias voltage for $r = 1 \mu\text{m}$ and $f/r = 0.3$ .	58
3-5	Procedure for determining $\beta$ .	68
3-6	Experimental $\beta$ data.	71
3-7	Effect of facet formation as a function of emitter radius for $I' \sim 0.8$ mA/sr, $\phi = 2.8$ eV.	85
3-8	Computer simulations of angular intensity distributions $T = 1800$ K, $\phi = 2.8$ eV.	103
5-1	Summary of voltage values required for 1 mA/sr at 1800 K and the total emission current, $I_T$ , for various emitters. $I_c$ is the central emission beam current obtained through a 3.1 mrad full angle aperture.	128
5-2	SCWIM program results.	159

1

LIST OF FIGURES

FIGURE	Page
1-1 ZrO/W <100> point cathode emitter showing zirconium on shank.	2
1-2 Overall electron gun structure and equipotentials.	4
1-3 Emitter/suppressor/anode test structure.	5
2-1 Micrographs and field electron patterns (a) before and (b) after faceting.	9
2-2 Micrograph of emitter tilted 60° from SEM axis showing end and side facets.	10
2-3 Faceted 1 μm radius emitter tip and computed equipotentials at 50, 100, 200 and 500 volts.	11
2-4 Angular distribution of emission as a function of time: t <sub>1</sub> = 0, t <sub>2</sub> = 1 hr, t <sub>3</sub> = 4.5 hr.	15
2-5 Schematic of arrangement of (100) net planes where (a), (b) and (c) correlate with the Figure 2-4 emission distributions t <sub>1</sub> , t <sub>2</sub> and t <sub>3</sub> respectively. (d) is the stable end form and corresponds to the emission distribution of Figure 2-6.	16
2-6 Experimental angular intensity distribution for a ZrO/W emitter at 1800 K and various voltages A to G 3700 to 4300 V in 100 V increments. Full angle subtended by Faraday cup = .0031 rad.	17

2-7 (a-d)	Sequence of field electron patterns during field build up of a ZrO/W(100) emitter operating at $T = 1900$ K and $V = 5779$ . Pattern (a) is the initial unbuilt emitter.	19
2-7 (e-h)	Photos (e) to (g) are continuation of Figure 2-7 field electron patterns. Pattern (h) was obtained from pattern (g) by operating the emitter at 1800 K with no applied voltage for the indicated time.	20
2-8	Experimental angular intensity distribution for a ZrO/W emitter at 1800 K and 4700 volts. The total current was 105 and 167 $\mu$ A respectively for the curve taken at $t = 0$ and the curve taken later at $t = 15$ hrs.	21
2-9	Geometrical description for build-up. Taken from Reference 5.	23
2-10 (a-b)	Orthogonal views at $60^\circ$ tilt of emitter showing different cone angles.	25
2-10 (c)	End-on ( $0^\circ$ tilt) view of emitter showing square (100) facet barely visible in dark area.	26
3-1	Experimental angular distributions. Curves A through L correspond to anode voltages 1800 V through 2900 V in 100 V increments. Emitter radius $\approx 0.8$ $\mu$ m.	30
3-2	Experimental angular distributions. Curves A through I correspond to anode voltages 2900 V through 3700 V in 100 V increments. Emitter radius $\approx 0.8$ $\mu$ m.	31



3-3	Experimental angular distribution. Curves A through G correspond to anode voltages 3700 through 4300 V in 100 V increments. Emitter radius $\approx 0.8 \mu\text{m}$ .	32
3-4	Experimental angular distribution. Curves A through F correspond to anode voltages 4300 V through 4800 V in 100 V increments. Emitter radius $\approx 0.8 \mu\text{m}$ .	33
3-5	Two-dimensional current distribution at 1800 K and 4700 V taken by x-y movement of the Faraday collector. Initial x and y positions were 9 and 10 mm respectively for the lowest curve. Subsequent curves in increasing x were incremental 0.25 mm. Vertical scale on lower right indicates current scale factor.	34
3-6	Two-dimensional current distribution at 1800 K and 3800 V taken by x-y movement of the Faraday collector. Initial x and y positions were 9 and 10 mm respectively for the lowest curve. Subsequent curves in increasing x were incremental 0.25 mm. Vertical scale on lower right indicates current scale factor.	35
3-7	Experimental angular distribution for the $\beta_c = 1.18 \times 10^3 \text{ cm}^{-1}$ Zr/W emitter at 4700 volts and various temperatures. A to I 1100 to 1900 K in $100^\circ$ increments.	37
3-8	Central ( $I_c$ ) and edge ( $I_e$ ) current vs temperature at various voltages from the Figure 3-7 emitter results. (a) 4700 V; (b) 4500 V; (c) 4000 V.	38

3-9	Experimental angular intensity distributions. Curves A through E correspond to temperatures 1600, 1700, 1800, 1850, 1900 K.	39
3-10	Experimental angular intensity distribution for a Zr/W emitter at 1800 K and various voltages: A to I 5500 to 6300 V in 100 V increments. Faraday cup full angle = .0031 rad. Emitter radius $\approx 2.3 \mu\text{m}$ .	41
3-11	Schottky plot of the total, edge and central emission current of the Figure 3-3 emitter. The dashed lines are extensions of the Schottky slopes. Background current seen in angular distributions was subtracted from central and edge emission. Emitter radius $\approx 0.8 \mu\text{m}$ .	42
3-12	Schottky plot of the total, edge and central emission current of the Figure 3-10 emitter. The dashed lines are extensions of the Schottky slopes. Background current seen in angular distributions was subtracted from central and edge emission. Emitter radius $\approx 2.3 \mu\text{m}$ .	43
3-13	Emitter profiles with equipotentials for emitter radii 0.2, 0.5 and 1.0 $\mu\text{m}$ . Facet radius/emitter radius = $f/r = 0.3$ for all cases.	47
3-14	Normalized surface field for the three emitter profiles of Figure 3-13. Emitter radii are indicated.	48
3-15	Emitter profile with equipotentials for $r = 1 \mu\text{m}$ , $f/r = 0.1$ .	50

3-16	Emitter profile with equipotentials for $r = 1 \mu\text{m}$ , $f/r = 0.6$ .	51
3-17	Normalized surface field for $r = 1 \mu\text{m}$ , $f/r = 0.1, 0.2,$ $0.3, 0.4, 0.5, 0.6$ .	52
3-18	Normalized surface field at emitter apex for all radii emitters, variable $f/r$ .	54
3-19	Surface field at apex of emitter for $V_{\text{ANODE}} = 7500 \text{ V}$ , $V_{\text{BIAS}} = -300 \text{ V}$ . Resulting values of field factor for apex emission ( $\beta_c$ ) appear in right hand vertical axis.	55
3-20	Solid lines show the boundaries in terms of field and temperature that separate the indicated emission regimes.	61
3-21	Theoretical Schottky plots based on numerical integration of the electron supply function and barrier transmission coefficient. Simplified computer program giving current density is given in Appendix B.	64
3-22	Normalized Schottky slopes from theoretical calculations for Figure 3-21.	66
3-23	Theoretical Schottky plots with region of practical operation for various emitter radii.	70
3-24	Trajectory slope throughout electron gun. Initial conditions: $0 \text{ eV}$ ; five initial positions ( $R_0$ ) in $\mu\text{m}$ from the emitter axis indicated in figure. $V_{\text{BIAS}} = -300,$ $V_{\text{ANODE}} = 7500$ .	75
3-25	Trajectory position tangent ( $R/Z$ ) throughout electron gun. Initial conditions: $0 \text{ eV}$ ; five initial positions ( $R_0$ )	76

	in $\mu\text{m}$ from the emitter axis indicated in figure. $V_{\text{BIAS}} =$ -300, $V_{\text{ANODE}} = 7500$ .	
3-26	Final beam angle vs launch position angle for trajectories from apex to edge of facet.	79
3-27	Central emission angular magnification as a function of anode voltage and emitter radius. Bias voltage = -300 V. $f/r = 0.3$ .	81
3-28	Cathode field, current density and K factor for 1 $\mu\text{m}$ faceted emitter.	87
3-29	Cathode field, current density and K factor for 1 $\mu\text{m}$ faceted emitter.	88
3-30	Computer calculated angular intensity distribution.	90
3-31	Computer calculated angular intensity distribution.	91
3-32	Computer calculated angular intensity distribution.	92
3-33	Computer calculated angular intensity distribution.	93
3-34	Computer calculated angular intensity distribution.	94
3-35	Computer calculated angular intensity distribution.	95
3-36	Computer calculated angular intensity distribution.	96
3-37	Computer calculated angular intensity distribution.	97
3-38	Computer calculated angular intensity distribution.	98
3-39	Computer calculated angular intensity distribution.	99
3-40	Computer calculated angular intensity distribution.	100
3-41	Computer calculated angular intensity distribution.	101
4-1	Power spectral density function of apertured central emission current. Aperture defines $\Omega$ given in figure.	106

4-2	Variation of the spectral density function $W(f)$ with probe current $I_p$ .	108
4-3	Normalized spectral densities for three different emitters. Radii are A2 = 0.8 $\mu\text{m}$ , G7 = 2.3 $\mu\text{m}$ and G10 = 2.7 $\mu\text{m}$ .	110
4-4	Variable aperture noise power spectra.	112
4-5	Noise percentage vs aperture half angle.	114
4-6	Relative noise amplitude $\Delta I_{\text{rms}}/I_p$ and voltage $V/V_0$ for a given angular intensity beam shown as a function of emitter temperature. $I_p/I_t$ is the beam transmission.	115
4-7	Coherence function.	117
4-8	Noise spectral density. $I_p = 43$ nA unbiased stage. $I_p$ = Probe current (Apertured central emission current). $I_T$ = Total current (Anode current). $I_{\text{COH}}$ = Coherent component of current.	118
4-9	Normalized power spectral density for probe and total currents.	120
4-10	Normalized total current power spectral density.	123
4-11	Emitter and heating filament.	124
5-1	Suppressor control of current with constant anode voltage. Fixed aperture at 1.00 inch distance from emitter.	129
5-2	Transmission vs suppressor bias for constant angular intensity. $\alpha = 0.00156$ rad.	131

5-3	Constant angular intensity (constant field) variation of anode voltage with suppressor bias.	132
5-4	Angular distribution for variable suppressor bias. Anode voltage adjusted to maintain constant angular intensity.	133
5-5	Angular magnification for gun with $V_{\text{ANODE}} = 7500 \text{ V}$ , $V_{\text{BIAS}} = \text{variable}$ . Sequence of graphs from upper to lower: $-100 \text{ V}$ , $-300 \text{ V}$ , $-500 \text{ V}$ , $-700 \text{ V}$ .	135
5-6	(a) Thermal end form. (b) Thermal-field end form showing side $\langle 100 \rangle$ -type facets.	137
5-7	Trajectories launched from various positions on emitter. Note that side (100) facet emission and shank emission do not get through anode aperture. Initial kinetic energy = $0 \text{ eV}$ . Z and R axis dimensions are in $\mu\text{m}$ .	138
5-8	Trajectories launched from emitter shank. Initial electron energy was $0.1 \text{ eV}$ , the anode potential was $7.5 \text{ kV}$ and the suppressor potential was $-300 \text{ volts}$ . Launch positions range from end of shank to emission cutoff point, with all launch angles normal to shank surface. Z and R axis dimensions are in $\mu\text{m}$ .	139
5-9	Magnified view of Figure 5-8.	140
5-10	Calculated backscattered trajectories from the anode. Initial electron energy was $7 \text{ keV}$ , the anode potential	142

was 7.5 kV and the suppressor was -300 volts. The launch radii were 350, 400, 450 and 500  $\mu\text{m}$  and the launch angles were varied from  $\theta = 2^\circ$  to  $\theta = 20^\circ$ , in 2 degree increments.

- 5-11 Calculated backscattered trajectories from the anode. 143  
Initial electron energy was 7 keV, the anode potential was 7.5 kV and the suppressor potential was -300 volts. The launch radius was 250  $\mu\text{m}$  and the launch angles were varied from  $\theta = 2^\circ$  to  $\theta = 20^\circ$ , in 2 degree increments.
- 5-12 Calculated backscattered trajectories from the anode. 144  
Initial electron energy was 7 keV, the anode potential was 7.5 kV and the suppressor potential was -300 volts. The launch radius was 350  $\mu\text{m}$  and the launch angles were varied from  $\theta = 2^\circ$  to  $\theta = 20^\circ$ , in 2 degree increments.
- 5-13 Calculated backscattered trajectories from the anode. 145  
Initial electron energy was 7 keV, the anode potential was 7.5 kV and the suppressor potential was -300 volts. The launch radius was 450  $\mu\text{m}$  and the launch angles were varied from  $\theta = 2^\circ$  to  $\theta = 20^\circ$ , in 2 degree increments.
- 5-14 Calculated backscattered trajectories from the anode. 146  
Initial electron energy was 7 keV, the anode potential was 7.5 kV and the suppressor potential was -300 volts. The launch radius was 500  $\mu\text{m}$  and the launch angles were varied from  $\theta = 2^\circ$  to  $\theta = 20^\circ$ , in 2 degree increments.

5-15	Point cathode modeled as an equipotential of a sphere-on-orthogonal cone. From Wiesner. <sup>6</sup>	149
5-16	Extrapolation of trajectory back to axis crossing point.	151
5-17	A Schottky emission gun with tip radius of 1 $\mu\text{m}$ and the calculated trajectories for spherical tip (solid line) and faceted tip (dashed line). The upper portion shows initial paths of the trajectories.	154
5-18	Least squares fit for $C_s$ from $\alpha$ electrons.	156
5-19	Least squares fit for $C_c$ from $v_T$ electrons.	157
5-20	Least squares fit for $C_c$ from $v_N$ electrons.	158
5-21	Virtual source contributions.	161
5-22	Virtual source size for emitter radii 0.3 to 3.0 $\mu\text{m}$ . Spherical end form.	162
5-23	Virtual source size for emitter radii 0.3 to 3.0 $\mu\text{m}$ . Faceted end form.	163
5-24	Minimum virtual source size.	165
5-25	Experimental measurement of virtual source size.	167
A-1	ZRWGUN flow chart.	184
A-2	Mesh structure.	185
A-2	(continued)	186
A-3	Space charge virtual mesh.	188
A-4	Cold electron trajectories.	193
A-5	Alpha electron trajectories.	194



A-6	V electron trajectories.	195
A-7	Spherical-end emitter.	198
A-8	ZRWGUN structure with 3000 $\mu\text{m}$ max z coord.	199
A-9	Gun geometry for ZRWGUN program data input.	201
A-10	Tape 14 output data files.	204
A-11	Clarification of U and U1 arrays.	216
A-12	Electron gun.	222
A-13	Diagram of the emitter protection circuit used in this study.	223
A-14	Coherence function experimental apparatus.	225

## ABSTRACT

### EMISSION CHARACTERISTICS AND ELECTRON OPTICAL PROPERTIES OF THE ZrO/W POINT CATHODE

David William Tuggle  
Oregon Graduate Center

Supervising Professor: Dr. Lynwood W. Swanson

The Zr/W point cathode electron source is a high brightness, low noise point source of electrons which has been used in several electron optical systems. It has the capability of forming a high current, narrow cone angle focused electron beam at a relatively large working distance. In particular, it exceeds the performance of the LaB<sub>6</sub> thermionic cathode, its closest competitor, in systems where a sub-quarter micron, several nanoampere electron beam is required.

In order to apply this emitter to an electron optical system, characteristics such as angular intensity distribution, beam energy spread, beam noise, I-V curves, electron gun transmission and virtual source size should be known as a function of emitter radius, current density, temperature and other variable parameters. The present work covers all of the above characteristics except energy spread. Experimental data, theoretical explanations and computer simulations are included.

## CHAPTER 1

## INTRODUCTION

The purpose of the work presented in this dissertation is to improve the understanding of the emission characteristics and electron optical properties of the zirconiated tungsten (ZrO/W) point cathode electron source. This cathode has been used in several electron optical systems.<sup>1-4</sup> It provides an extremely high brightness, relatively low noise electron source which, when combined with low aberration electron lenses, is capable of producing a small diameter ( $< 1 \mu\text{m}$ ) high current density focussed beam of small half angle with a long working distance. The source is particularly suited to electron beam lithography applications using a Gaussian beam. Emittance considerations<sup>5</sup> seem to preclude using the source to form shaped beams, at least for the tip radii ( $0.2 - 2 \mu\text{m}$ ) normally produced by electrochemical etching.

Physically, the emitter consists of a triple-pass zone refined  $\langle 100 \rangle$  oriented tungsten wire (.005 in dia.). The wire is spot welded to a tungsten hairpin filament and electrochemically etched to the desired radius. A zirconium hydride ring attached to the emitter shank provides the zirconium which, when heated in a vacuum system, diffuses out to the end of the tip and establishes a Zr/O/W surface which lowers the work function of the (100) facet on the apex of the tip. Figure 1-1 shows the emitter with the zirconium on the shank.

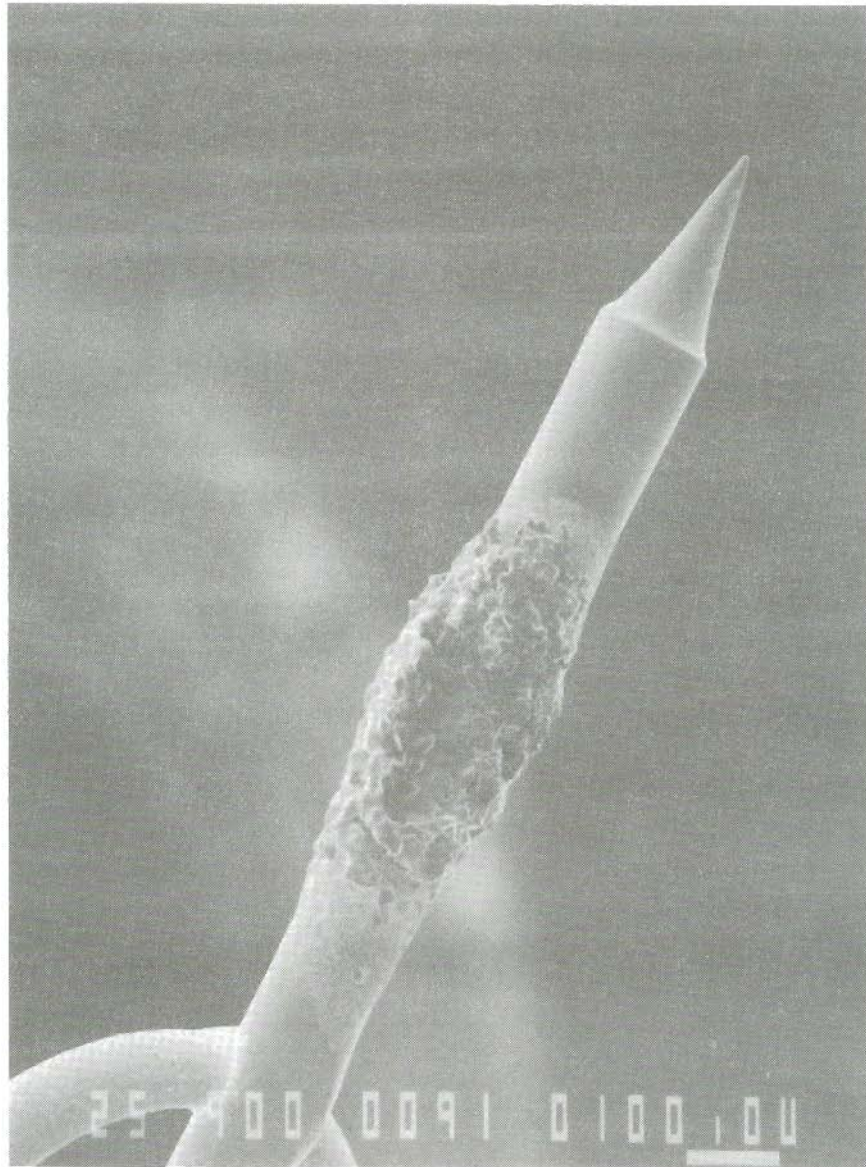


Figure 1-1. Zr/W <100> thermal field emitter showing zirconium on shank.

Most of the experimental data and all computer studies presented here were done for the particular electron gun structure shown in Figure 1-2. The voltages shown on the figure are typical operating voltages and were used for most of the computer studies of the emitter. The purpose of the thermionic shield operating at - 300 V is to prevent thermionic emission from the hairpin filament and emitter shank from bombarding the anode and causing excessive outgassing in the gun.

A photograph of the electron gun structure is shown in Figure 1-3. The upper part of the photo shows the assembled gun and the lower part shows the component parts. The gun was constructed of molybdenum, with tungsten support wires and 1720 Pyrex glass as the insulating support material.

Measurements of the angular distribution of current from this gun with various emitters operating under various conditions were done, as well as computer calculations which attempted to predict the observed distribution. Measurement of current fluctuation (noise) and interpretation of noise correlations in terms of thermal fluctuation was accomplished. Current-voltage curves were plotted and an attempt was made to determine emitter radius and work function from these curves. Angular distribution as a function of temperature yielded some unexpected data where, in certain conditions, an increase in temperature produced a decrease in current.

The electron optical characteristics of the source-gun assembly were studied by experiment and computer calculations. The effect of suppressor bias on trajectories was shown both experimentally

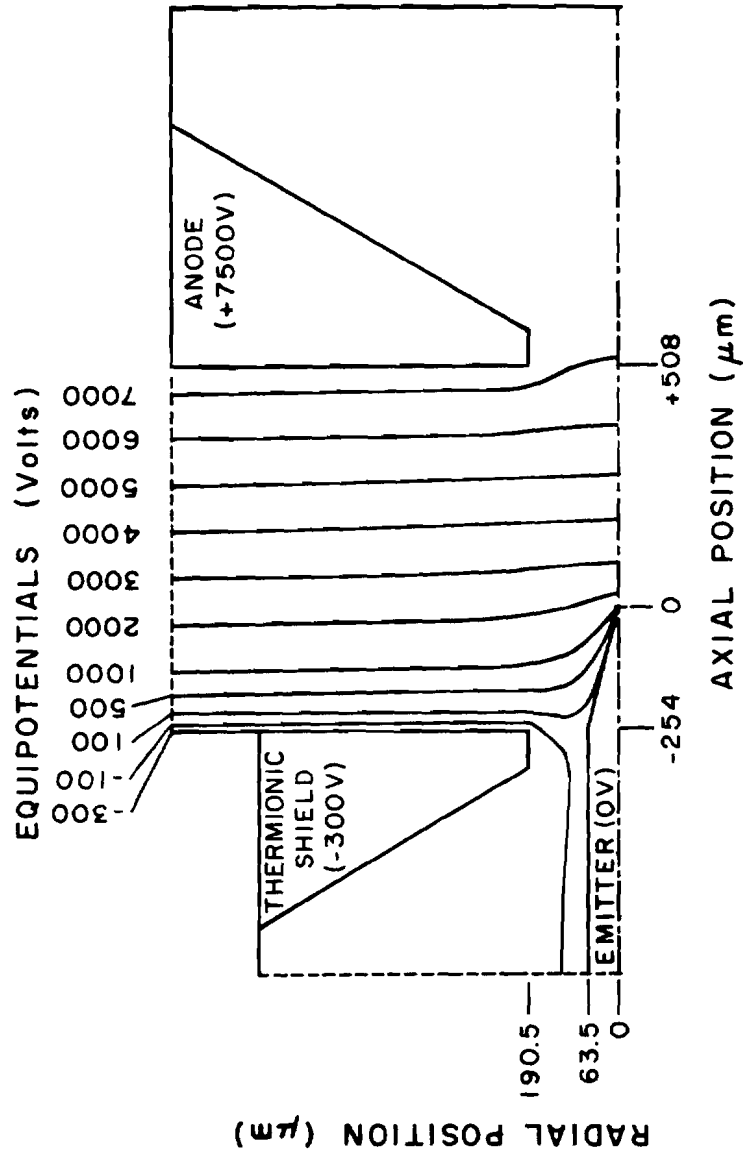


Figure 1-2. Overall electron gun structure and equipotentials.

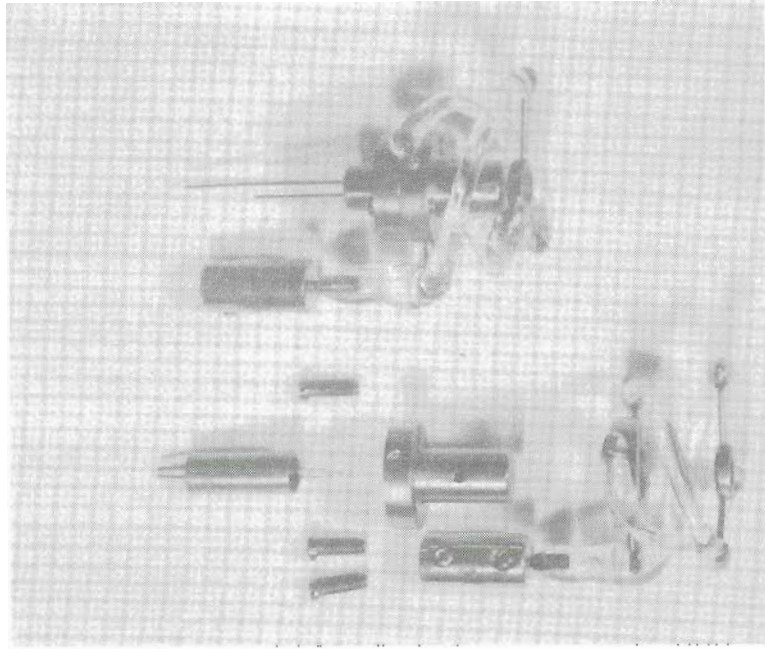


Figure 1-3. Emitter/suppressor/anode test structure.

and theoretically, and virtual source size was predicted for various operating conditions. Stray emission, due to low work function areas on the emitter at positions other than the apex and also due to backscattered trajectories from the anode, was investigated since under certain conditions it can be projected onto the image plane of an electron optical system.



## REFERENCES

1. D. Tuggle, L. W. Swanson, and J. Orloff, J. Vac. Sci. Technol. 16, 1699 (Nov/Dec 1979).
2. J. Kelly, T. R. Groves, and H. P. Kuo, Hewlett-Packard Journal, p. 14 (May 1981).
3. W. R. Livesay, Microelectronic Mfg. and Testing 7, (3) 59 (1984).
4. D. W. Tuggle and S. G. Watson, Proc. 42nd Ann. Mtg. of the Electron Microscopy Soc. of America, 454 (1984).
5. M. Nakasoji and H. Wada, J. Vac. Sci. Technol. 17, 1367 (1980).

## CHAPTER 2

## FIELD BUILD UP PROCESS

In order to characterize the angular intensity distribution of the ZrO/W point cathode emitter as a function of temperature, field, and emitter geometry we pursued both theoretical and experimental approaches. Micrographs taken of this type of emitter after several hours of operation with applied field and temperature (See Figures 2-1 and 2-2) have shown that a (100) crystal facet forms at the tip. The effect of this facet on the electric field at the surface of the tip was studied by a computer model of the emitter using a finite difference technique to compute the electric field. The tip profile and surrounding equipotentials are shown in Figure 2-3. The most obvious result of this emitter faceting is to increase the field at the edge of the facet and to decrease the field at the center of the facet from the values expected for a sphere-on-cone model of the emitter. The main thrust of this chapter is to understand the field-thermal induced shape changes that the emitter undergoes during operation. We present here a brief analysis of the dynamics involved in the field induced emitter shape change.

According to early studies carried out by Dyke and coworkers<sup>1</sup> an applied d.c. electric field causes "field build up" to occur on a field emitter at elevated temperature. The motivation for field build up is the lowering of the thermodynamic chemical potential

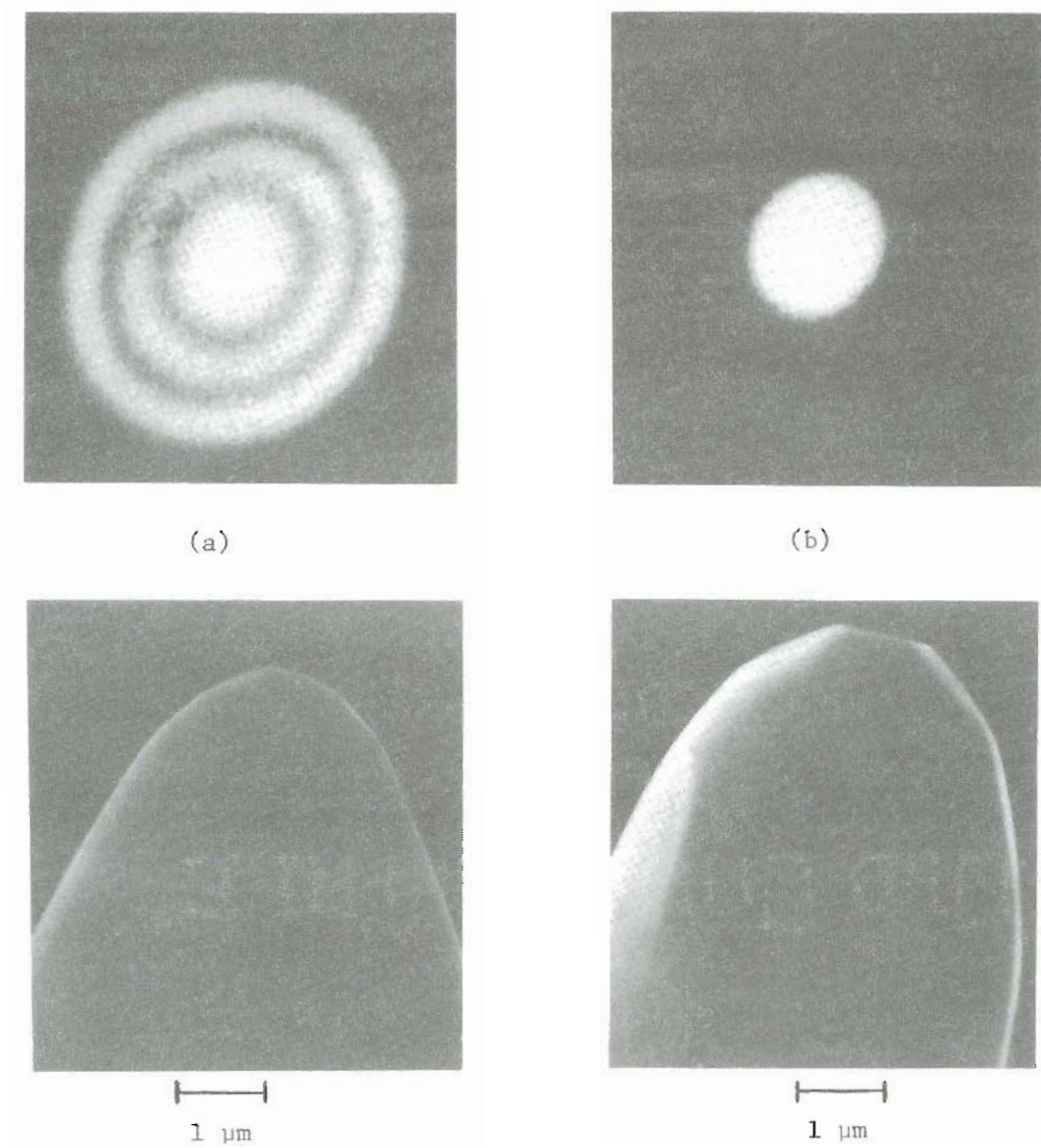


Figure 2-1. Micrographs and field electron patterns (a) before and (b) after faceting.

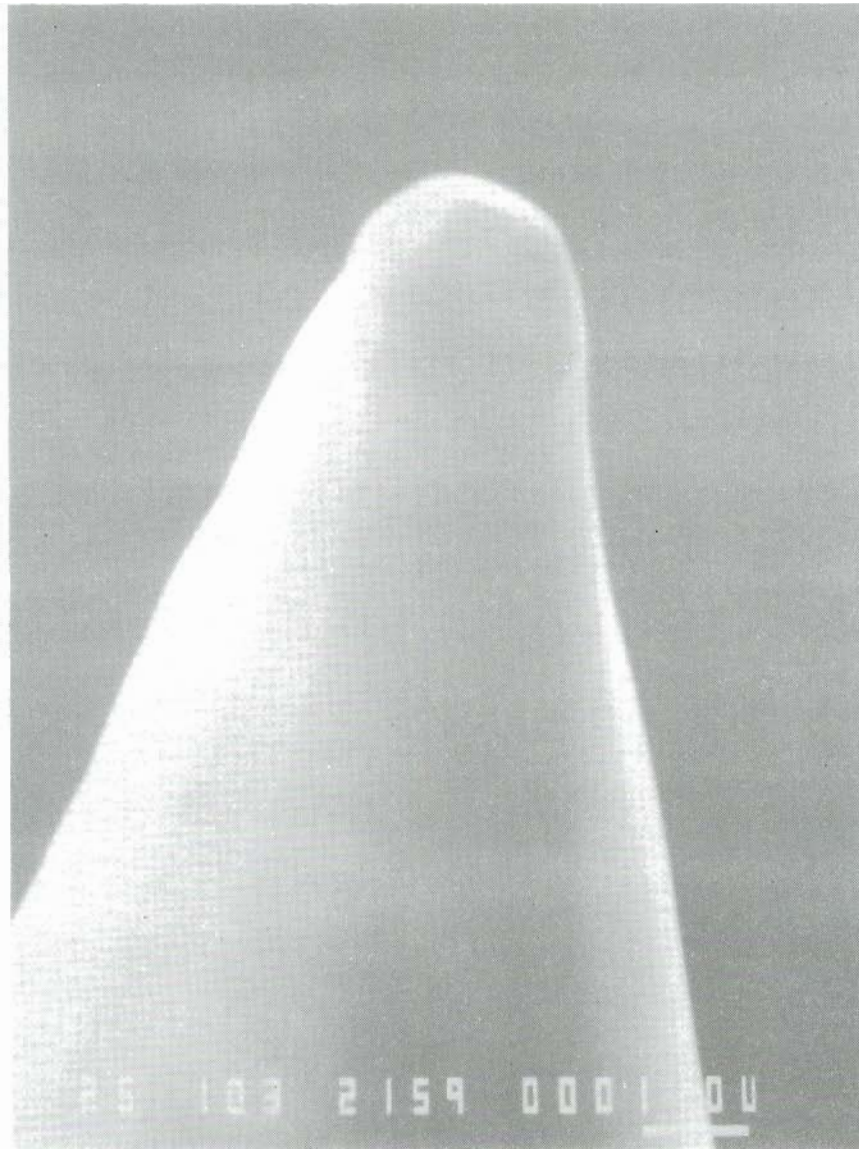


Figure 2-2. Micrograph of emitter tilted  $60^\circ$  from SEM axis showing end and side facets.

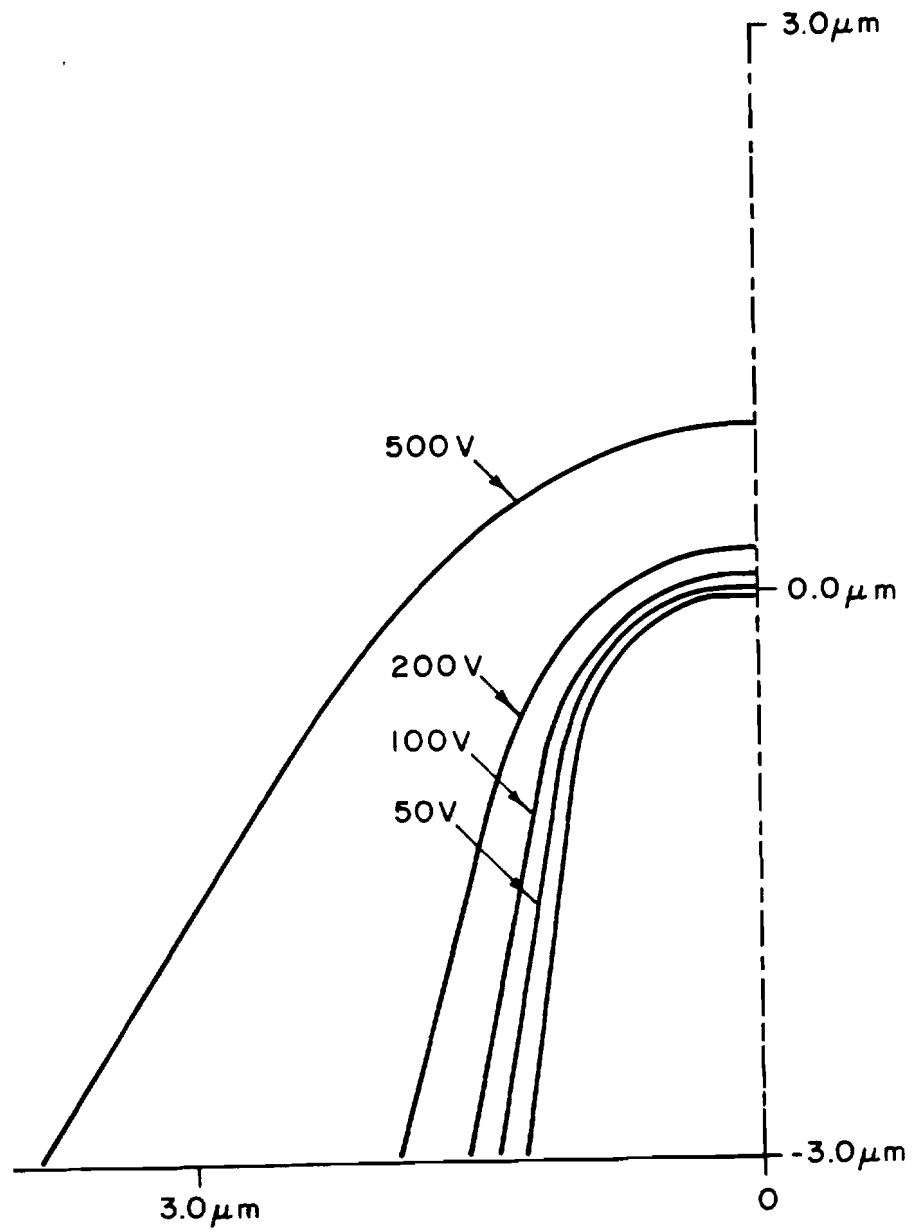


Figure 2-3. Faceted  $1\ \mu\text{m}$  radius emitter tip and computed equipotentials at 50, 100, 200 and 500 volts.

at the emitter tip which in turn motivates surface migration of surface atoms toward the higher field regions of the emitter apex. The rate of this process can be given in terms of the rate of change of the emitter radius

$$\left(\frac{dr}{dt}\right)_F = \left(\frac{dr}{dt}\right)_O \left(1 - \frac{rF^2}{8\pi\gamma}\right) \quad (2-1)$$

and

$$\left(\frac{dr}{dt}\right)_O = 1.25 \gamma v_a D_o \alpha \exp\left(-\frac{E_d}{kT}\right) (A_o kTr^3)^{-1} \quad (2-2)$$

where  $\gamma$  is the surface tension ( $\gamma = 2900$  dyn/cm for W),  $v_a$  is the volume per atom,  $A_o$  is the surface area per atom,  $D_o$  is the diffusivity constant ( $D_o = 4$  cm<sup>2</sup>/sec for W),  $E_d$  is the activation energy for surface diffusion ( $E_d = 3.14$  eV for W) and  $\alpha$  is the emitter cone half angle. For clean W we obtain for the zero field rate of emitter dulling

$$\left(\frac{dr}{dt}\right)_O = 2.6 \times 10^{-11} \alpha \exp\left(-\frac{36300}{T}\right) (Tr^3)^{-1} \left(\frac{\text{cm}}{\text{sec}}\right) . \quad (2-3)$$

It can be seen that the sign of  $\left(\frac{dr}{dt}\right)_F$ , i.e. emitter dulling or build up, is governed by the conditions:

- (a)  $\frac{dr}{dt} > 0$  if  $F < \left(\frac{8\pi\gamma}{r}\right)^{1/2}$
- (b)  $\frac{dr}{dt} = 0$  if  $F_o = \left(\frac{8\pi\gamma}{r_m}\right)^{1/2}$
- (c)  $\frac{dr}{dt} < 0$  if  $F > \left(\frac{8\pi\gamma}{r}\right)^{1/2}$

In practice when condition (c) occurs the overall emitter radius does not decrease but rather the planes of low surface free energy (i.e. large  $\gamma$ ) increase in size at the expense of lower  $\gamma$  crystal faces. This leads to a polyhedral shaped emitter end form and, in the case of clean W, a radical change in the emission distribution.<sup>2</sup> For clean W condition (b) above is given by

$$F_o = 8.1 \times 10^4 r_m^{-1/2} \text{ (V/cm)} \quad (2-4)$$

for  $r_m$  in cm. The useful range of current densities ( $J = 10^4$  to  $10^8$  A/cm<sup>2</sup>) corresponds to fields in the  $4 \times 10^7$  to  $8 \times 10^7$  V/cm range for clean W at  $T = 1800$  K. In view of Eq. (2-4) the necessity to avoid field build up precludes TF operation of cathodes with  $r > 8 \times 10^{-6}$  cm. This is an unrealistically small emitter radius, thus for any emitter of practical size and current density field build up always occurs.

In the case of a ZrO/W cathode the work function of the (100) plane of W is selectively lowered to 2.6 eV thereby confining the emission to this one crystal face.<sup>3,4</sup> In addition, a lower  $F$  is required to achieve a useful current density of say  $5 \times 10^6$  A/cm<sup>2</sup>. Thus, for the latter case  $F = 1 \times 10^7$  V/cm at 1800 K and the condition on  $r$  to preclude field build up is  $r < 6.5 \times 10^{-5}$  cm.

The approach we have taken in the case of the ZrO/W TF cathode is to use very large radius emitters and allow field build up to occur to completion. Fortunately, the (100) and (110) planes facet thus giving a large, low work function (100) plane which is normal to the emitter axis for  $\langle 100 \rangle$  oriented emitters. Several advantages accrue to the emission characteristics by use of large radius emitters. Fortunately, the unusual work function lowering of the (100) plane by Zr allows one to use a large radius emitter without causing an unacceptable increase in operating voltage.

The process of field build up for the ZrO/W emitter at  $T = 1800$  K requires several hours for emitters of gross radius 1 to 2  $\mu\text{m}$ . Figure 2-4 shows the sequence of emission distribution changes during the field build up. The emission pattern during this process consists of two or three concentric rings of emission with the inner ones slowly collapsing with time. Figure 2-5 shows the anticipated geometric shape of the emitter that correlates with the Figure 2-4 emission distributions. The process of field build up occurs by the outward diffusion of the surface atoms from the edge of each net plane. Eventually the final stable end form, (d) in Figure 2-5, is achieved which leads to the emission distribution shown in Figure 2-6.

Upon reducing the field while maintaining the emitter at elevated temperature, the build up end form relaxes and the original ring structure emission distribution shown in Figure 2-4 is re-established. In other words, for large emitters, the process is



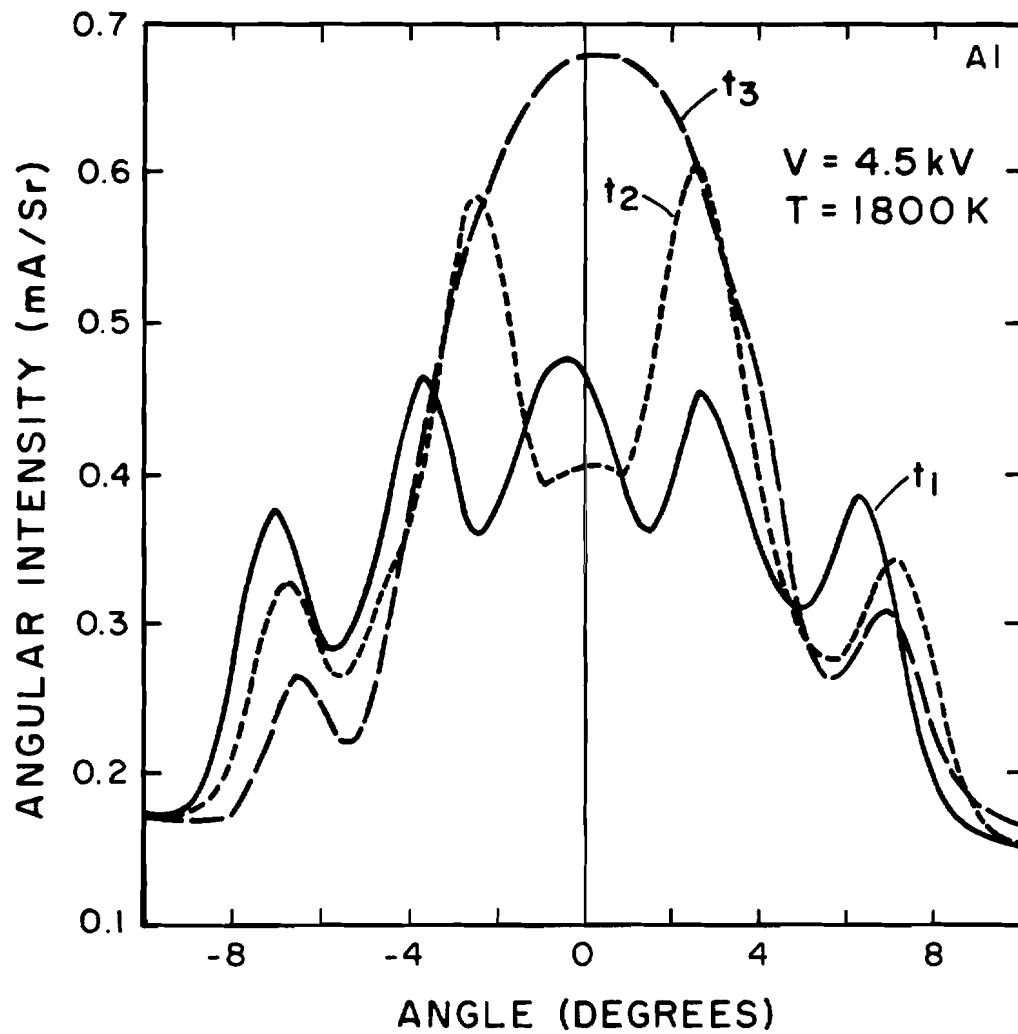


Figure 2-4. Angular distribution of emission as a function of time:  $t_1 = 0$ ,  $t_2 = 1$  hr,  $t_3 = 4.5$  hr.

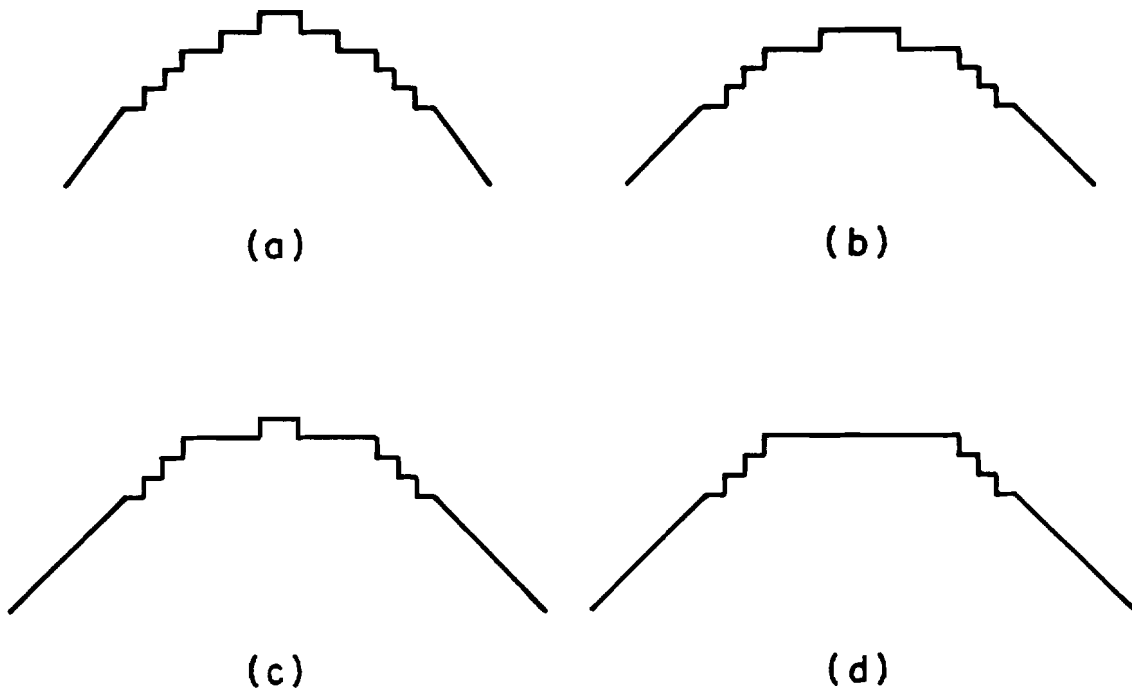


Figure 2-5. Schematic of arrangement of (100) net planes where (a), (b) and (c) correlate with the Figure 2-4 emission distributions  $t_1$ ,  $t_2$  and  $t_3$  respectively. (d) is the stable end form and corresponds to the emission pattern of Figure 2-6.

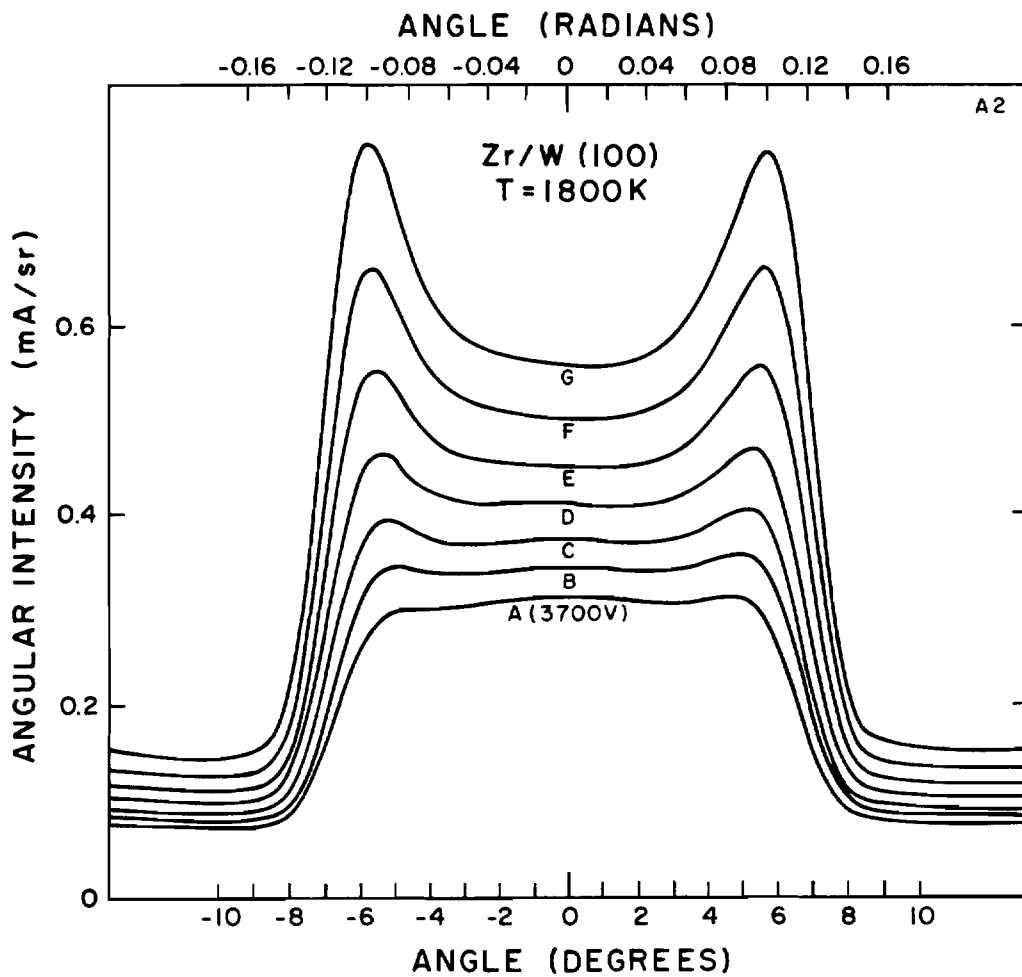


Figure 2-6. Experimental angular intensity distribution for a ZrO/W emitter at 1800 K and various voltages A to G 3700 to 4300 V in 100 V increments. Full angle subtended by Faraday cup .0031 rad.

reversible over many such cycles. The exact size of the step heights depicted in Figure 2-5 are unknown, but may be several layers. Also the makeup of the net plane layers is presumably a composite of Zr/O/W.<sup>4</sup> From previous work we have concluded that the optimum Zr/W TF emitter consists of a bulk ternary phase of Zr/O/W where ZrO concentration is < 1% atomic weight.<sup>4</sup>

In Figure 2-7 we show the sequence of emission patterns obtained in the field electron microscope during the build up process of the ZrO/W(100) emitter. The concentric ring structure is clearly shown for the zero field, thermal end form in photo (a). Upon application of the high voltage at T = 1900 K the two outer rings slowly disappear without radial movement (see photo c). The inner bright disc of emission goes through several repetitive sequences of collapsed rings (i.e. photos d to f) during which time the central, on axis emission cycles through maxima and minima. Finally, after ~70 min. the single, bright emission spot shown in photo (g) is obtained and remains without further major change. A minor increase in the width of the central emission disc and current level occur as shown in the Figure 2-8 emission distribution scan after which no further change occurs.

Upon raising the temperature above 1950 K the central spot will disappear (i.e. no emission), however it reversibly returns upon lowering the temperature. At lower temperatures (e.g. T < 1900 K) the pattern sequence shown in Figure 2-7(a) to (g)

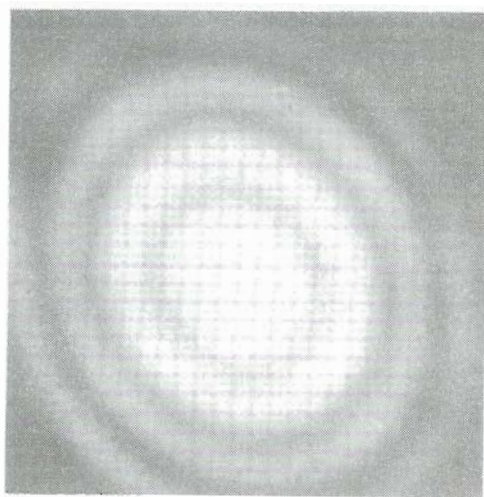
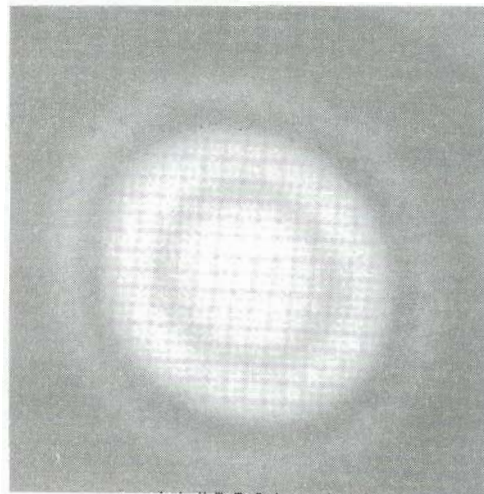
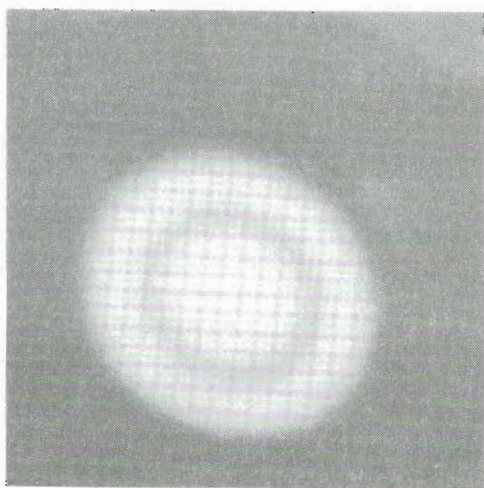
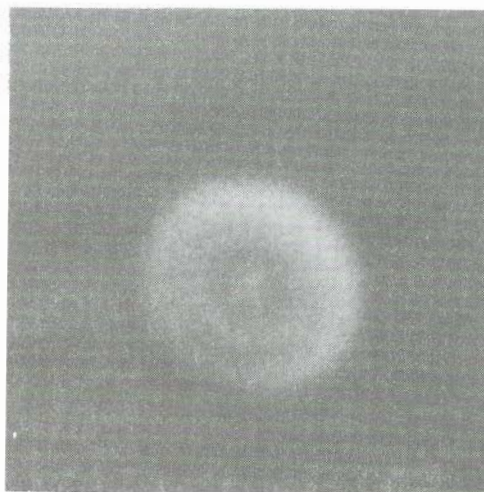
(a)  $t = 0$ (b)  $t = 1 \text{ min}$ (c)  $t = 3 \text{ min}$ (d)  $t = 40 \text{ min}$ 

Figure 2-7(a-d). Sequence of field electron patterns during field build up of a Zr/W(100) emitter operating at  $T = 1900 \text{ K}$  and  $V = 5779$ . Pattern (a) is the initial unbuilt emitter.

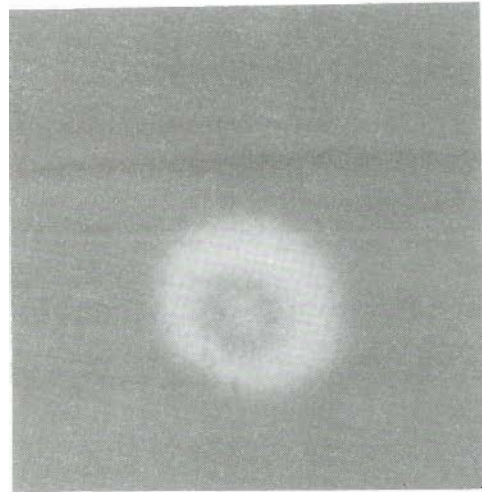
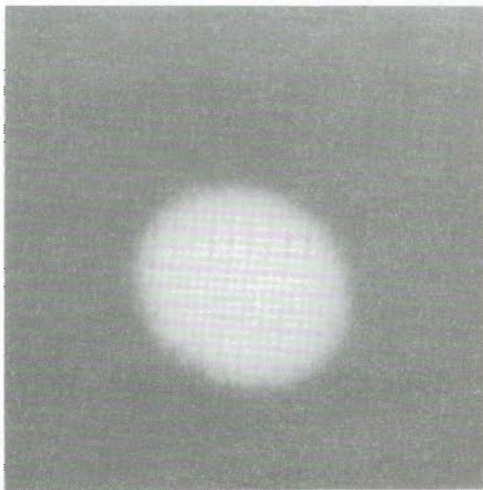
(e)  $t = 42$  min(f)  $t = 60$  min(g)  $t = 72$  min(h)  $t = 47$  hrs

Figure 2-7(e-h). Photos (e) to (g) are continuation of Fig. 2-7 field electron patterns. Pattern (h) was obtained from pattern (g) by operating the emitter at 1800 K with no applied voltage for the indicated time.

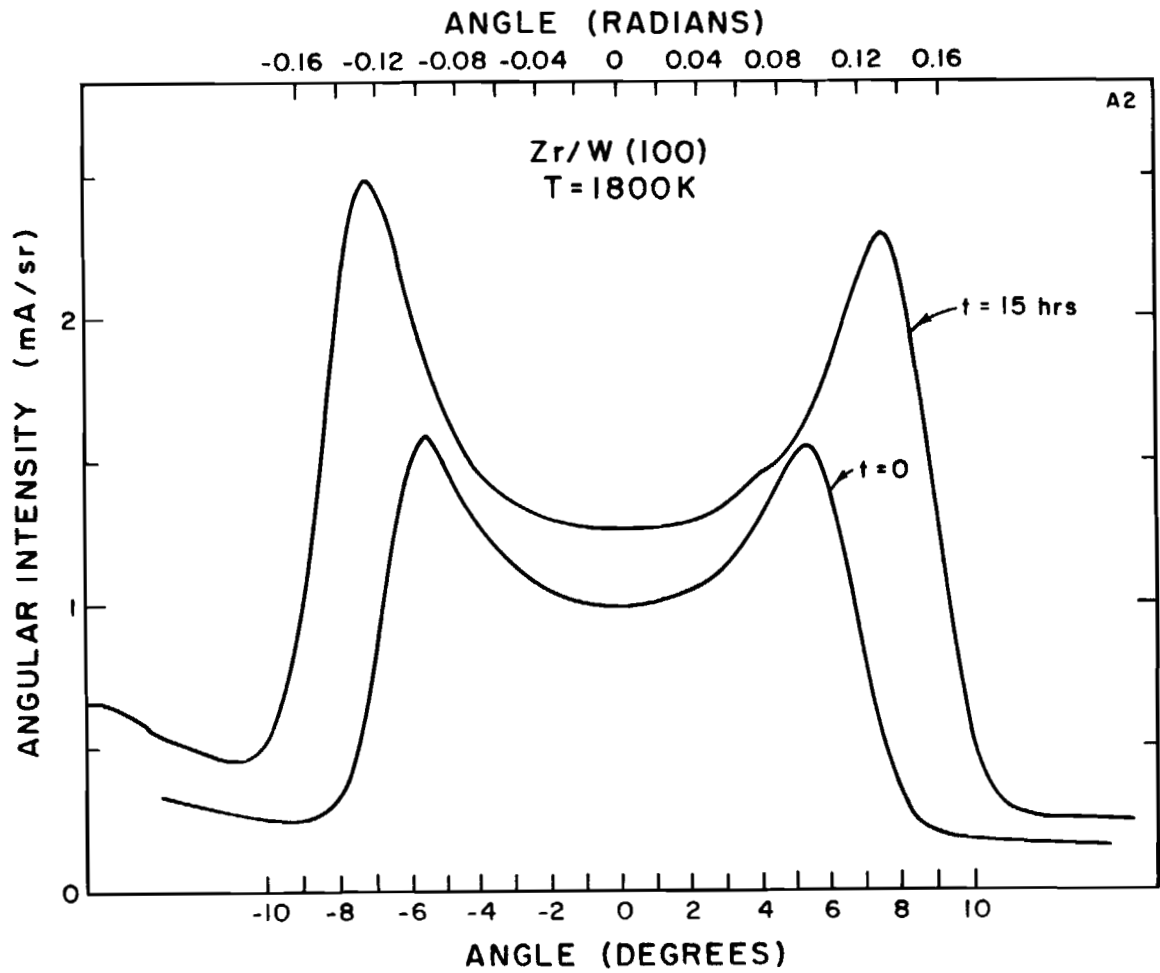


Figure 2-8. Experimental angular intensity distribution for a ZrO/W emitter at 1800 K and 4700 volts. The total current was 105 and 167  $\mu\text{A}$  respectively for the curve taken at  $t = 0$  and the curve taken later at  $t = 15$  hrs.

occurs but at a much slower rate. Since dissolution of the net plane edge atoms occurs via surface diffusion we expect the rate to be temperature dependent according to  $\cdot e^{-E_d/kT}$  where  $E_d$  is the activation energy for removal of atoms from kink sites.

Heating the field built up end form of Figure 2-7(g) in the absence of an applied electric field causes a change shown in pattern (h) which is a return to the initial pattern (a) distribution. The unbuilding process occurs at a slower rate than the build up process at a common temperature. In operation it is advisable to leave the emitter at room temperature when the field is off in order to eliminate the need to repeat the build-up sequence.

The theoretical geometry of the final end form has been previously considered<sup>5</sup> and is presented here since present measurements confirm the theoretical prediction. The original shape of the emitter was assumed to be spherical. It was also assumed that build-up was tangential to the spherical surface on the low index planes, except in the  $\langle 001 \rangle$  direction. From Figure 2-2, the faceted planes adjacent to the (100) end facet are evidently (112) and (110) type planes, the (112) type being along the sides of the (100) facet and the (110) type at the corners of the square (100) facet. As shown in Fig. 2-9, the atomic layers are added to the end facet until the (110) planes form the corners of the (100) facet, at which point further build-up must come from expansion of the (110) planes until the (112) and (100) planes disappear. In the condition shown



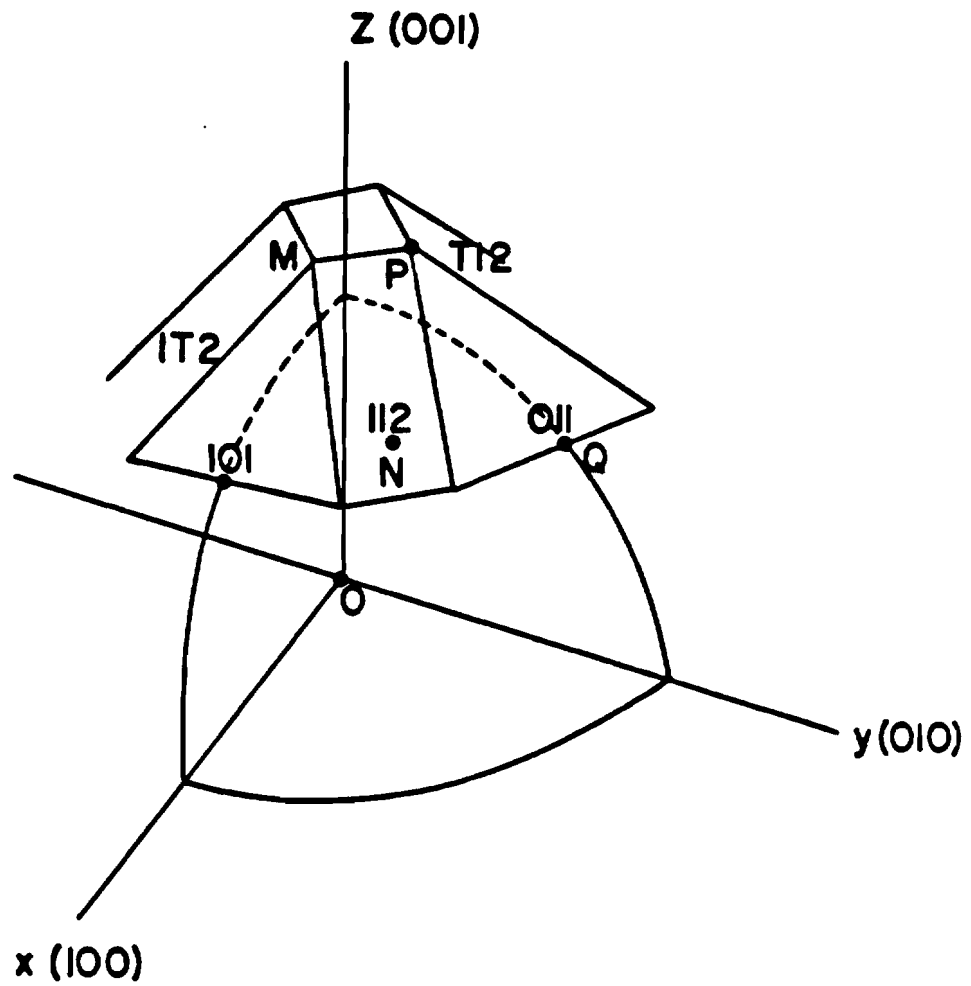


Figure 2-9. Geometrical description for build-up. Taken from Reference 5.

in Figure 2-9, the coordinates of a typical point P are found as the intersection of planes:

$x = 0$                       the plane of the y and z axes

$y + z = r\sqrt{2}$  ,            the tangent plane at Q, (011),

and  $x + y + 2z = r\sqrt{6}$ , the tangent plane at N, (112),

where r is the radius of the sphere. The simultaneous solution yields

$$x_p = 0$$

$$y_p = 0.379 r,$$

and  $z_p = 1.035 r.$

Therefore, the half-diagonal of the end (100) facet is 0.379 r and the radius of the facet, taken as  $y_p/\sqrt{2}$ , is

$$f = \frac{0.379 r}{\sqrt{2}} = 0.268 r$$

Examination of several micrographs, such as Figure 2-1, has given an experimental value of  $f \approx 0.3 r$ .

Under certain conditions (not too well-understood at present) the emitter etching process leaves a spade-shaped tip, with radically different cone angles in orthogonal directions. Figure 2-10 shows micrographs of such a tip. Notice that the (100) end facet maintains its four-fold symmetry but that the sizes of the (110) and (112) facets adjust to conform to the oval cross section created by the etching. The orthogonal axes of the oval correspond

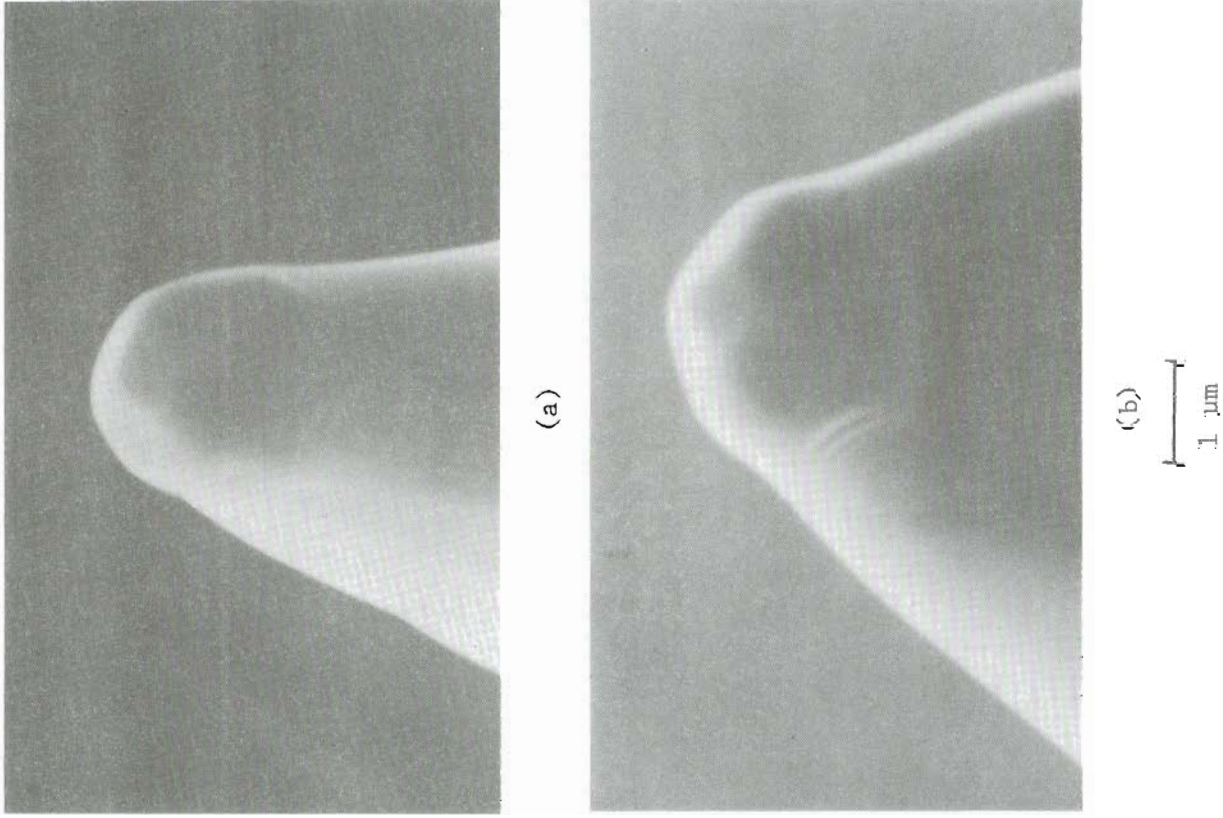


Figure 2-10(a-b). Orthogonal views at  $60^\circ$  tilt of emitter showing different cone angles.

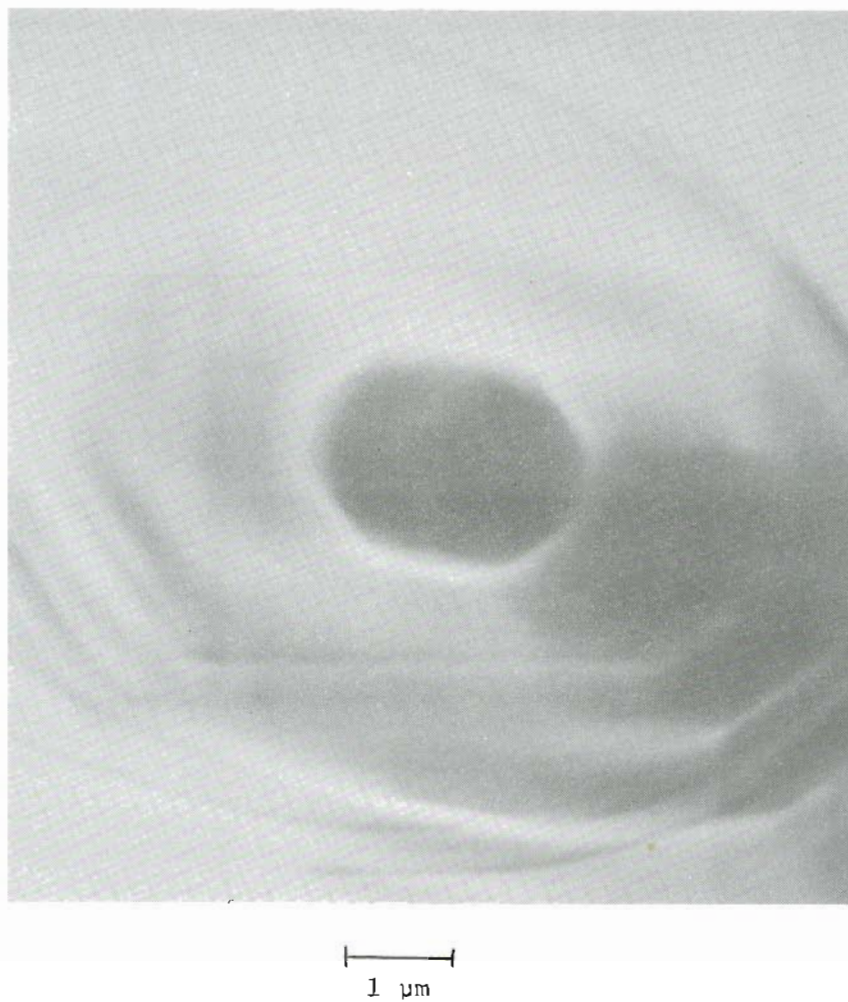


Figure 2-10(c). End-on ( $0^\circ$  tilt) view of emitter showing square (100) facet barely visible in dark area.

to the  $\langle 100 \rangle$  directions.

Another thing to note concerning the Figure 2-10 micrographs is the radical contrast between the set of end facets and the emitter cone. This effect has previously been observed.<sup>6</sup> The Figure 2-10 micrographs were taken at 25 kV. It seems likely that this contrast is due to electron channeling in the  $\langle 100 \rangle$  direction.

The electron optical effect of an emitter such as that in Figure 2-10 is a large astigmatism, which, when corrected by a stigmator (operating at unusually high excitation) still results in an unacceptably large spot diameter in a focused beam system. This has been confirmed experimentally in a dual magnetic lens column.<sup>7</sup>

## REFERENCES

1. J. P. Barbour, F. M. Charbonnier, W. W. Dolan, W. P. Dyke, E. E. Martin and J. K. Trolan, Phys. Rev. 117, 1452 (1960).
2. P. C. Bettler and F. M. Charbonnier, Phys. Rev. 119, 85 (1960).
3. L. W. Swanson and N. A. Martin, J. Appl. Phys. 46, 2029 (1975).
4. L. R. Danielson and L. W. Swanson, Surf. Sci. 88, 14 (1979).
5. R. W. Strayer et al., Field Emission Research, Final Report 1 May 1957 to 30 April 1960, Contract Nonr -2341(00) Authority NR 372-171, Linfield Research Institute, McMinnville, OR.
6. P. B. Mee, J. Appl. Phys., 47, 3904 (1976).
7. D. Tuggle, L. W. Swanson, and J. Orloff, J. Vac. Sci. Technol. 16, 1699 (1979).

## CHAPTER 3

## ANGULAR DISTRIBUTION CHARACTERISTICS

## A. Experimental Angular Distribution Studies

A complete set of angular distributions as a function of anode voltage for Emitter No. A2 of Figure 2-6 is shown here in Figures 3-1 through 3-4. These data were taken at a constant temperature of 1800 K. The voltage range covers 1800 V to 4800 V on the anode with a constant -300 V suppressor voltage. Note that the character of the distribution changes dramatically from the low voltages (Figure 3-1) to the higher voltages (Figures 3-3 and 3-4). The appearance of the "horns" on the sides of the angular distribution at higher voltages can be accounted for by the edges of the (100) facet, which cause a local increase in surface electric field. The absence of the "horns" at low voltage can be ascribed to a shift in the regime of emission from Extended Schottky to Schottky as the voltage is decreased. More quantitative descriptions of these effects are presented later in this section and in the following sections.

Figures 3-5 and 3-6 show two-dimensional contour maps of the emission distribution at two different voltages. The more uniform emission for the lower voltage is clearly observed. In addition a slight elliptical shape of the emission cross section can be seen. In most cases the emission cross section is circular; the elliptical

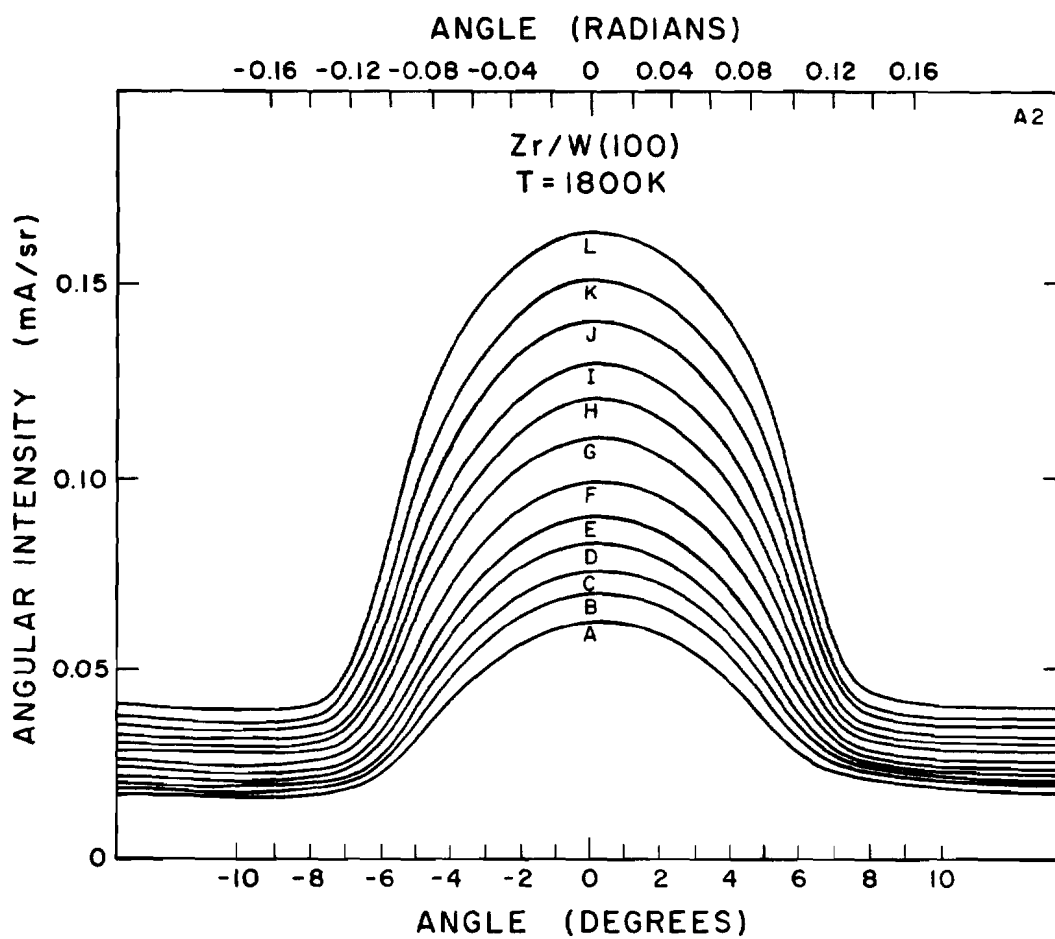


Figure 3-1. Experimental angular distributions. Curves A through L correspond to anode voltages 1800 V through 2900 V in 100 V increments. Emitter radius  $\approx 0.8 \mu\text{m}$ .



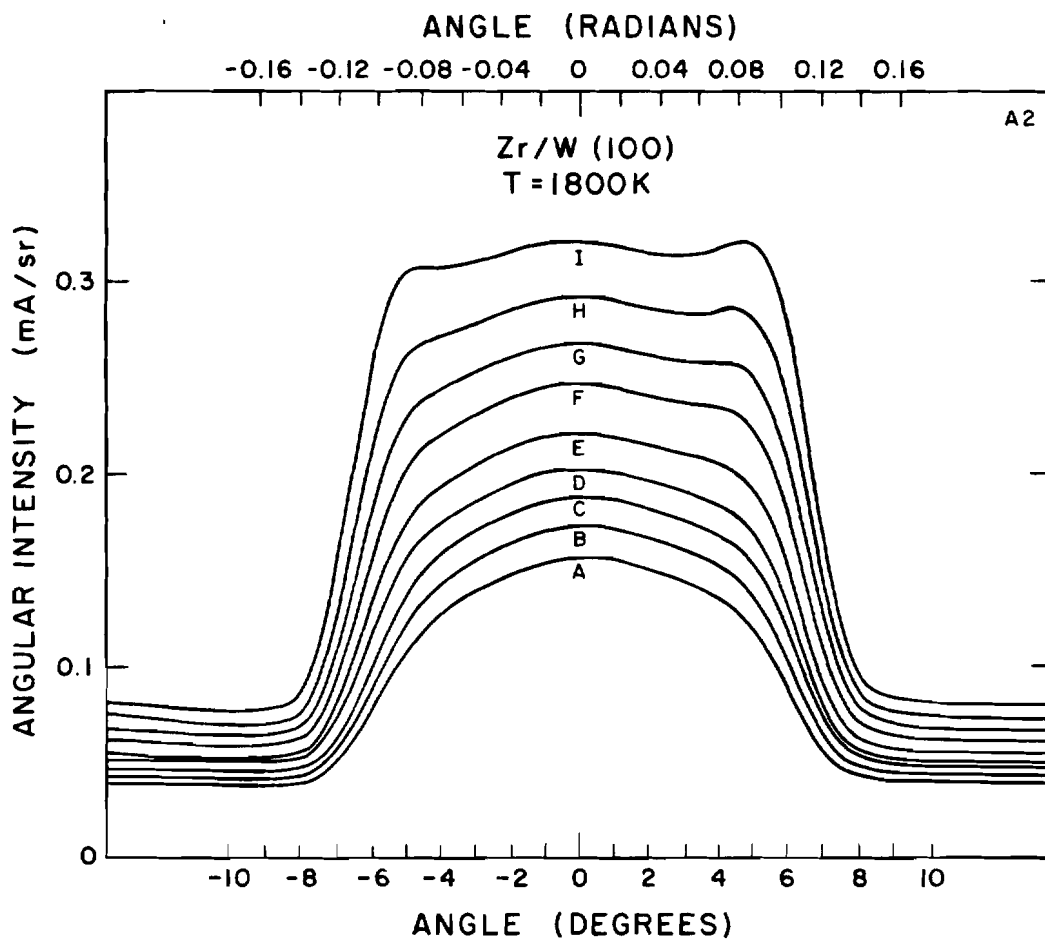


Figure 3-2. Experimental angular distributions. Curves A through I correspond to anode voltages 2900 V through 3700 V in 100 V increments. Emitter radius  $\approx 0.8 \mu\text{m}$ .

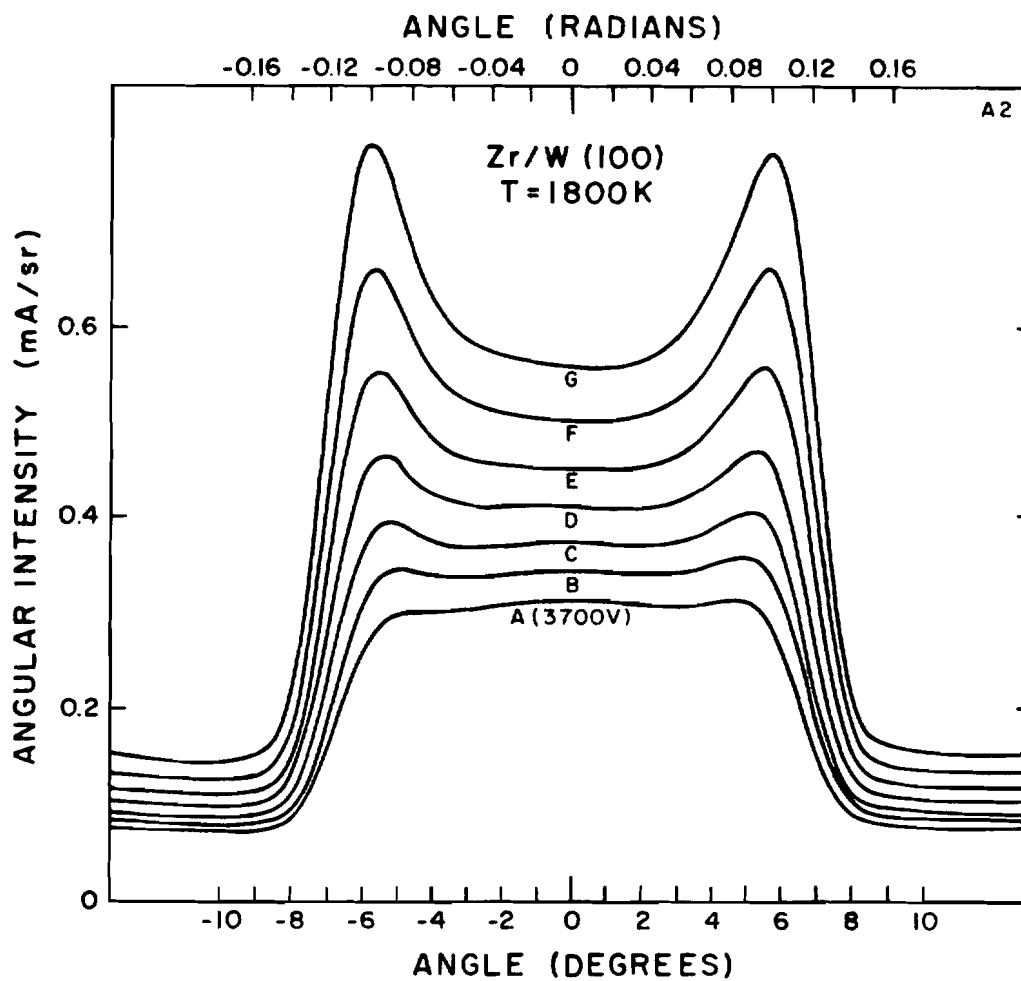


Figure 3-3. Experimental angular distribution. Curves A through G correspond to anode voltages 3700 through 4300 V in 100 V increments. Emitter radius  $\approx 0.8 \mu\text{m}$ .

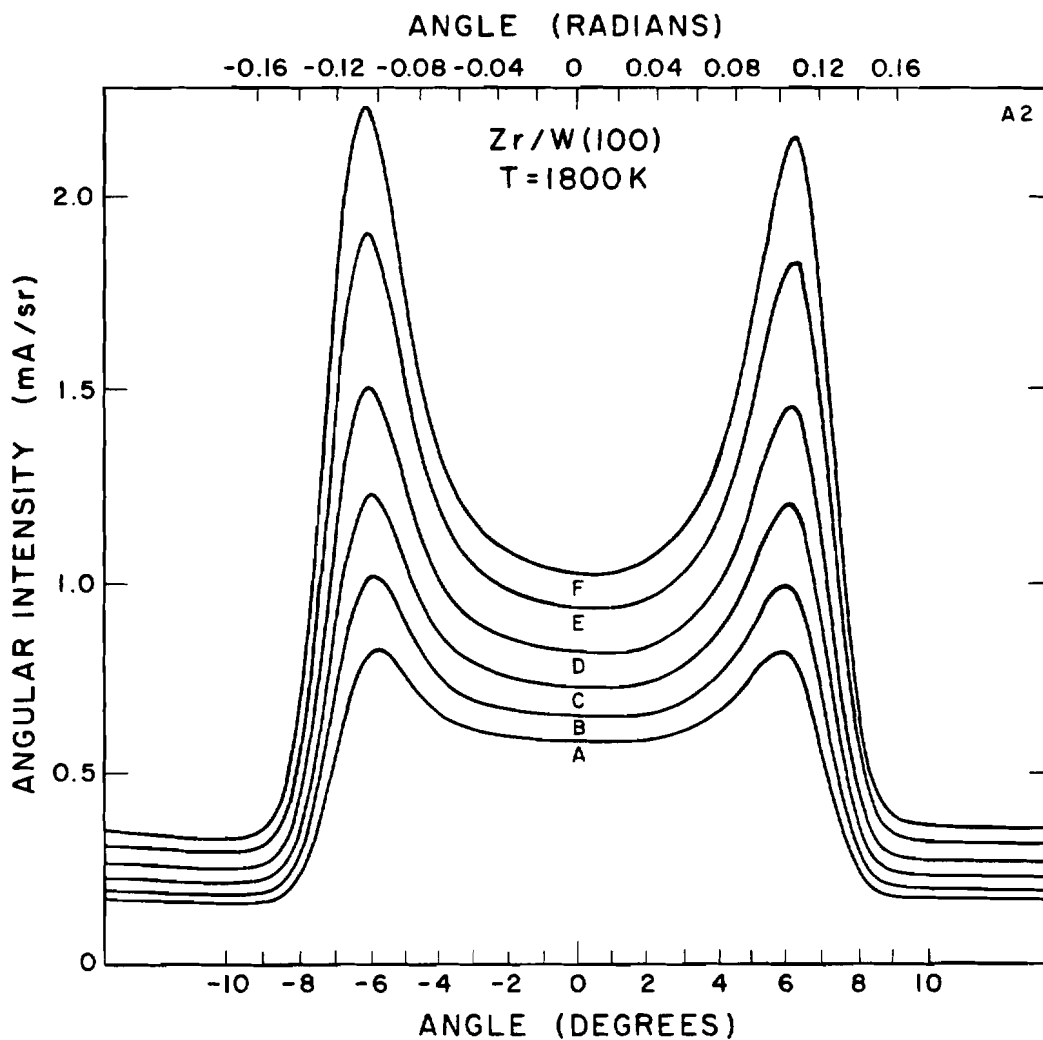


Figure 3-4. Experimental angular distribution. Curves A through F correspond to anode voltages 4300 V through 4800 V in 100 V increments. Emitter radius  $\approx 0.8 \mu\text{m}$ .

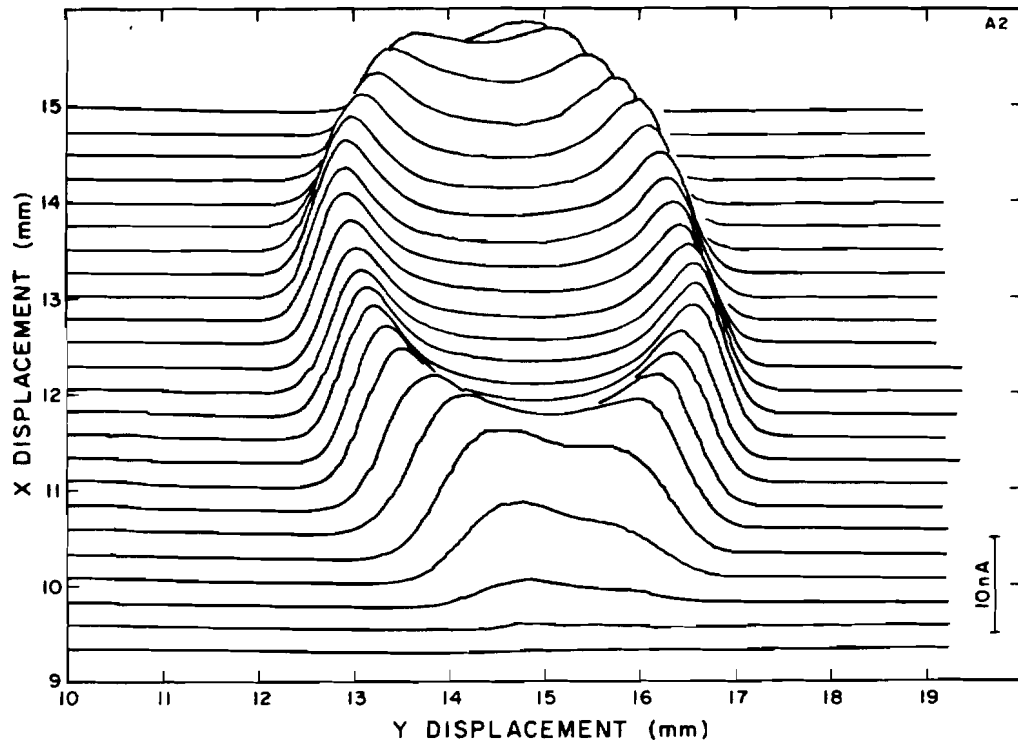


Figure 3-5. Two-dimensional current distribution at 1800 K and 4700 V taken by x-y movement of the Faraday collector. Initial x and y positions were 9 and 10 mm respectively for the lowest curve. Subsequent curves in increasing x were incremental 0.25 mm. Vertical scale on lower right indicates current scale factor.

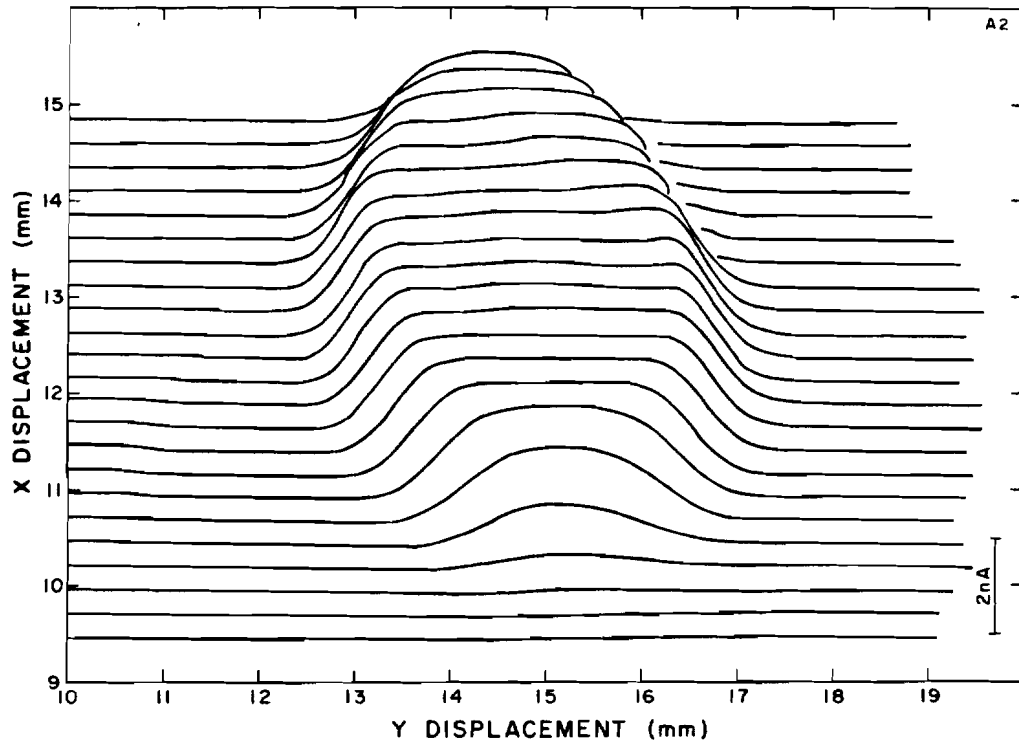


Figure 3-6. Two-dimensional current distribution at 1800 K and 3800 V taken by x-y movement of the Faraday collector. Initial x and y positions were 9 and 10 mm respectively for the lowest curve. Subsequent curves in increasing x were incremental 0.25 mm. Vertical scale on lower right indicates current scale factor.

cross section is believed to be due to an elliptical cross section of the conical portion of the emitter, as in Figure 2-10.

In Figure 3-7, the emission angular intensity distribution of a Zr/W(100) emitter is shown at various temperatures. For this particular emitter an interesting result was observed in which the central emission current  $I_c$  increased with  $T$  while the edge current  $I_e$  went through a maximum. This result is shown in more detail in Figure 3-8 where  $I_e$  and  $I_c$  are plotted vs  $I$  at three different voltages. As seen in Figure 3-8 the maximization in  $I_e$  vs  $T$  is more dramatic at the higher voltages and results in an enhanced uniformity of the emission distribution. A similar temperature effect also occurs in the ring structure distribution obtained during field build-up. Figure 3-9 shows this case. Although the currents detected from the rings do not go through a maximum, it is obvious that they are not proportional to the central emission current.

This temperature effect on edge emission current density is not easily explainable, given a uniform (100) facet with only a field gradient (no work function or temperature gradient). Even assuming fixed gradients along the surface, a current density decrease is never predicted for an increase in temperature, so it is likely that either a local field decrease at the facet edge or a local work function increase as a function of temperature is occurring. The coverage of cesium adsorbed on a tungsten emitter has been shown to be a function of the local electric field.<sup>4</sup> The facet edge is a region of high electric field relative to the center.

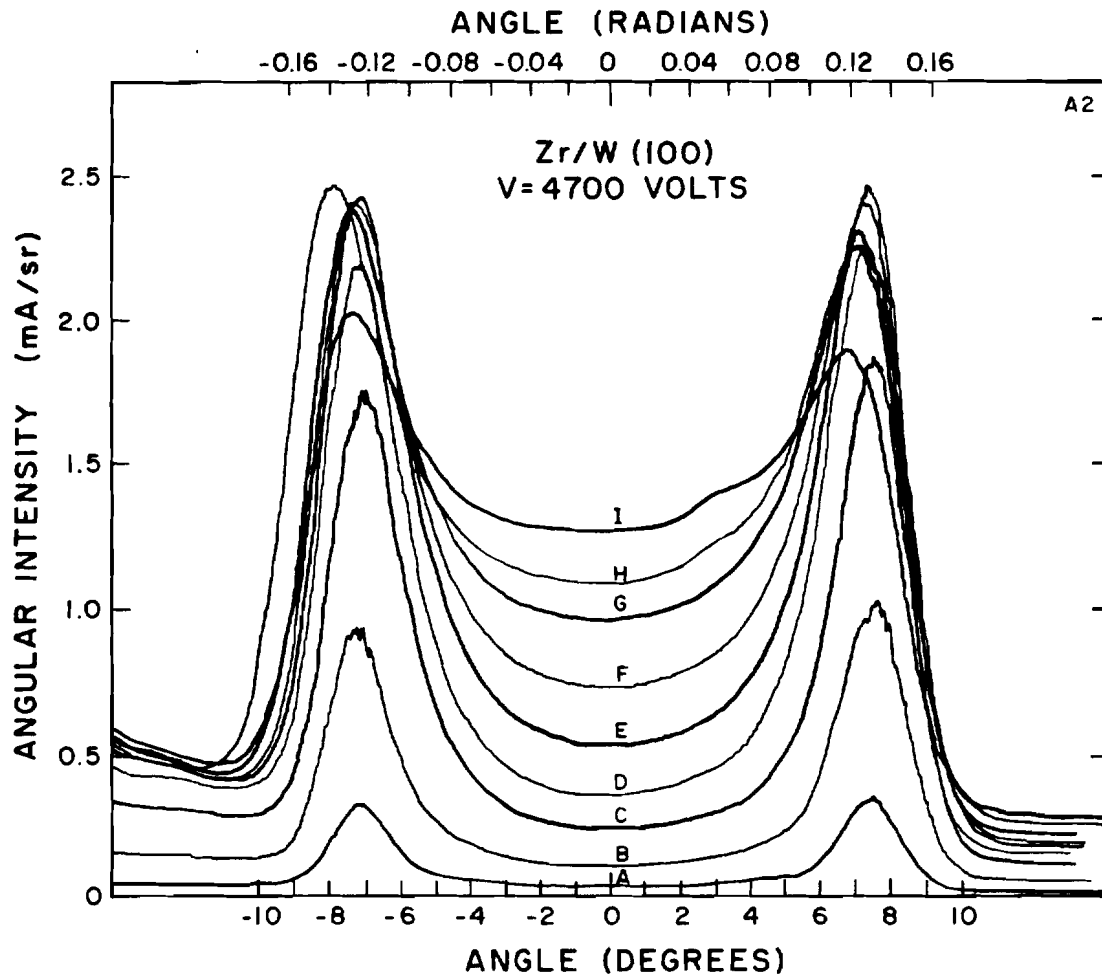


Figure 3-7. Experimental angular distribution for the  $\beta_c = 1.18 \times 10^3 \text{ cm}^{-1}$  Zr/W emitter at 4700 volts and various temperatures. A to I 1100 to 1900 K in  $100^\circ$  increments.

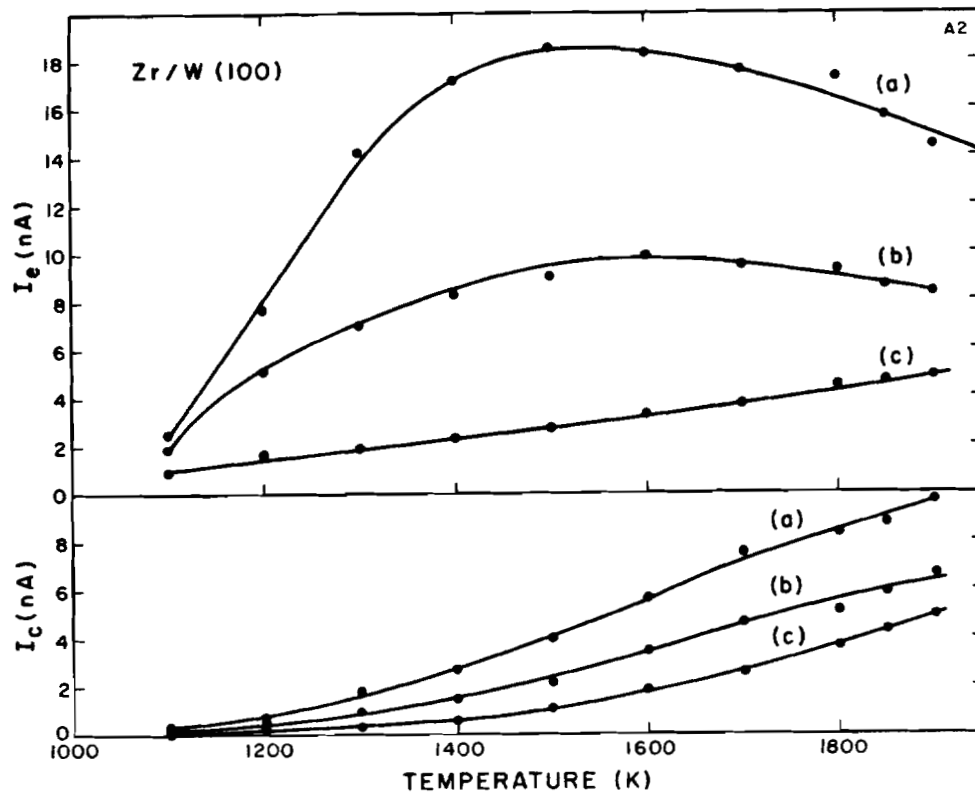


Figure 3-8. Central ( $I_c$ ) and edge ( $I_e$ ) current vs temperature at various voltages from the Figure 3-7 emitter results. (a) 4700 V; (b) 4500 V; (c) 4000 V.



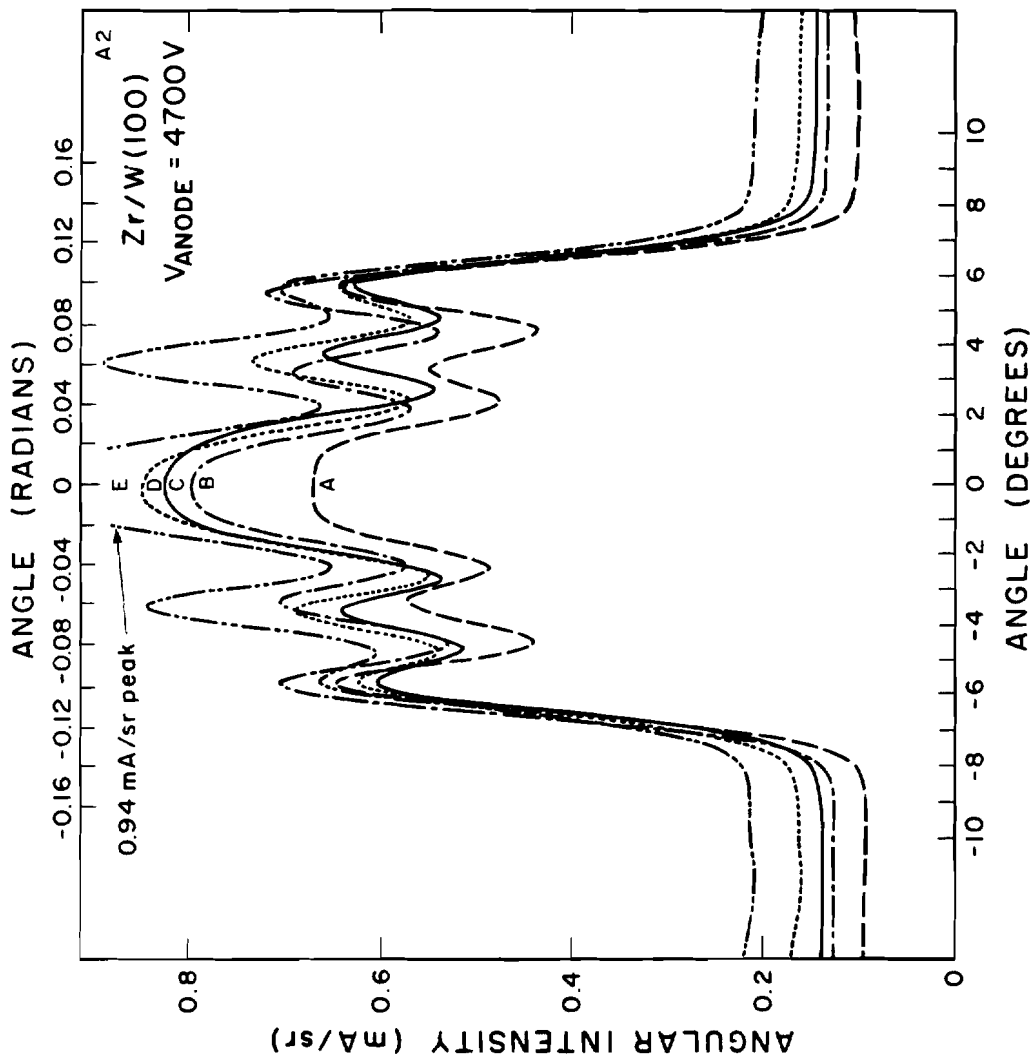


Figure 3-9. Experimental angular intensity distributions. Curves A through E correspond to temperatures 1600, 1700, 1800, 1850, 1900 K.

Figures 3-3 and 3-10 are comparisons of Zr/W emitters of radii 0.8 and 2.3 micrometers, respectively. Several important effects of emitter size can be noted from these results. First, the increase in emission due to the field enhancement at the net plane edge occurs at a much larger angular intensity for the larger radius emitter. For example, the condition of a nearly flat emission distribution occurs at 0.35 mA/sr for the Figure 3-3 emitter, whereas for the larger radius Figure 3-10 emitter it occurs at 1.4 mA/sr. However, for both emitters the half angle of emission is  $\sim 7^\circ$ .

One of the more unexpected results is shown in Figures 3-11 and 3-12 where the total emission current and the emission from the central and edge portions of the net planes (using a Faraday cup subtending a 0.0031 rad full angle at the emitter) are plotted according to the Schottky formula, that is

$$\ln I_p = A + 3.8 \frac{(\beta V)^{1/2}}{kT} \quad (3-1)$$

where  $\beta = F/V$  is in  $\text{\AA}^{-1}$  and  $k = 8.61 \times 10^{-5}$  eV/K. Note that the probe current  $I_p$  has been assumed to be proportional to  $J$ , implying a constant emitting area. Justification for this assumption will be given in Section D of this chapter. The background current (the current measured by the Faraday cup at angles  $>10^\circ$  off emission axis) was subtracted from the central and edge emission to minimize error

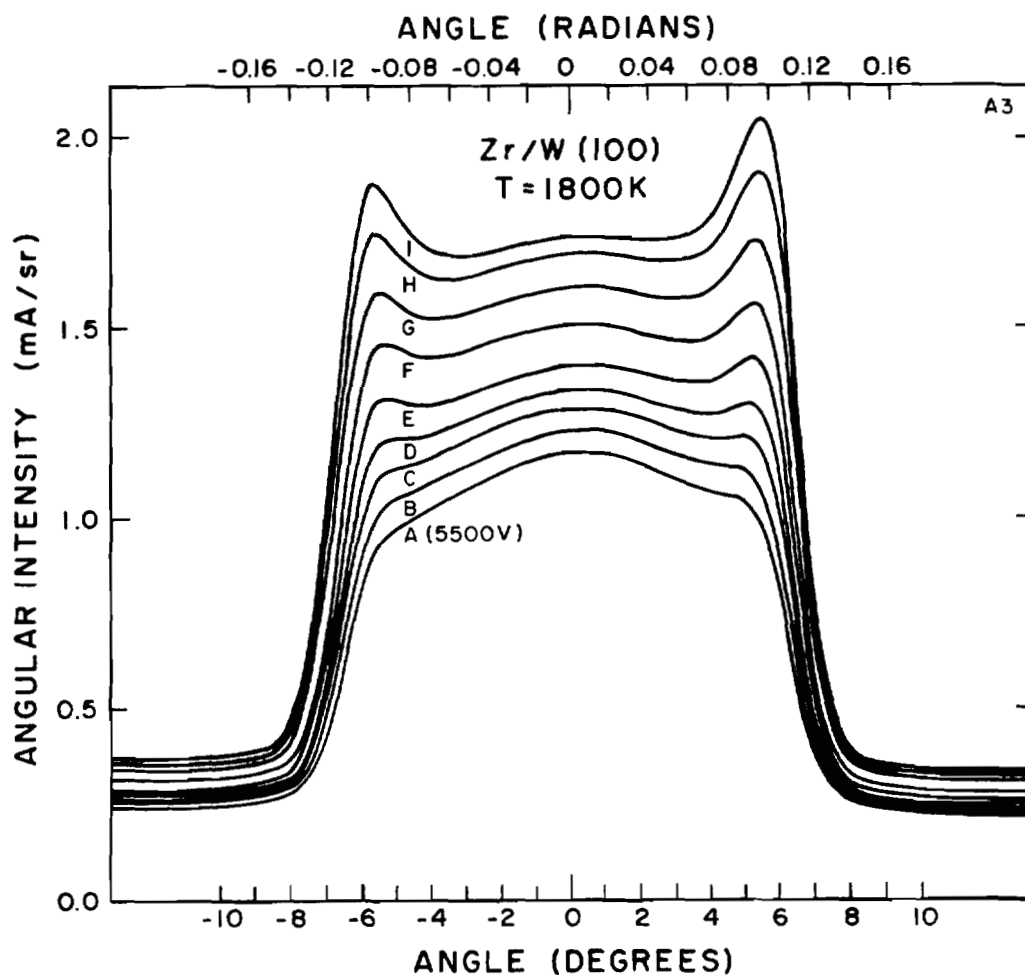


Figure 3-10. Experimental angular intensity distribution for a Zr/W emitter at 1800 K and various voltages: A to I 5500 to 6300 V in 100 V increments. Faraday cup full angle = .0031 rad. Emitter radius  $\approx 2.3 \mu\text{m}$ .

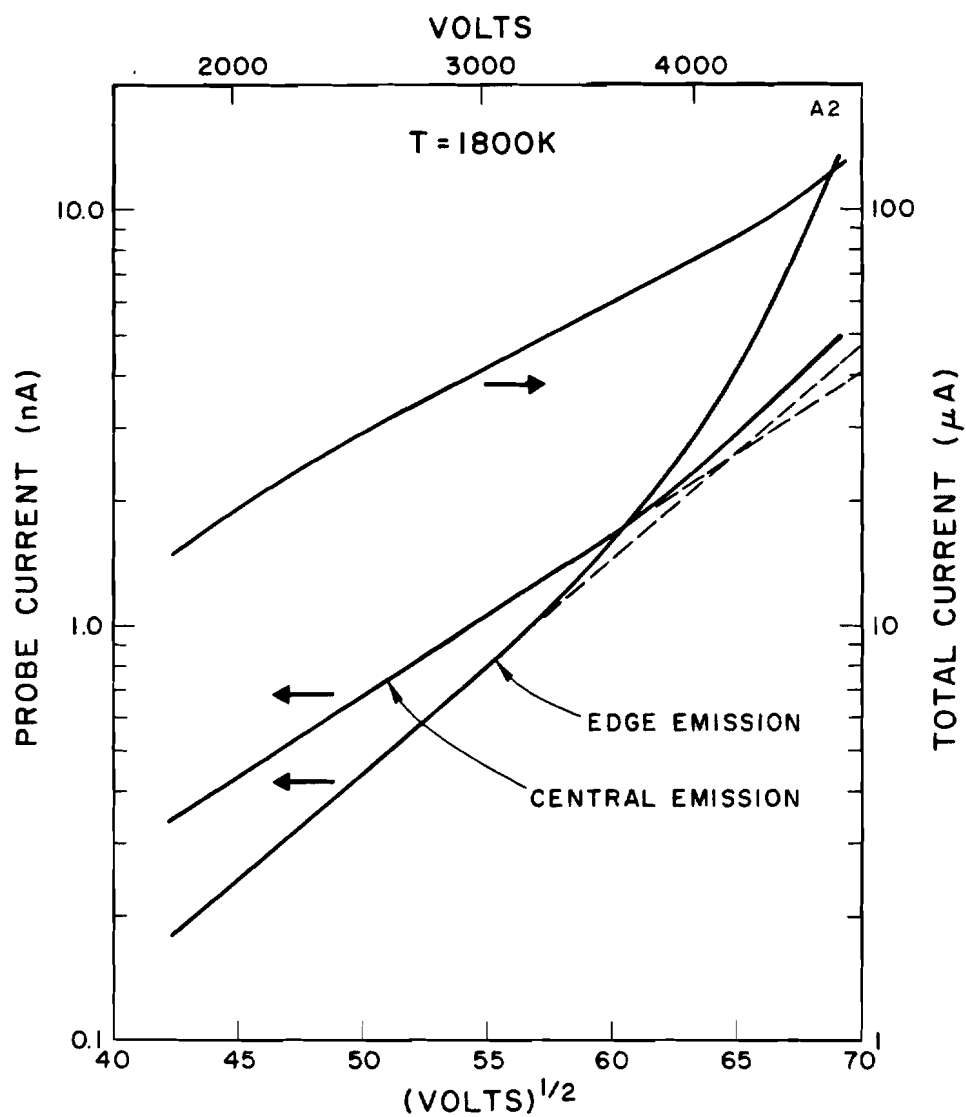


Figure 3-11. Schottky plot of the total, edge and central emission current of the Figure 3-3 emitter. The dashed lines are extensions of the Schottky slopes. Background current seen in angular distributions was subtracted from central and edge emission. Emitter radius  $\approx$  0.8  $\mu\text{m}$ .

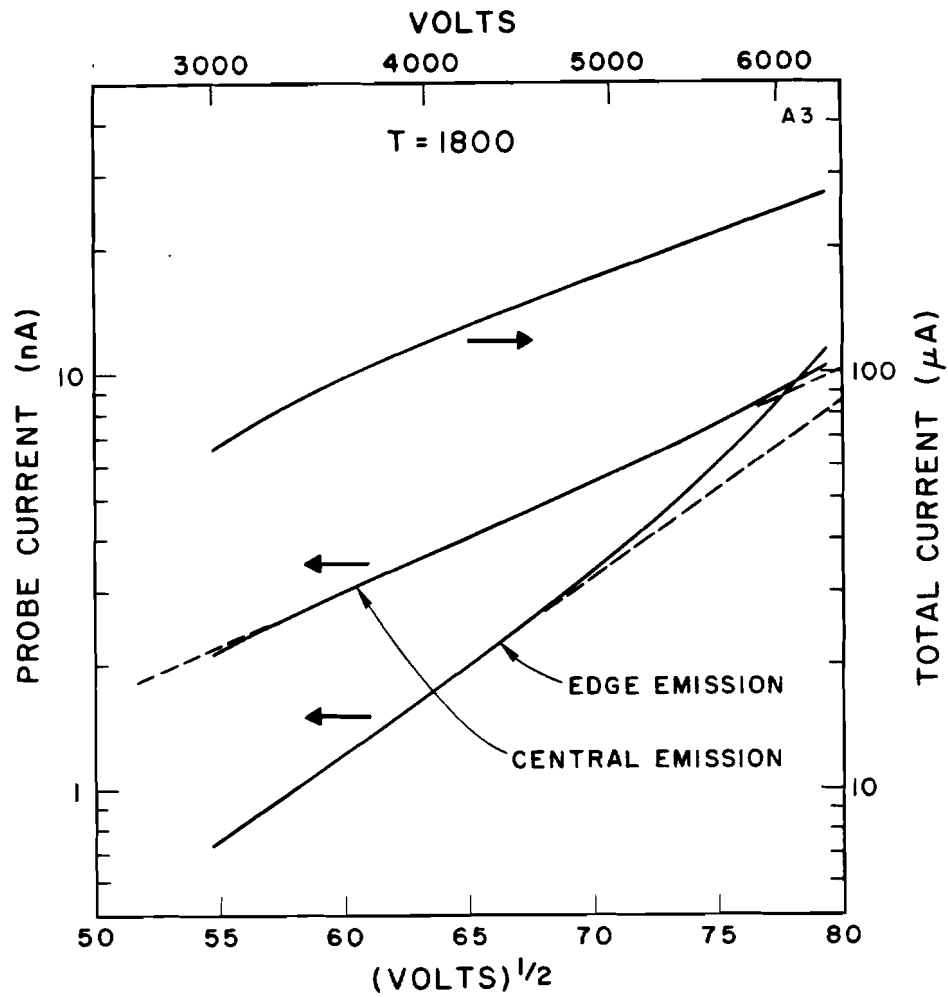


Figure 3-12. Schottky plot of the total, edge and central emission current of the Figure 3-10 emitter. The dashed lines are extensions of the Schottky slopes. Background current seen in angular distributions was subtracted from central and edge emission. Emitter radius  $\approx 2.3 \mu\text{m}$ .

in the Schottky slope. For the larger emitter result shown in Figure 3-12 the Schottky formula agrees with the central emission results up to an emission level of  $\sim 1$  mA/sr. In contrast the small emitter results in Figure 3-11 show agreement with the Schottky formula only up to 0.26 mA/sr for the central emission. These results show, somewhat surprisingly that for emitter radius  $> 0.9 \mu\text{m}$  that in the range of useful emission levels the central emission from these emitters is basically Schottky mode emission.

By plotting the straight line portion of the Figures 3-11 and 3-12 data according to Eq. (3-1) the values of  $\beta$  for the central ( $\beta_c$ ) and edge ( $\beta_e$ ) emission regions could be calculated (see Table 3-1). From Eq. (3-1),  $\beta$  is related to the base-10 log slope by

$$\beta(\text{cm}^{-1}) = 0.2724 (\text{Slope}_{10})^2 T^2 \quad (3-2)$$

where

$$(\text{slope}_{10}) = \frac{\Delta(\log I_p)}{\Delta(V^{1/2})}$$

and  $T$  = absolute temperature.

Interestingly, the ratio of  $\beta_e/\beta_c$  is 2.52 and 1.76 for the large and small radius emitters respectively. This is probably due to the larger size of the facet for the large radius emitter which means a greater depression of the central net plane field. SEM photos of the fully built up emitters suggest that the radius of the facet is 0.3  $r$ , where  $r$  is the overall emitter radius.

Table 3-1

Summary of the values of  $\beta_e$  and  $\beta_c$  and the central emission field strengths  $F_c$  and voltages  $V$  required for 1 mA/sr for emitters of two different radii  $r$ . The total current is  $I_T$  and  $T = 1800$  K.

Emitter No.	$\beta_c$ (cm <sup>-1</sup> )	$\beta_e$ (cm <sup>-1</sup> )	$F_c$ *(V/cm)	V*(volts)	$I_T$ (μA)
A2 $r = 0.8 \mu\text{m}$	1321	2321	$6.8 \times 10^6$	5140	130
A3 $r = 2.3 \mu\text{m}$	623	1570	$3.5 \times 10^6$	5625**	180

\*Values for on axis emission levels of 1 mA/sr (corrected for background emission)

\*\*Extrapolated value.

## B. Computer Studies of Surface Electric Field for the Faceted Emitter

Since the angular distribution of current is highly dependent on the field at the surface of the emitter, and since at present we know of no studies of the emitter surface field which take into account the effect of the facet at the apex of the emitter, we have done a series of computer calculations to investigate the surface field and resulting current density for various conditions.

Most of the experimental angular distributions show a relatively flat central current distribution with peaks or "horns" at the edges of the distribution. The field distribution across the facet can be used in conjunction with the work function and the temperature to compute the current density at the surface of the emitter. This initial current distribution is then used to predict the angular current distribution observed downstream of the anode aperture by making use of trajectories calculated from the emitter surface to a region of field-free space past the anode. At high current densities, an iterative space charge calculation will reduce the electric field at the emitter surface and therefore reduce the current density. In this section, we will not take space charge into account.

Figure 3-13 shows three emitter profiles and the surrounding equipotentials for faceted emitters of radii 0.2, 0.5, and 1.0  $\mu\text{m}$ . The facet radius in all three cases is 0.3 times the emitter radius, which is typical of the emitters we have micrographed. The calculated field at the surface normalized to the apex field is shown in Figure



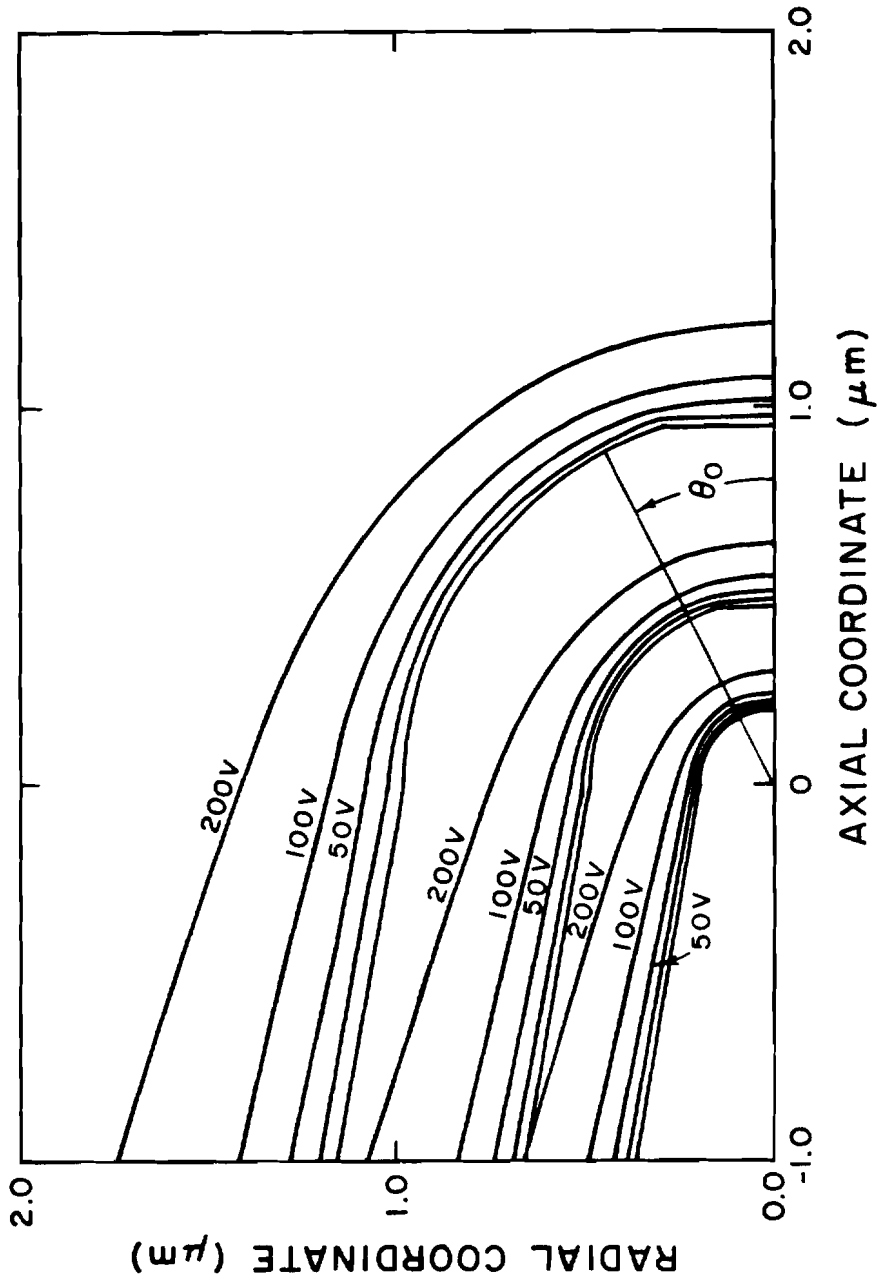


Figure 3-13. Emitter profiles with equipotentials for emitter radii 0.2, 0.5 and 1.0  $\mu\text{m}$ . Facet radius/emitter radius =  $f/r = 0.3$  for all cases.

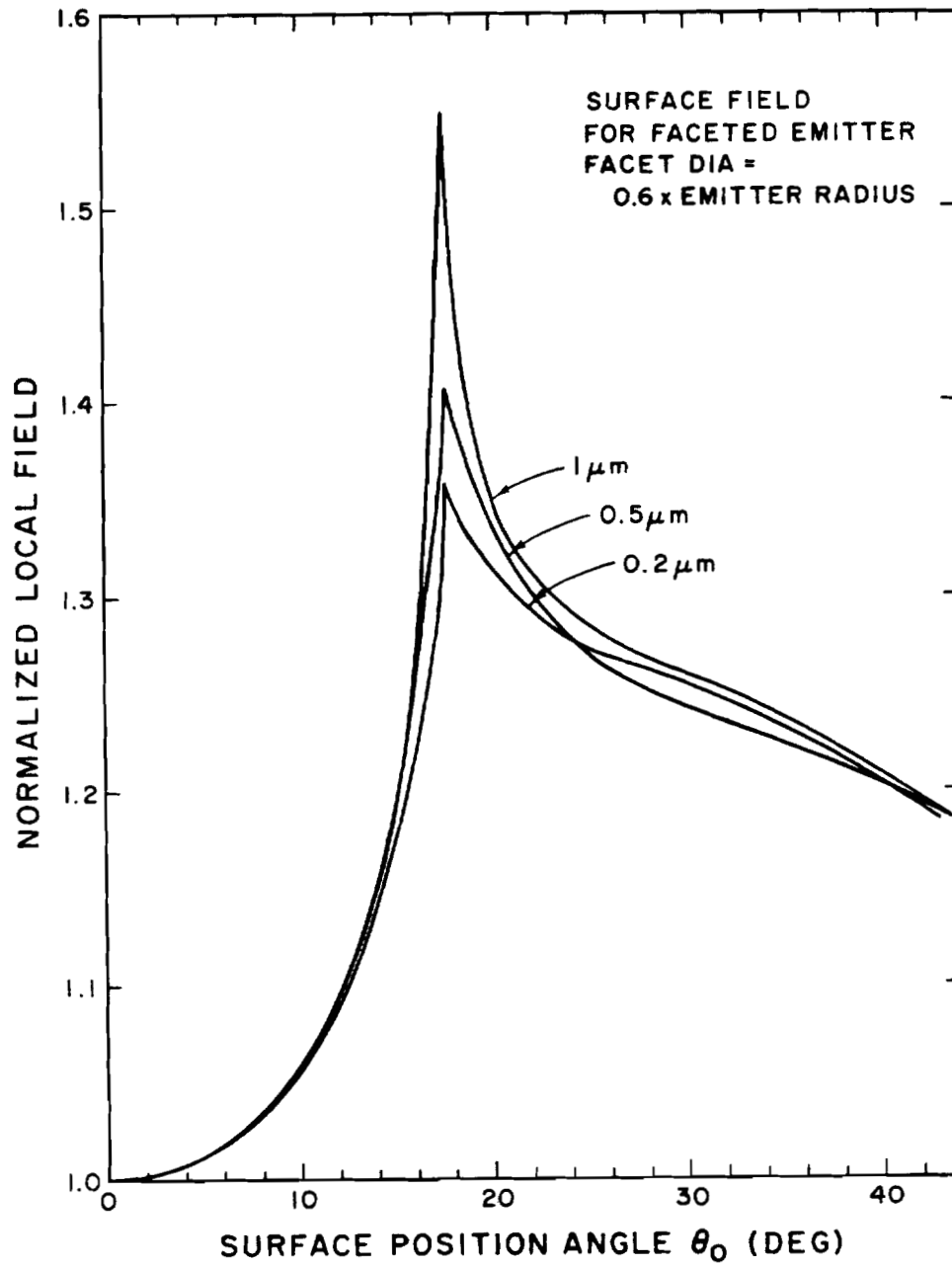


Figure 3-14. Normalized surface field for the three emitter profiles of Figure 3-13. Emitter radii are indicated.

3-14. The absolute values of the field will be treated later. It is apparent from Figure 3-14 that if the facet radius is in fact a fixed fraction of the emitter radius then the surface field distribution is virtually unchanged over most of the facet and the only effect of increasing emitter radius is to increase the ratio of edge to central field. This would result in a larger ratio of edge to central emission, neglecting space charge effects. The unexpected field distribution crossover occurring at  $\theta_0 \approx 24^\circ$  is apparently due to a difficulty in resolving the curved emitter surface with a rectangular finite difference mesh.

Having held the ratio of facet radius to emitter radius ( $f/r$ ) constant at 0.3 and changed the emitter radius, we now hold the emitter radius constant at 1  $\mu\text{m}$  and vary the  $f/r$  ratio from 0 (spherical end) to 0.6. Figures 3-15 and 3-16 show the equipotentials for the cases  $f/r = 0.1$  and  $f/r = 0.6$  respectively. The resulting normalized surface field is shown in Figure 3-17. We see here a very significant change in surface field with facet size for a constant radius emitter. Since we have already observed collapsing rings of emission in the angular distribution pattern (c.f. Figure 2-7), Figure 3-17 indicates how we would expect the surface field to change as the facet collapses. If the  $f/r$  ratio is a function of radius or of temperature then we can predict the ratio  $\beta_e/\beta_c$  where  $\beta = F/V$  and  $e$  and  $c$  refer to edge and central areas of the angular distribution respectively.

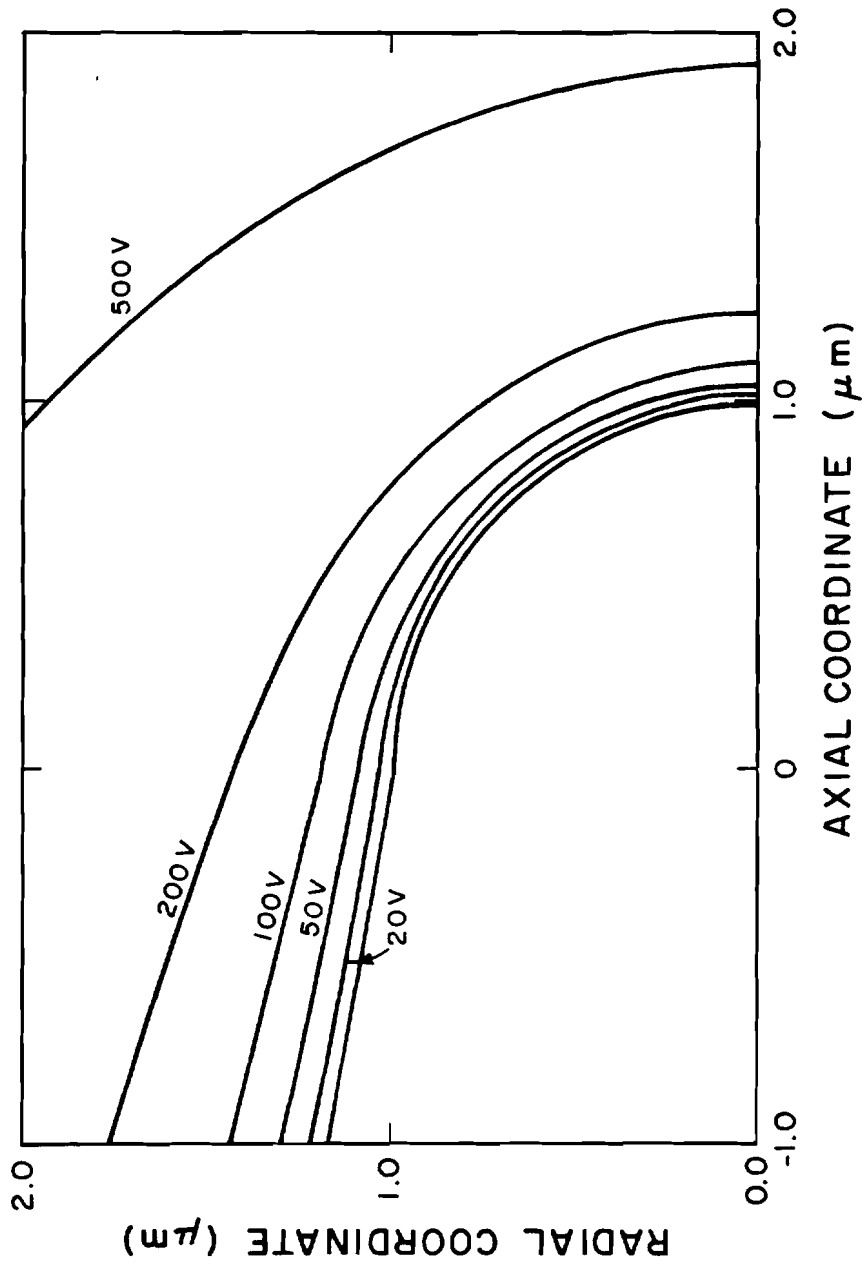


Figure 3-15. Emitter profile with equipotentials for  $r = 1 \mu\text{m}$ ,  $f/r = 0.1$ .

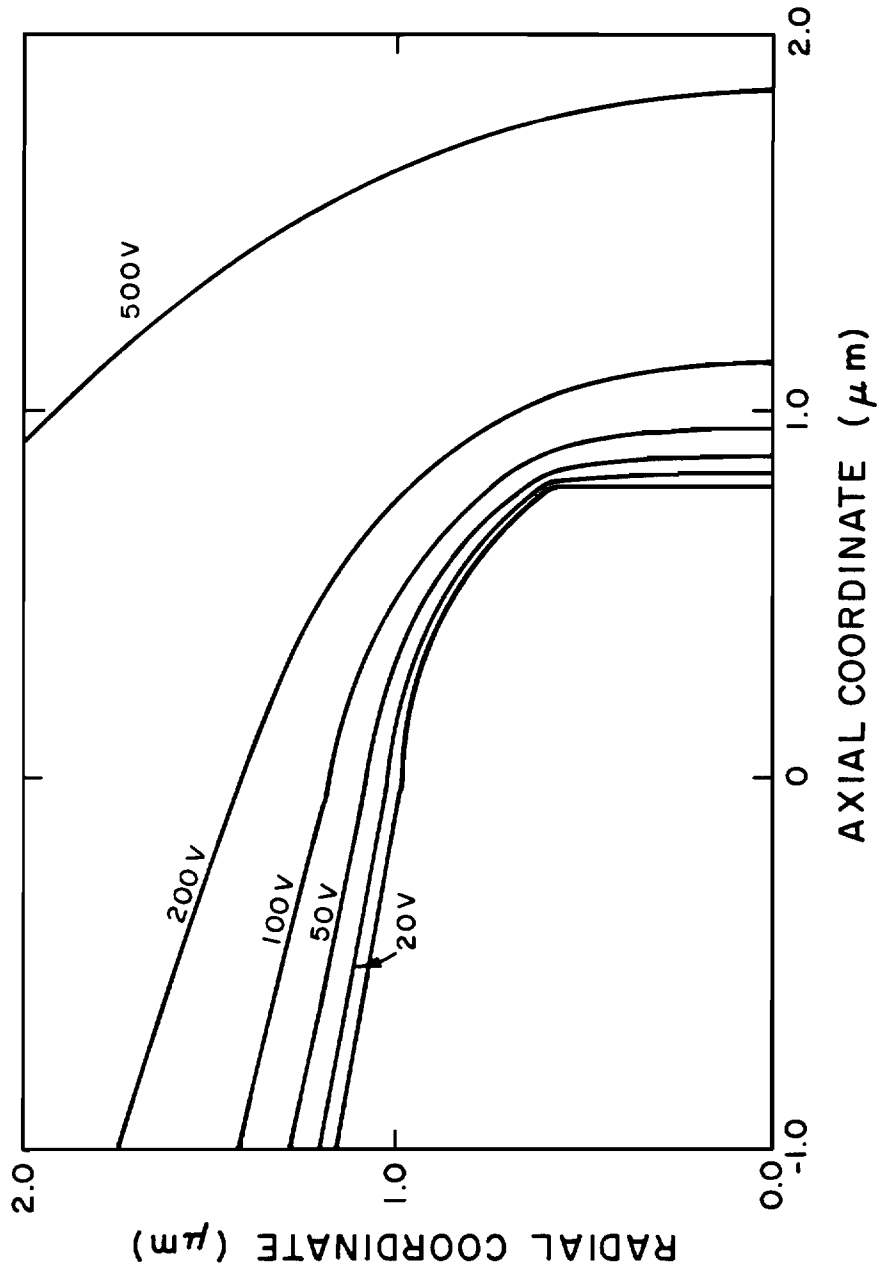


Figure 3-16. Emitter profile with equipotentials for  $r = 1 \mu\text{m}$ ,  $f/r = 0.6$ .

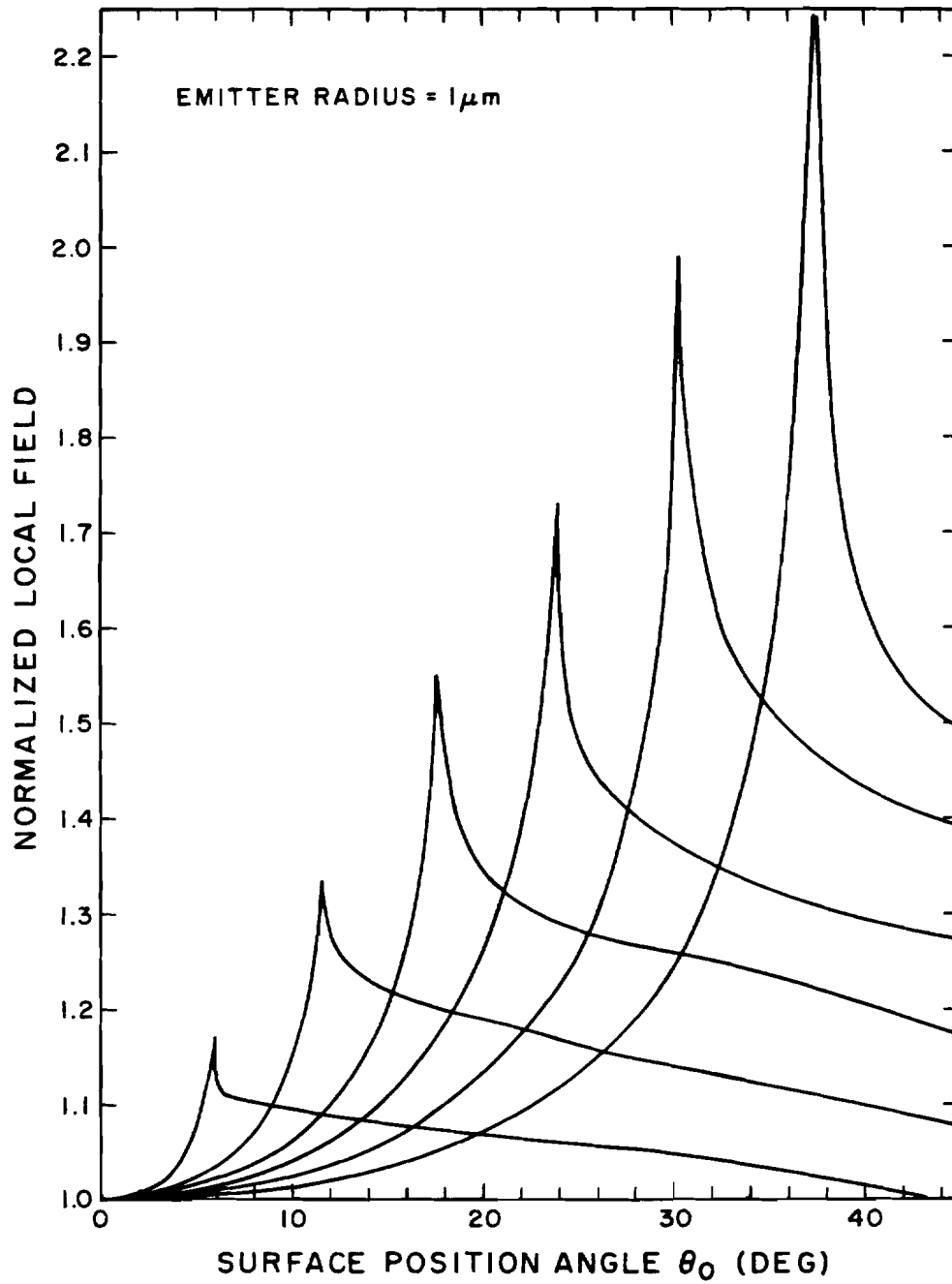


Figure 3-17. Normalized surface field for  $r = 1 \mu\text{m}$ ,  $f/r = 0.1, 0.2, 0.3, 0.4, 0.5, 0.6$ .

If a series of calculations is made for various emitter radii and various  $f/r$  ratios, all of the data on the field produced at the apex for a constant anode voltage can be reduced to two graphs for nearly two decades change in emitter radius. These are Figures 3-18 and 3-19. In Figure 3-18 the apex field vs. facet size is plotted. This latter curve was found to be independent of emitter radius for values from 0.1 to 10.0  $\mu\text{m}$ . In Figure 3-19 the apex field for a spherical and faceted ( $f = 0.6 r$ ) emitter is plotted as a function of emitter radius for the typical conditions of anode voltage = 7500 V, suppressor voltage = -300 V with respect to the emitter. The corresponding field factor  $\beta_c = F/V$  for the central area (apex) on the facet is also given in Figure 3-19.

In Table 3-2 we summarize  $\beta_c$  and  $\beta_e$  for the two different emitters investigated.

TABLE 3-2

 $\beta$  Ratio from Table 3-1 Data

<u>Emitter No.</u>	<u><math>\beta_c</math> (<math>\text{cm}^{-1}</math>)</u>	<u><math>\beta_e</math> (<math>\text{cm}^{-1}</math>)</u>	<u><math>\beta_e / \beta_c</math></u>
A2	1321	2321	1.76
A3	623	1570	2.52

Using Figure 3-19 and the Table 3-2 values of  $\beta_c$  we infer radii of 2.0 and 0.8  $\mu\text{m}$  respectively for A2 and A3. Using the Table 3-2  $\beta_e / \beta_c$  values and the results of Figure 3-14 (since Figure 3-14 was calculated for constant anode voltage  $V$ ,  $\beta$  is directly proportional

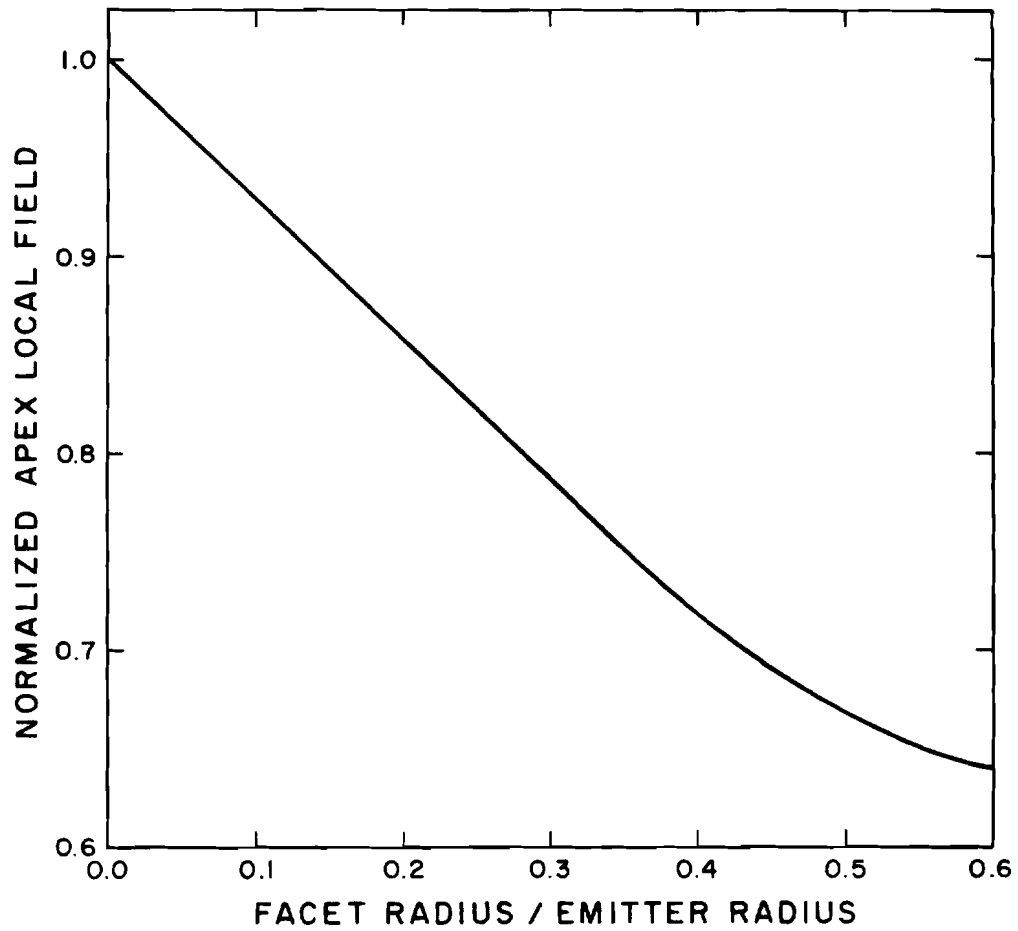


Figure 3-18. Normalized surface field at emitter apex for all radii emitters, variable  $f/r$ .



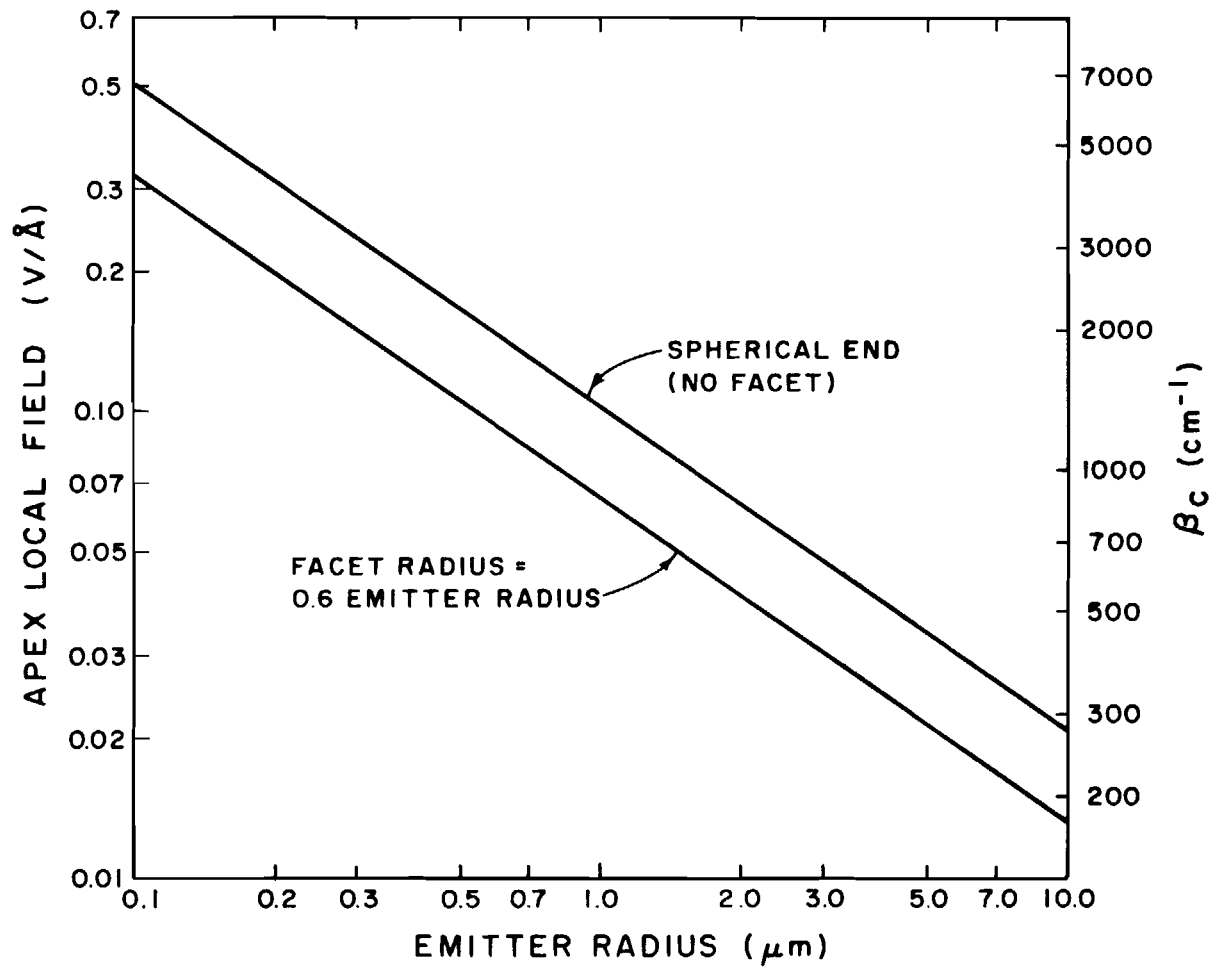


Figure 3-19. Surface field at apex of emitter for  $V_{\text{ANODE}} = 7500 \text{ V}$ ,  $V_{\text{BIAS}} = -300 \text{ V}$ . Resulting values of field factor for apex emission ( $\beta_c$ ) appear in right hand vertical axis.

to F) and Figure 3-17 we can estimate the size of the facet.

Assuming for the moment the values 2.0  $\mu\text{m}$  and 0.8  $\mu\text{m}$  for the radii, the  $\beta_e/\beta_c$  value of 2.52 appears unreasonable for any  $f/r$  in Figure 3-17. For emitter A2 the value  $\beta_e/\beta_c = 1.76$  is too high if  $f/r = 0.3$ ; by going to Figure 3-17 we find that if  $f/r = 0.4$  then  $\beta_e/\beta_c = 1.75$  for  $r = 1.0 \mu\text{m}$ . We conclude from measurements of  $\beta_e$  and  $\beta_c$  the following characteristics for the emitters.

TABLE 3-3

Experimental  $r$  and  $f/r$  Values

<u>Emitter No.</u>	<u><math>\beta_c</math> (<math>\text{cm}^{-1}</math>)</u>	<u><math>\beta_e</math> (<math>\text{cm}^{-1}</math>)</u>	<u><math>\beta_e/\beta_c</math></u>	<u><math>r</math> (<math>\mu\text{m}</math>)</u>	<u><math>f/r</math></u>
A2	1321	2321	1.76	0.8	0.4
A3	623	1570	2.52	2.0	>0.6

The fairly reasonable results for radius make it probable that from the  $\beta_c$  values one can directly infer the emitter radius. The unreasonable  $f/r > 0.6$  value derived from  $\beta_e/\beta_c$  indicates a problem with the  $\beta_e$  data. A possible explanation for an erroneous value of  $\beta_e$  lies in the fact that the Schottky slope for the edge emission is derived from the low voltage end of the I-V data (see Figures 3-11 and 3-12). The low voltages produce angular distributions with no definite "horns," as in Figure 3-1. The inability to determine (at low voltages) just where in the angular distribution the edge emission occurs probably causes the inaccuracy in  $\beta_e$ . In order to

make a Schottky plot of edge emission, it was necessary to take the angular position of the last observable "horns" and fix that position for current readings at lower voltages.

The  $\beta$  factor is a function of the suppressor voltage and the gun geometry. Since a "standard" geometry (Figure 1-2) and "standard"  $V_B$  of -300 V has been used for the previous calculations of  $\beta$ , it is necessary to determine how sensitive  $\beta$  is to variations in  $V_B$  and geometry. Table 3-4 shows the calculated  $\beta$ 's for various tip-to-anode distances and anode aperture diameters. A  $\pm 25 \mu\text{m}$  error in tip-anode spacing at a nominal spacing of 508  $\mu\text{m}$  (.020 inch) results in a  $\beta$  error of approximately  $\pm 35 \text{ cm}^{-1}$  from a nominal  $\beta$  of 1148  $\text{cm}^{-1}$ , only a  $\pm 3\%$  error. Table 3-4 also shows the effect of varying the suppressor bias  $V_B$  from -300 to -700 V. Again this produces a minor effect, approximately a 5% change in  $\beta$  for a 200 V change in  $V_B$ .

The  $\beta$  factors shown in Table 3-4 were calculated by maintaining a constant anode voltage and calculating emitter apex surface fields for the various conditions. Since there are three electrodes in this gun, the  $\beta$ 's calculated by adjusting anode voltage to maintain a constant apex field are not exactly the same as those in Table 3-4. However, the differences, for reasonable anode voltages ( $> 2000 \text{ V}$ ) are small. This was verified in several cases by doing the  $\beta$  factor calculation both ways, using fixed anode voltage and or fixed electric field at the cathode apex.

TABLE 3-4

Sensitivity of  $\beta$  to Geometry of Gun and Bias Voltage for  $r = 1 \mu\text{m}$   
and  $f/r = 0.3$ .

Tip-to Anode Spacing ( $\mu\text{m}$ )	Anode Aperture Diameter ( $\mu\text{m}$ )	$\beta = F/V \text{ (cm}^{-1}\text{)}$ ( $V_A = 7500 \text{ V}$ , $V_B = -300 \text{ V}$ )
254	635	1624
	381	1742
	127	1804
508	635	1119
	381	1148*
	127	1157
762	635	825
	381	836
	127	838

\*"Standard" Geometry: Tip-to-Anode = 508  $\mu\text{m}$

Anode Aperture Diameter = 381  $\mu\text{m}$

$V_B \text{ (V)}$ ("Standard" Geometry)	$\beta = F/V \text{ (cm}^{-1}\text{)}$ ( $V_A = 7500 \text{ V}$ )
-300	1148
-500	1105
-700	980

### C. Computer Simulation of I-V Characteristics

As mentioned previously, because of the low work function of the Zr/W(100) field emitter, at elevated temperatures one can attain operational conditions which cause emission to be primarily Schottky emission. This can be understood by considering the range of validity of the various emission equations ranging from pure field to Schottky emission. The emission equations for Schottky  $J_S$ , extended Schottky  $J_{ES}$ , thermal field (TF)  $J_{TF}$  and field emission  $J_{FN}$  are given by<sup>2</sup>

$$J_S = \frac{4\pi m e (kT)^2}{h^3} \exp[-(\phi - e^{3/2} F^{1/2})/kT] \quad (3-3)$$

$$J_{ES} = J_S \pi q / \sin \pi q \text{ for } q < 1 \quad (3-4)$$

$$J_{TF} = J_{FN} \pi p / \sin \pi p \text{ for } p < 1 \quad (3-5)$$

$$J_{FN} = \frac{e^3 F^2}{8\pi \phi} \exp[-4(2m\phi^3)^{1/2}/3\hbar e F] \quad (3-6)$$

where  $p = 2(2m\phi)^{1/2} kT/\hbar e F$  and  $q = \hbar e^{1/4} F^{3/4}/\pi(2m)^{1/2} kT$ . The conditions for validity of the various emission equations above are given in Figure 3-20 where the boundary  $F_2(\phi, T)$  and  $F_1(T)$  separating TF and extended Schottky emission is given by

$$F_1(T) = [\pi(2m)^{1/2} kT/\hbar e^{1/4}]^{4/3} = 1746 T^{4/3} \text{ (V/cm)} \quad (3-7)$$

$$F_2(\phi, T) = 3(m\phi)^{1/2} kT/\hbar e = 9.4 \times 10^3 \phi^{1/2} T \text{ (V/cm)} \quad (3-8)$$

The upper limit of field occurs when the work function barrier is reduced to the Fermi level and is given by

$$F_3(\phi) = \phi^2/e^3 = 7 \times 10^6 \phi^2 \text{ (V/cm)} \quad (3-9)$$

The hashed region in Figure 3-20 between the applicability of TF and extended Schottky expressions has no analytical expression for current density. The dashed lines in Figure 3-20 are the critical conditions where for  $q = 0.5$  electrons are emitted symmetrically above and below the work function barrier and for  $p = 0.5$  electrons are emitted symmetrically above and below the Fermi level.

We may eliminate the problem of having to change from one equation to another depending on the temperature, field and work function if we use the following procedure.

Murphy and Good<sup>3</sup> have given a unified treatment of the emission of electrons which is valid for the thermionic, field, and the intermediate transition region as well. They form expressions for the transmission coefficient through the potential barrier,  $D(F,W)$  and for the number of electrons per second per unit area incident on the barrier,  $N(T,\phi,W)$  and integrate the product to find the emission current density:

$$J(F,T,\phi) = e \int_{-W_a}^{\infty} D(F,W) N(T,\phi,W) dW \quad (3-10)$$

where  $W_a$  is the energy at the bottom of the Sommerfeld potential well in the metal. The following potential energy diagram illustrates the relevant energy and position parameters.

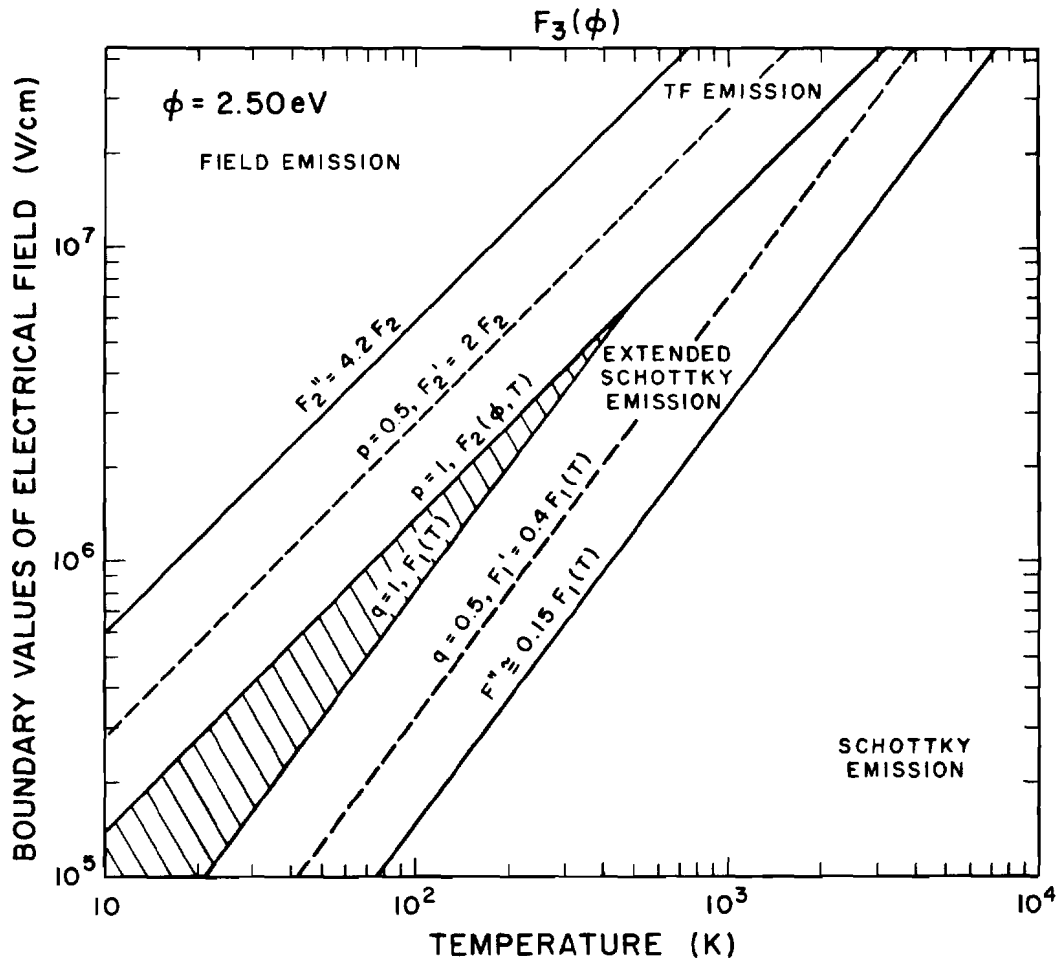
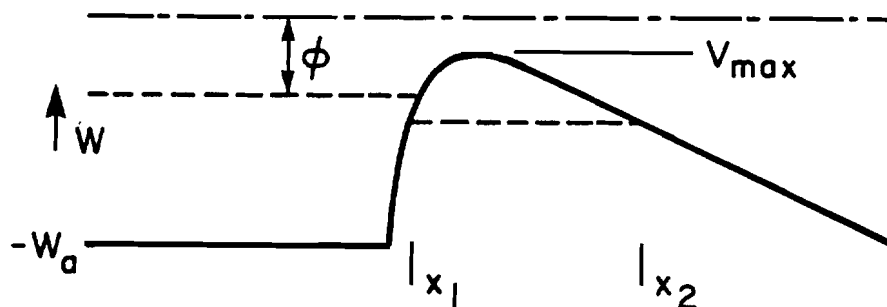


Figure 3-20. Solid lines show the boundaries in terms of field and temperature that separate the indicated emission regimes.



Field emission tunneling diagram.

The transmission coefficient is taken to be unity for  $W > V_{max}$ . For  $W < V_{max}$ , it is evaluated by a parabolic WKB-type approximation which depends on the shape of the potential curve between the points  $x_1$  and  $x_2$  for a given  $W$ .

Using the expressions from Murphy and Good and integrating numerically rather than using analytic approximations with limited regions of validity, El-Kareh, Wolfe, and Wolfe<sup>4</sup> have generated graphs of  $J$  vs  $F$  for various temperatures and work functions and also normal, tangential, and total energy distributions for the emitted electrons. The authors indicate that their theoretical results agree with published experimental results, at least over the range of current densities considered.

Using the same procedure, theoretical Schottky plots have been generated<sup>5</sup> for various fields and work functions at a constant temperature of 1800 K. Although the emission current can be varied by temperature as well as by anode and suppressor voltages, in practice temperatures above  $\sim 1900$  K result in a loss of the low



work function Zr-O-W (100) surface and temperatures below  $\sim 1600$  K allow the surface to become contaminated after several hours in a  $10^{-9}$  torr environment, which results in a long term decrease in emission current. Therefore, the calculated curves for 1800 K (the nominal operating temperature) pertain to practical operating conditions for the emitter.

Figure 3-21 shows the calculated current densities vs. the square root of the field. The purpose of providing graphs for work functions from 2.5 to 4.5 is that it is not certain exactly what the work function is for the Zr-O-W (100) surface at 1800 K. The measured value for a macroscopic single crystal surface at room temperature is 2.67 eV, as determined by a field emission retarding potential measurement.<sup>6</sup> Assuming we are dealing with an identical surface on the end of the emitter, we still do not know the work function at an elevated temperature. Some measurements of total energy distribution from this emitter seem to indicate a work function in the region of 3.0 eV at 1800 K. The work function for clean tungsten is 4.5 eV, so these curves cover what is considered to be the range of possible work functions.

The fields applied to the emitter can be related to the anode voltages required in the standard gun (standard geometry,  $V_{\text{BIAS}} = -300$  V) by means of Figure 3-19 in section B. These anode voltages are shown in Figure 3-21 for emitter radii for 0.3 to 3.0  $\mu\text{m}$ . The range of 2 to 15 kV was chosen to describe the anode voltages for normal

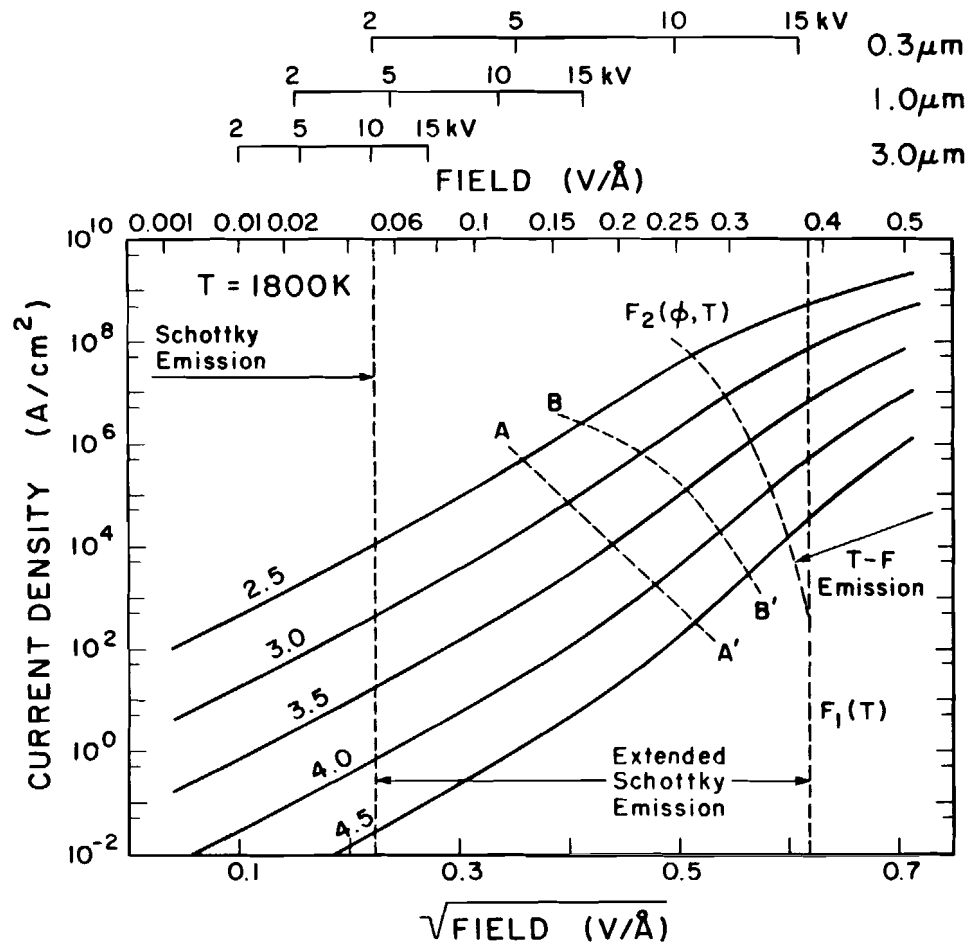


Figure 3-21. Theoretical Schottky plots based on numerical integration of the electron supply function and barrier transmission coefficient. Simplified computer program giving current density is given in Appendix B.

operation, < 2 kV being generally too low to get any measurable emission and > 15 kV approaching an arcing condition in the gun. The regimes of emission described by field boundary equations (3-7) and (3-8) are shown in the figure, as well as a boundary between the Schottky and Extended Schottky regimes, estimated at  $F = 0.15 F_1 (T)$ .

Having already attempted to measure Schottky slopes and experimentally determine a  $\beta$  factor, it can be seen that these  $\beta$  factors will in general be too high, since the operating regime for typical radii Zr/W emitters is in the extended Schottky regime. Since the experimental data indicate we can obtain Schottky-type slopes in the extended Schottky regime, at least over the decade or so current range available experimentally, it is of interest to see what these experimental data mean and also if there is some way an accurate  $\beta$  factor can be determined.

If we plot the normalized slopes of the calculated Schottky curves in Figure 3-21, we obtain the interesting result shown in Figure 3-22. The slopes of the curves in the Schottky regime are given by:

$$\frac{e^{3/2}}{kT} \quad ,$$

which is used as the normalizing factor for Figure 3-22. It can be seen that the Schottky slopes all increase together, independent of work function, until at a critical field strength, which is dependent on work function, they diverge from the main curve.

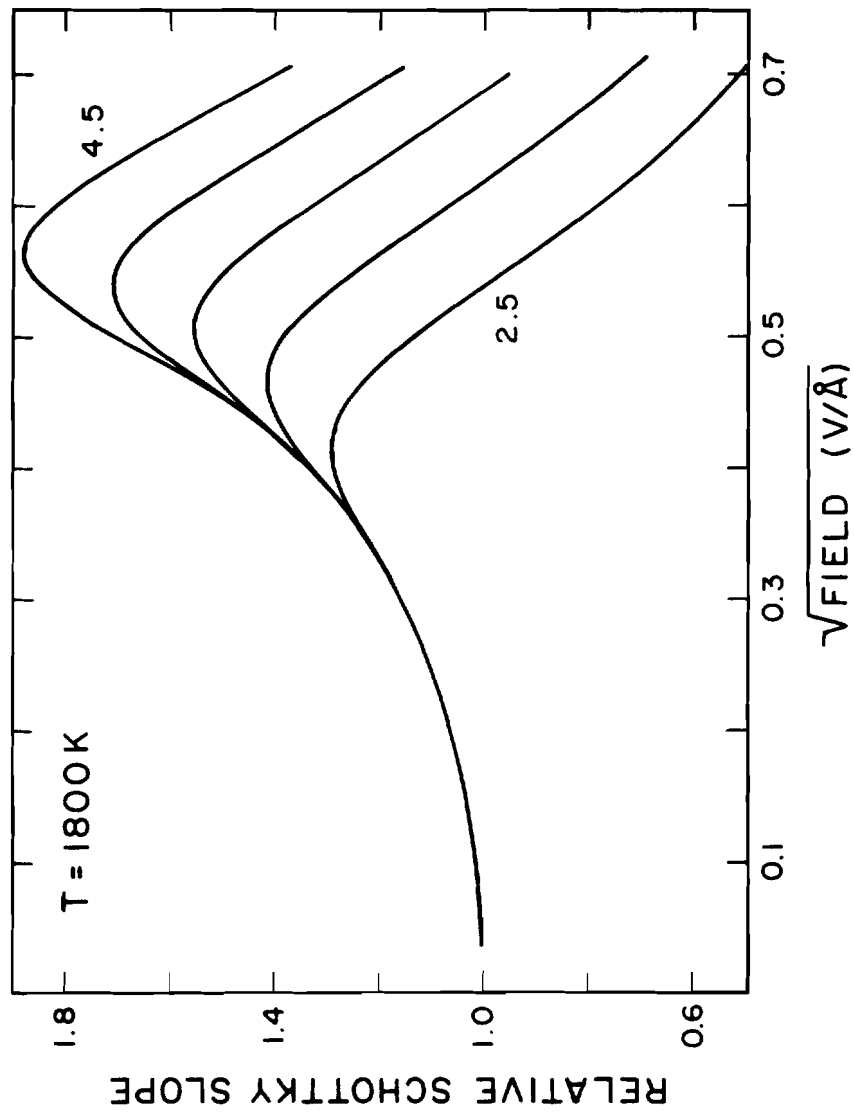


Figure 3-22. Normalized Schottky slopes from theoretical calculations for Figure 3-21.

The implication of this behavior is that if we stay below the critical fields, we have a prescription for determining the apparent increase in  $\beta$  and therefore the true  $\beta$  value from experimental data. If the critical fields at which the curves in Figure 3-22 diverge are plotted on Figure 3-21, the line A-A' results. The increase in Schottky slope from the Schottky regime out to A-A' can be accounted for independently of work function by Figure 3-22, which is fortunate since the exact work function is unknown. In an experimental situation, if we can set a lower limit on the expected work function and then measure  $\beta$  at a field less than or equal to the critical field for that work function, the corrected  $\beta$  will be valid and independent of work function.

There is a bit of circular argument in the preceding discussion, that is, if we know  $\beta$ , we can determine the field and if we know the field we can determine the true  $\beta$ . Fortunately, an iterative procedure as outlined in Table 3-5 will converge to a value for  $\beta$ . This procedure was applied to the experimental results in Table 3-3 and reduced both  $\beta$ 's by  $\sim 8\%$ . To correctly apply this iterative procedure, we must be sure that we start the iterations to the left of the maxima in the Figure 3-22 curves. The location of these maxima on the Figure 3-21 plot is shown by line B-B'.

Figure 3-21 covers a current density range of more than 10 decades, obviously not a realistic range for experimental measurement. By restricting operation of the various radii emitters to the practical anode voltage ranges in Figure 3-21, and by borrowing results from

TABLE 3-5

Procedure for Determining  $\beta$ 

1. Measure experimental Schottky slope and anode voltage  $V_0$  at center of slope measurement span.
2. Estimate  $\beta_{(1)}$  from Schottky slope ( $\beta$  estimate will be higher than true  $\beta$ ).
3. Calculate the field  $F_{(1)} = \beta_{(1)} V$  ( $F_{(1)}$  will be higher than true field).
4. Use Fig. 3-22 to find factor  $\left( \frac{\beta_{(1)}}{\beta_{(2)}} \right)^{1/2}$  \* .
5. Calculate  $\beta_{(2)}$  ( $<$  true  $\beta$ ).
6. Use this  $\beta$  at  $V$  to find  $F_{(2)} = \beta_{(2)} V$  ( $F_{(2)} <$  true  $F$ ).
7. Use Figure 3-22 to find factor  $\left( \frac{\beta_{(1)}}{\beta_{(3)}} \right)^{1/2}$  .
8. Calculate  $\beta_{(3)}$  ( $>$  true  $\beta$ ).
9.  $F_{(3)} = \beta_{(3)} V$  ( $>$  true  $F$ ).
10. Go to step 4.
11. Iterate to convergence.

\* note: Schottky slope  $\propto \beta^{1/2}$

In step 3 if  $F_{(1)} < .15 F_1 = 36 T^{4/3}$  then stop. Already in Schottky regime.

Computer program performing this procedure is shown in Appendix A.

section D of this chapter to relate measured angular intensity to theoretical cathode current density, the practical operating areas can be defined as in Figure 3-23. The boxes for the three different radii emitters all define the same experimental operating region; anode voltages from 2 to 15 kV and angular intensities from 0.1 to 1.0 mA/sr. Again the line A-A' is plotted, and we can see that large radii emitters ( $r > 1 \mu\text{m}$ ) lie to the left of the line and therefore  $\beta$ 's are measurable experimentally with the help of Figure 3-22. In the case of  $r < 1 \mu\text{m}$  for low work function,  $\phi = 2.5$  to 3.0 eV,  $\beta$  is still calculable from experimental measurements, but for  $\phi = 3.5$  to 4.5 eV it is not, unless the work function is known with some precision, in which case Figure 3-22 can be used past the critical field. Another factor worth mentioning for  $r < 1 \mu\text{m}$  is that space charge effects with the current densities encountered for reasonable angular intensities may change both the voltage-field relationship and the angular intensity - current density relationship. The boundaries in Figure 3-23 are calculated neglecting space charge.

Implicit in this section has been the assumption that  $J$ , the cathode current density is directly proportional to  $I_p$ , the experimentally measured probe current into an apertured Faraday cup. The next section in the calculation of trajectories will show the validity of this assumption.

The  $\beta$ -determining procedure was applied to data taken from 7 emitters.<sup>7</sup> Unfortunately, none of the emitter radii were known. Table 3-6 shows the results of applying the Table 3-5 procedure

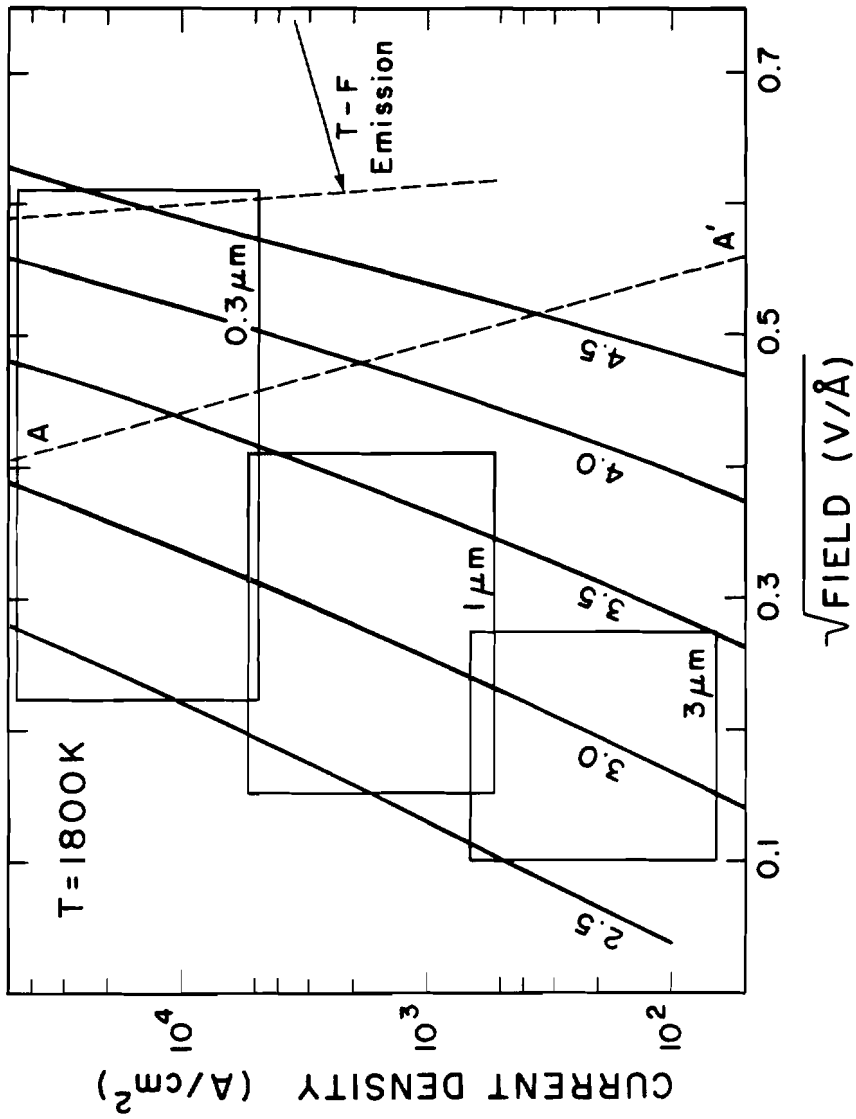


Figure 3-23. Theoretical Schottky plots with region of practical operation for various emitter radii.



TABLE 3-6  
Experimental  $\beta$  Data

Emitter No.	Experimental Measurement				$\beta_{\text{true}}$ ( $\text{cm}^{-1}$ )	radius ( $\mu\text{m}$ )	1 mA/sr		$\phi$ (eV)
	Temp. (K)	Voltage (1 mA/sr)	Voltage ( $\beta_{\text{meas}}$ )	$\beta_{\text{meas}}$ ( $\text{cm}^{-1}$ )			F (V/Å)	J (A/cm <sup>2</sup> )	
A2	1800	5200 (est.)	2500	1321	1207	0.8	.063	6600	2.673
A3	1800	5670	4400	623	578	2.3	.033	1050	2.684
1	1825	5100	4625	2282	1760	0.55	.090	15375	2.767
2	1800	5810	4900	2250	1718	0.6	.100	12920	2.835
* 3	1800	6400	6561	4050	2344	0.35	.150	37105	2.974
* 3'			5400		2528	0.3	.162	49380	2.997
4	1820	4750	3364	3501	2633	0.3	.125	49380	2.802
5	1800	4650	4800	3300	2417	0.35	.112	37105	2.748

\* Possible error:  $\beta_{\text{meas}}$  • Voltage results in initial field too large for application of theory, beyond line B-B' in Figure 3-21.

$\bar{\phi}$  excluding 3 and 3' = 2.75 eV

to the emitter data. Note that the voltage at which  $\beta_{\text{meas}}$  was taken is used with  $\beta_{\text{meas}}$  to produce  $\beta_{\text{true}}$ . Then  $\beta_{\text{true}}$  is used with Figure 3-19 to compute the emitter radius. Then the field  $F$  required to obtain 1 mA/sr is just  $F = \beta_{\text{true}} \cdot \text{Voltage (1 mA/sr)}$ . The current density  $J$  corresponding to 1 mA/sr is calculated from Eq.(3-12) (next section) using the emitter radius as inferred above. Finally, given a field  $F$ , current density  $J$  and temperature  $T$ , the work function  $\phi$  can be determined. In this case, since the emission is confined to the Schottky and extended Schottky regimes, a simple program was written to calculate  $\phi$  from the analytical expression, Eq. (3-4). See Appendix C.

The values for  $\phi$  calculated from the experimental data at 1800 K are not too different from the room temperature value of 2.67 eV.<sup>6</sup> Although this is a very indirect way of determining work function, it gives reasonable results from emitters with a wide range of applied fields and current densities.

---

#### D. Computer Calculations of "Cold Electron" Trajectories

Relating the predicted current density at the emitter surface to the measurable angular intensity in the field-free region downstream of the anode requires knowledge of the electron trajectories from the tip to the measuring plane. Accurately calculating trajectories through many orders of magnitude change in electric field requires extreme accuracies in the field. A computer program<sup>8</sup> using a variable mesh size in spherical coordinates centered on the emitter tip permits field accuracies on the order of  $10^{-7}$ . A rectangular mesh program used to calculate the surface fields on the emitter gave sufficient accuracy for that purpose but proved to be very inefficient for calculating fields of extreme accuracy. Moreover, the rectangular mesh program required the use of the successive magnification technique to resolve the facet on the emitter surface as well as to include the anode and suppressor. There seems to be a fundamental, built-in error with the successive magnification technique.<sup>9</sup> Since the spherical coordinates with increasing mesh (SCWIM) technique is able to handle the entire gun with one mesh configuration, it is expected to be inherently more accurate than programs which successively calculate fields and change the mesh between calculation to arrive at a final field. See Appendix D for SCWIM program details.

The trajectories calculated for the purpose of determining angular distributions were spaced at equal intervals along the facet from the apex to the edge. The initial energies were all zero. These

electrons will be referred to as "cold electrons," after Wiesner.<sup>10</sup>

Figure 3-24 is a plot of trajectory slope ( $\Delta R/\Delta Z$ ) from rays originating  $R_0$  from the axis for a 1  $\mu\text{m}$  emitter. It can be seen that the trajectories initially diverge, then converge throughout most of the gun and again diverge due to the "cathode lens" effect of the anode aperture. The trajectory marked  $R_0 = .30$  is from the edge of the facet, where the surface electric field and therefore the current density is highest. This would be expected to correspond to the "horns" on the angular distribution graphs. This trajectory ( $R_0 = .300$ ) leaves the gun with a slope angle  $\text{Arctan}(\Delta R/\Delta Z)$  of 0.11974 rad at  $Z = 1694 \mu\text{m}$ . However, at the measuring plane downstream of the anode aperture it is not the trajectory slope  $\text{Arctan}(\Delta R/\Delta Z)$  but rather the position angle  $\text{Arctan}(R/Z)$  which is experimentally measured, with  $Z = 0$  corresponding to the emitter position. Figure 3-25 shows behavior of  $R/Z$  throughout the gun. Again notice the  $R_0 = .300$  trajectory which has a position tangent of approximately 0.12236 at 1694  $\mu\text{m}$ . The radial position at  $Z = 1694 \mu\text{m}$  is therefore 208.3  $\mu\text{m}$ . At this position the electron continues on in field-free space with a slope angle = 0.11974 rad until it reaches the measuring plane at  $Z = 16 \text{ mm}$  at which point its position tangent is

$$\frac{R}{Z} = \frac{0.2083 \text{ mm} + \tan(0.11974) 14.306 \text{ mm}}{16 \text{ mm}} = 0.1206$$

It can be seen that  $R/Z$  approaches the value of  $\Delta R/\Delta Z$  as the measuring plane moves away from the anode aperture but it can be slightly

---

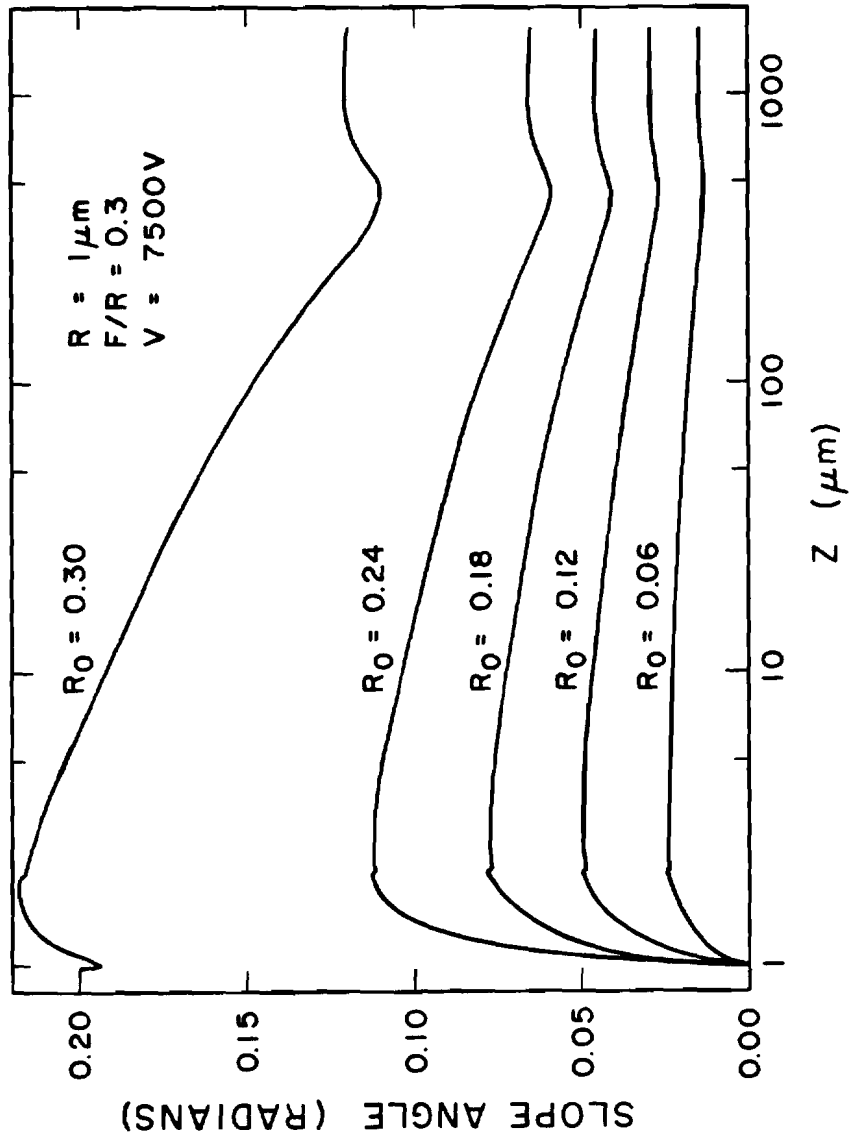


Figure 3-24. Trajectory slope throughout electron gun. Initial conditions: 0 eV; five initial positions ( $R_0$ ) in  $\mu\text{m}$  from the emitter axis indicated in figure.  $V_{\text{BIAS}} = -300$ ,  $V_{\text{ANODE}} = 7500$ .

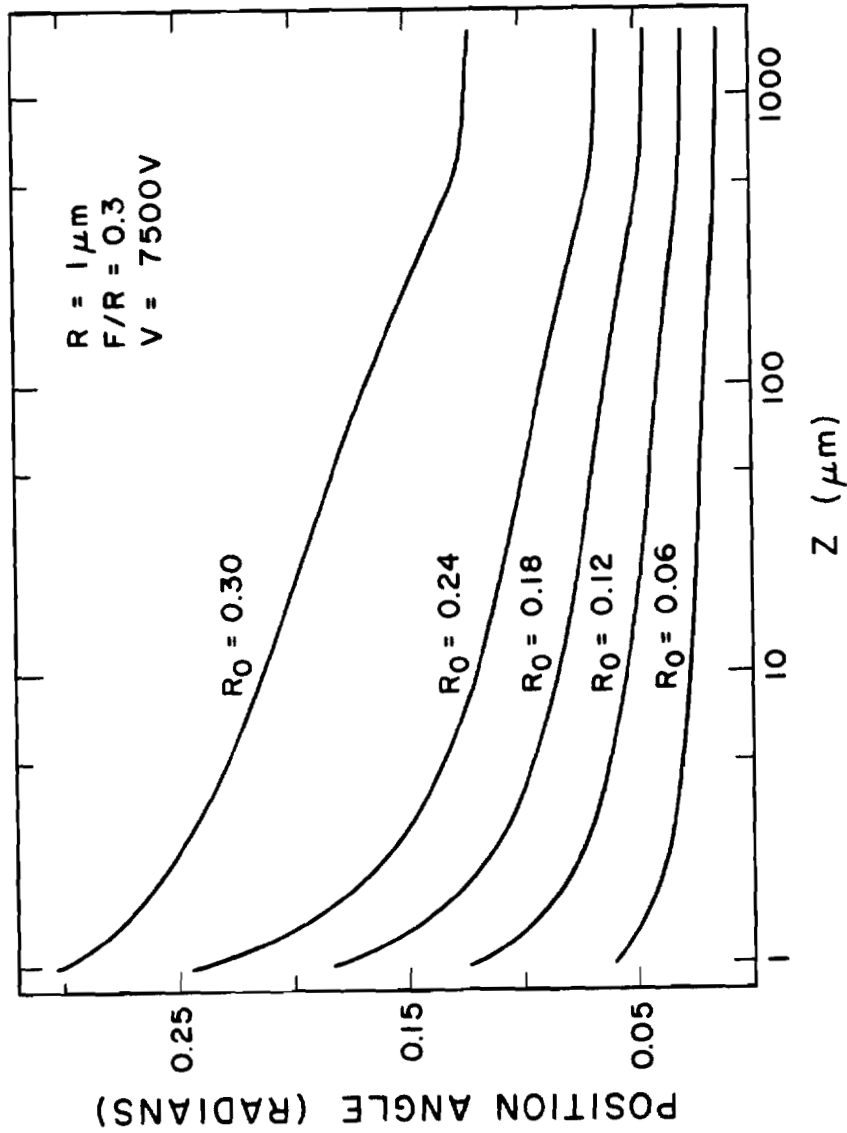


Figure 3-25. Trajectory position tangent ( $R/Z$ ) throughout electron gun. Initial conditions: 0 eV; five initial positions ( $R_0$ ) in  $\mu\text{m}$  from the emitter axis indicated in figure.  $V_{\text{BIAS}} = -300$ ,  $V_{\text{ANODE}} = 7500$ .

different from  $\Delta R/\Delta Z$  if the measuring plane is very close to the aperture. Since

$$\text{Arctan } (R/Z) = \text{Arctan } (0.1206) \approx 6.88^\circ$$

the position of the "horns" on the angular distribution resulting from the high electric field at the edge of the facet should be at  $6.88^\circ$  off the axis. Experimental angular distributions show a range of from  $5.8^\circ$  to  $7^\circ$  in the position of the "horns." This is a good agreement considering that this theoretical prediction was done for only one emitter radius and gun voltage condition and the experimental data were taken over a range of radii and voltages.

This agreement is somewhat fortuitous, however, since the model used for the computer calculations has a sharp edge at the transition from the facet surface to the spherical surface (See Fig. 3-13). The trajectory launched from the facet edge rapidly acquires an initial slope, as seen in Figure 3-24. This initial slope, which affects the final slope, is a function of the mesh spacing in the computer program. Variations of angular mesh intervals over reasonable ranges have produced variations in this trajectory final angle of from  $6.25^\circ$  to  $6.88^\circ$ . The other trajectories launched from the facet ( $R_o < 0.3$ ) do not show this dependence on mesh spacing. Therefore, the exact position of the "horns" of the angular distribution must be provided by an improved model of the emitter, which includes a small radius at the facet edge instead of a sharp edge.

We can use the surface position angle ( $\theta_o$ ), as shown in Figure 3-13, to describe the trajectory launch position and use the beam half angle ( $\alpha$ ) in field free space to describe the angle measured by the Faraday cup position. A series of 16 trajectories were calculated with zero initial velocity and equal position increments from the apex of the emitter ( $\theta_o = 0$ ) to the edge of the facet ( $\theta_o = 17.46^\circ$ ). A similar set of trajectories was calculated for the spherical-ended emitter model. The results of those calculations for a 1  $\mu\text{m}$  emitter are shown in Figure 3-26.

The spherical-end emitter results are interesting since they show approximately the predictions of trajectory behavior based on the sphere-on-cone emitter model. The angular magnification for central emission can be determined from the slope of Figure 3-26. The slopes for  $\theta_o \leq 6^\circ$  are 0.223 for the faceted emitter and 0.507 for the spherical emitter. Note that these angular magnifications are a function of emitter radius and that Figure 3-26 is for a 1  $\mu\text{m}$  emitter. The trajectories would be unchanged for all anode voltages were it not for the suppressor electrode at voltage  $V_B$ . The presence of this additional electrode affects the angular magnifications at low anode voltages as shown in Figure 3-27. The suppressor tends to compress the beam angle at low anode voltages and thereby reduces the angular magnification.

---



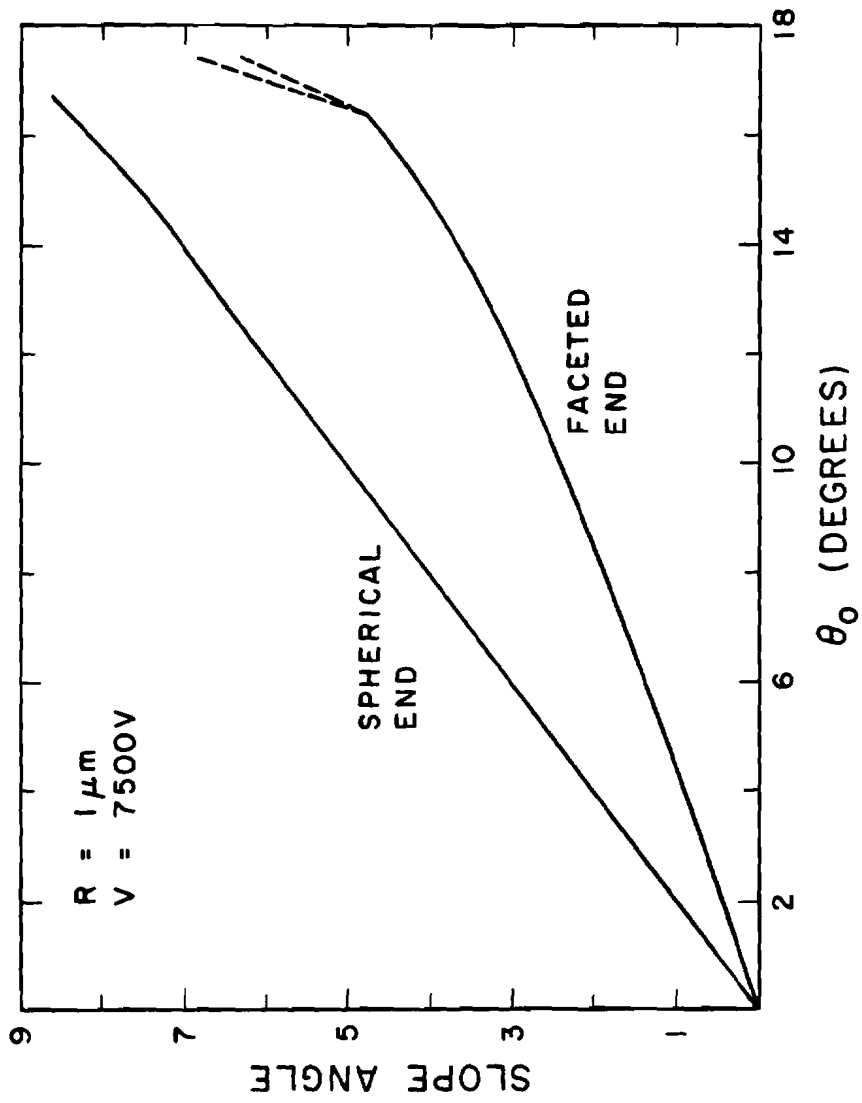


Figure 3-26. Final beam angle vs launch position angle for trajectories from apex to edge of facet.

We can now see an additional complicating factor involved in the determination of  $\beta$  from the I-V data. If the voltage on the anode is too low when the Schottky plot is made, then the relationship  $I_p \propto J$  breaks down due to the spreading of the trajectories with increasing anode voltage. A possible solution to this problem is to make  $V_B \propto V_A$  for the plotting of a Schottky slope. However, for  $V_A > 3$  kV and a fixed  $V_B$  of -300 V, a Schottky slope taken over a reasonable voltage span ( $\Delta V = 2$  kV) will produce an error in the  $I_p$  to J relationship of  $\sim 6\%$ , which will in turn cause a  $\beta$  error of only  $\sim 3\%$ .

Figure 3-27 was used to establish the current density boundaries on Fig. 3-23. The angular intensity is related to the cathode current density by

$$I' = \frac{dI}{d\Omega} = J \frac{dA}{d\Omega}$$

where  $\Omega$  = solid angle downstream of anode,  $I$  = current,  $J = dI/dA$  = current density. The cathode area  $dA$  corresponding to a solid angle  $d\Omega$  for a faceted emitter is given by

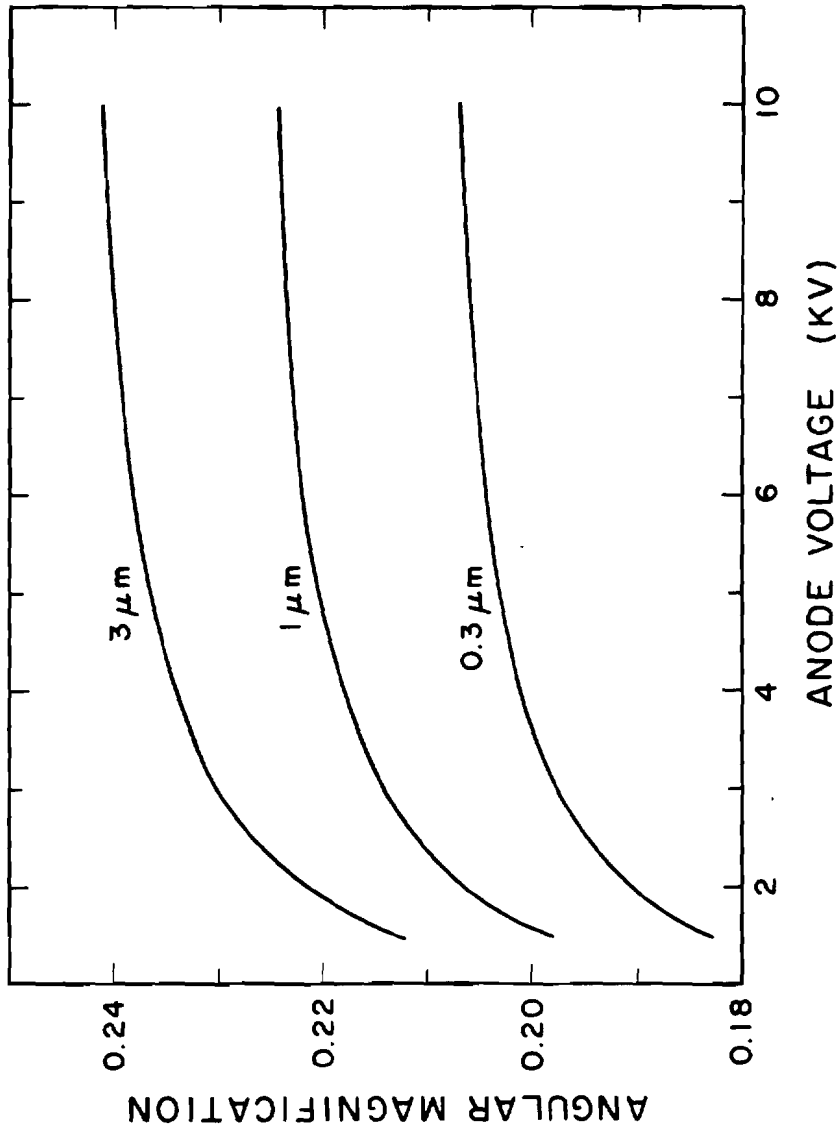


Figure 3-27. Central emission angular magnification as a function of anode voltage and emitter radius. Bias voltage = -300 V.  $f/r = 0.3$ .

$$\begin{aligned}
\frac{dA}{d\Omega} &= \frac{d[\pi r^2 \sin^2 \theta_o]}{d[2\pi(1 - \cos \alpha)]} \\
&= r^2 \frac{\sin \theta_o \cos \theta_o d\theta_o}{\sin \alpha d\alpha} \\
&= r^2 \left( \frac{d\theta_o}{d\alpha} \right)^2
\end{aligned}$$

if  $\theta_o \ll 1$  rad,  $\alpha \ll 1$  rad and  $\frac{d\theta_o}{d\alpha} = \frac{\theta_o}{\alpha}$ .

where  $\theta_o$  = surface position angle on cathode and  $\alpha$  = beam half angle downstream of anode. Therefore

$$I' = Jr^2 \left( \frac{d\theta_o}{d\alpha} \right)^2$$

Since Figure 3-27 provides the values of angular magnification ( $d\alpha/d\theta_o$ ), the values of  $d\theta_o/d\alpha$  are known and the angular intensity-current density relationship at  $V_A = 6$  kV,  $V_g = -300$  V is therefore

$$I' = KJr^2 \quad \text{with}$$

$$K \approx \begin{Bmatrix} 23.8 \\ 20.3 \\ 17.7 \end{Bmatrix} \quad \text{for } r = \begin{Bmatrix} 0.3 \\ 1.0 \\ 3.0 \end{Bmatrix} \mu\text{m} \quad (3-11)$$

With only these data, the best equation to describe  $I'$  is

$$I' = 20.42 J r^{1.871}$$

or in more practical units

$$I' = (2.042 \times 10^{-4}) J r^{1.871} \quad (3-12)$$

with  $I'$  in mA/sr,  $J$  in A/cm<sup>2</sup>, and  $r$  in  $\mu\text{m}$ .

To compare the faceted emitter to the spherical-ended emitter, we look at the case for  $r = 1 \mu\text{m}$ . As in Eq. (3-11)

$$I' = K J r^2 \quad \text{with}$$

$K \cong 20.11$  for a faceted emitter,  $r = 1 \mu\text{m}$ ,  $f/r = 0.3$ ,  $V_A = 7500 \text{ V}$

and  $K \cong 3.89$  for a spherical emitter,  $r = 1 \mu\text{m}$ ,  $V_A = 7500 \text{ V}$ .

Therefore, the effect of the facet is to compress the electron trajectories such that a given cathode current density will produce  $\sim 5.2$  times the angular intensity. Conversely, at a given angular intensity (the important parameter for an electron optical system) only  $\sim 0.19$  times the cathode current density will be required of a faceted emitter as compared to a spherical-ended emitter.

Of course, the depression of the apex field due to the facet lowers the current density available from the faceted emitter for a given radius and anode voltage. According to Figure 3-18, the apex field is lowered by  $\sim 0.78$  relative to the spherical-ended emitter. This produces a reduction in cathode current density of  $\sim 0.39$  (from Figure 3-23). The net effect of the formation of the facet at a constant radius and anode voltage is to increase the angular intensity by a factor of

$$5.2 \times 0.39 \approx 2$$

The changes in cathode apex surface field, apex current density, angular magnification and angular intensity occurring upon formation of the facet on a thermally annealed emitter are shown in Table 3-7. These parameters are all calculated for a constant work function of 2.8 eV and typical operating angular intensities  $\sim 0.8$  mA/sr. Note that the per cent reduction in field and angular magnification is independent of radius, while the reduction in current density and increase in angular intensity depends on the absolute values of cathode field, not the relative values. The change in J as a function of F can be obtained from Figure 3-21.

TABLE 3-7

Effect of Facet Formation as a Function of

Emitter Radius for  $I' \sim 0.8$  mA/sr,  $\phi = 2.8$  eV

Emitter Radius ( $\mu\text{m}$ )	Anode Voltage (kV)	Emitter End Shape	Cathode Field ( $\text{V}/\text{\AA}$ )	Current Density ( $\text{A}/\text{cm}^2$ )	Angular Magnification ( $d\alpha/d\theta_0$ )	Angular Intensity (mA/sr)
0.3	4	Spherical	0.1437	$1.4014 \cdot 10^5$	0.4549	0.6086
		Faceted	0.1117	$3.5814 \cdot 10^4$	0.2006	0.7170
		Ratio (F/S)	0.78	0.26	0.44	1.18
1.0	6	Spherical	0.08942	$1.3629 \cdot 10^4$	0.5036	0.5386
		Faceted	0.06950	$5.2943 \cdot 10^3$	0.2211	0.9693
		Ratio (F/S)	0.78	0.39	0.44	1.80
3.0	8	Spherical	0.05311	$2.0485 \cdot 10^3$	0.5466	0.6186
		Faceted	0.04124	$1.0356 \cdot 10^3$	0.2394	1.4565
		Ratio (F/S)	0.78	0.51	0.44	2.35

All calculated parameters for conditions on cathode apex or axis of electron gun.

### E. Computer Simulation of Angular Intensity Distributions

Sections B, C, and D of this chapter provide the information necessary to compute the angular distributions observed in Section A. Currents are associated with each trajectory by multiplying the current density (as computed in Section C from the temperature, work function, and cathode field) by the cathode area represented by that trajectory. In field free space downstream of the anode, these currents are associated with the trajectory slope angles and corresponding solid angles, to produce the angular intensities  $dI/d\Omega$  as a function of  $\alpha$ , the trajectory slope. This computation is incorporated as a subroutine in the field and trajectory program. The only problem which occurs with this method is at the facet edge. The indeterminate nature of the trajectory slope at this point has already been mentioned. Another problem is the huge electric field due to the sharp edge, which produces unrealistic current densities. The rapid increase in angle  $\alpha$  always outweighs the increase in current density so that the facet edge trajectory always has a smaller angular intensity associated with it than the trajectory next to the edge. This means that the exact position of the "horn" and the exact angular intensity there is uncertain.

The behavior of the experimental angular distribution as a function of voltage can be understood by considering Figure 3-28 and 3-29. Both Figures show the behavior of the surface electric field, the cathode current density and the factor  $K$  as a function of



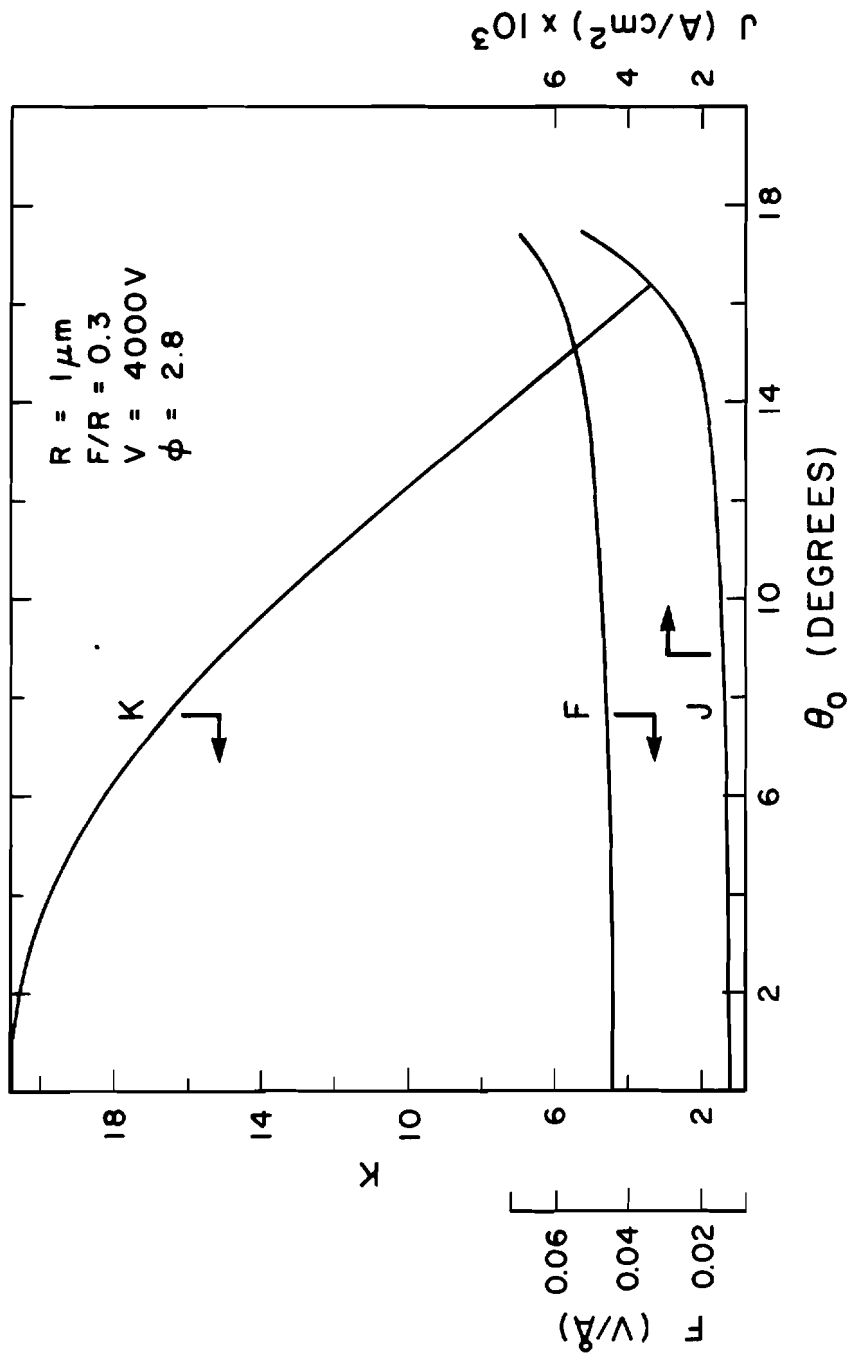


Figure 3-28. Cathode field, current density and K factor for 1  $\mu\text{m}$  faceted emitter.

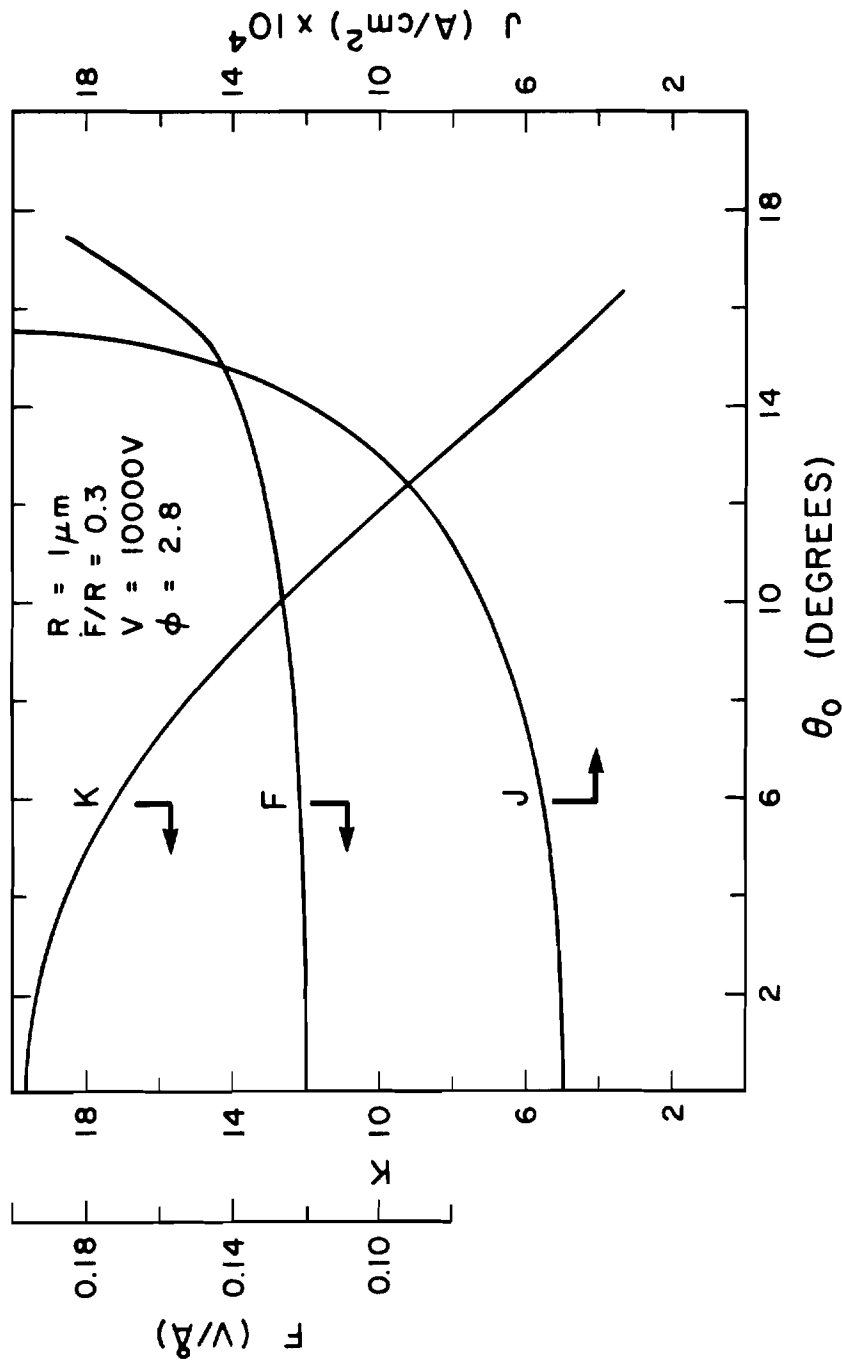


Figure 3-29. Cathode field, current density and K factor for 1  $\mu\text{m}$  faceted emitter.

$\theta_0$  where

$$I' = K J r^2.$$

and  $\theta_0$  = the cathode surface position angle. For relatively low anode voltages, the emitter is operating closer to the Schottky mode and the electric field produces an almost flat J curve as in Figure 3-28. For higher anode voltages, the emission regime moves further away from the Schottky mode where the dependence of J on F is greater and so the J curve in Figure 3-29 increases more quickly. For the low voltages the shape of the angular intensity is dominated by the shape of the K curve, while at higher voltages the shape is more strongly affected by the shape of the J curve.

Figures 3-30 to 3-41 show computed angular intensity distributions for various emitter radii and anode voltages. Angular intensities greater than  $4^\circ$  off axis are shown by dotted lines for two reasons. Since the existence of the sharp transition between the facet and the rounded portion of the emitter caused an extremely rapid variation of final angle with initial launch position, only three trajectories lie beyond  $4^\circ$  off axis. Also, the sharp facet edge produced an unrealistically high surface field and angular intensity, so that in no case did the "horns" disappear, as they did in the experimental results of Figures 3-1 and 3-2. It would be better to provide a small radius at the facet edge and adjust the radius until the experimental angular distributions were reproduced. However, the computer program did not allow such a modification to be easily made.

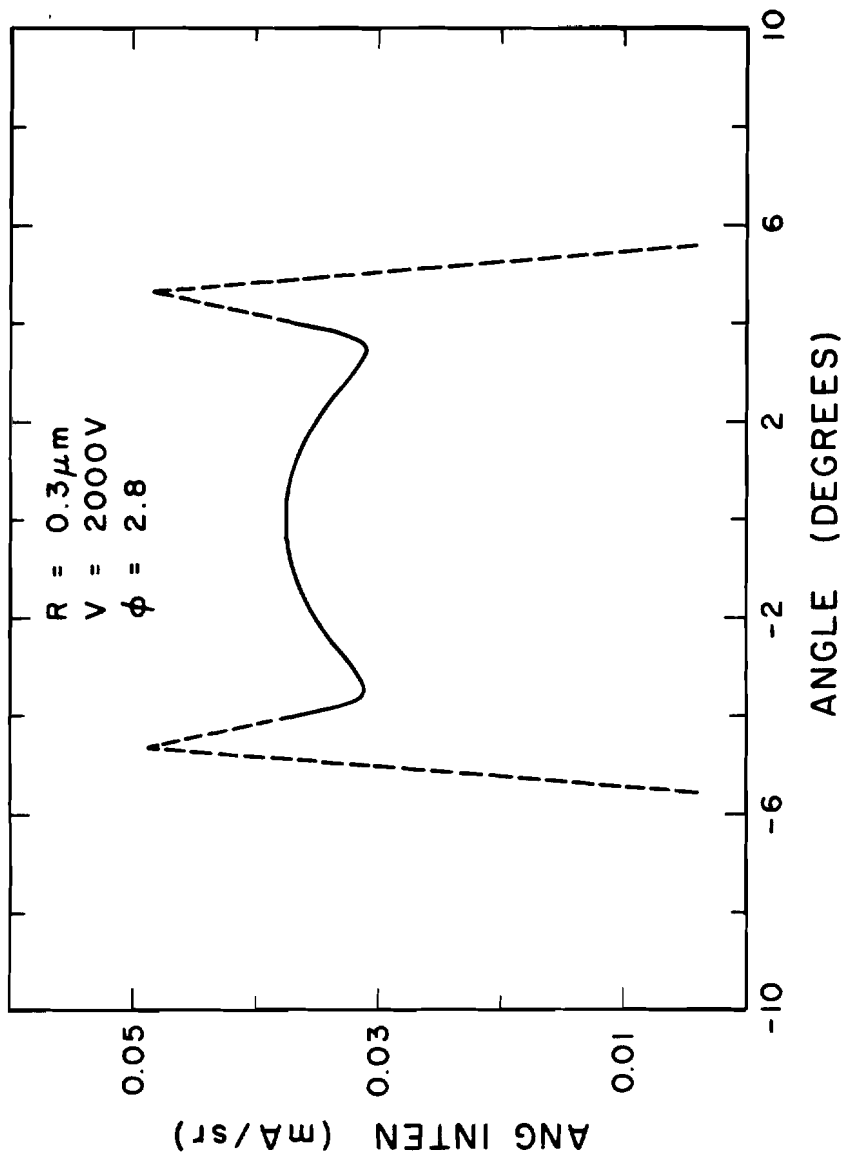


Figure 3-30. Computer calculated angular intensity distribution.

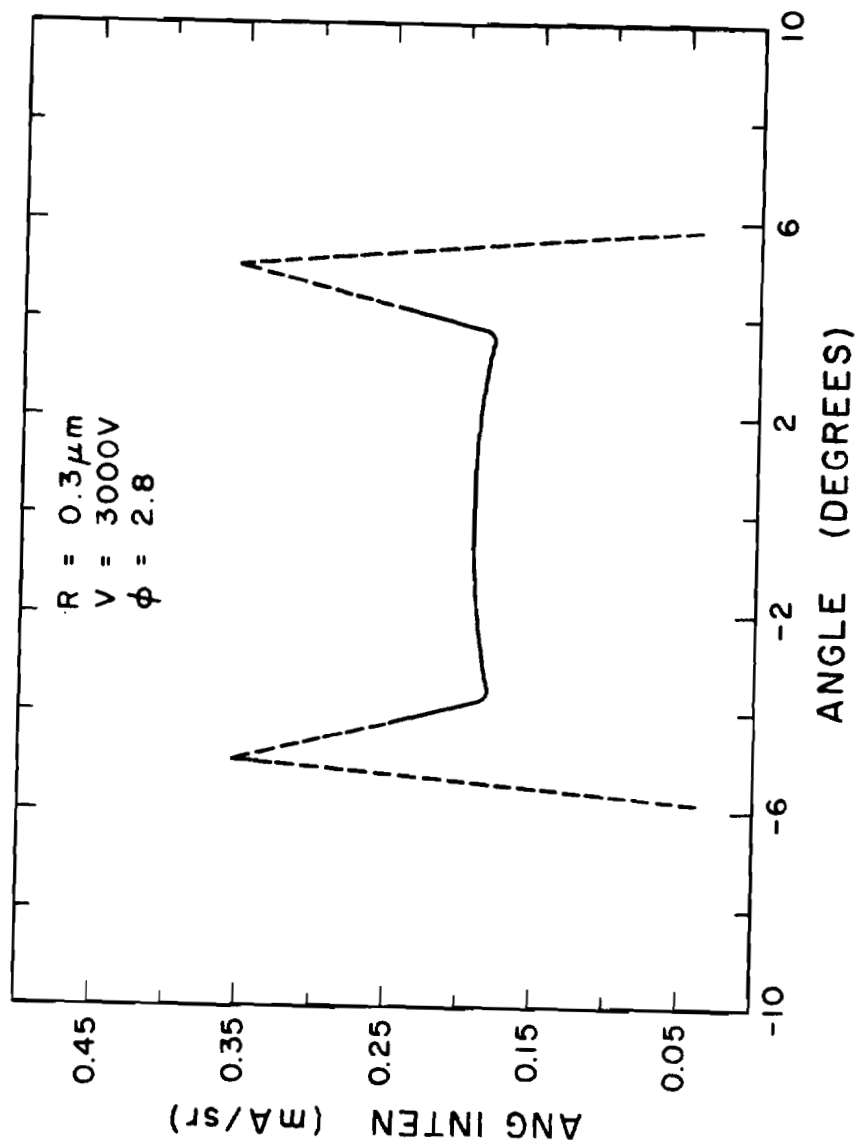


Figure 3-31. Computer calculated angular intensity distribution.

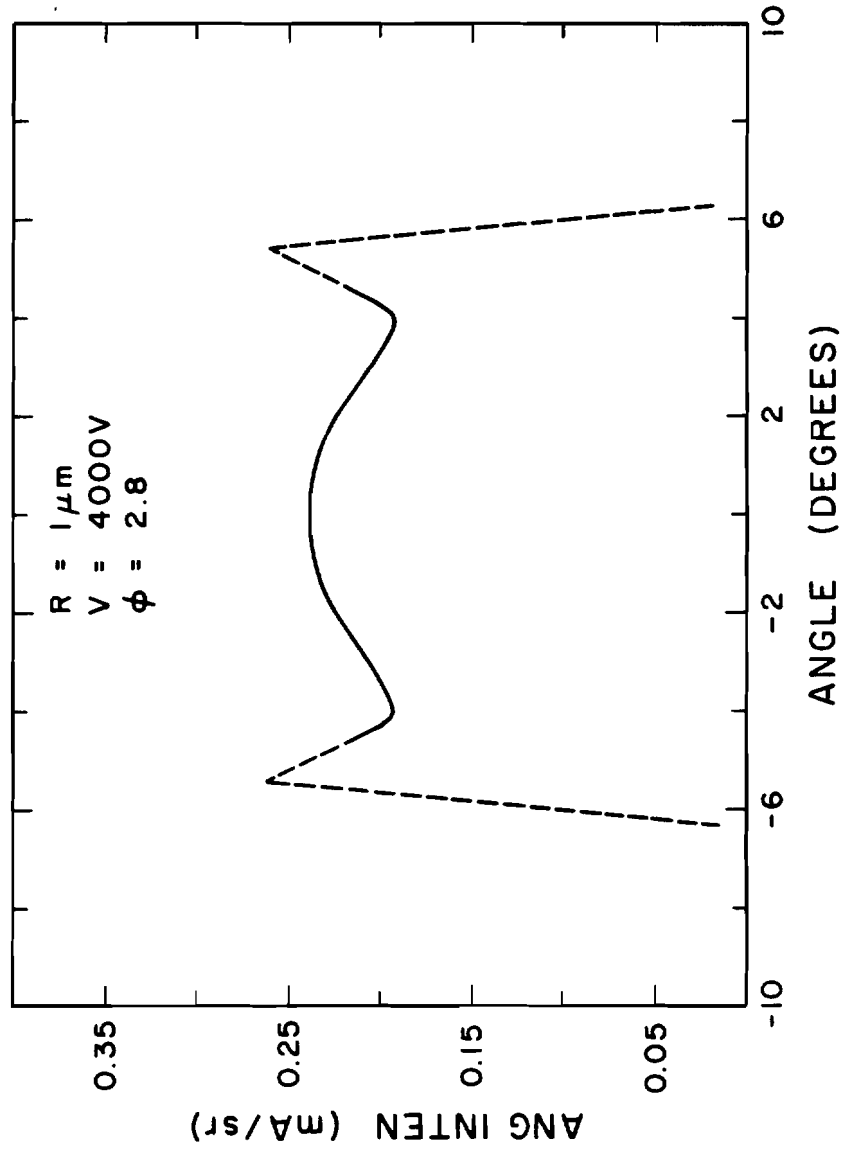


Figure 3-32. Computer calculated angular intensity distribution.

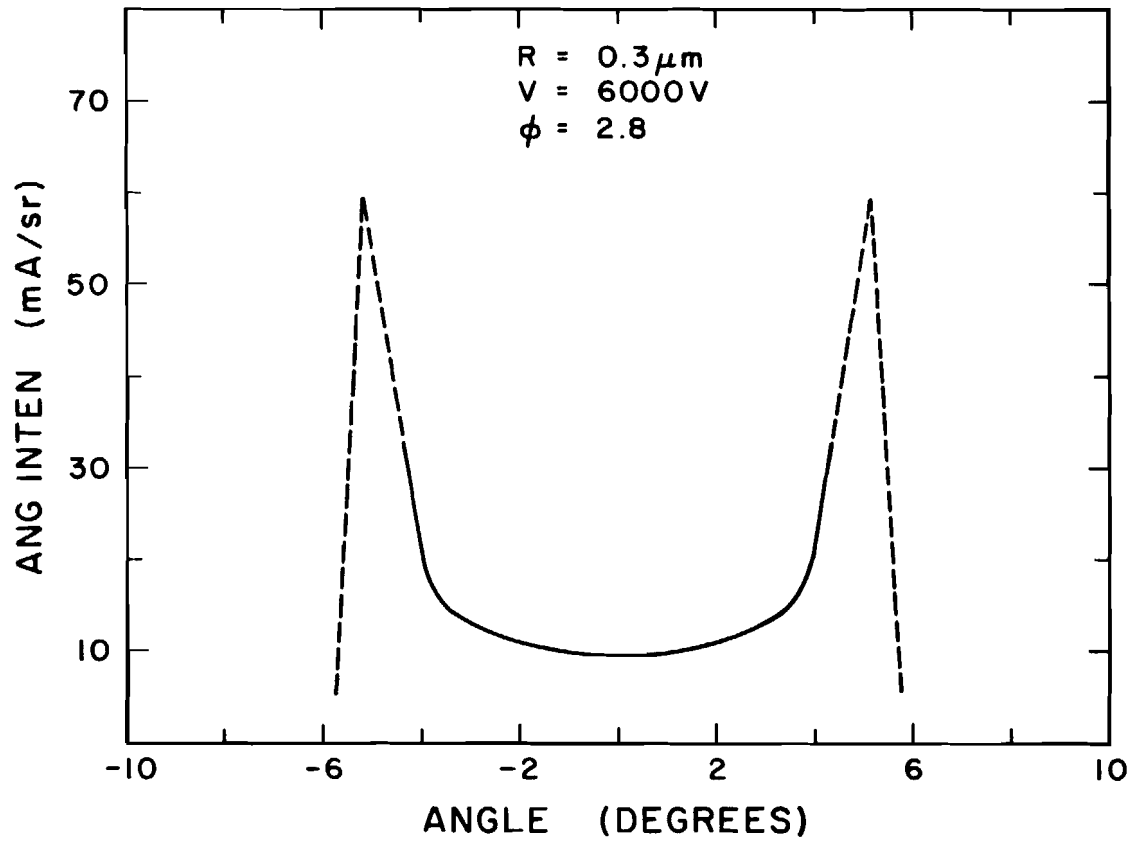


Figure 3-33. Computer calculated angular intensity distribution.

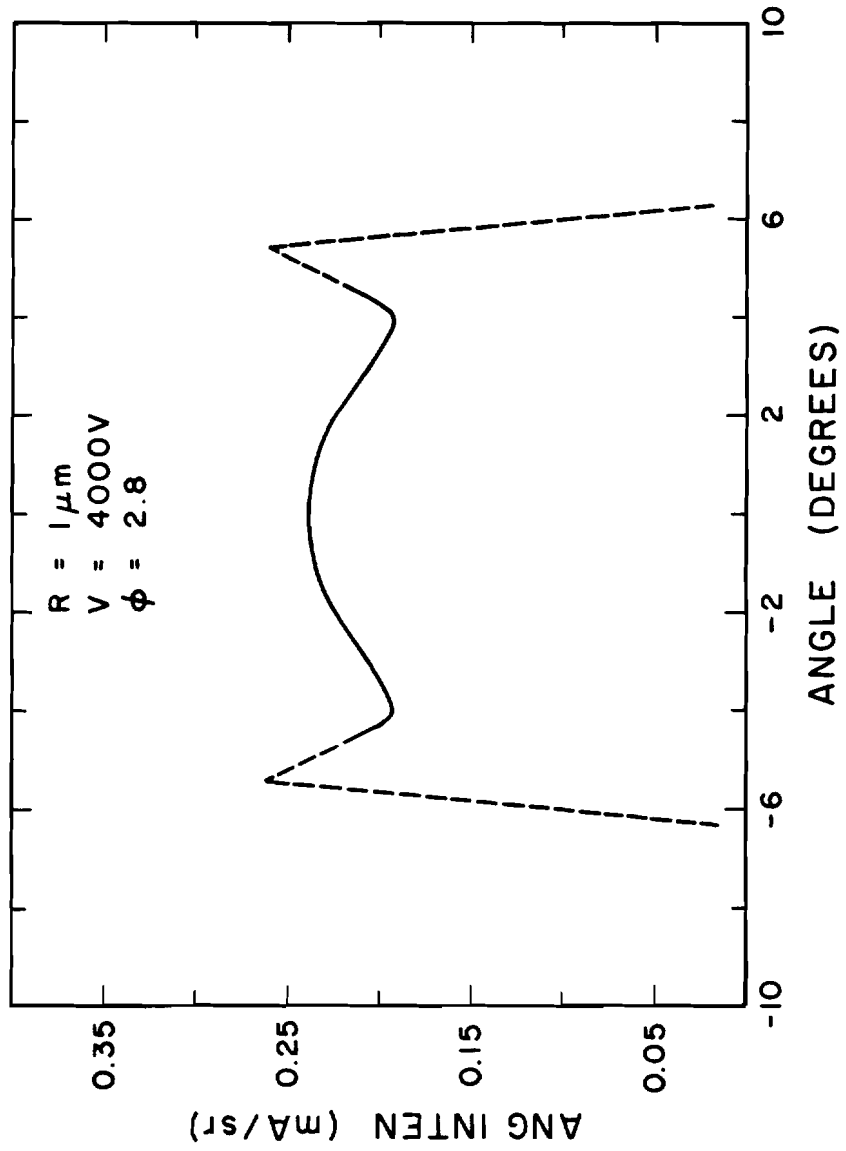


Figure 3-34. Computer calculated angular intensity distribution.



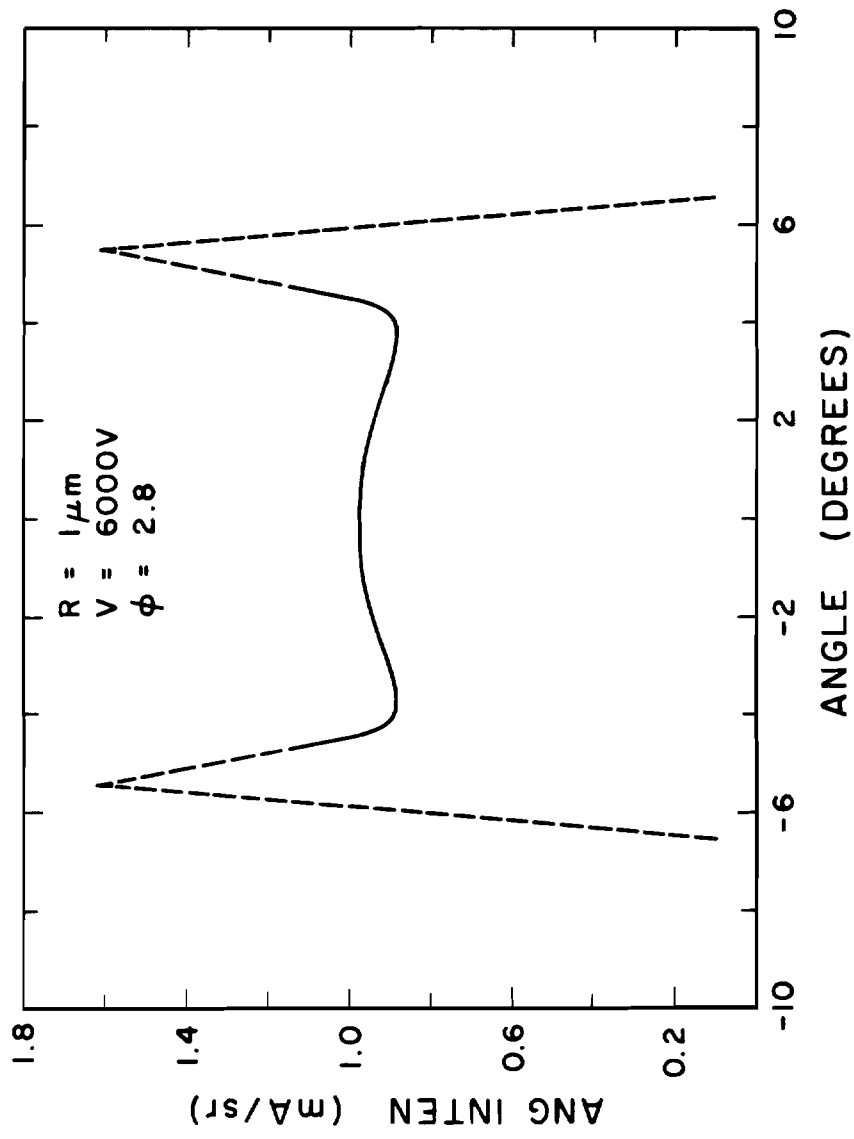


Figure 3-35. Computer calculated angular intensity distribution.

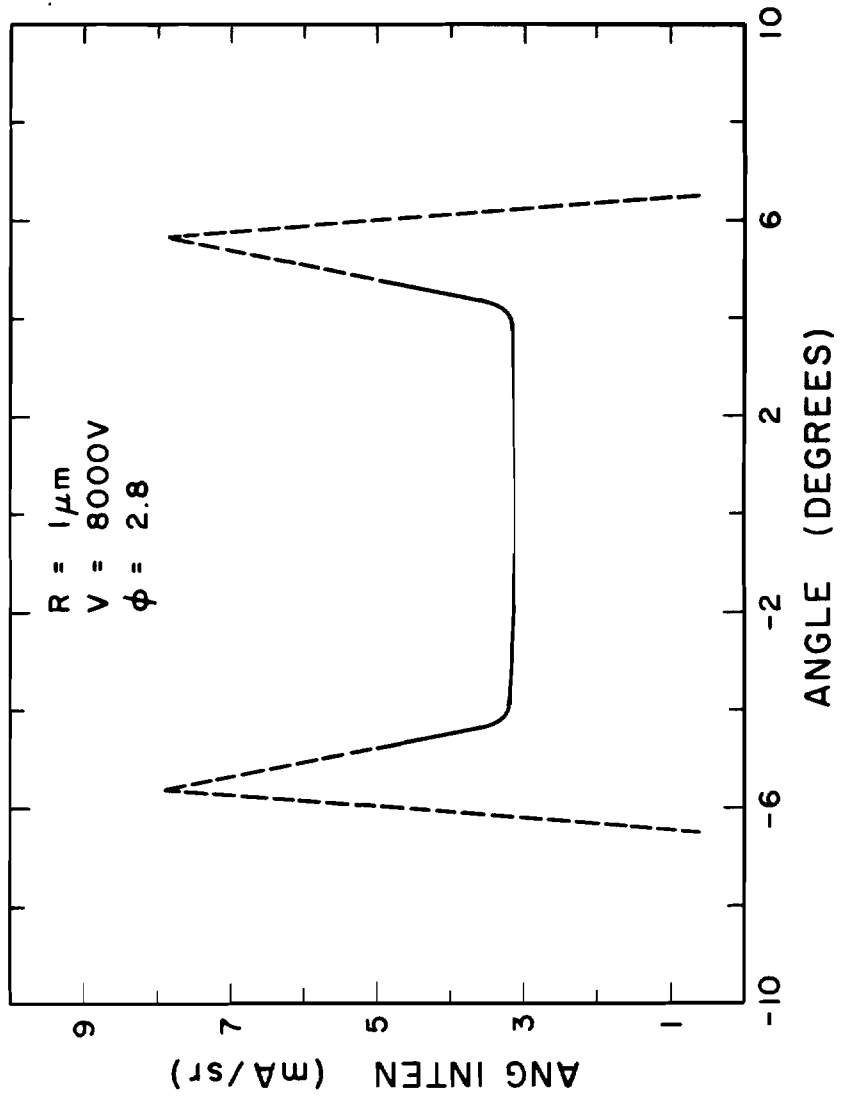


Figure 3-36. Computer calculated angular intensity distribution.

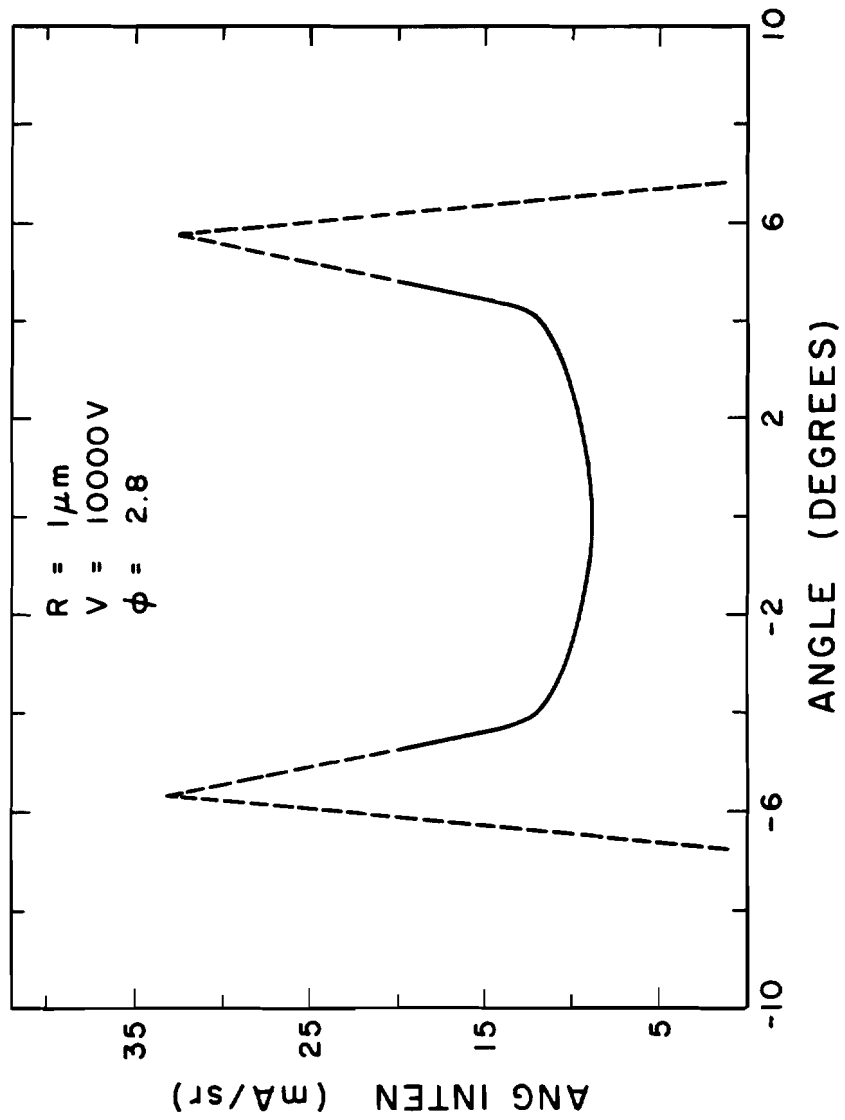


Figure 3-37. Computer calculated angular intensity distribution.

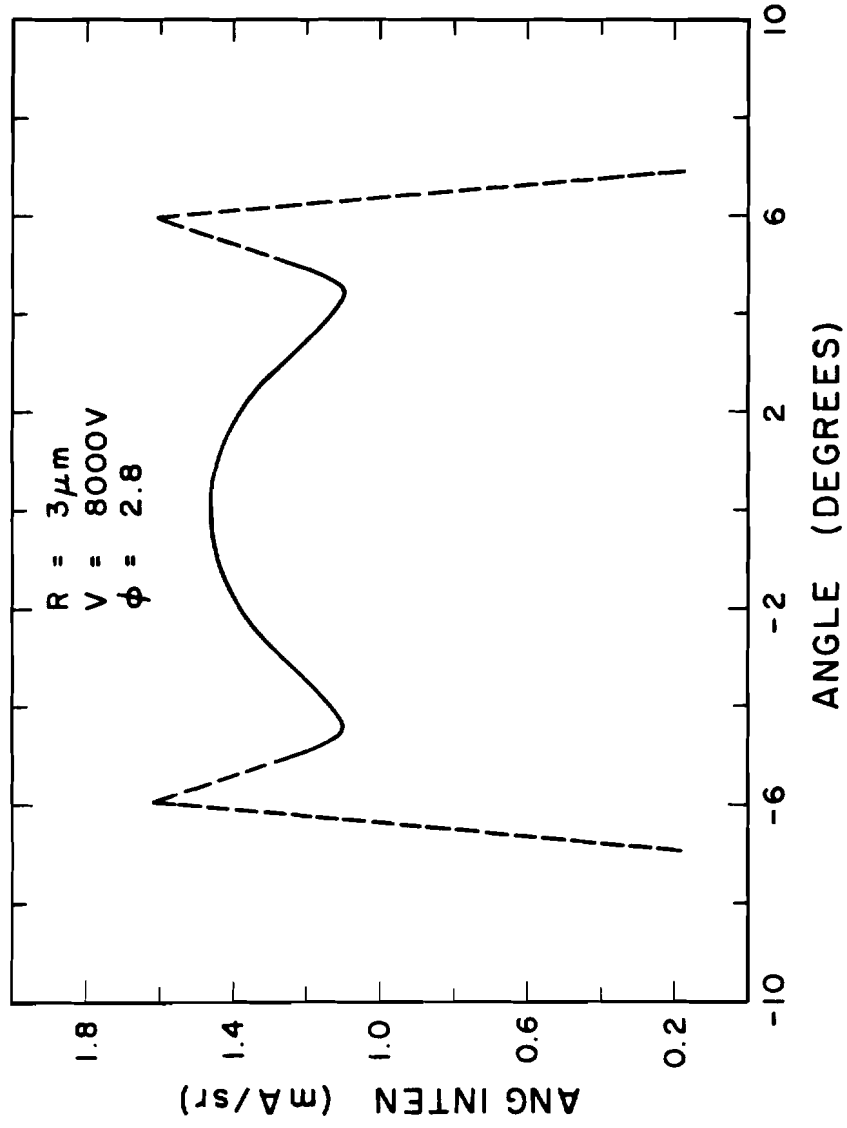


Figure 3-38. Computer calculated angular intensity distribution.

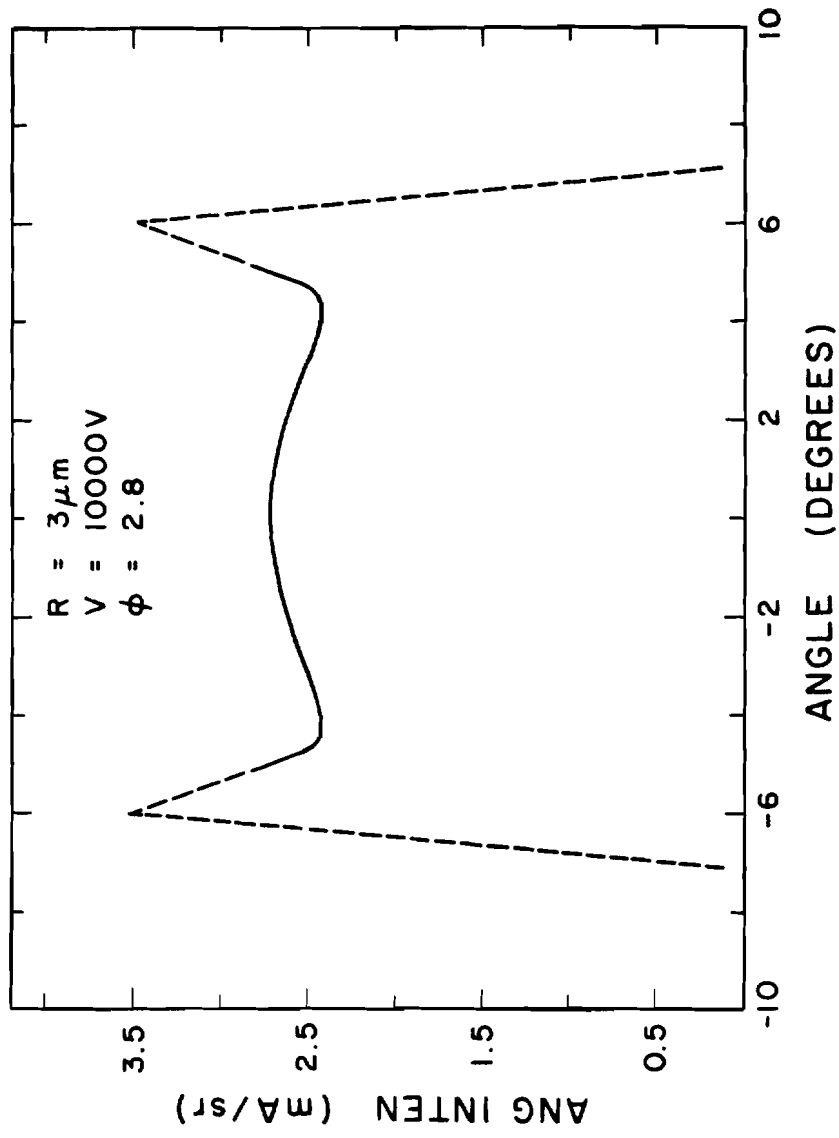


Figure 3-39. Computer calculated angular intensity distribution.

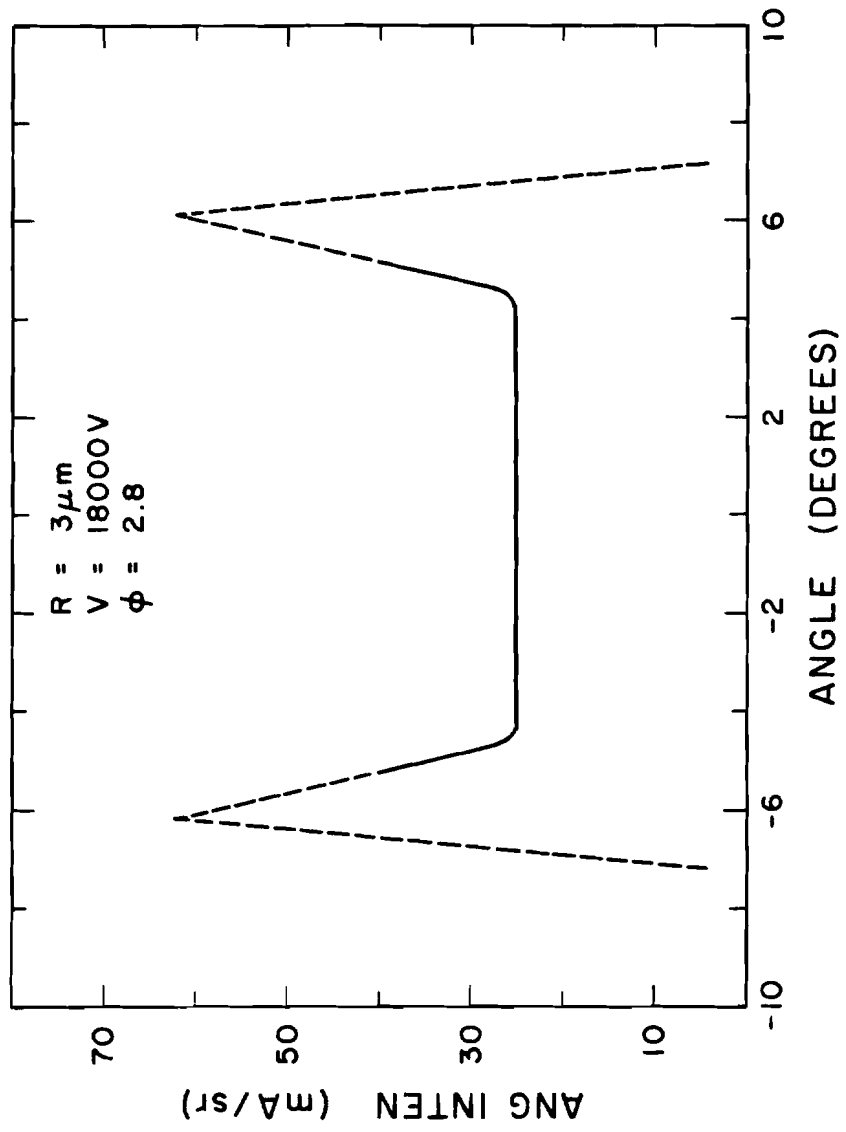


Figure 3-40. Computer calculated angular intensity distribution.

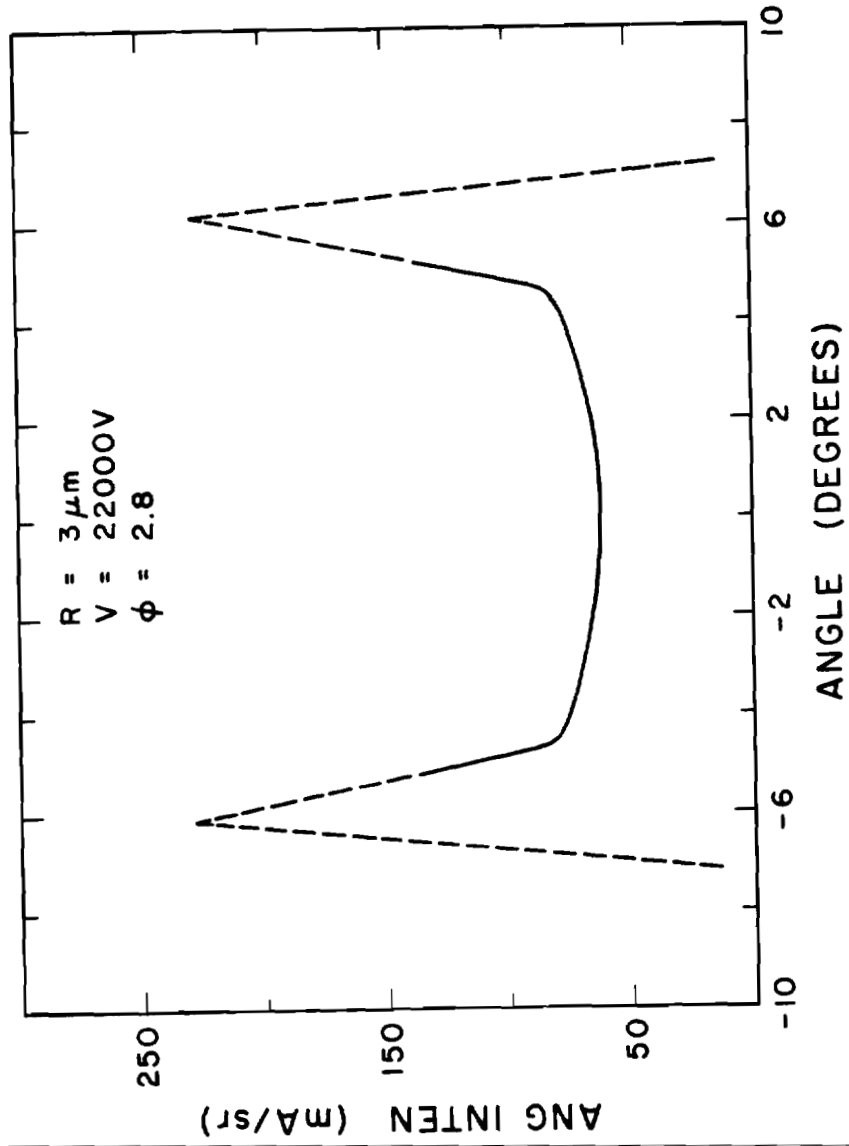


Figure 3-41. Computer calculated angular intensity distribution.

The work function chosen for these calculations was 2.8 eV as it gave reasonable results. Changing the work function by increments of 0.1 eV causes approximate factors of 1.9 change in the angular intensities ( $e^{0.1/kT}$ ). Since the J to F relationship (Schottky plot slope) is independent of work function for our operating regime ( $F < 0.12 \text{ V/\AA}$ ) (see Figure 3-22), a work function change should affect only the absolute values of the angular distributions, not their shapes. A listing of the conditions for the calculations of Figures 3-30 to 3-41 is given in Table 3-8. As the emission distribution shapes progress from convex to concave, they go through a region in which the distribution is approximately flat. This condition occurs at higher voltages and at higher angular intensities as emitter radius is increased, in agreement with the experimental results presented in Section A.



TABLE 3-8

## Computer Simulations of Angular Intensity Distributions

$$T = 1800 \text{ K} \quad \phi = 2.8 \text{ eV}$$

<u>Emitter Radius</u>	<u>Anode Voltage</u>	<u>Central Emission Intensity I'</u>	<u>Central Emission Distribution Shape</u>
0.3 $\mu\text{m}$	2000 V	0.038 mA/sr	convex
	3000	0.2	flat
	4000	0.75	concave
	6000	9.0	concave
1.0 $\mu\text{m}$	4000	0.24	convex
	6000	0.96	convex
	8000	3.1	flat
	10000	8.5	concave
3.0 $\mu\text{m}$	8000	1.45	convex
	10000	2.75	convex
	18000	24.5 *	flat
	22000	70.0 *	concave

\* Values of  $I' > 10 \text{ mA/sr}$  have not been observed in any experiments to date. Also, anode voltages  $> 15 \text{ kV}$  are not reasonable for this electron gun.

## REFERENCES

1. L. W. Swanson, R. W. Strayer and F. M. Charbonnier, Surf. Sci. 2, 177 (1964).
2. L. W. Swanson and A. E. Bell, Advances in Electronics and Electron Physics 32, 193 (1973).
3. E. Murphy and R. Good, Jr., Phys. Rev. 102, 1464 (1956).
4. A. El-Kareh, J. C. Wolfe and J. E. Wolfe, J. Appl. Phys. 48, 4749 (1977).
5. Program written by A. E. Bell.
6. L. R. Danielson and L. W. Swanson, Surf. Sci. 88, 14 (1979).
7. Data from G. Schwind.
8. N. K. Kang, et al., J. Vac. Sci. Technol. 19, 1077 (1981).
9. N. K. Kang, Private Communication.
10. J. C. Wiesner and T. E. Everhart, J. Appl. Phys. 44, 2140 (1973).

## CHAPTER 4

## CURRENT FLUCTUATION STUDY

## A. Experimental Current Fluctuation Results

Electron beam noise spectra were taken for several different emitters in different experimental arrangements and using different spectrum analyzers. A typical noise spectrum is shown in Figure 4-1. The vertical axis of Figure 4-1 is the power spectral density  $W(f)$  where

$$\langle \Delta I^2 \rangle_{f_1 \dots f_2} = \int_{f_1}^{f_2} W(f) df.$$

Experimentally, the mean square of the current fluctuations in a specified frequency range ( $f_1$  to  $f_2$ ) is measured by a bandpass amplifier followed by some type of averaging circuit to extract the mean square or more often, the root-mean-square values. Alternatively, digital signal analysis techniques can be applied to a probe current signal to achieve the same results. The data of Figure 4-1 was taken with an analog type spectrum analyzer. The beam current was amplified with a PAR model 181 current sensitive preamplifier and the output was fed to a Quantech model 304 spectrum analyzer. The preamplifier frequency response was DC to 5 kHz. Discrete data points were taken for several runs through the spectrum from 1 Hz to 5000 Hz. A spectrum with the beam turned off was

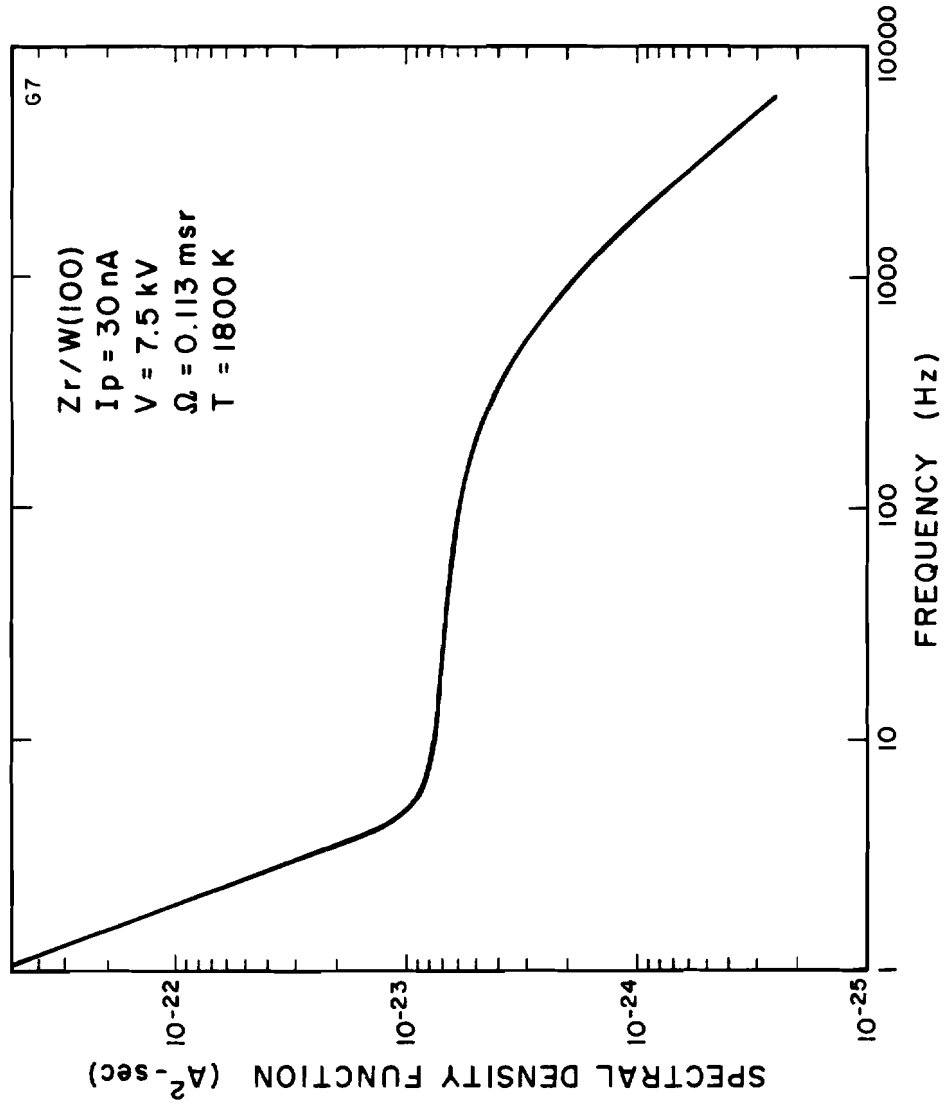


Figure 4-1. Power spectral density function of apertured central emission current. Aperture defines  $\Omega$  given in figure.

subtracted from the beam noise spectrum to correct for background. These data were analyzed with a computer and integrated to obtain the final overall noise percentage.

In order to compare noise spectra taken with different probe currents of the spectral density was normalized by dividing it by the square of the probe current. The justification for normalizing the noise power spectral density to the square of the probe current (beam current) can be seen in Figure 4-2, where the noise power spectral density in three different regions of the spectrum is plotted versus the probe current,  $I_p$ . The noise power is proportional to the square of the probe current, at least for the frequencies and currents considered in Figure 4-2. This is equivalent to saying that the noise percentage remains constant with respect to probe current.

Space charge suppression of noise can be significant at high current densities for field emitters. Pushpavati and Van der Ziel<sup>1</sup> have shown theoretically that noise current increases with beam current until the current density attains a value on the order of  $10^5$  to  $10^6$  A/cm<sup>2</sup> at which point space charge noise suppression should cause the noise current to decrease with a further increase in beam current. Since for our groups of emitter radii and angular intensities we do not go above  $\sim 5 \cdot 10^4$  A/cm<sup>2</sup> (see Figure 3-23), we do not have to consider this effect. Space charge noise suppression can be seen in previous data taken on a Zr/W emitter of smaller radius.<sup>2</sup>

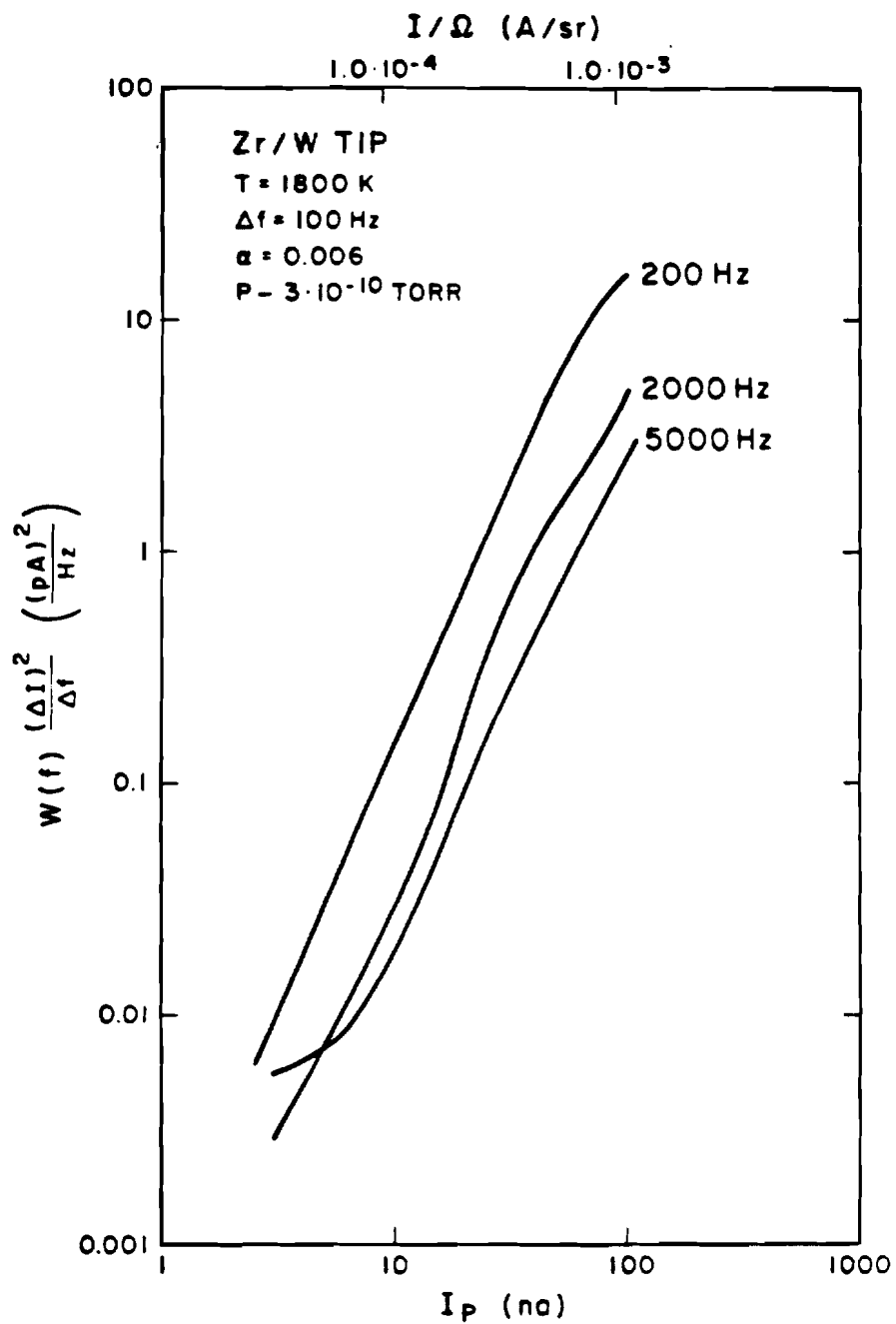


Figure 4-2. Variation of the spectral density function  $W(f)$  with probe current  $I_p$ .

Considering Figure 4-1, the total integrated noise current from 1 Hz to 5000 Hz is 0.26%.

Note that the high frequency end of the spectrum falls off as  $1/f$  (-3 dB/octave). Assuming that this behavior continues all the way down to shot noise level, we can determine the frequency at which this occurs and the additional contribution that this extrapolated high frequency portion would make to the total rms noise percentage. The frequency at which the extrapolated noise level would reach shot noise is 190.5 kHz. The additional rms noise in the  $> 5$  kHz region is 0.27%. Therefore, the total rms noise percentage would be 0.53%, if one can assume that the  $1/f$  decrease continues all the way to shot noise.

Figure 4-3 shows noise spectra taken from three different emitters in two different experimental arrangements. The following conditions pertain to Figure 4-3.

<u>Emitter</u>	<u>Experimental Apparatus</u>	<u>Approximate Radius</u>	<u>Electron Beam Half Angle</u>	<u>Spectrum Analyzer</u>
A2	Angular Distribution	0.8 $\mu\text{m}$	.00156 rad	Analog
G7	Optical Column	2.3	.006	Analog
G10	Optical Column	2.7	.006	Digital

Figure 4-3 shows the relative noise percentages under various conditions. As can be seen, increasing emitter radius reduces the noise level, as would be expected since a greater emitting surface area

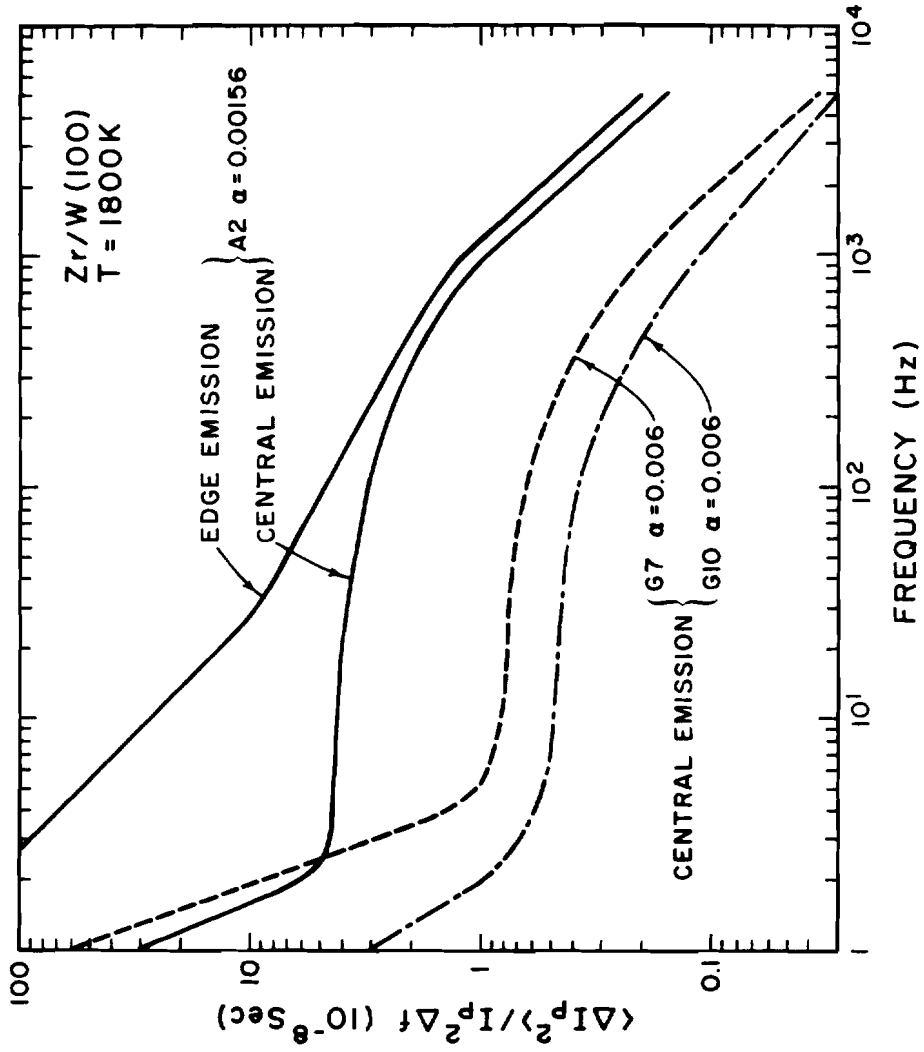


Figure 4-3. Normalized spectral densities for three different emitters. Radii are A2 = 0.8  $\mu\text{m}$ , G7 = 2.3  $\mu\text{m}$  and G10 = 2.7  $\mu\text{m}$ .



reduces the percentage contribution from individual fluctuations.

Reducing the aperture half-angle  $\alpha$  and reducing the emitter radius, as is done for emitter A2, compounds the reduction of cathode surface emission area; in this case, aperture angle and emitter radius reduction each contribute approximately a factor of 10 emitting area reduction, with the result that the emitting area of A2 is  $\sim 0.01$  times that of G7. Emitter A2 was mounted in the angular distribution measuring apparatus, so that both the central and the facet edge emission could be examined. The increase in noise at the facet edge is mainly confined to the low frequencies ( $< 100$  Hz).

An attempt was made, using emitter G10, to observe directly the effect on the noise of changing the aperture angle. In this experiment, a focusing magnetic lens was used to compress the electron trajectories (reduce the angular magnification) so that with a fixed aperture 0.012" diameter at 1.0" from the tip, the effect of a variable aperture could be obtained. The result of this experiment is shown in Figure 4-4. The normalized power spectral density decreases with increasing aperture angle for frequencies  $> 5$  Hz. This is expected behavior if the relative noise power is due to random uncorrelated emission sites on the surface. Taking a larger surface would be expected to include a greater number of sites. The behavior of the variable aperture spectrum for  $f < 5$  Hz is unexpected. Even if all the emission sites were correlated at  $f < 5$  Hz, the fractional noise power would only remain constant with aperture angle, not increase.

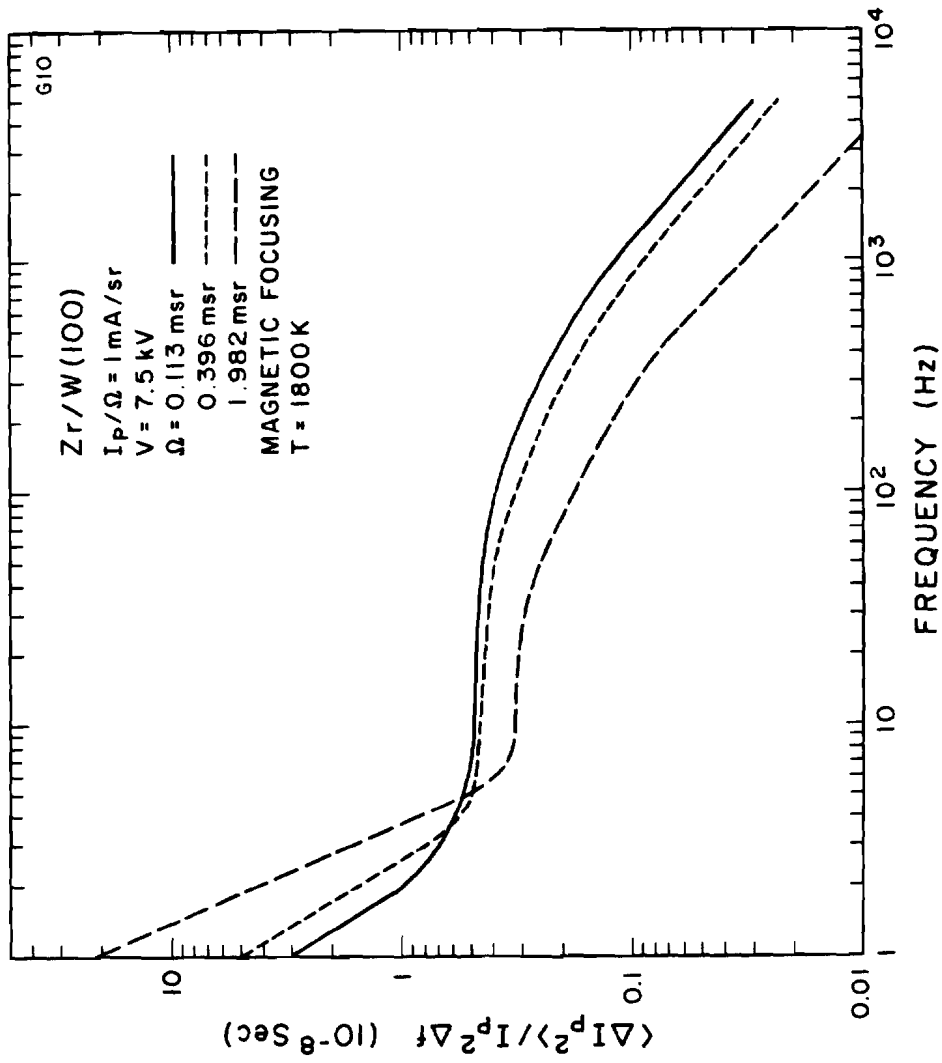


Figure 4-4. Variable aperture noise power spectra.

In this experiment, if the probe current is used to indicate the increase in  $\alpha$  (assuming a constant cathode current density), then the total integrated r.m.s. noise percentage vs.  $\alpha$  is given by Figure 4-5. This plot shows a functional relationship of:

$$\% \text{ rms noise current} \propto \alpha^{-1/3}$$

Figure 4-6 shows the variation in noise current percentages as a function of temperature. The 1800 K normal operating temperature of this emitter is close to the noise minimum for high frequencies but beyond the minimum for low frequencies ( $f \sim 200$  Hz). This data may be compared with earlier data (reference 2) which covers a different temperature range (300 K - 1600 K).

One last set of experimental data was obtained by means of a Hewlett Packard 5420A Digital Signal Analyzer. This instrument has two input channels and can measure cross-correlation and the coherence function as well as the usual power spectrum and auto-correlation using a single channel. Emitter G10 of Figure 4-3 was used in the unfocused mode, that is,  $\alpha = 0.006$ . The coherence function is

$$\gamma^2(f) = \frac{\overline{G_{yx}(f) \cdot G_{yx}(f)^*}}{\overline{G_{xx}(f) \cdot G_{yy}(f)}}, \quad 0 \leq \gamma^2 \leq 1$$

where  $\overline{\quad}$  denotes an average

and  $G_{yx}(f) = S_y(f) \cdot S_x(f)^*$ .

---

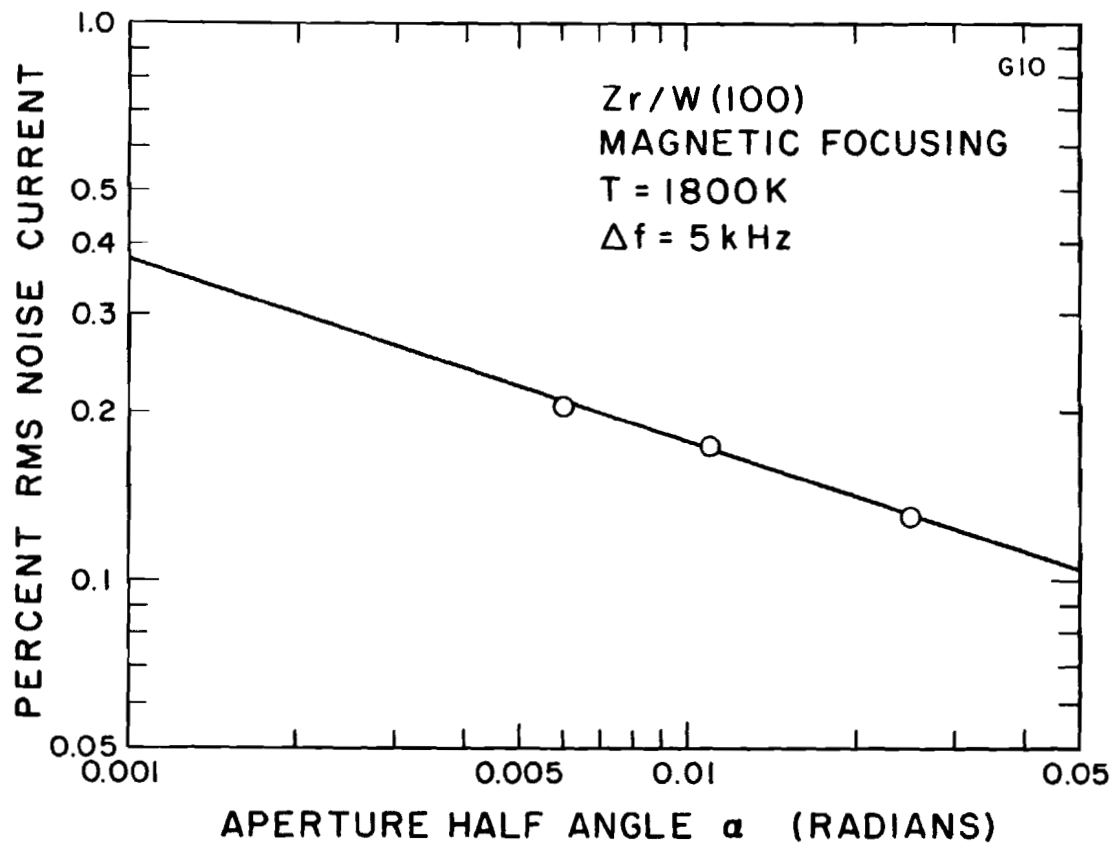


Figure 4-5. Noise percentage vs aperture half angle.

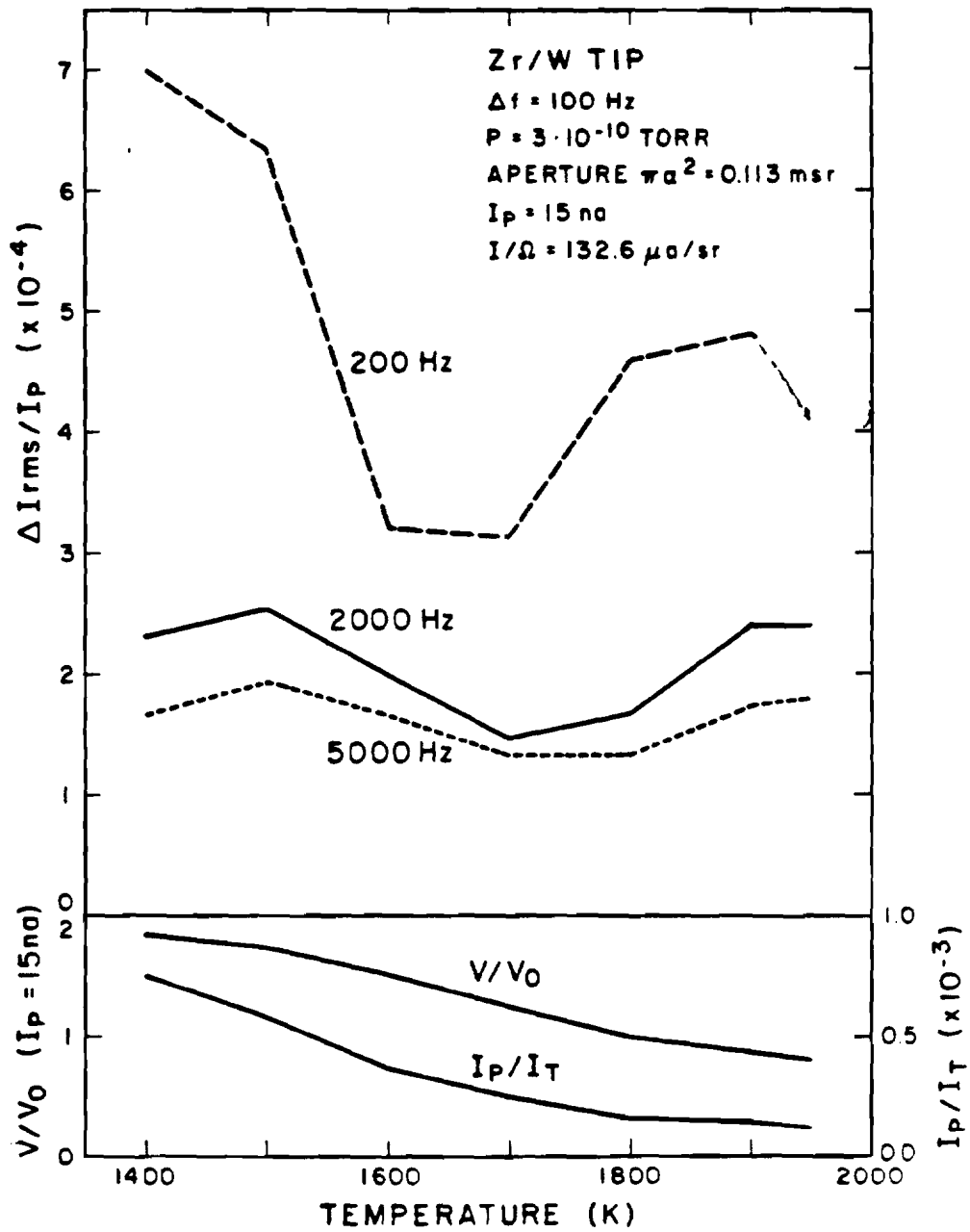


Figure 4-6. Relative noise amplitude  $\Delta I_{rms}/I_p$  and voltage  $V/V_0$  for a given angular intensity beam shown as a function of emitter temperature.  $I_p/I_t$  is the beam transmission.

The linear spectrum,  $S_x(f)$ , is the Fourier transform of the input voltage signal,  $x(t)$ .

$$\text{Channel 1} \quad S_x(f) = F x(t)$$

$$\text{Channel 2} \quad S_y(f) = F y(t)$$

The coherence function between the probe current and total current for emitter G10 is shown in Figure 4-7. The increase in noise power with decreasing frequency in the range  $f < 10$  Hz seems to be due to a different type of current fluctuation, one in which the entire emitting surface fluctuates in phase, rather than as individual random emission sites. The phase was determined from the cross-spectrum to be  $\sim 0^\circ$  for the coherent part of this spectrum. This behavior suggests that the low frequency portion of the spectrum may be due to thermal fluctuations, rather than surface diffusion of atoms. This viewpoint will be explored in the following section.

Figure 4-8 shows the spectral density for the same emitter showing both the probe  $I_p$  and total  $I_T$  noise currents. Each spectrum is also multiplied by the coherence function to give the coherent noise power. Notice that the total current shows a much steeper slope than the probe current in the region where  $f < 10$  Hz. Also, the transition from the flat intermediate portion of the spectrum to the steep low frequency portion occurs at  $\sim 2$  Hz for the probe current and at  $\sim 20$  Hz for the total current.

---

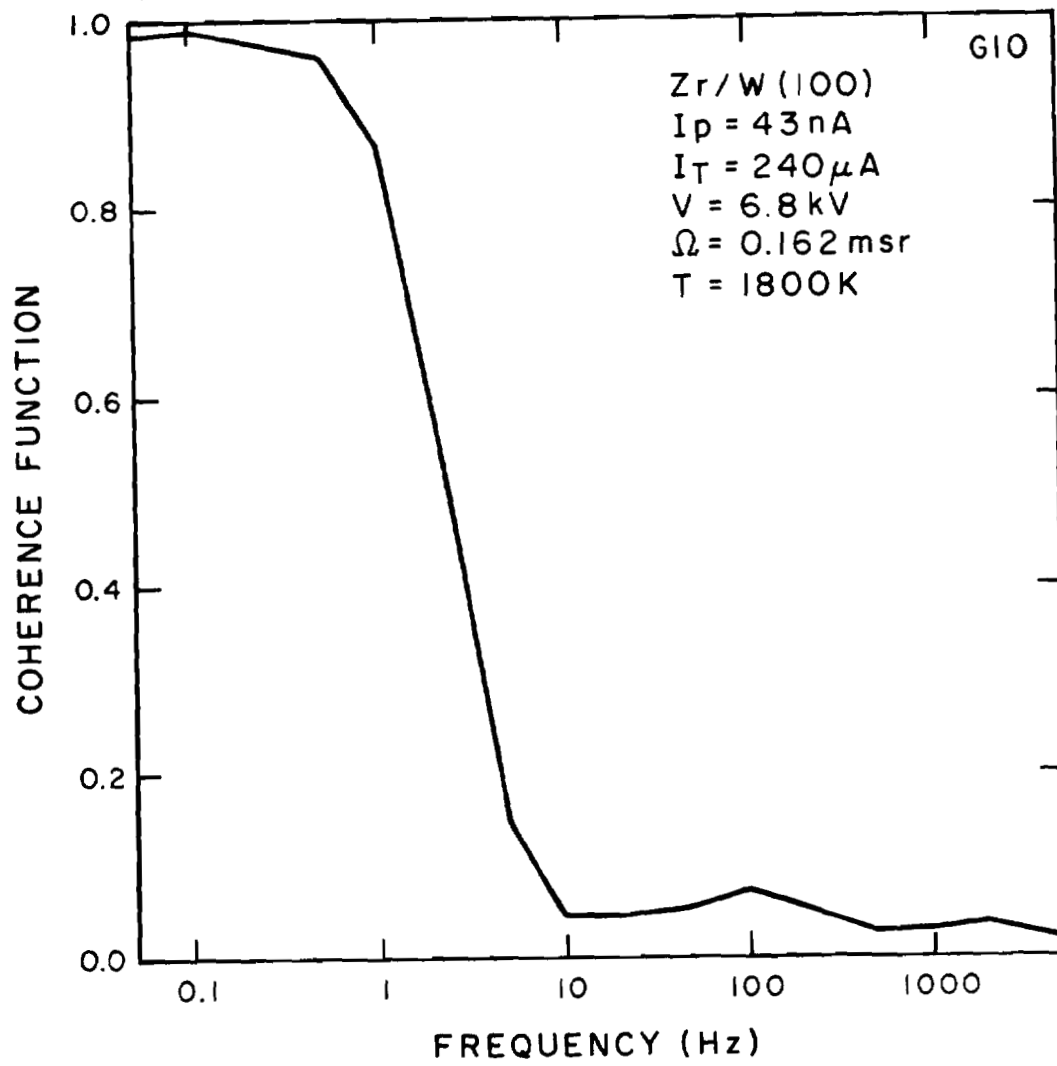


Figure 4-7. Coherence function.

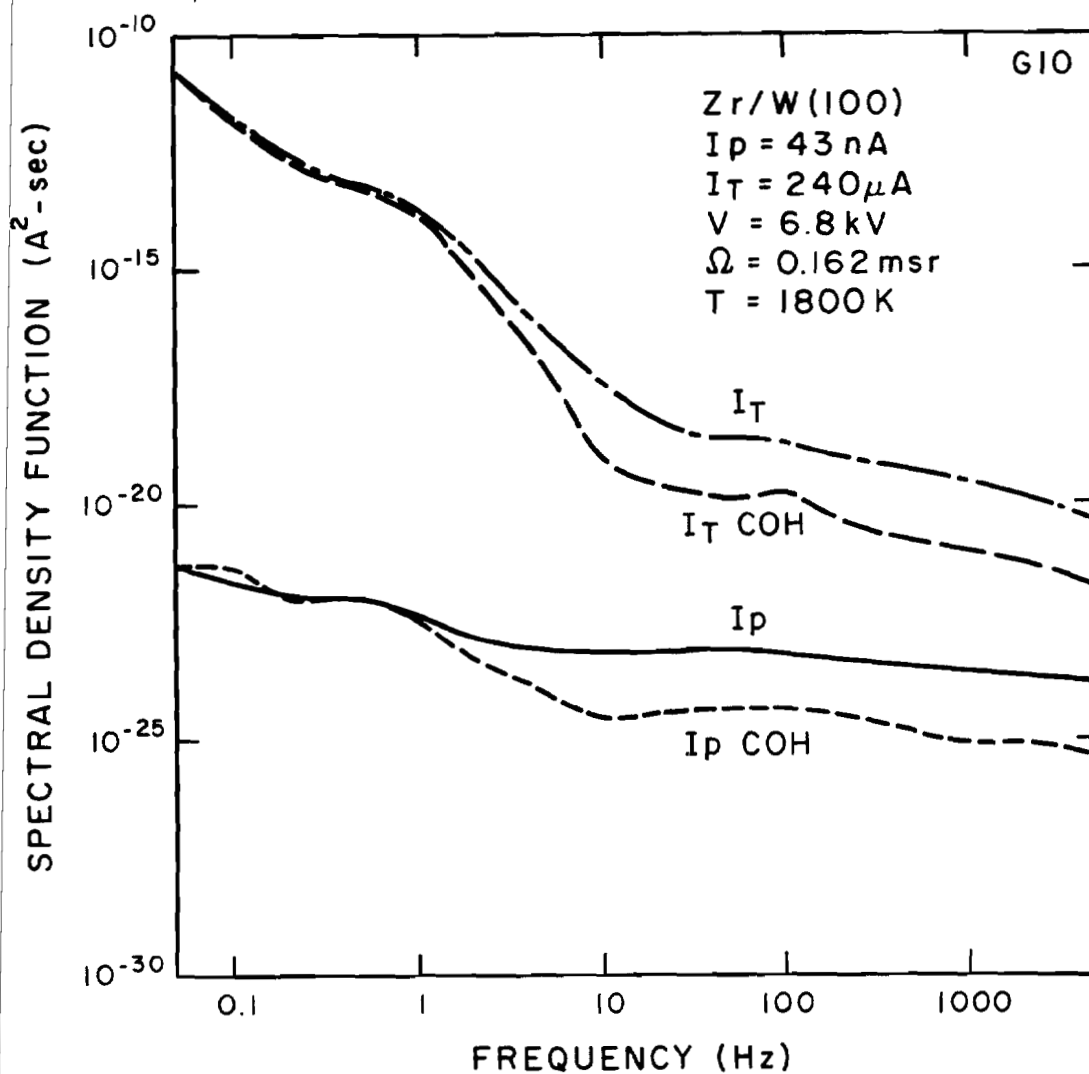


Figure 4-8. Noise spectral density.

$I_p = 43 \text{ nA}$  unbiased stage.

$I_p =$  Probe current (Apertured central emission current).

$I_T =$  Total current (Anode current).

$I_{\text{COH}} =$  Coherent component of current.



Figure 4-9 shows the noise spectra in Figure 4-8 normalized. We see the same general phenomenon as in Figures 4-3 and 4-4, namely, that an increase in emission area, whether accomplished by changing emitter radius, changing aperture size or shifting from probe to total current measurements, produces a lowering of the power spectral density for  $f \gtrsim 10$  Hz and increases the low frequency noise power ( $f \lesssim 2$  Hz). It appears that if a sufficiently small area were probed, the low frequency noise component would disappear and the spectrum would be flat down to 1 Hz.

#### B. Thermal Fluctuations - Theoretical

One of the most peculiar experimental results in the preceding section concerned the low frequency ( $f \lesssim 10$  Hz) noise power. Because of the behavior of the coherence function it seems reasonable to attempt to explain this part of the spectrum in terms of thermal fluctuations. First, an estimate of the magnitude of thermal fluctuations required to produce the observed low frequency spectrum is calculated. We have seen that the emission regime is basically Schottky with an increased  $\beta$  factor. The governing equation is Eq. (3-3)

$$J_S = 120 T^2 \exp [-\phi - e^{3/2} F^{1/2})/kT]. \quad (4-1)$$

The derivative with respect to temperature is

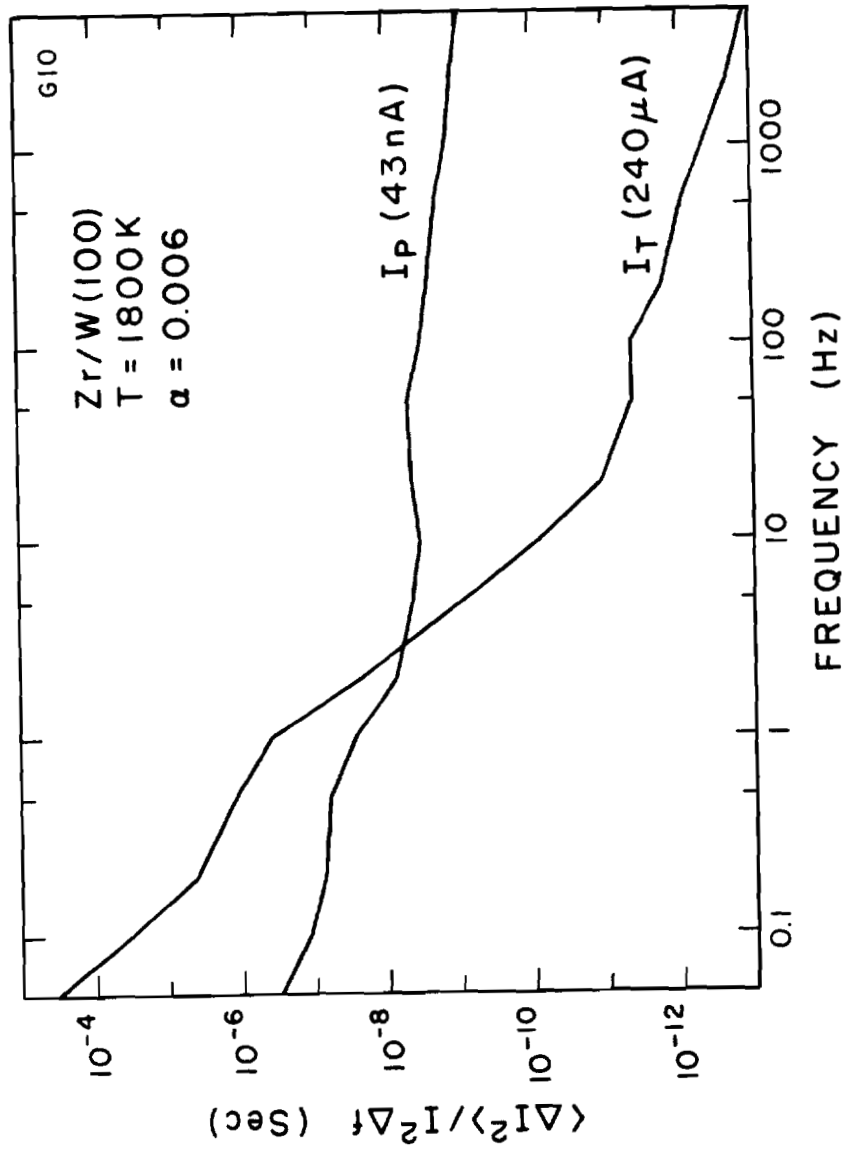


Figure 4-9. Normalized power spectral density for probe and total currents.

$$\frac{dJ_S}{dT} = \frac{J_S}{T} \left( 2 + \frac{(\phi - e^{3/2} F^{1/2})}{kT} \right)$$

or

$$\frac{dJ_S}{J_S} = \frac{dT}{T} \left( 2 + \frac{\phi - e^{3/2} F^{1/2}}{kT} \right) .$$

For  $T = 1800$  K,  $\phi = 2.8$  eV,  $F = 0.08$  V/Å

$$\frac{dJ_S}{J_S} = 13 \frac{dT}{T} . \quad (4-2)$$

Therefore, a 1°K temperature fluctuation produces a 0.7% fluctuation in  $J_S$ . From Figure 4-9, current fluctuations in  $I_T$  for 0.1 to 2.0 Hz amount to  $\sim 0.14\%$  ( $\Delta I$  rms/ $I$ ). This could be produced from  $\sim 0.2$  K temperature fluctuations in the same frequency band.

The next step is to determine why the temperature fluctuations are confined to the low frequency region of the spectrum. Blik<sup>2</sup> has given a diffusion model for samples of finite dimensions which generates noise power spectra having regions of  $f^{-1/2}$ ,  $f^{-1}$ ,  $f^{-3/2}$  and  $f^{-2}$ . The boundaries of these regions are derived from the sample dimensions.

In our case, the heat conductivity or diffusion equation is

$$\frac{\partial u}{\partial t} = D \nabla^2 u$$

where  $\mu$  = thermal energy density, the diffusion coefficient

$$D = \frac{k}{\rho c} \quad \text{and}$$

$k$  = thermal conductivity = 1.03 W/cm K (1800 K)

$\rho$  = density = 19.3 gm/cm<sup>3</sup>

---

$c = \text{specific heat} = 0.036 \text{ cal/gm } ^\circ\text{C (1000 } ^\circ\text{C)},$   
 therefore  $D = 0.3541 \text{ cm}^2/\text{sec}.$

Bliek's theory states that for wire-like samples such as our heating filament, the  $f^{-1}$  spectral region should vanish. The result of fitting lines of the remaining slopes to the total current data of Figure 4-9 is shown in Figure 4-10. The breakpoints of the lines are at approximately 5.7 Hz and 20 Hz. Bliek's theory relates these breakpoints to dimensions of the sample by means of

$$L_x^2 = \frac{2\pi D}{f}$$

where  $L_x = \text{sample dimension and}$   
 $f = \text{breakpoint frequency.}$

The breakpoints in Figure 4-10 correspond to tungsten sample dimensions of 0.625 cm and 0.344 cm.

Figure 4-11 shows a drawing of the emitter and its heating filament. The two dimensions derived above may relate to the full length and half length of the tungsten hairpin filament. The relation to the full length ( $\sim 0.6 \text{ cm}$ ) of the filament is easy to understand from Bliek's theory. The half length is possibly related to the thermal discontinuity produced by the emitter spot welded at the half-way point on the filament.

The preceding is meant to suggest an explanation for the total current noise spectrum and the coherent part of the probe current noise spectrum. Further data will have to be taken on different filament lengths using different materials before this explanation can be confirmed.

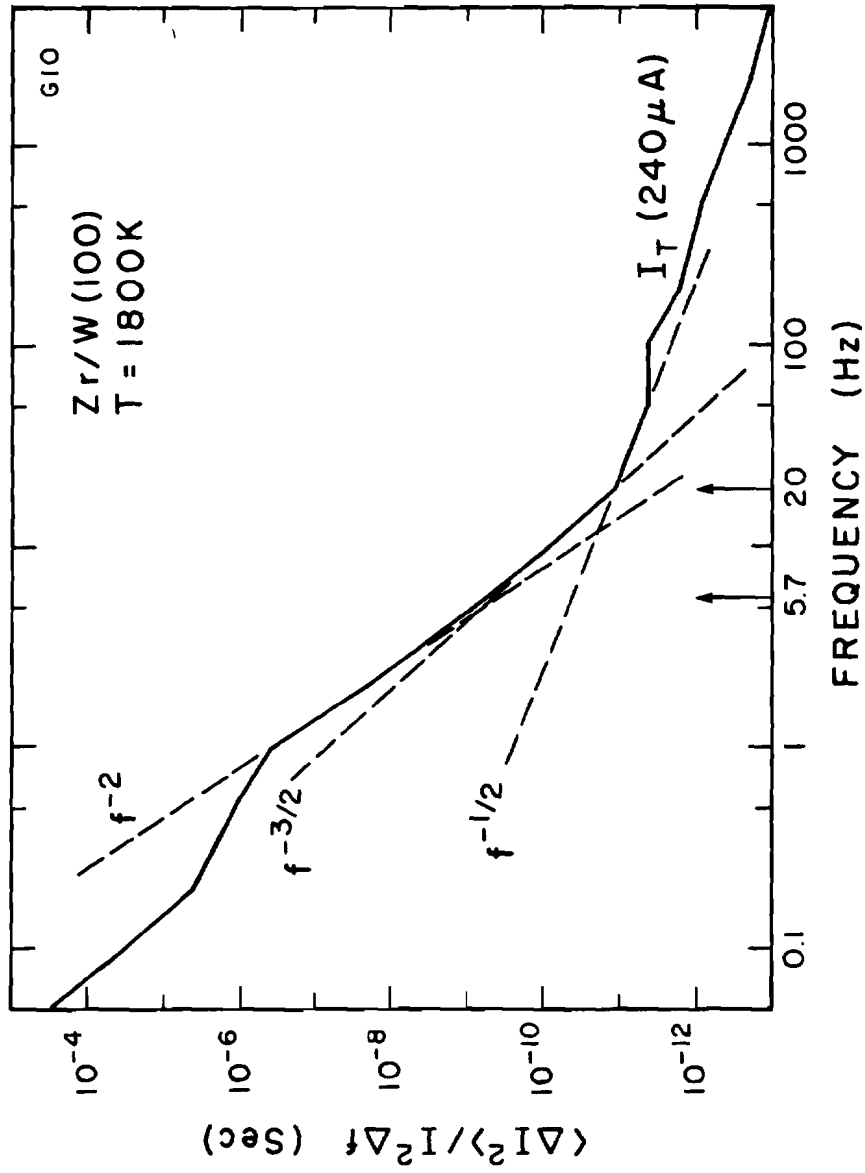


Figure 4-10. Normalized total current power spectral density.

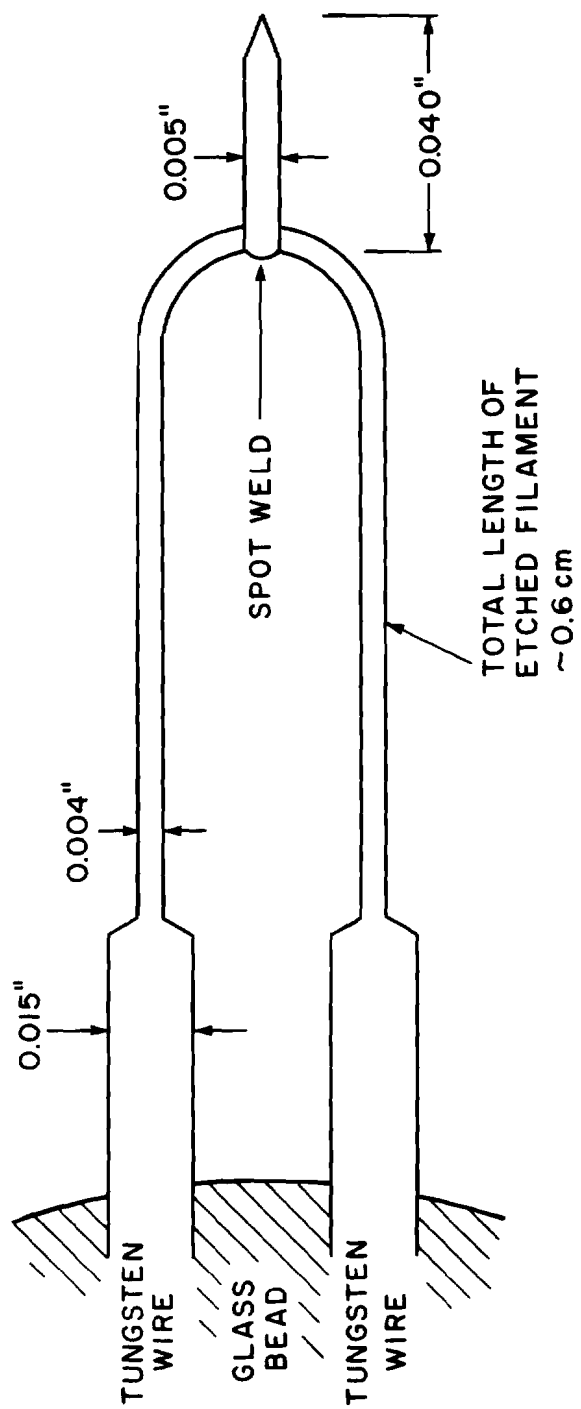


Figure 4-11. Emitter and heating filament.

## REFERENCES

1. P. J. Pushpavati, and A. Van der Ziel, IEEE Trans. on El. Dev. ED-12 395-398 (1965).
2. L. Blik, in Recent Developments in Condensed Matter Physics, Vol. 3, Ed. by DeVreese, Lemmens, Van Doren, Van Royen; N.Y., 333-338 (1981).

## CHAPTER 5

## ELECTRON OPTICAL CHARACTERISTICS

## A. Electron Gun Transmission

We define the electron gun transmission to be the probe current divided by the total current, where the probe current is that which passes through a beam defining aperture and is used to form the focused beam. The total current is that which leaves the emitter, as measured by a microammeter in series with the tip. For practical reasons, the current measured at the anode is combined with the current striking the beam defining aperture plate (or Faraday cup aperture) and this is considered to be the total current. There is evidence<sup>1</sup> that the low current density background (seen in the angular intensity experimental data) extends out from the anode aperture to angles which make it impossible to attribute this background to emission from the tip to shank. This is probably backscattered current from the anode, which will be discussed in the next section. This background current may not be entirely collected by the angular distribution experimental arrangement.

The gun transmission or efficiency is an important practical consideration for this emitter. Since considerable thermionic emission occurs from the conical portion of this emitter, and from the four (100) areas orthogonal to the end (100) facet, this results

---



in anode outgassing and creation of an effective gas source in the vicinity of the emitter tip. A high local pressure in the vicinity of the emitter creates several problems. One problem is a reduction in current density brought about by high residual  $O_2$  pressures. Also, ion sputtering of the tip by electron bombardment ionization of the residual gas and greater probability of a destructive arc occur with increasing pressure. The suppressor electrode reduces the anode bombardment, but also reduces the electric field at the tip. The radius of the emitter also controls the electric field at the emitter apex relative to the cone shank, since the cone angle is more or less the same for various emitter radii.

Table 5-1 lists the beam transmission at an angular intensity of 1 mA/sr for emitters of various radii (i.e. different operating voltages). From the Table 5-1 results it is clear that beam transmission decreases with increasing operating voltage. This result can be understood on the basis of larger radii emitters requiring greater voltages for a given angular intensity while the geometry of the cone and shank does not change much with tip radius. Thus, while doubling the anode voltage may compensate for an increase in tip radius, it overcompensates for the slight geometrical change on the cone and shank thus causing more shank emission.

Table 5-1

Summary of voltage values required for 1 mA/sr at 1800 K and the total emission current,  $I_T$ , for various emitters.  $I_c$  is the central emission beam current obtained through a 3.1 mrad full angle aperture.

<u>Voltages (kV)</u>	<u><math>I_T</math> (<math>\mu</math>A)</u>	<u><math>I_c/I_T</math></u>
9.1	340	$2.3 \times 10^{-5}$
5.0	180	$4.3 \times 10^{-5}$
4.7	130	$6.0 \times 10^{-5}$

The thermionic emission suppressor electrode has been operated at -300 V with respect to emitter potential for the data shown in Table 5-1. It is of interest to determine the effect of variable suppressor bias on the transmission ( $I_{\text{probe}}/I_{\text{total}}$ ), the anode voltage required for a given angular intensity on axis and the angular distribution.

Figure 5-1 is a plot of total and probe currents taken with a constant anode voltage and variable suppressor voltage. This data was taken for a gun with a fixed aperture in an electron optical column. It can be seen that the total current decreases faster than the probe current, implying a better transmission for higher suppressor voltages.

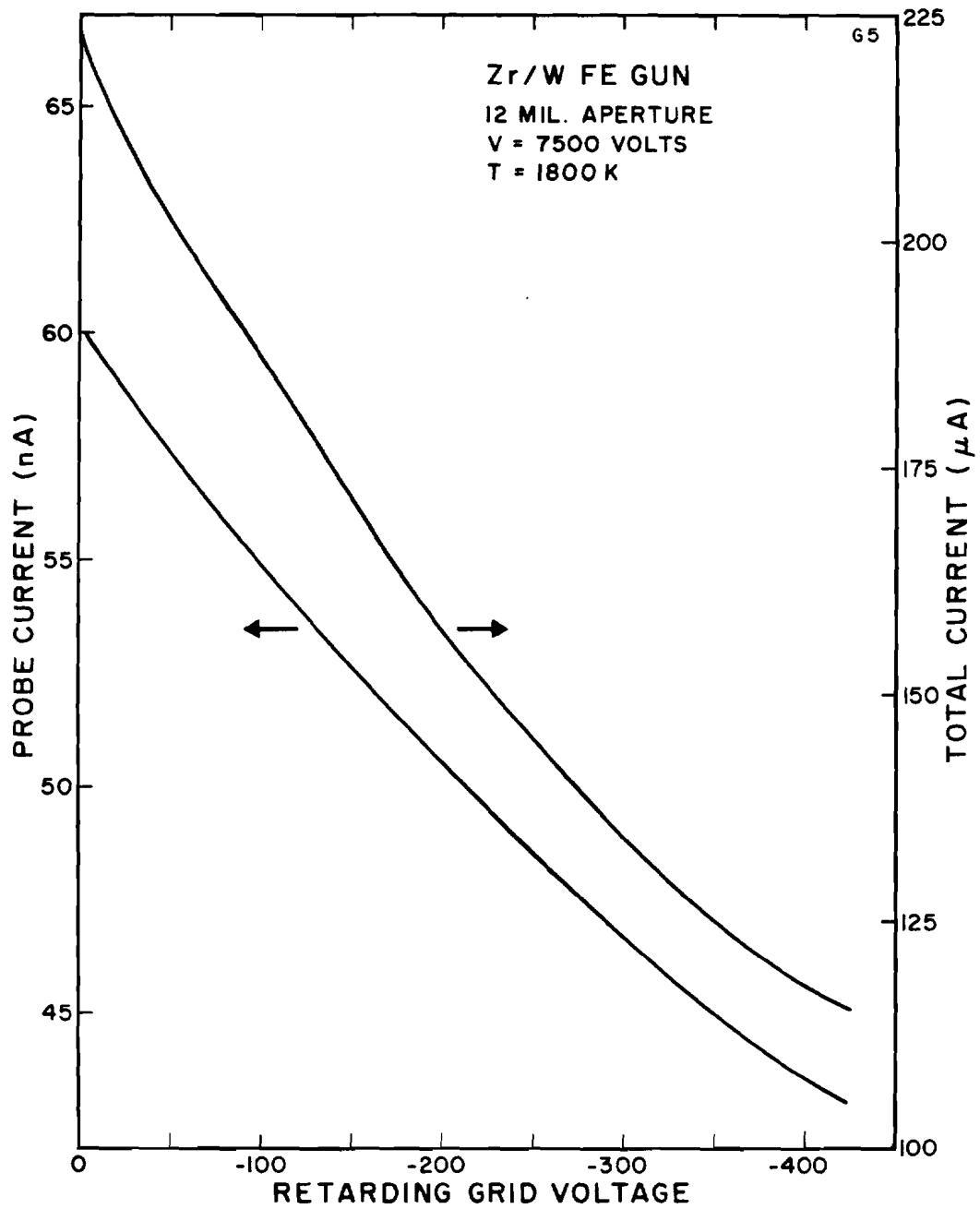


Figure 5-1. Suppressor control of current with constant anode voltage. Fixed aperture at 1.00 inch distance from emitter.

Using Emitter No. A3, in the condition shown in Figure 3-10, beam transmission vs suppressor bias for a constant central angular intensity (constant field at apex of tip) was measured. This was done for three different angular intensities. Figure 5-2 shows the increase in transmission for increasing suppressor bias. There is evidence that for suppressor bias of 0 to -100 V, the focused electron spot in an optical column becomes diffuse due to inclusion of emission in the probe current which comes from the shank and not the tip. The fact that below about -125 V the transmission curves cross over would tend to indicate that this region includes emission from the different areas on the emitter than the region above -125 V.

The anode voltage required to maintain the constant angular intensities in Figure 5-2 is plotted in Figure 5-3. It can be seen that as the anode voltage increases, the suppressor bias becomes a smaller proportion of the anode voltage and so has less effect on the field at the tip.

Figure 5-4 is a plot made using Emitter No. 3A with the angular distribution characteristics shown in Figure 3-10. This is a plot of the angular distribution for suppressor bias of -100, -300 and -500 volts, with the anode voltage readjusted at each suppressor voltage to maintain a constant central angular intensity. There is a very slight compression of the angular spread with increasing bias voltage, but in the region of beam half angle up to 0.040 rad.

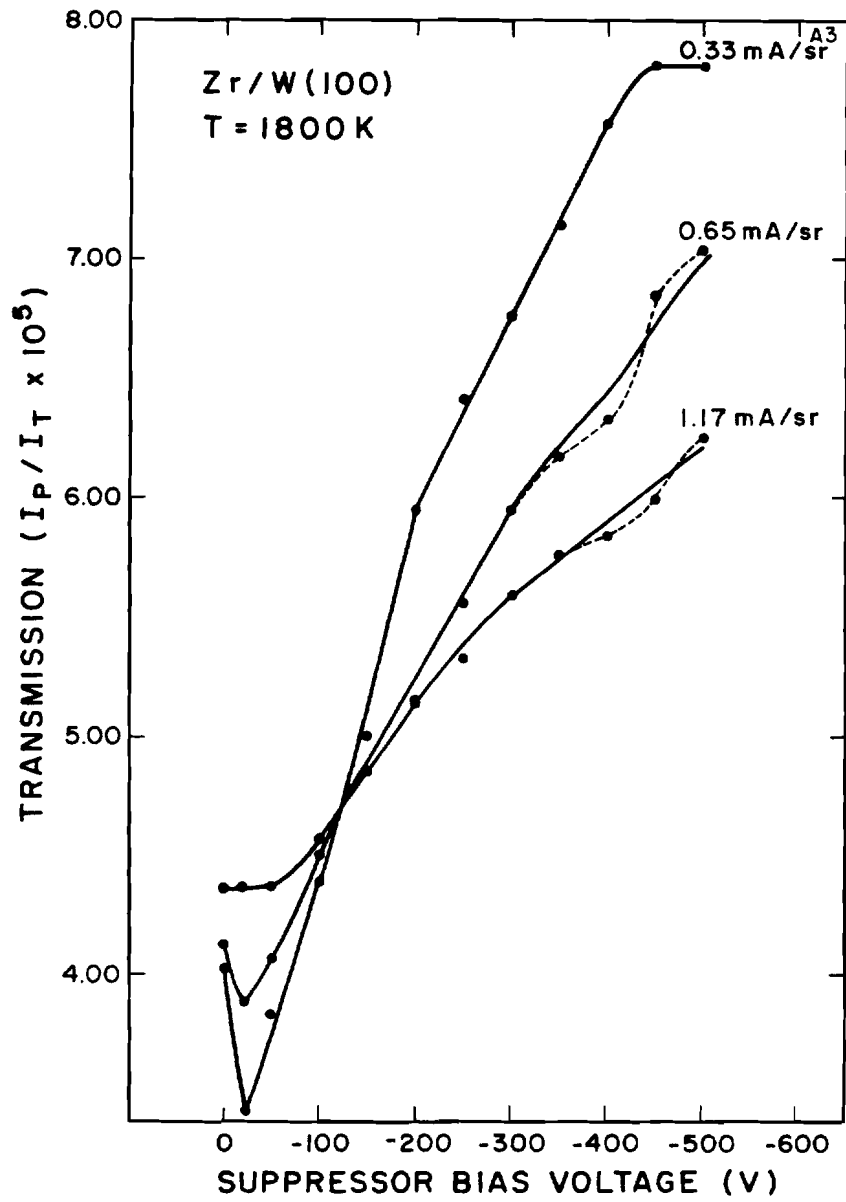


Figure 5-2. Transmission vs suppressor bias for constant angular intensity.  $\alpha = 0.00156$  rad.

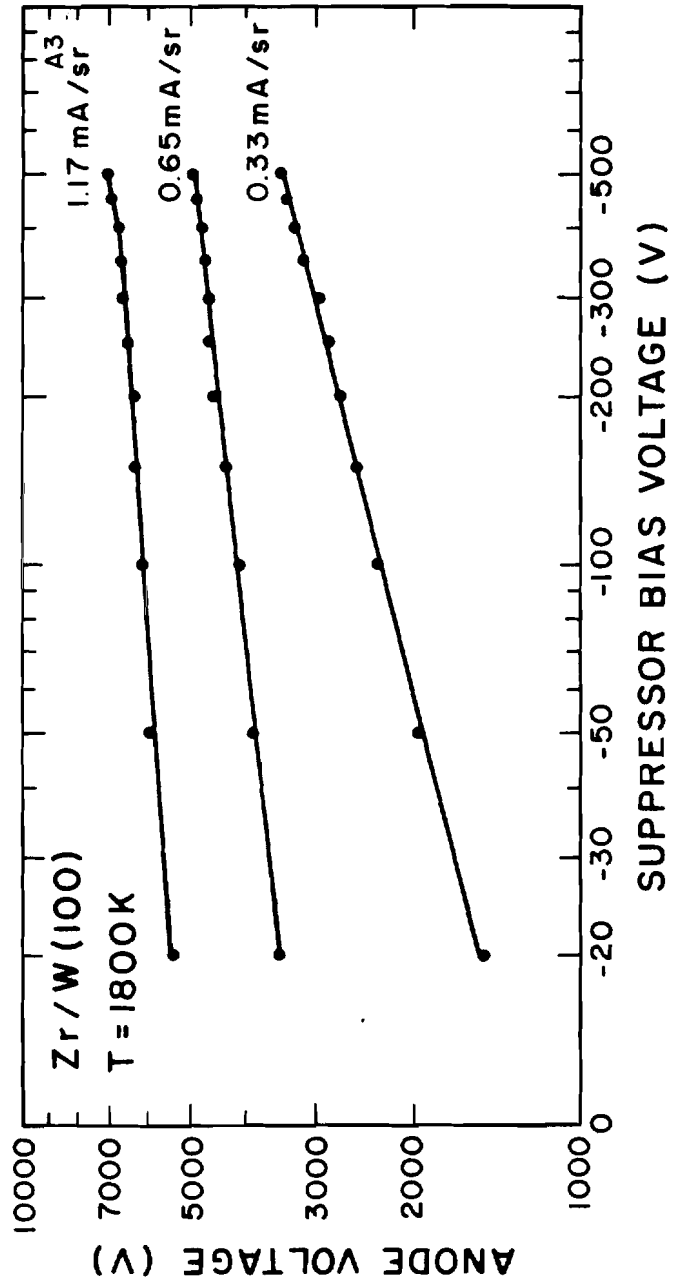


Figure 5-3. Constant angular intensity (constant field) variation of anode voltage with suppressor bias.

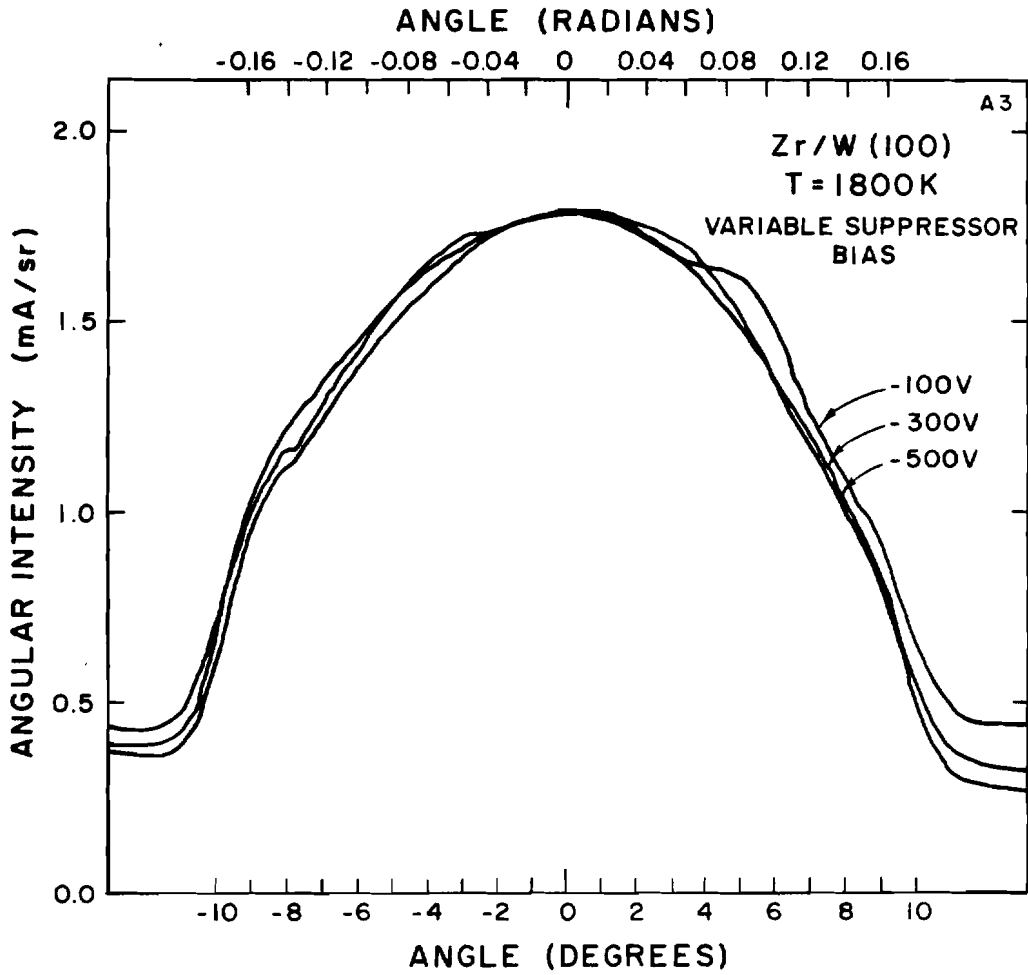


Figure 5-4. Angular distribution for variable suppressor bias. Anode voltage adjusted to maintain constant angular intensity.

there is virtually no change in the distribution. We can infer from these data (Figure 5-4) that the effect of the suppressor probably does not have to be included in electron optical calculations, since even wide angle trajectories seem to be unaffected by suppressor bias variations as long as the field at the surface of the emitter remains constant.

The experiment corresponding to Figure 5-4 was done for the computer model of the faceted 1  $\mu\text{m}$  tip, however for this simulation the anode voltage was held constant. The angular magnification graph (trajectory angle  $\alpha$  leaving gun vs trajectory launch position angle  $\theta_0$ ) is given in Figure 5-5. As the negative bias is increased from -100 to -700 V, there is a slight compression of the angular distribution for beam half angles  $\alpha > 1^\circ$  but very little effect on trajectories where  $\alpha < 1^\circ$ . This agrees very well with the experimental results of Figure 5-4. The central emission angular magnification  $K$  varies with bias  $\sim 0.002/100$  V.

In section C. the effect of various gun parameters on the virtual source size of the emitter will be investigated. It will be seen that suppressor voltage has negligible effect on virtual source size.

#### B. Computer Studies of Backscattered Trajectories in Gun

The effect of the Zr/O/W complex in lowering the work function of the (100) crystal face of tungsten is responsible for the high brightness, angularly confined beam which is emitted from the (100)



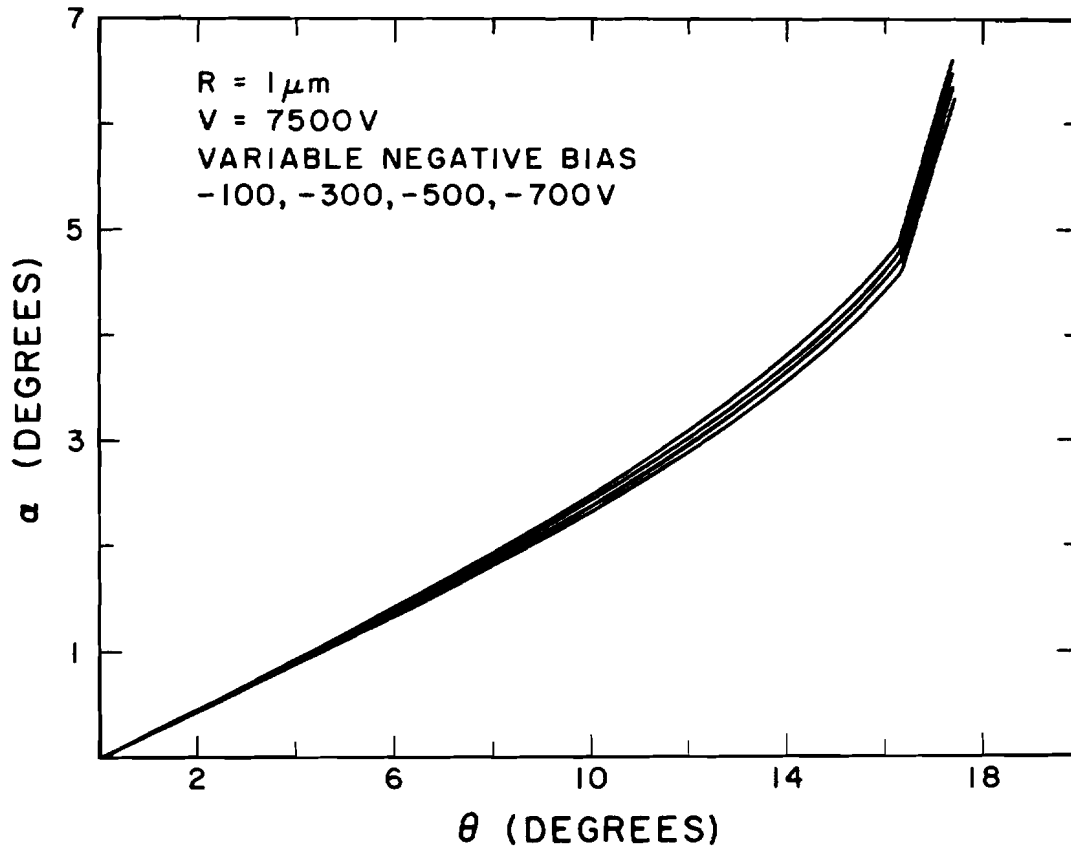


Figure 5-5. Angular magnification for gun with  $V_{ANODE} = 7500$  V,  $V_{BIAS}$  = variable. Sequence of graphs from upper to lower: -100 V, -300 V, -500 V, -700 V.

facet on the end of a  $\langle 100 \rangle$  oriented zone-refined etched tungsten emitter.<sup>2</sup> Due to the cubic crystal structure of tungsten, four other (100)-type crystal faces, all perpendicular to the wire axis, are exposed at the emitter tip. After operation at normal temperature and with an applied field, in addition to the formation of the facet on the end of the emitter (which has been seen to affect angular distribution) other low index facets form and the emitter end becomes slightly elongated, as in Figure 5-6. The amount of elongation depends on the radius, with large radius emitters ( $r \sim 1 \mu\text{m}$ ) showing very little elongation. The other four (100)-type facets, perpendicular to the emitter axis, are also regions of low work function which produce a high current density similar to that of the end (100) facet. This results in four bright spots of emission surrounding the central spot.

Trajectories for emission from various positions along the emitter tip and shank are shown in Figure 5-7. All emission except the central emission from the end facet is intercepted by the anode and does not leave the gun. Due to the negative bias on the suppressor electrode, trajectories from past the cutoff point never leave the emitter surface while those just ahead of the cutoff point are pushed toward the axis and strike the anode closer to the axis than those trajectories coming from the side (100) facets on the emitter tip (see Figures 5-8 and 5-9). In a gun structure with the dimensions shown none of the side (100) facet emission or shank (100) emission should get past the anode aperture.

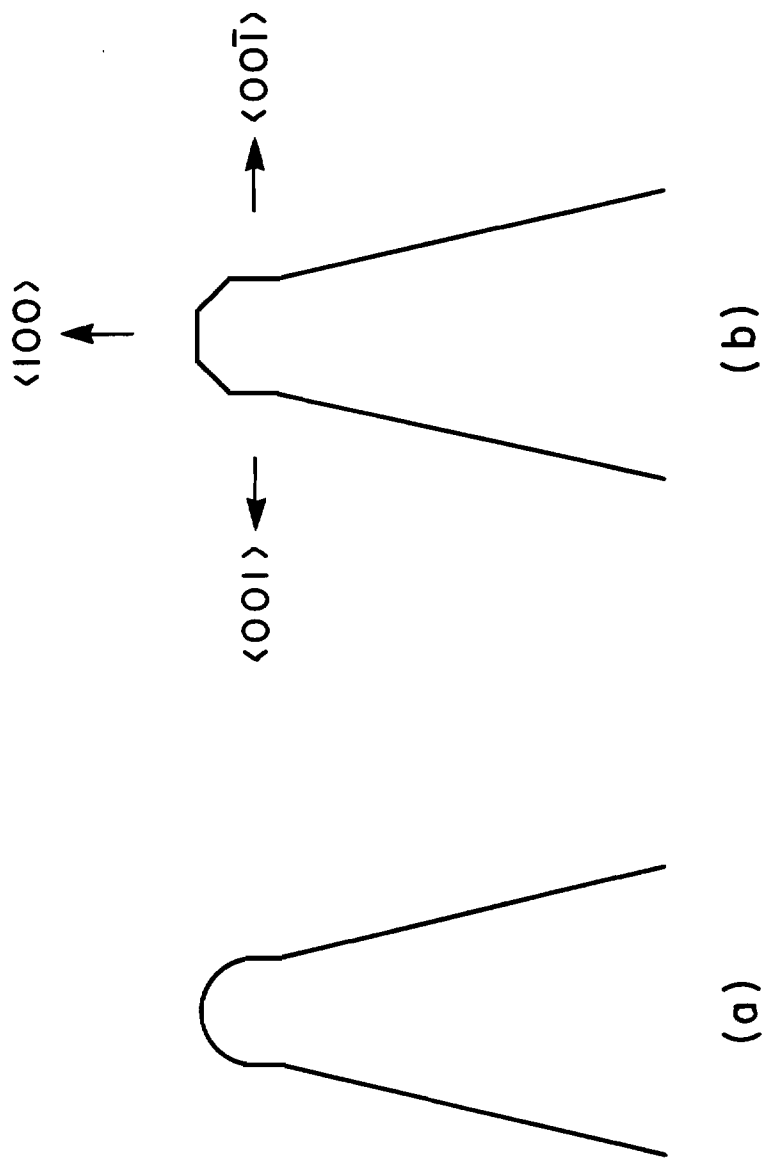


Figure 5-6. (a) Thermal end form. (b) Thermal-field end form showing side  $\langle 100 \rangle$ -type facets.

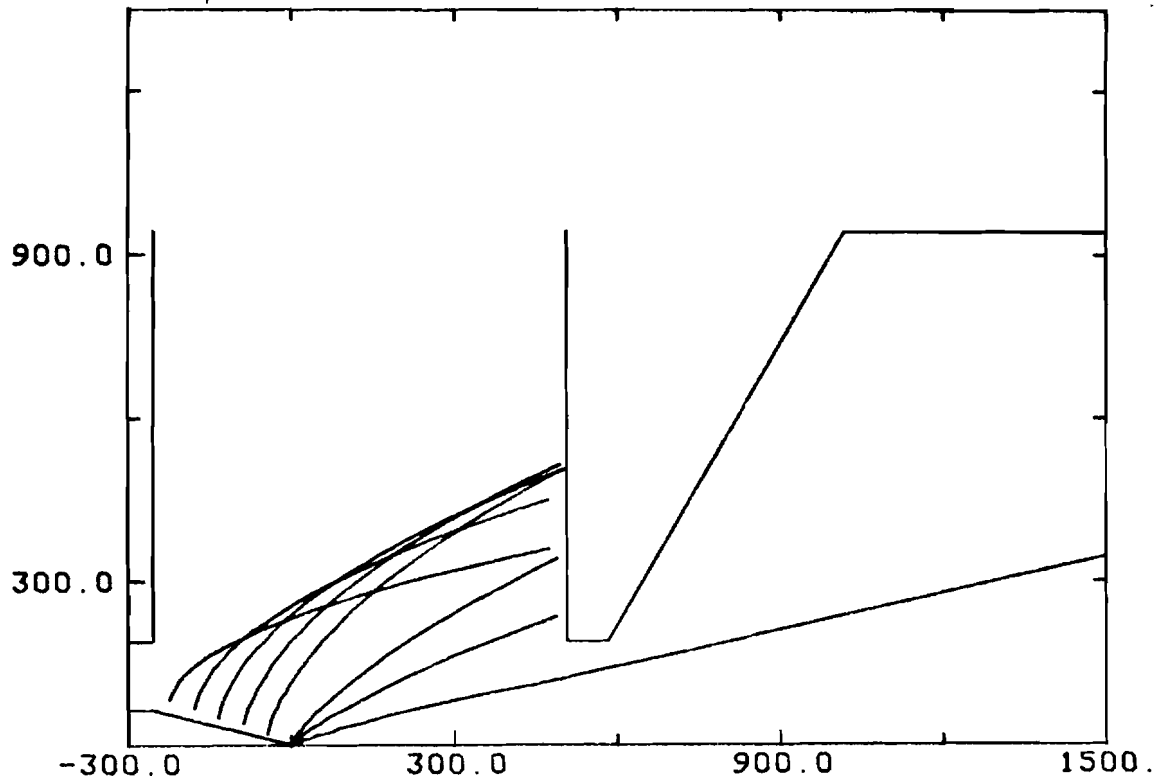


Figure 5-7. Trajectories launched from various positions on emitter. Note that side (100) facet emission and shank emission do not get through anode aperture. Initial kinetic energy = 0 eV. Z and R axis dimensions are in  $\mu\text{m}$ .

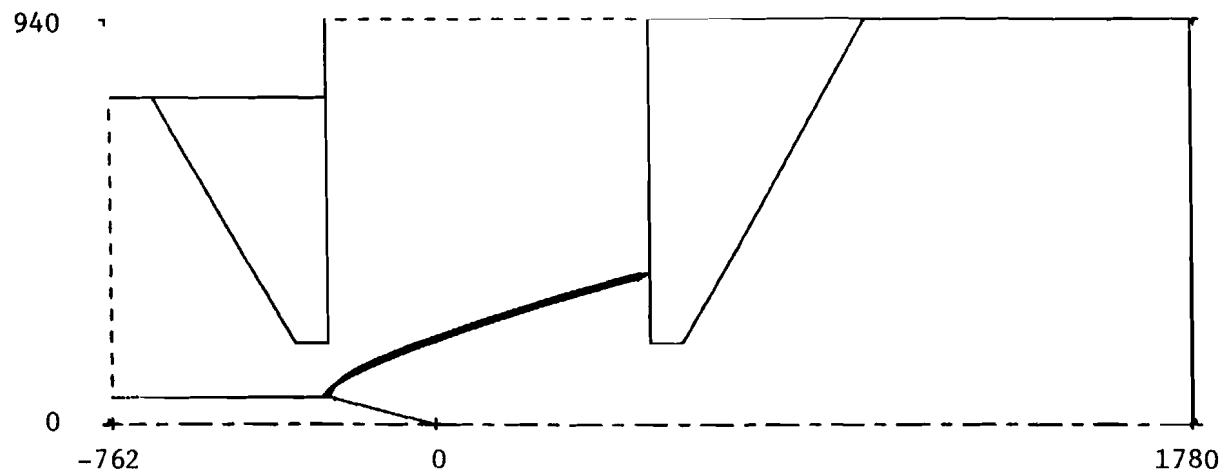


Figure 5-8. Trajectories launched from emitter shank. Initial electron energy was 0.1 eV, the anode potential was 7.5 kV and the suppressor potential was -300 volts. Launch positions range from end of shank to emission cutoff point, with all launch angles normal to shank surface. Z and R axis dimensions are in  $\mu\text{m}$ .

130 R

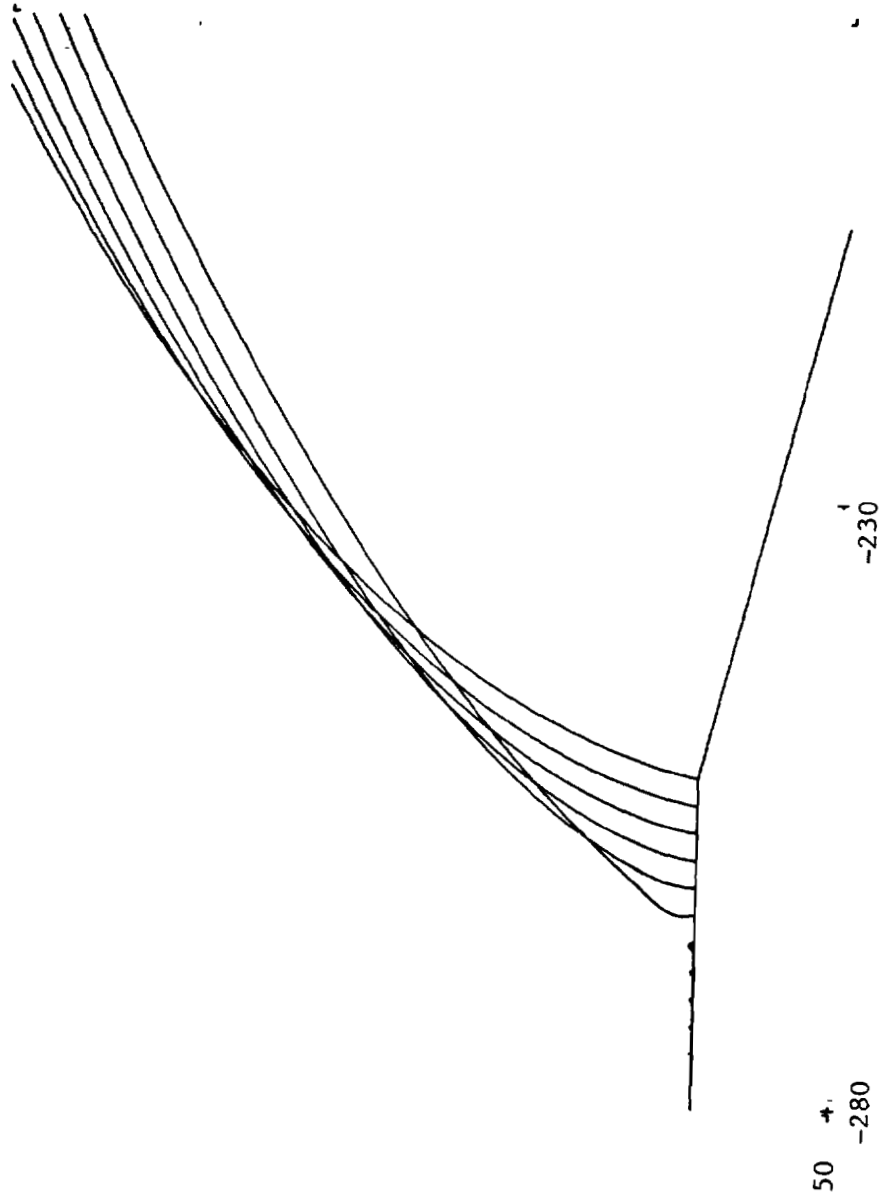


Figure 5-9. Magnified view of Figure 5-8.

Electron backscattering from the anode surface can result in trajectories which leave the gun at relatively large angles. The emission from the side (100) facets and from the shank strikes the anode and the backscattered electrons can be reflected in an electron mirror formed by the anode and suppressor, as shown in Figure 5-10. The total backscatter coefficient for molybdenum (the anode material) is 36.7% for 5 keV and 38.1% for 10 keV primary electron energies at normal incidence.<sup>3</sup> Non-normal incidence generally increases the backscatter coefficient. The energy distribution of backscattered electrons for elements in the vicinity of molybdenum ( $Z = 42$ ) shows a peak at  $\sim 95\%$  of the incident energy.<sup>4</sup> For our "standard electron gun" with  $V_{\text{ANODE}} = 7500$  V, the backscatter would peak at 7125 V. Figure 5-10 shows backscattered trajectories, all with initial kinetic energies of 7000 eV, launched at  $R = 350, 400, 450$  and  $500 \mu\text{m}$  and at  $Z = 508 \mu\text{m}$  (anode surface). Figures 5-11 through 5-14 trajectories launched from  $R = 250, 350, 450$  and  $500 \mu\text{m}$  from the anode surface, respectively.

In Figure 5-11, the backscattered trajectories do not get past the anode and thus do not contribute to beam current. In Figure 5-12 a few trajectories get through the anode aperture but are deflected by the diverging lens effect of the aperture and are therefore easily removed by a downstream beam-defining aperture. In Figures 5-13 and 5-14, however, some trajectories actually cross the axis at various distances from the anode and these trajectories

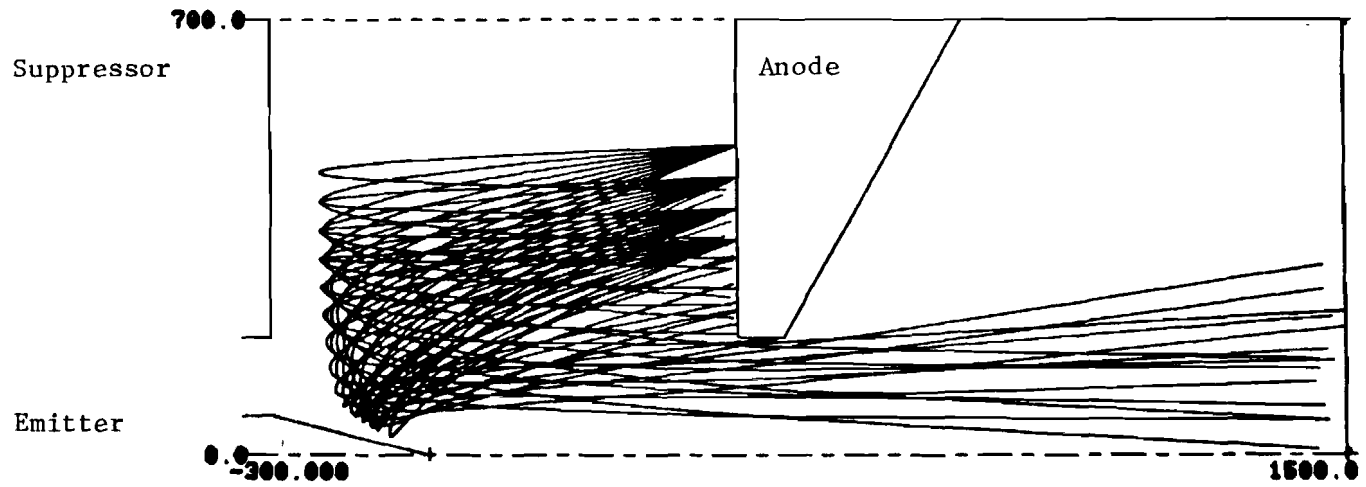


Figure 5-10. Calculated backscattered trajectories from the anode. Initial electron energy was 7 keV, the anode potential was 7.5 kV and the suppressor was -300 volts. The launch radii were 350, 400, 450 and 500  $\mu\text{m}$  and the launch angles were varied from  $\theta = 2^\circ$  to  $\theta = 20^\circ$ , in 2 degree increments.



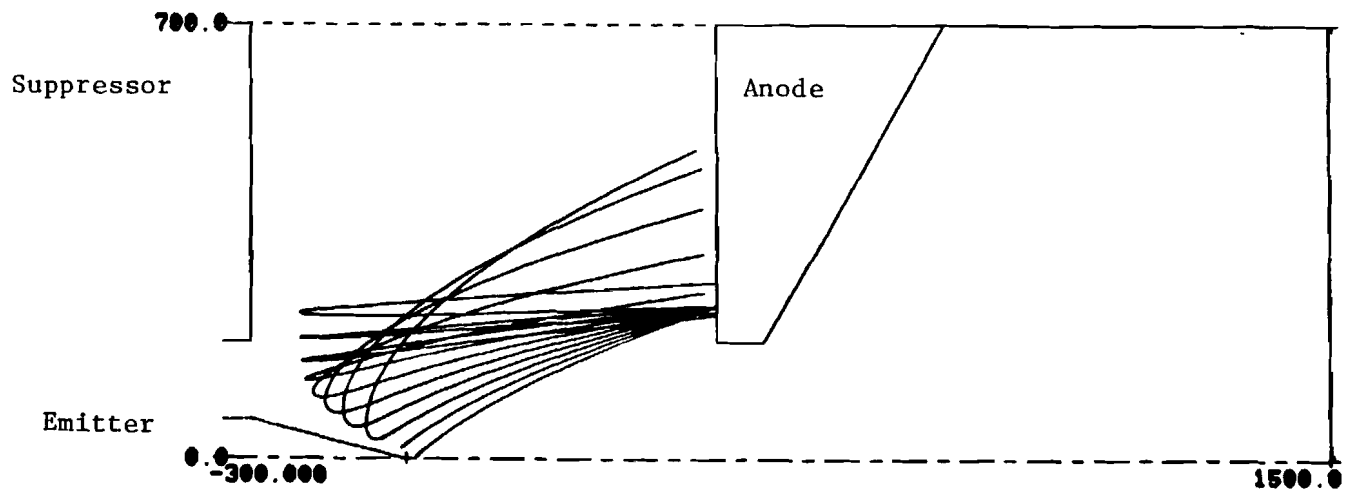


Figure 5-11. Calculated backscattered trajectories from the anode. Initial electron energy was 7 keV, the anode potential was 7.5 kV and the suppressor potential was -300 volts. The launch radius was 250  $\mu\text{m}$  and the launch angles were varied from  $\theta = 2^\circ$  to  $\theta = 20^\circ$ , in 2 degree increments.

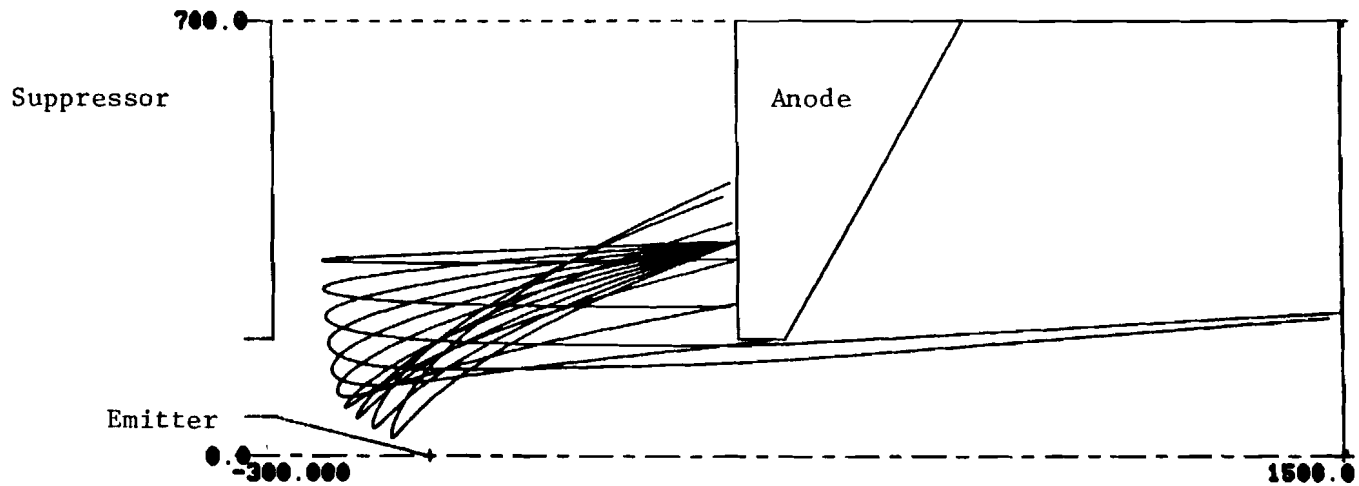


Figure 5-12. Calculated backscattered trajectories from the anode. Initial electron energy was 7 keV, the anode potential was 7.5 kV and the suppressor potential was -300 volts. The launch radius was 350  $\mu\text{m}$  and the launch angles were varied from  $\theta = 2^\circ$  to  $\theta = 20^\circ$ , in 2 degree increments.

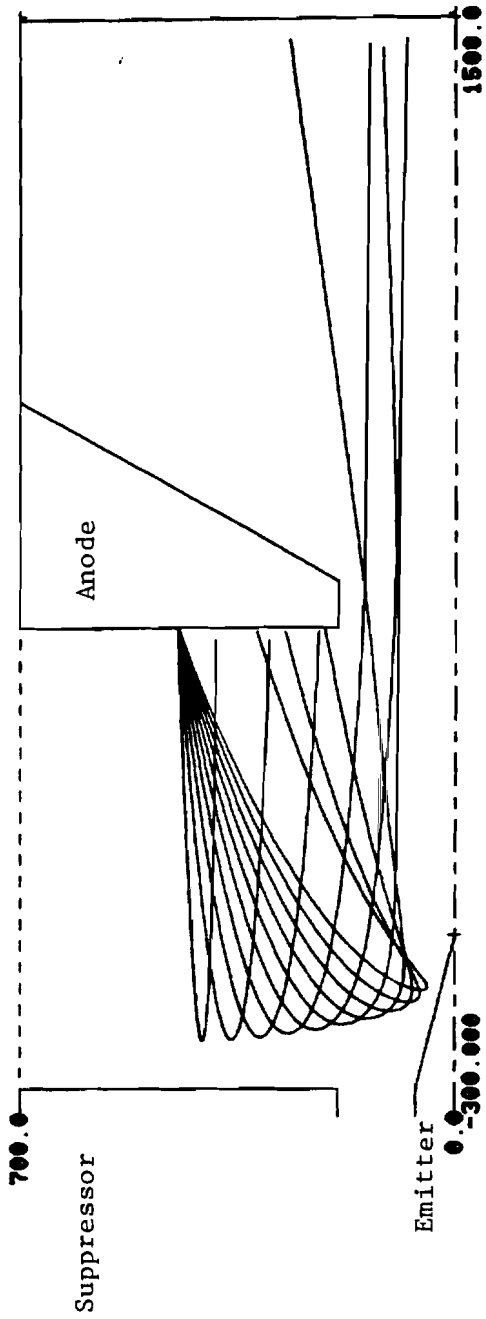


Figure 5-13. Calculated backscattered trajectories from the anode. Initial electron energy was 7 keV, the anode potential was 7.5 kV and the suppressor potential was -300 volts. The launch radius was 450  $\mu\text{m}$  and the launch angles were varied from  $\theta = 2^\circ$  to  $\theta = 20^\circ$ , in 2 degree increments.

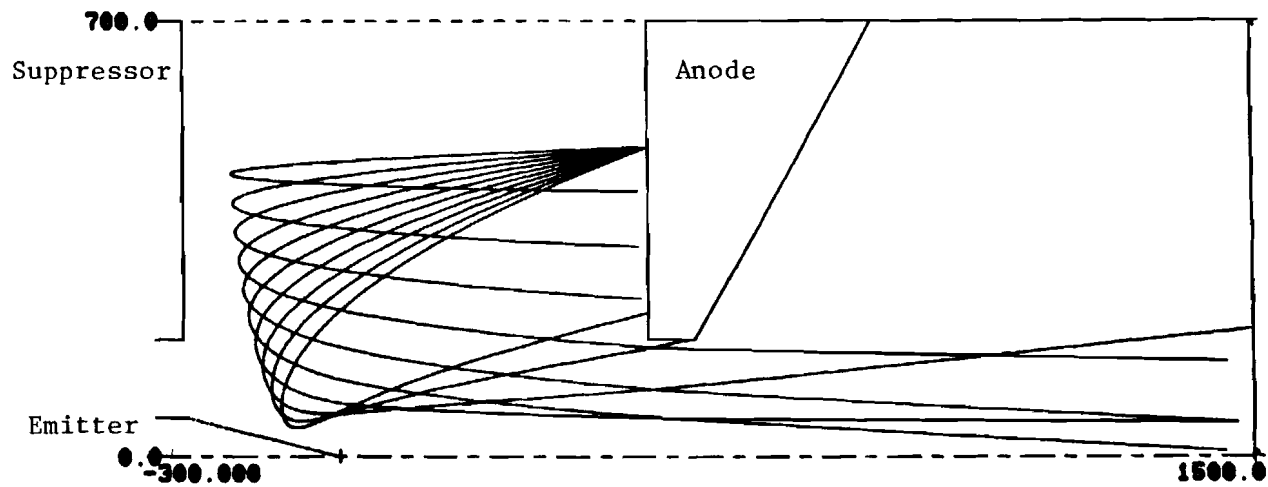


Figure 5-14. Calculated backscattered trajectories from the anode. Initial electron energy was 7 keV, the anode potential was 7.5 kV and the suppressor potential was -300 volts. The launch radius was 500  $\mu\text{m}$  and the launch angles were varied from  $\theta = 2^\circ$  to  $\theta = 20^\circ$ , in 2 degree increments.

may pass through a downstream beam defining aperture to create "side lobes" in a fourfold symmetric pattern around the main beam. This fourfold symmetry is due to the fact that the primary beams causing the backscatter originate from the four (100)-type stripes on the emitter conical section. This can be seen by noticing the results from Figures 5-11 through 5-14, namely that launch positions  $r < 500 \mu\text{m}$  on the anode do not transmit electrons near the optical axis. At  $r = 500 \mu\text{m}$ , we can see from Figure 5-7 that the incident beam comes from the conical portion of the emitter.

These lobes have been observed in an apertured gun where the beam defining aperture is placed approximately 1.0 inch from the emitter.<sup>5</sup> One approach to eliminate the lobe emission would be to shape the anode or the suppressor in such a way that the backscattered trajectories never get past the anode. The current density in the side lobes in some cases is  $\sim 1\%$  that of the main beam and ordinarily does not cause a problem in focused beam applications. However the existence of multiple beams in a column, no matter what the intensity, is an undesirable situation.

### C. Virtual Source Size Calculation

The virtual source of the ZrO/W (100) emitter in the electron gun configuration is the waist of the crossover formed by the projection (back into the emitter) of all electron trajectories which pass through the beam defining aperture. This includes electrons leaving the emitter with the various initial directions and velocities predicted by emission theory.

Wiesner<sup>6,7</sup> has developed a formalism for dealing with a calculation of this type. Rather than do a "brute force" calculation of hundreds of trajectories leaving the emitter surface with all possible initial conditions, Wiesner treats the emitter-anode region as an electron optical lens with the cathode emitting surface as the object and the virtual source as the image. This permits an evaluation of the size of the virtual source from the quadrature sum of the Gaussian, spherical aberration, chromatic aberration and diffraction disk diameters. The Gaussian disk is the aberration-free image of the cathode surface.

In order to calculate the above quantities, Wiesner used a sphere-on-cone<sup>8</sup> (SOC) model of the emitter-anode space. See Figure 5-15. This model provides an analytical expression for the electric field and potential at all points between the emitter and anode. Wiesner uses the fields and potentials to calculate trajectories of electrons from the emitter to the anode. The

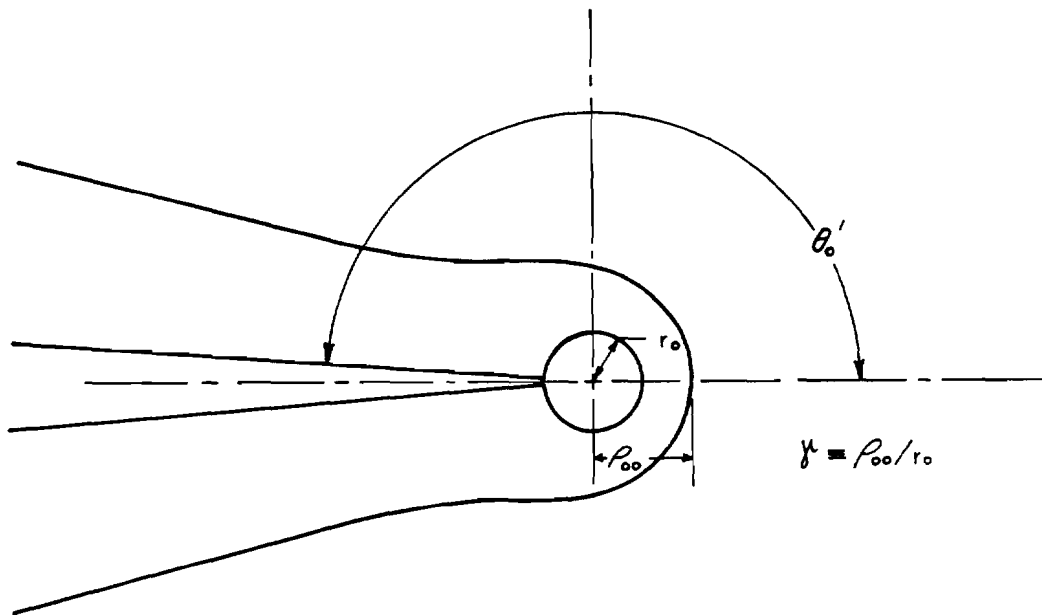


Figure 5-15. Point cathode modeled as an equipotential of a  
sphere-on-orthogonal cone. From Wiesner.<sup>6</sup>

---

trajectories are all calculated in a meridian plane of the system, i.e. no skew trajectories are considered. The electrons are divided into three groups:

cold electrons - zero initial velocity  
various initial positions on  
cathode surface

alpha electrons - fixed initial velocity  
various initial directions  
initial position on cathode apex

v electrons - various initial velocities  
initial direction tangent to surface at  
apex; initial position on cathode apex;  
also other positions on cathode

Wiesner extrapolates the final position and slope of the calculated trajectories back to the point at which they cross the axis. See Figure 5-16.

The Abbe sine law:

$$v_o \sin \alpha_o = M v \sin \alpha$$

where  $v_o$  = initial velocity       $\alpha_o$  = initial angle

$v$  = final velocity       $\alpha$  = final angle (slope)

makes use of the alpha electron data to determine the magnification  $M$  and image position of the cathode image.

The spherical aberration is calculated by fitting the alpha electron results to the longitudinal spherical aberration equation:

$$\Delta z = -C_s \alpha^2$$



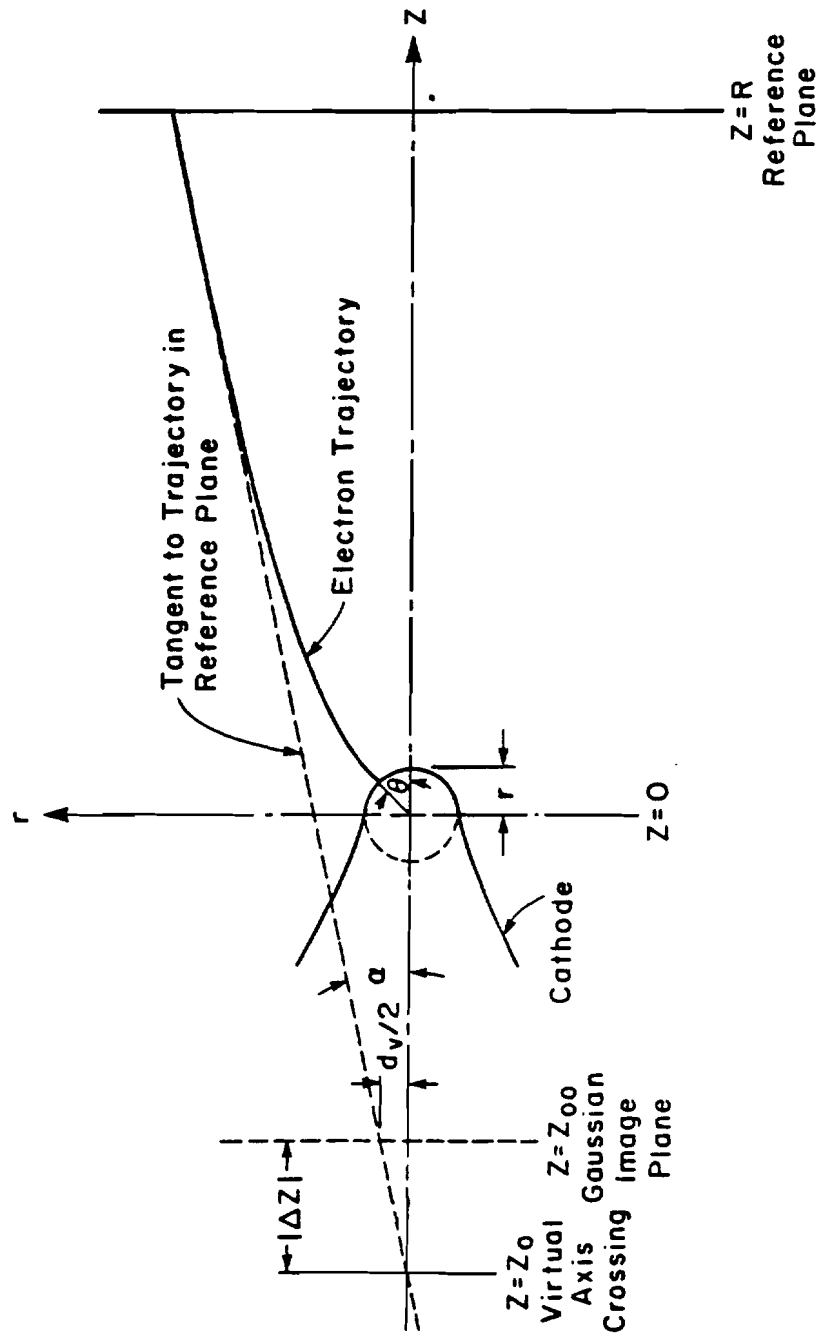


Figure 5-16. Extrapolation of trajectory back to axis crossing point.

where  $\Delta z$  is the difference in the axis crossing coordinates for a paraxial and a marginal (slope =  $\alpha$ ) trajectory,  $C_s$  is the spherical aberration coefficient and  $\alpha$  is the trajectory angle with the axis. The spherical blur disk radius is

$$r_s = C_s \alpha^3$$

in the Gaussian plane, however in the plane of least confusion it is

$$r_s = \frac{1}{4} C_s \alpha^3.$$

Chromatic aberration makes use of the  $v$  electron data to obtain a value for  $C_c$  in the longitudinal chromatic aberration equation

$$z = -C_c \Delta V/V.$$

The chromatic disk radius is

$$r_c = C_c \frac{\Delta V}{V} \alpha.$$

The diffraction term contributes a disk radius

$$r_d = \left( \frac{6.1 \cdot 10^{-4}}{\alpha} \right) \left( \frac{1.5}{V_A} \right)^{1/2}$$

The cold electron trajectories are used to determine the Gaussian image disk size by fitting the data to

$$\alpha = m \theta_0$$

where

$m$  = angular magnification

$\theta_0$  = initial angular position on cathode.

Obtaining  $M$  from the Abbe sine law, Wiesner finds the Gaussian disk radius

---

$$r_g = a(M/m)\alpha$$

where  $a$  = cathode apex radius.

The quadrature sum

$$r_{as} = (r_g^2 + r_c^2 + r_s^2 + r_d^2)^{1/2}$$

gives the radius of the apparent or virtual source. Wiesner's procedure is used in the calculations presented here, however the SCWIM program<sup>9</sup> was used to generate the trajectory data for the cold, alpha and V electrons.

Figure 5-17 shows the effect on the cold electron trajectories of the spherical and faceted end shapes. Since Wiesner's results were generated for a rounded-end emitter with no suppressor and no anode aperture it is expected that there will be some difference between the data from the SOC model and the present spherical end emitter. The data from these two shapes should be close enough, however, to establish that the SCWIM program is consistent with the analytical SOC model. The new data presented here is the effect on virtual source size of the facet. Since the facet enhances angular intensity by the increased angular demagnification, it is of interest to see if there is any electron optical penalty to be paid for the increased beam current.

Using the SCWIM program, "alpha" electrons were launched from the emitter apex with initial launch energies of 0.5, 1.0, and 2.0 eV. For each launch energy, the launch angle was varied

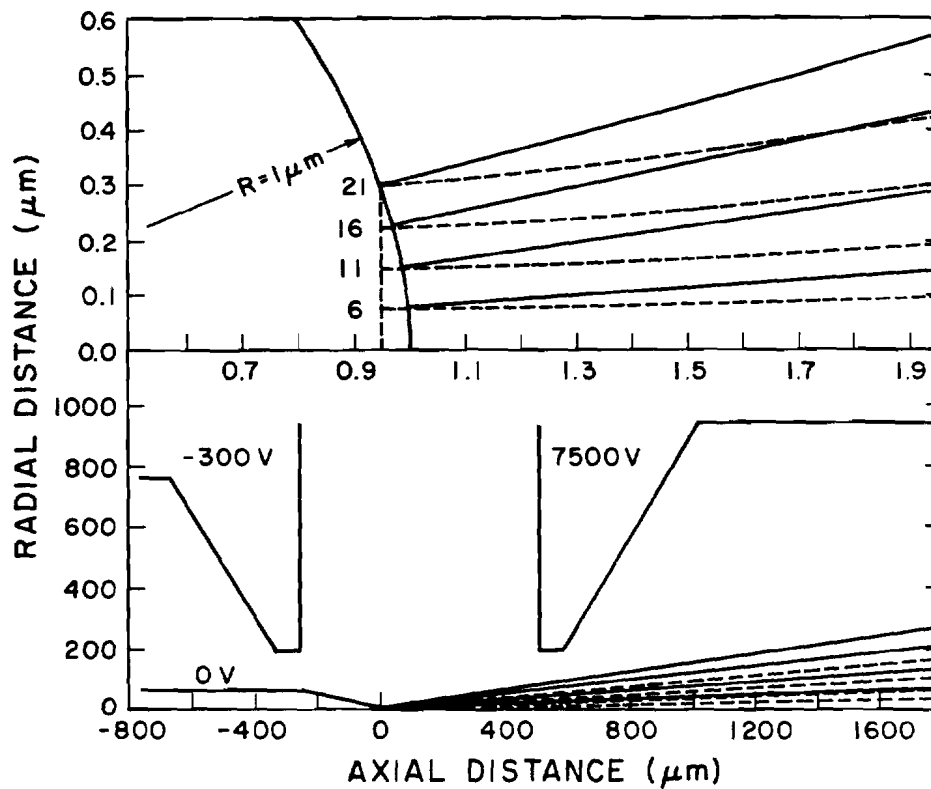


Figure 5-17. A Schottky emission gun with tip radius of  $1\ \mu\text{m}$  and the calculated trajectories for spherical tip (solid line) and faceted tip (dashed line). The upper portion shows initial paths of the trajectories.

from 0 to 90 degrees. Figure 5-18 shows the result for a 1  $\mu\text{m}$  spherical-ended emitter. The different launch energies all gave the same value for  $C_s$ .

The "v" electrons were subdivided into two classes. The normal  $v_N$  and the tangential  $v_T$ . The  $v_T$  electrons were launched with an initial direction tangent to the emitter surface and at the emitter apex with varying initial energies, as shown in Figure 5-19. These electrons gave consistent results for  $C_c$ , except for the cases of the 3  $\mu\text{m}$  radius emitter, where  $C_c$  changed sign and was only valid for  $\alpha < 5$  mr. The  $v_N$  electrons were launched normal to the emitter surface at a position angle of 0.05 rad. See Figure 5-20. These electrons gave  $C_c$  values generally negative and smaller than the  $C_c$  values obtained from the  $v_T$  electrons.

The least-square regression fits such as in Figures 5-18 through 5-20, values for  $C_s$  and  $C_c$  were computed for spherical-end and faceted-end emitters of radii from 0.3 to 3.0  $\mu\text{m}$ . Table 5-2 shows the aberration coefficients and linear and angular magnifications (M and m) computed as indicated above. "Cold" electron data was also plotted to obtain a value for  $C_s$ . As can be seen from Table 5-2, the cold electron  $C_s$  agrees with the  $\alpha$  electron  $C_s$  for the spherical-end emitter but not for the faceted-end emitter. This indicates the presence of off-axis third-order geometrical aberrations for the faceted-end emitter.

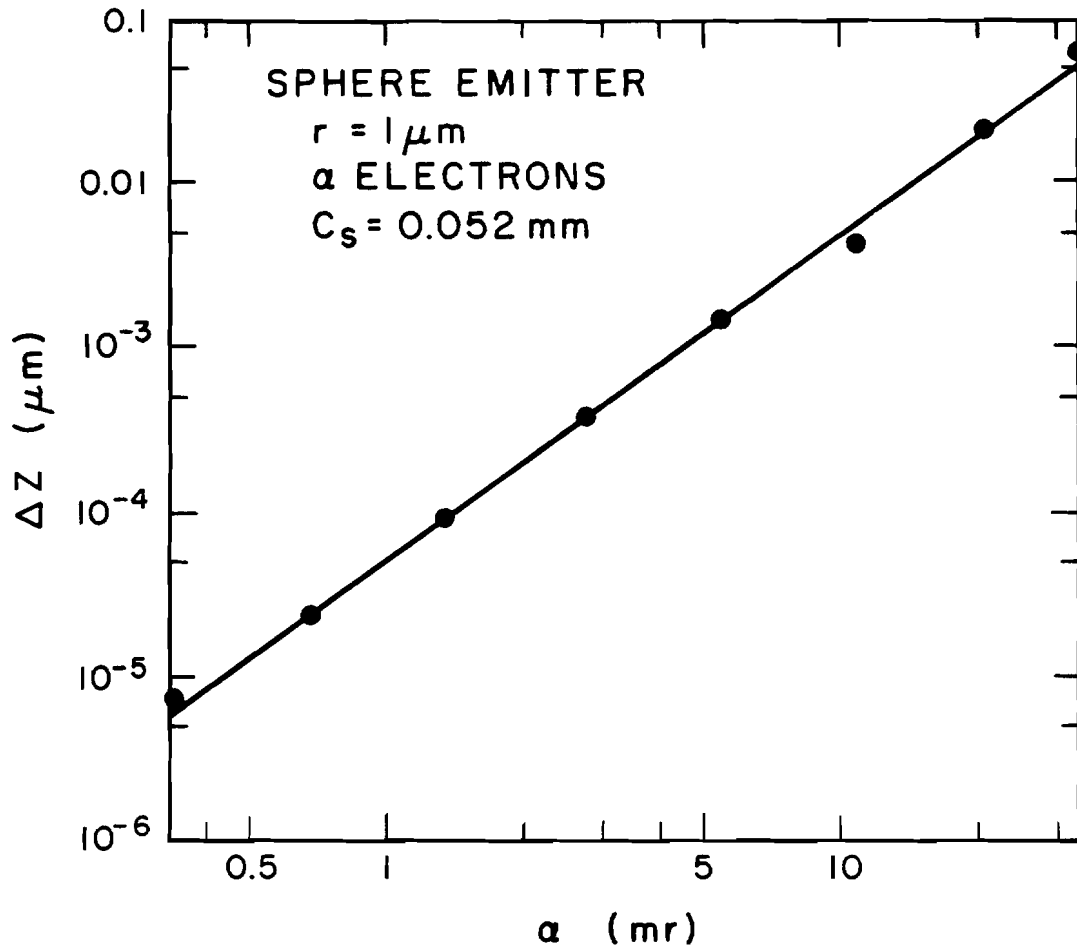


Figure 5-18. Least squares fit for  $C_s$  from  $\alpha$  electrons.

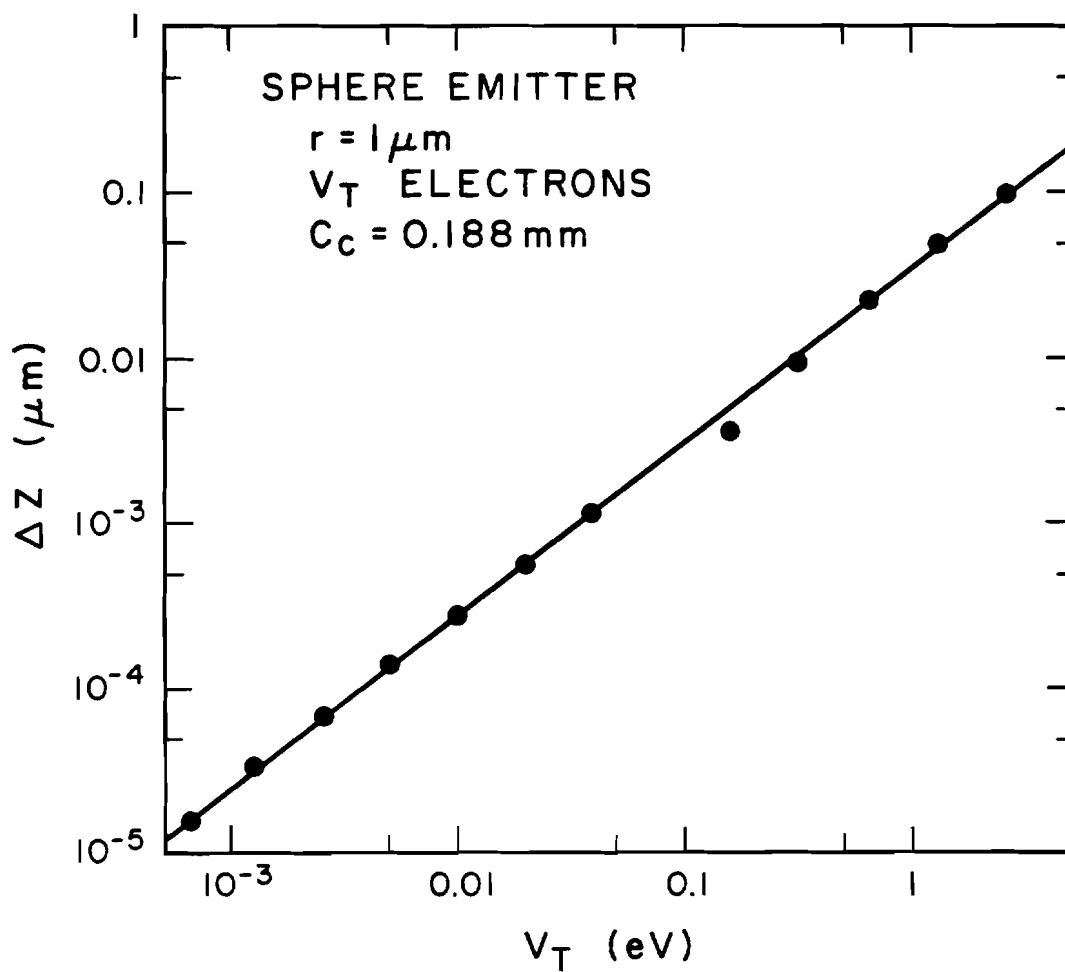


Figure 5-19. Least squares fit for  $C_c$  from  $v_T$  electrons.

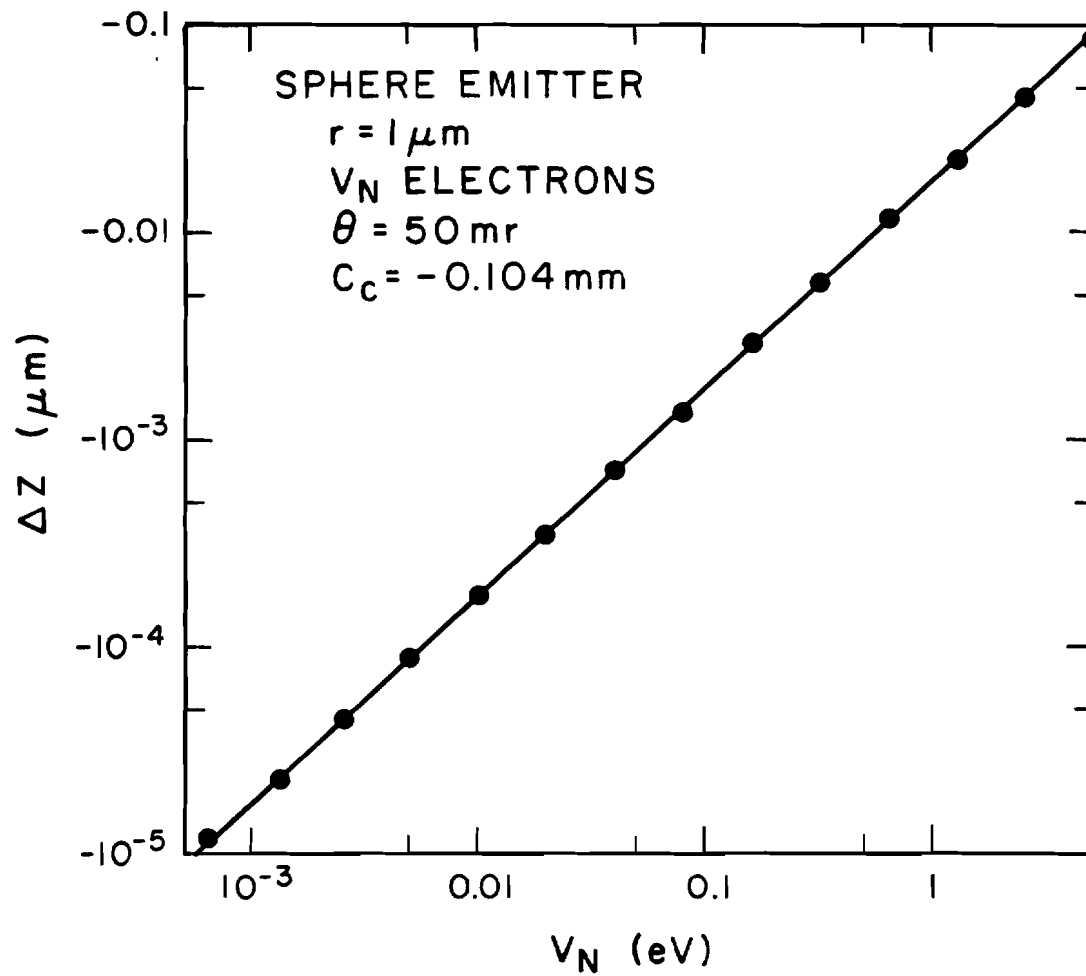


Figure 5-20. Least squares fit for  $C_c$  from  $v_N$  electrons.



TABLE 5-2

## SCWIM Program Results

Shape	Radius ( $\mu\text{m}$ )	$C_s$ (mm)	CoId	$C_s$ (mm)	$C_\alpha$ (mm)	$C_{cT}$ (mm)	$C_{cN}$ (mm)	$C_{cV}$ (mm)	$M$	$\bar{m}$	$V_{\text{ANODE}}$ (kV)	$I'$ (mA/sr)	$F$ (V/Å)
Spherical	0.3	.050	.047	.236	.3690	.452	4	.661	.144				
	0.5	.053	.049	.226	.3759	.473	5	.726					
	1.0	.052	.052	.188	.3872	.504	6	.541	.0894				
	2.0	.055	.045	.116	.3996	.532	7	.543					
	3.0	.058	.052	-.004*	.4085	.543	8	.618	.053				
Faceted	0.3	.042	.061	.273	.3852	.211	4	.721	.111				
	0.5	.006	.048	.171	.3943	.219	5	.978					
	1.0	-.012	.055	.144	.4067	.222	6	.974	.0695				
	2.0	-.070	.056	.026	.4206	.234	7	1.063					
	3.0	-.115	.062	-.057*	.4302	.252	8	1.459	.0412				

\*  $\alpha < .005$  rad.

Further work will be required to extract the off-axis aberration coefficients from these data. From Table 5-2, we can see that the  $C_c$  calculated from  $v_N$  electron trajectories is generally smaller in magnitude and of opposite sign of  $C_c$  from the  $v_T$  electrons. Wiesner<sup>7</sup> takes this to mean that "the effects due to a spread in normal velocity components can be neglected in comparison with transverse effects." It will be seen shortly that both spherical and chromatic aberration contributions to the virtual source size are negligible with respect to the diffraction and Gaussian source terms, so that off-axis geometrical aberrations and distinctions between transverse and normal  $C_c$  will not affect the final result.

Figure 5-21 shows a typical result obtained for a 1  $\mu\text{m}$  radius faceted-end emitter. The spherical, chromatic, diffraction and Gaussian contributions to the virtual source are shown along with the quadrature sum (dashed line). The spherical and chromatic contributions are evaluated from the  $\alpha$  and  $v_T$  trajectories. The virtual source size is dominated by the diffraction and Gaussian terms.

Figures 5-22 and 5-23 show the virtual source size for various radii emitters with spherical and faceted end forms. In general, the presence of the facet causes the virtual source size to approximately double, for angles at which the diffraction term is not dominant. Where the diffraction term is dominant, at the small angles, the emitter radius has no

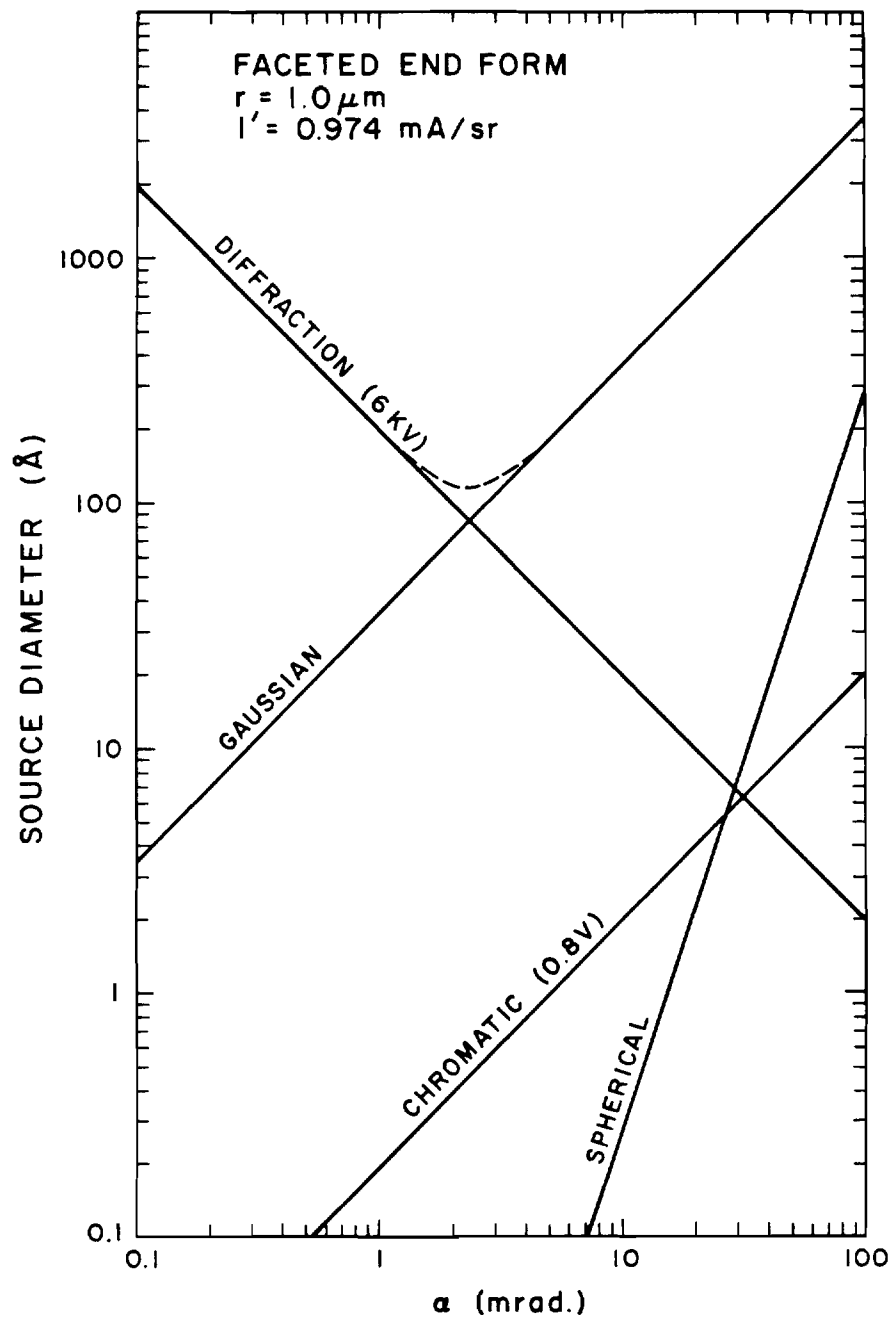


Figure 5-21. Virtual source contributions.

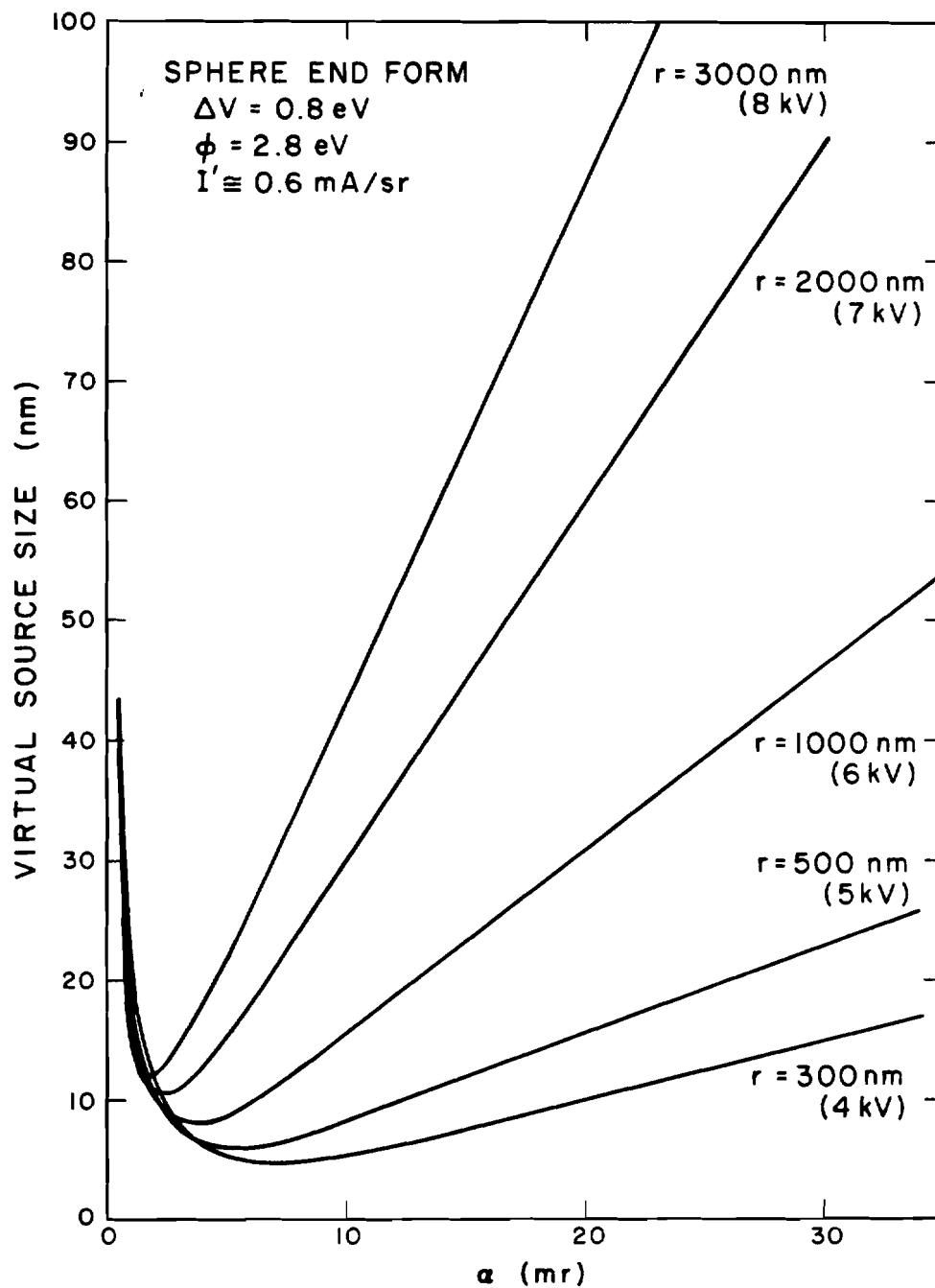


Figure 5-22. Virtual source size for emitter radii 0.3 to 3.0  $\mu\text{m}$ . Spherical end form.

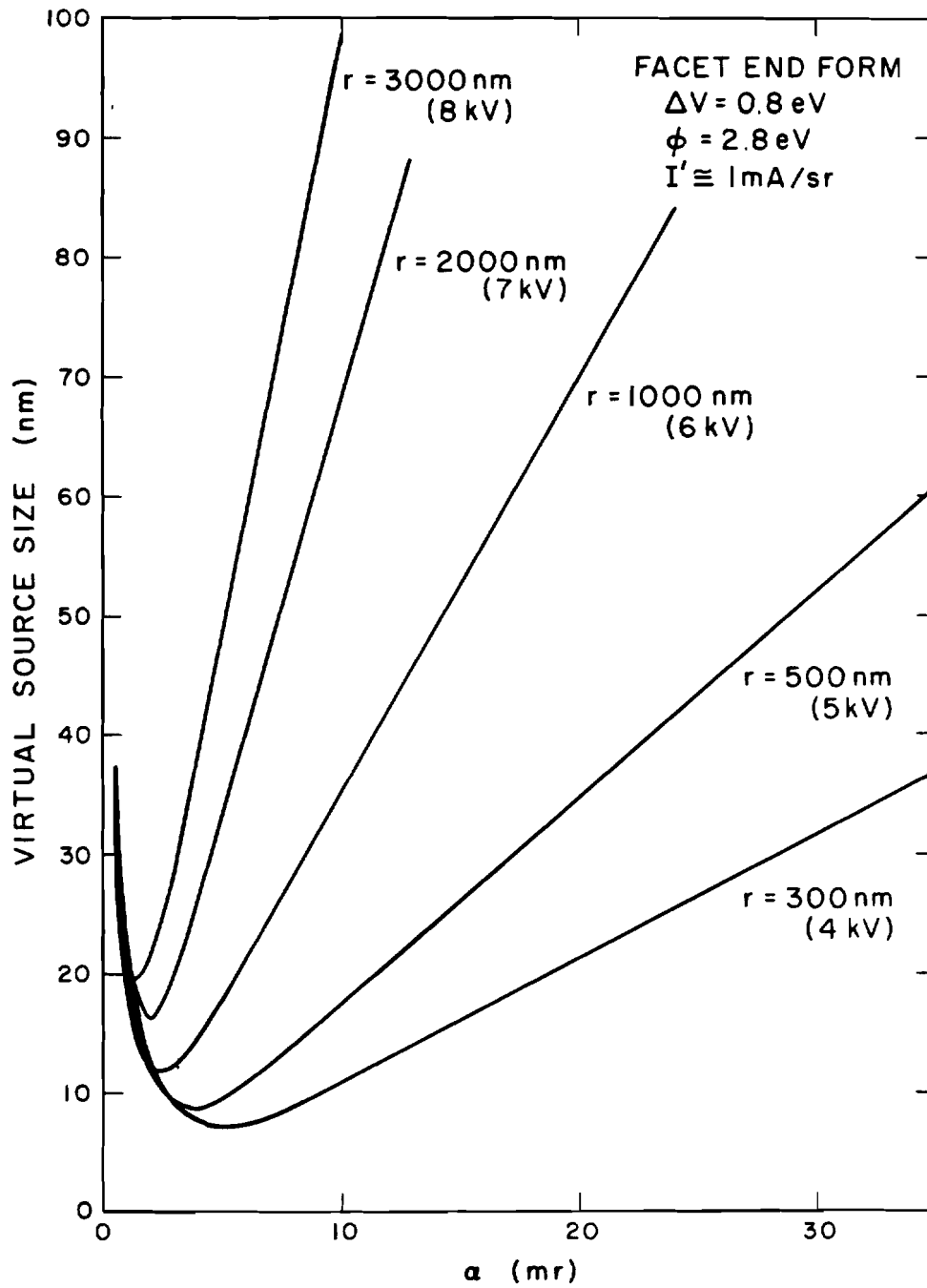


Figure 5-23. Virtual source size for emitter radii 0.3 to 3.0  $\mu\text{m}$ . Faceted end form.

effect on virtual source size. Figure 5-24 shows the minimum virtual source size as a function of emitter radius. From this, it is obvious that a smaller emitter radius always produces a smaller virtual source size, however the disadvantages of a small emitter are increased energy spread due to the Boersch effect, greater emission current noise and an increased susceptibility to destruction by a vacuum arc.

#### D. Virtual Source - Experimental Consideration

Experimental measurement of the electron virtual source size can be accomplished by either a conventional electron optical system which magnifies the virtual source to a measurable size or by an electron interference pattern technique which measures the spatial coherence of the beam by the number of fringes in the pattern created by a beam split with an electrostatic bi-prism. The system we consider here will be based on the former principle. The constraints on such a system are as follows:

- 1) Aperture angle must be small enough so that system aberration effect on beam size is negligible.
- 2) Aperture angle must be large enough that diffraction limiting of beam size does not occur.
- 3) Angular intensity must be small enough so that excessive  $\Delta V$  does not produce a chromatically limited beam size (Boersch effect).

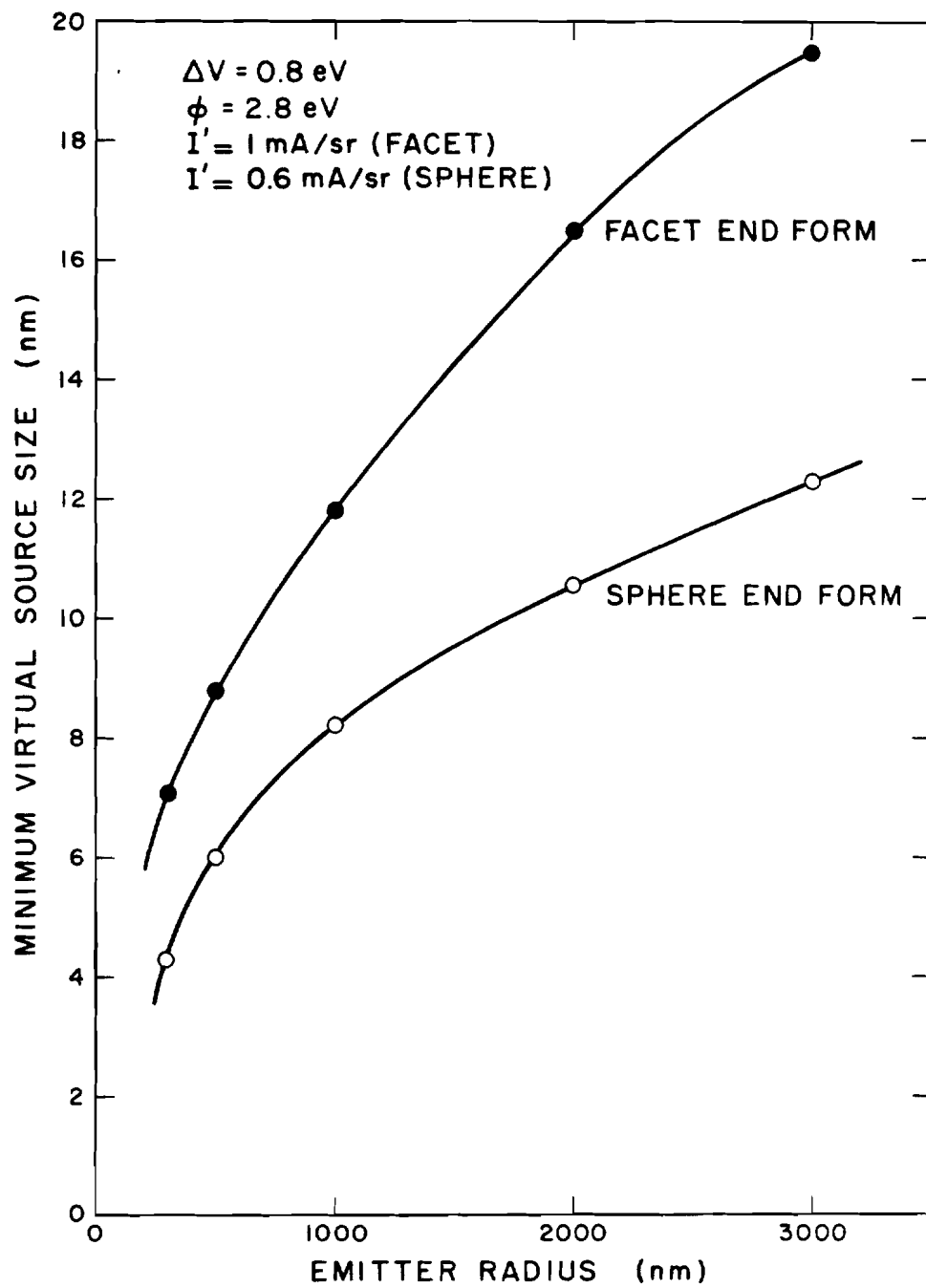


Figure 5-24. Minimum virtual source size.

- 4) Angular intensity must be large enough so that signal to noise ratio allows accurate beam size measurement.
- 5) System magnification must be great enough to produce a final beam size which is easily measurable ( $\sim 0.1 \mu\text{m}$ ).

If we use a commercially available magnetic lens (Celco NF-434-366) and operate our electron gun at 6 kV, we can use the magnetic lens to magnify the virtual source of a Zr/W TF emitter. The beam diameter vs beam half angle  $\alpha$  for the lens operating with a magnification of 17.34 is shown in Figure 5-25.

As shown in Figure 5-25, the final beam diameter will be primarily determined by the Gaussian virtual source diameter for  $0.005 < \alpha < 0.015$ .

For the same range of  $\alpha$ , if an angular intensity of 0.1 mA/sr is used to minimize the Boersch effect, the range of beam currents is 79 nA to 707 nA, an easily measurable current range. The predicted range of beam diameters, from the magnified Gaussian diameter, is 0.31  $\mu\text{m}$  to 0.91  $\mu\text{m}$ , an easily measurable range. Therefore, an experiment like this should be able to easily measure the virtual source size.



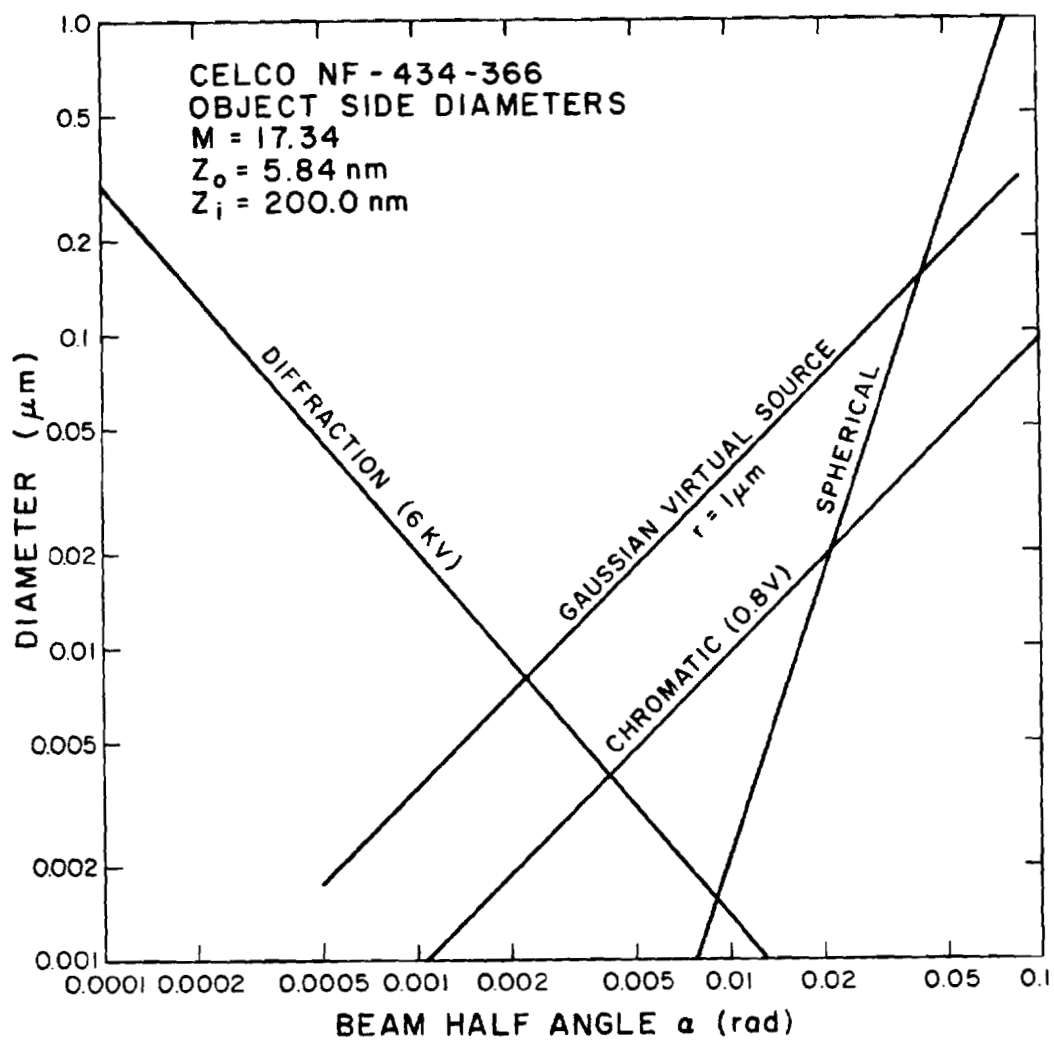


Figure 5-25. Experimental measurement of virtual source size.

## REFERENCES

1. G. Schwind, Private Communication.
  2. L. W. Swanson and L. C. Crouser, J. Appl. Phys. 40, 4741 (1969).
  3. Quantitative Scanning Electron Microscopy, Ed. by Holt, Muir, Grant and Boswarva, Academic Pres, 1974, London p. 52.
  4. Ibid, p. 54.
  5. D. Tuggle, L. W. Swanson and J. Orloff, J. Vac. Sci. Technol., 16, 1699 (1979).
  6. J. C. Wiesner, Point Cathode Electron Sources, Ph.D. Thesis University of California, Berkeley, (1970).
  7. J. C. Wiesner and T. E. Everhart, J. Appl. Phys., 44, 2140 (1973).
  8. W. P. Dyke, J. K. Trolan, W. W. Dolan, and G. Brown, J. Appl. Phys. 24, 570 (1953).
  9. N. K. Kang, D. Tuggle and L. W. Swanson, Optik 63, 313 (1983).
-

## CHAPTER 6

## SUMMARY AND CONCLUSIONS

The results presented in the preceding chapters can be separated into five categories: 1) angular intensity distribution, 2) I-V characteristics, 3) current fluctuation characteristics, 4) gun structure effects (transmission and backscatter) and 5) virtual source size calculations. The following paragraphs summarize the results obtained for each of these categories.

Angular intensity distributions provide a powerful method for examining the field build up process and the stability of the faceted end-form of the emitter. The size of the facet relative to the emitter radius agrees with that predicted by crystalline geometry considerations. The character of the angular distribution changes from convex to flat to concave with increasing anode voltage and can be explained in terms of variation of emission regimes and angular magnification across the facet. A computer program using a spherical mesh to calculate electric potential was used to generate angular intensity distributions which agreed qualitatively with the experimental results. Uncertainties in work function distributions across the facet and in local radius at the facet edge prevent absolute quantitative agreement.

Current-voltage characteristics gave information on the central emission regime and showed it to be primarily Schottky and extended Schottky emission, with probe current varying as  $\exp[e^{3/2} F^{1/2} / kT]$  in the Schottky case. The facet edge emission is much more strongly dependent on the electric field  $F$  and probably lies in the thermal field regime at high fields. A procedure using I-V data was developed to determine emitter radius and work function. This procedure gave reasonable results when applied to several emitters. The sensitivity of this determination to gun geometry and suppressor bias voltage was small (see Table 3-4), amounting to about a 10% error in radius determination in the vicinity of  $1 \mu\text{m}$  (see Figure 3-19) for reasonable variations in geometry and bias. Attempting to determine the size of the facet based on ratios of central to facet edge I-V data was unsuccessful, pointing out the fact that more investigation of the local edge field and work function is necessary to completely understand this emitter.

Current fluctuation studies on several different emitters showed similar behavior, a  $1/f^2$  spectral region below a few Hertz, a flat spectral region from  $\sim 10$  to  $\sim 100$  Hertz and a  $1/f$  region beyond a few hundred Hertz. The low frequency  $1/f^2$  noise is completely correlated between the probe and total emission currents. An argument was made to explain these correlated fluctuations in terms of random thermal fluctuation on

the heated filament which supports the emitter. A typical noise to signal ratio is 0.5% at a 200 kHz bandwidth for an aperture half angle of 0.006 rad and an emitter radius of  $\sim 2 \mu\text{m}$ . It can be shown<sup>1</sup> that the noise from a cathode surface area  $A$  is proportional to  $A^{-1/2}$ . This implies a noise dependence on emitter radius  $r$  and aperture half angle  $\alpha$  of

$$\frac{\Delta I}{I} \propto \frac{1}{r \alpha^{1/2}} .$$

The experimentally measured dependence  $\frac{\Delta I}{I} \propto \alpha^{-1/3}$  is probably due to the technique used to obtain a variable aperture, namely magnetic focusing of the beam between the emission point and the beam defining aperture.

Electron gun transmission (probe current/total current) generally has a value of 5 to  $7 \cdot 10^{-5}$  for a half angle  $\alpha$  of 0.00156 rad. This implies an angular intensity to total current relationship of  $\sim 7.85 \text{ mA/sr}$  probe angular intensity per mA total current. The suppressor voltage has a small effect on gun transmission, at least in the present geometry. More suppressor control can be achieved by reducing the emitter protrusion from the suppressor, but this may have undesirable effects on the virtual source size.

An artifact of the gun is due to the negative potential on the suppressor electrode forming an electron mirror for electrons backscattered from the anode. Four diffuse spots surrounding the focused spot can be seen in some focused beam systems using a phosphor screen in the image plane. These four spots are caused by emission from the four (100) type low work function stripes on the conical portion of the emitter, bombarding the anode in a 4-fold symmetric pattern and generating backscattered electrons which are reflected by the negative potential on the suppressor and can travel through the anode aperture close enough to the axis to permit them to pass through the beam defining aperture.

Virtual source size calculations show that the effect of the facet on the emitter apex is to approximately double the source diameter, relative to an emitter with a spherical apex. This occurs at aperture half angles greater than a few milliradians. For smaller apertures, the virtual source size is diffraction limited and the shape of the emitter apex and the radius have no effect on the size. The virtual source size is on the order of a few hundred angstroms and is proportional to emitter radius for beam half angles greater than a few milliradians.

In several years of working with the ZrO/W emitters, techniques have evolved for obtaining reliability and long life from these sources. One of the most significant increases in lifetime and reliability occurred due to the work of Danielson

and Swanson,<sup>2</sup> which showed that the ZrO/W surface can be thermally removed and then restored by diffusion of Zr and O from the bulk tungsten. This work was a culmination of progress which led to the elimination of the O<sub>2</sub> partial pressure previously required to operate these emitters. A second technique which drastically reduced emitter failure due to arcs was providing adequate vacuum pumping directly at the emitter. A great deal of trouble with the emitter was experienced when using conductance limited pumping of the emitter-anode region. When a properly pumped electron gun chamber was used, lifetimes > 3000 hours became normal. Apparently, due to the outgassing of the anode, a large gas source is present in the emitter vicinity. This can cause the pressure in the region of the emitter to be orders of magnitude greater than the surrounding static pressure, particularly if the path to the pump is not direct and if there is not a large "vacuum ballast" space to absorb pressure transients from the emitter region.

## REFERENCES

1. R. Gomer, Surf. Sci. 38, 373 (1973).
2. L. R. Danielson and L. W. Swanson, Surf. Sci. 88, 14 (1979).



## APPENDIX A

COMPUTER PROGRAM FOR DETERMINING  $\beta$  FROM EXPERIMENTAL SCHOTTKY SLOPE

AT T = 1800K

This program uses a fourth order polynomial regression fit to the curves of Figure 3-22, neglecting the portions of the curves that branch off at different work functions. It was written in BASIC and run on a Tektronix 4051 Graphics Computer.

```
100     CO = 1.011264
110     C1 = -0.4007104
120     C2 = 5.255788
130     C3 = -14.01381
140     C4 = 21.0272
150     PRINT "Input Beta (1/cm), Voltage (V)"
160     INPUT B,V
170     B1 = B
180     PRINT "Iteration No.", "Field (V/A)", "Beta (1/cm)"
190     FOR I = 1 To 30
200     F = B1*V*1.0E-8
210     PRINT I, F, B1
220     IF F < 0.0078 THEN 300
230     IF F > 0.1764 THEN 320
240     IF F > 0.1444 THEN 340
250     F2 = SQR(F)
```

```
260     G = C0+F2*C1+F2+2*C2+F2+3*C3+F2+4*C4
270     B1 = B/G + 2
280     NEXT I
290     END
300     PRINT "Already in Schottky regime"
310     END
320     PRINT "Caution - Field beyond B-B' for this iteration if
        PHI = 2.5"
330     GO TO 250
340     PRINT "Caution - Field beyond A-A' for this iteration if
        PHI = 2.5"
350     GO TO 250
```

## APPENDIX B

Computer program using Schottky and extended Schottky equations to calculate current density from temperature, field and work function.

```

60     PRINT "INPUT TEMPERATURE (K)"
65     INPUT T
70     PRINT "INPUT FIELD (V/A)"
75     INPUT F1
80     PRINT "INPUT PHI (eV)"
90     INPUT P1
100    K=1.38E-16
120    P=P1*1.602E-12
130    F=333600*F1
140    E=4.803E-10
150    H=6.63E-27
160    M=9.11E-28
170    J1=120*T2*EXP((-P+E*(3/2)*F1/2)/(K*T))
180    C=H/(2*PI)*E0.25*F0.75/(PI*(2*M)0.5)
190    Q=C/(K*T)
200    J2=J1*PI*Q/SIN(PI*Q)
210    PRINT "                CURRENT DENSITY (A/CM2)"
220    PRINT "SCHOTTKY",J1
230    PRINT "EXTENDED SCHOTTKY",J2
235    PRINT

```

---

```
240 PRINT "Q =",Q
250 IF Q>0.75 THEN 270
260 END
270 PRINT "Q TOO HIGH FOR ACCURATE CALCULATION"
```

## APPENDIX C

Computer program using Schottky and extended Schottky equations to calculate work function from temperature, field, and current density.

```
60     PRINT "INPUT TEMPERATURE (K)"
65     INPUT T
70     PRINT "INPUT FIELD (V/A)"
75     INPUT F1
80     PRINT "INPUT CURRENT DENSITY (A/CM2)"
90     INPUT J2
100    K=1.38E-16
130    F=333600*F1
140    E=4.803E-10
150    H=6.63E-27
160    M=9.11E-28
170    X1=120*T2*EXP(E3/2*F1/2/(K*T))
180    C=H/(2*PI)*E0.25 F0.75/(PI*(2*M)0.5)
190    Q=C/(K*T)
200    X2=X1*PI*Q/SIN(PI*Q)
205    P=K*T*LOG(X2/J2)
210    PRINT "WORK FUNCTION PHI (eV) =",P/1.602E-12
235    PRINT
240    PRINT "Q =",Q
```

---

```
250     IF Q>0.75 THEN 270
260     END
270     PRINT "Q TOO HIGH FOR ACCURATE CALCULATION"
```

## APPENDIX D

## SCWIM Program Reference Guide

	Page
A. Introduction	182
B. Mesh Structure	182
C. Calculation of Potential	183
D. Calculation of Cathode Current Density	187
E. Calculation of Trajectories	187
F. Calculation of Space Charge	187
G. Program Improvements	189
H. Future Improvements	190
I. Input Data Preparation	191
J. Output Data Files	202
K. List of Program Variables	214
L. References	220

---

### A. Introduction

The SCWIM (Spherical Coordinates With Increasing Mesh) program has been written in three versions, LABGUN, ZRWGUN and LMIGUN for LaB<sub>6</sub> pointed cathodes, ZrO/W pointed cathodes and field emitters, and liquid metal ion sources respectively. The differences in the three versions are mainly in the nature of the mesh refinement in the vicinity of the emitter tip and the equations used to determine the emission current density. The LABGUN program deals with emitters of  $\sim 10 \mu\text{m}$  radius, the ZRWGUN program deals with  $\sim 1 \mu\text{m}$  radius and the LMIGUN is required to model emitters of  $\sim 100 \text{ \AA}$  radius. This guide was written for the ZRWGUN program, which was used in this dissertation. The flow chart for the ZRWGUN program is shown in Figure A-1.

### B. Mesh Structure

The calculation of potential uses a spherical coordinate system with an increasing mesh size as the mesh radiates from the emitter tip. The radial mesh size increases with radius according to a geometrical series with a term ratio  $(1 - h_{\theta})^{-1}$ , where  $h_{\theta}$  is the angular mesh size. To obtain finer resolution in the vicinity of the emitter surface in order to accurately resolve the facet, two regions with different angular mesh sizes are defined. See Figure A-2. Region I is the coarse mesh region with angular mesh size  $h_c$ ; Region II is the fine mesh region with angular mesh size  $h_{cc}$ , and  $h_{cc} = h_c / M_o$



where  $M_0$  is the demagnification factor for the fine mesh ( $M_0 = 3$  to 10). Further details can be found in reference 1.

### C. Calculation of Potential

The details of the mesh spacing, difference formulas, details of the convergence of the overrelaxation calculation can be found in references 1 and 3.

---

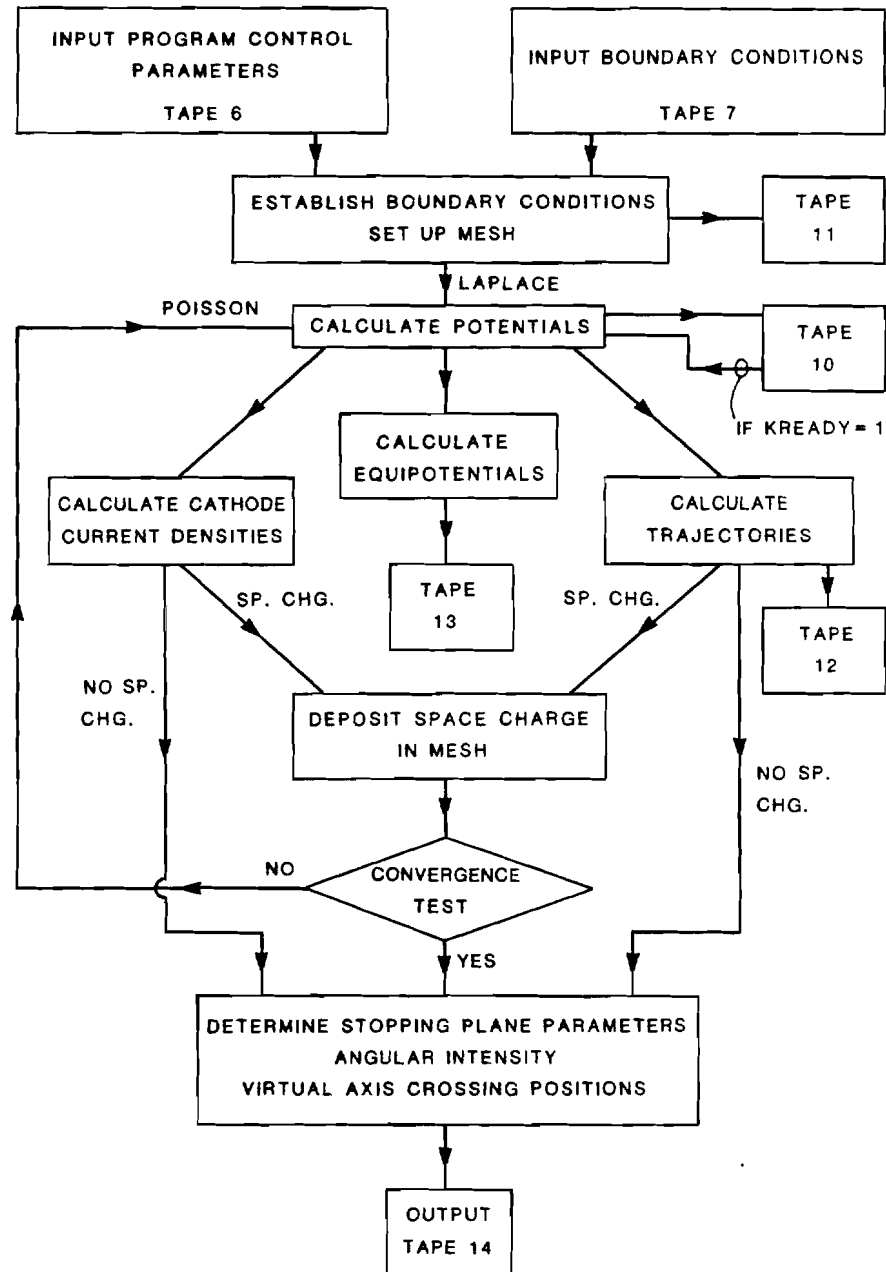
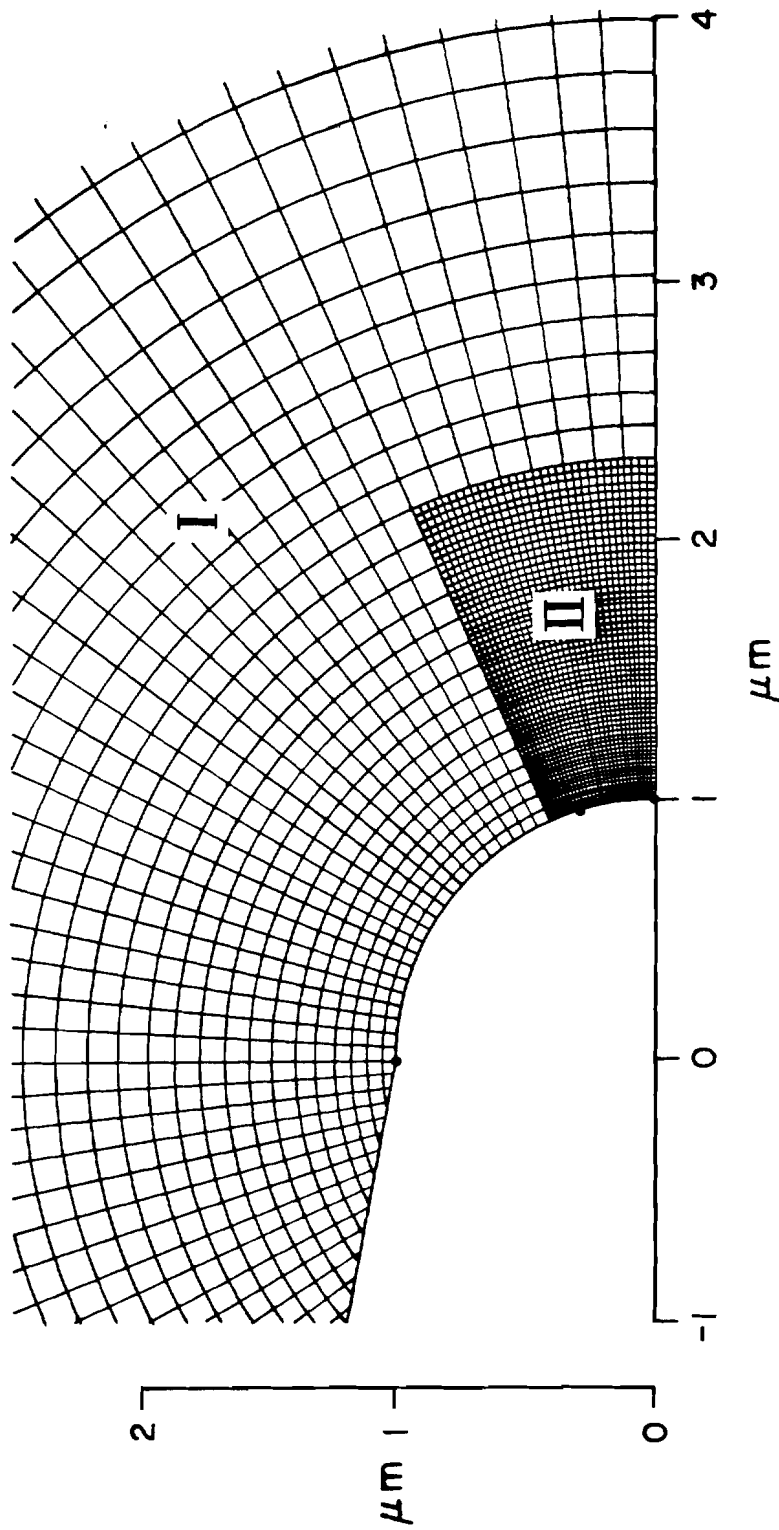


Figure A-1. ZRWGUN Flow Chart.



COARSE MESH REGION I  
FINE MESH REGION II

Figure A-2. Mesh structure.

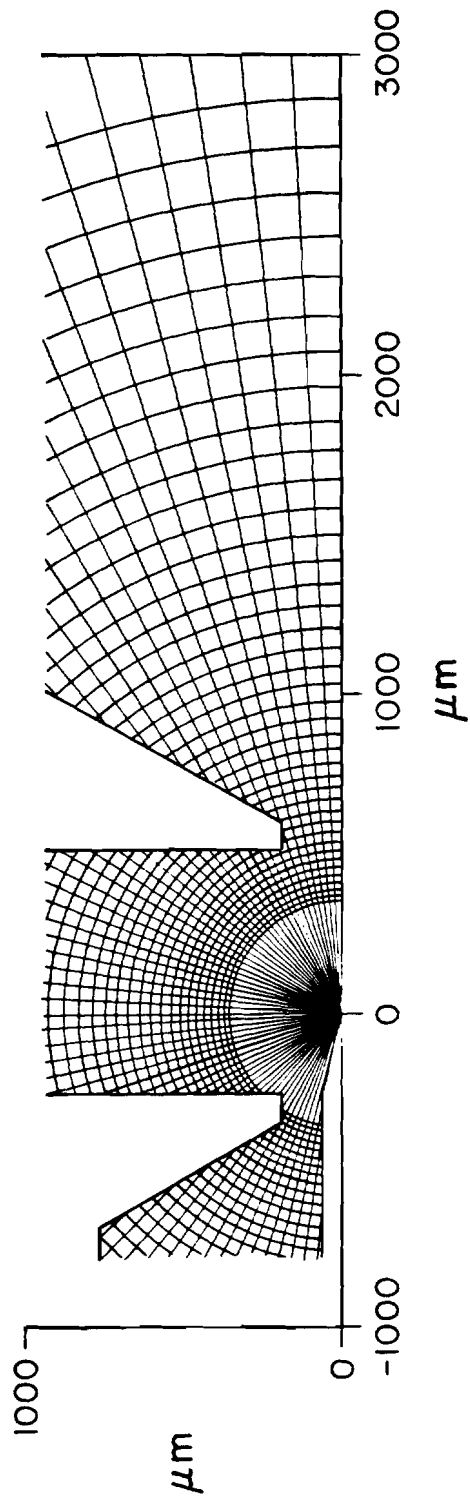


Figure A-2 (continued).

#### D. Calculation of Cathode Current Density

The cathode current density at each position on the cathode surface is calculated by inputting the work function and temperature (from Tape 6) and using the cathode surface field (calculated by the program) in a subroutine which integrates the product of the electron density in the emitting material and the potential barrier transmission coefficient with respect to energy. This subroutine gives the current density directly, without the necessity of using the analytic approximations valid only for certain ranges of  $\phi$ ,  $T$  and  $F$ . The subroutine is based on work done by El-Kareh, Wolfe and Wolfe.<sup>2</sup>

#### E. Calculation of Trajectories

The fourth order of Runge-Kutta method with automatic selection of steps is applied to integrate the equation of motion in spherical coordinates:

$$\begin{aligned}\ddot{R} &= R\dot{\theta}^2 - \eta E_R \\ \ddot{\theta} &= -2R\dot{\theta}/R - \eta E_\theta/R^2\end{aligned}$$

where  $\eta$  is the ratio of charge to mass;  $E_R$ ,  $E_\theta$  are radial and angular fields, respectively.

#### F. Calculation of Space Charge

A virtual auxiliary mesh system as shown by the dotted lines in Figure A-3 is established to evaluate the space charge density at any mesh point  $(i,j)$ :

$$\rho(i,j) = \frac{\sum_l \sum_n I_l \Delta t_n}{V_{ij}}$$


---

**SPACE CHARGE CELL**

Volume = VOLUME (I, J)

Charge Density =  $\rho$  (I, J)

Potential =  $V$  (I, J)

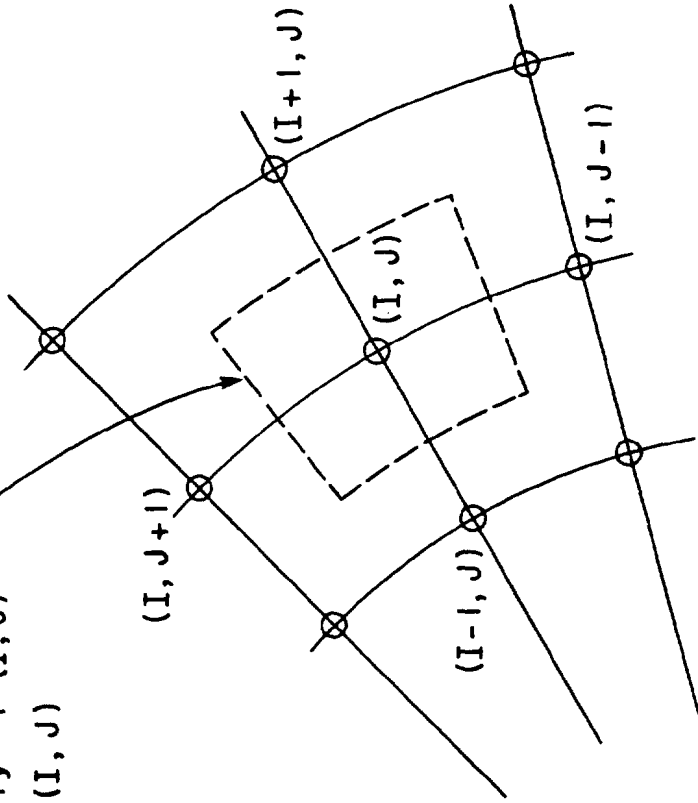


Figure A-3. Space charge virtual mesh.

where  $I_{\ell}$  is the current carried by the trajectory which falls in the auxiliary cell (i,j);  $\Delta t_n$  is the time interval of a step,  $V_{ij}$  is the volume of that mesh cell; the summation is performed only for those trajectories  $\ell$  and time intervals  $n$  which fall within the volume  $V_{ij}$ .

#### G. Program Improvements

Initial experience with the program disclosed problems with trajectory output data scatter. A smoothing routine was tried to fit trajectory slopes to a smooth curve of slope vs trajectory number. Although this technique improved the results, there were still problems whenever a trajectory crossed a radial mesh line and besides, the curve smoothing was only a "band-aid" approach applied to the output data. Use of a finer mesh produced a greater output data scatter. Finally, a new interpolation scheme was tried which calculated the potential, and the  $\theta$  and  $R$  electric field components, at any point in space, based on a Lagrange interpolation using 16 mesh nodes rather than the original 4 nodes. This interpolation not only produced smooth output data, but also caused the program to run faster. The more accurate interpolation resulted in larger trajectory integration step ( $\Delta t$ ) intervals, probably because less error in  $E_r$  and  $E_{\theta}$  resulted in a more accurate increment in electron position and velocity over longer time intervals. It was also found that the interpolation in the  $\theta$  direction could contain only even order terms, since the potentials are symmetric about the system axis. This was particularly important for trajectories close to the axis.

---

Further refinements were necessary when the program was required to generate data for the virtual source calculation. The backward projection of the trajectory final slopes determines the virtual axis crossing positions and, due to the long lever arm, a small scatter in the slope data produced large fluctuations in the axis crossing points. It was found that if a "stopping plane" was created beyond the anode and two trajectory points on either side of that imaginary plane were used to interpolate a slope, position and kinetic energy at the plane, the data scatter disappeared. It seems that, even in areas beyond the anode, in field free space, the field is not truly zero so that the original scatter in stopping plane positions for various trajectories was reflected in scatter in trajectory slopes.

The program was originally written in double precision, therefore all real numbers were in the form of 3.1416D0. The program was changed to single precision for the CYBER 175, since single precision on the CYBER is equivalent to double precision on some smaller computers. This is the reason real numbers appear in the somewhat awkward form 3.1416E0.

#### H. Future Improvements

The following items would benefit from some work:

- i) At low fields, the cathode current density subroutine doesn't work. This subroutine should be extended to the low Schottky and space charge regimes of emission.



## i) TAPE 6

This file contains program control variable values, flags, two lines of remarks which are reproduced in the main output file and physical parameters such as emitter temperature and work function. Figures A-4, A-5 and A-6 show three typical TAPE 6 files. An explanation of the file follows:

First two lines - character strings which are inserted in the main output file, TAPE 14.

TY - program control, increments either launch angle or initial K.E. of electrons.

Algorithms for incrementing are as follows:

$$(TY = 0) \alpha_0 = (1 \cdot 10^{-5}) (2^{L-1}) \text{ radians}$$

$$(TY = 1) eV_0 = (1 \cdot 10^{-5}) (2^{L-1}) \text{ eV}$$

Note that the number of trajectories (LT) determines the maximum  $\alpha_0$  and  $eV_0$ . Since  $\alpha_0$  must be  $< \pi/2$ ,  $LT = 18$  for the alpha electrons.

AF - initial accelerating factor for successive over-relaxation calculation of potential. See reference 3 for more information.

$$\text{Potential} = (AF) (\text{New Calculation of Potential}) + (1 - AF) (\text{Old Potential})$$

AF10 - Comparison accelerating factor used for first AF adjustment.

EVINIT - initial K.E. for trajectories. Note that if TY

---

**COLD ELECTRON TRAJECTORIES**

**16 TRAJECTORIES FROM APEX TO EDGE OF FACET**

0	TY	(0=COLD AND ALPHA, 1=V ELECTRON)
1.880E0	AF	(ACCELERATION FACTOR ITERATIONS)
0.E0	AF10	(INITIAL ACCELERATION FACTOR)
0.0E0	EVINIT	(INITIAL K.E. IN ELECTRON VOLTS)
1.0E-08	EPS	(CONTROL ACCURACY OF TRAJECTORY CALCULATIONS)
019	KA	(NUMBER OF MINOR ITERATIONS)
1	KB	(FLAG, ACCELERATING FACTOR, 1=CONSTANT, 0=CHANGING)
0	KU	(FLAG, 0=AUTO EQUIPOTENTIALS, 1=MANUAL EQUIPOTENTIALS)
016	LT	(NUMBER OF TRAJECTORIES FROM TIP)
0	KREADY	(FLAG =1:USE PREVIOUS POTENTIALS, =0:CALC. POTENTIALS)
1000.E0	T	(TIP TEMPERATURE IN DEGREES KELVIN)
2.8E0	WF	(WORK FUNCTION FOR TIP)
1.E0	DMASS	(RELATIVE MASS OF PARTICLE, ELECTRON=1)
04	M0	(DEMAGNIFICATION FACTOR OF FINE REGION 3 - 10)
015	IBOUND	(RADIAL INTEGER MESH # OF FINE REGION)
1	KFIELD	(FLAG, 0=FIELD, 1=TRAJ, 2=SPACE CHARGE)
3.E0	HC	(ANGULAR MESH SIZE IN DEGREES)
0	BATCH	(LOGICAL, 0=INTERACTIVE, 1=BATCH)
1	AUTOT	(LOGICAL, 1=AUTO TRAJECTORIES, 0=MANUAL TRAJ.)

Figure A-4.

ALPHA ELECTRON TRAJECTORIES  
 18 TRAJECTORIES WITH INITIAL KE = 1EV

0	TY	(0=COLD AND ALPHA, 1=V ELECTRON)
1.880E0	AF	(ACCELERATION FACTOR ITERATIONS)
0.E0	AF10	(INITIAL ACCELERATION FACTOR)
1.0E0	EVINIT	(INITIAL K.E. IN ELECTRON VOLTS)
1.0E-08	EPS	(CONTROL ACCURACY OF TRAJECTORY CALCULATIONS)
019	KA	(NUMBER OF MINOR ITERATIONS)
1	KB	(FLAG, ACCELERATING FACTOR, 1=CONSTANT, 0=CHANGING)
0	KV	(FLAG, 0=AUTO EQUIPOTENTIALS, 1=MANUAL EQUIPOTENTIALS)
018	LT	(NUMBER OF TRAJECTORIES FROM TIP)
1	KREADY	(FLAG =1:USE PREVIOUS POTENTIALS, =0:CALC. POTENTIALS)
1000.E0	T	(TIP TEMPERATURE IN DEGREES KELVIN)
2.8E0	WF	(WORK FUNCTION FOR TIP)
1.E0	DMASS	(RELATIVE MASS OF PARTICLE, ELECTRON=1)
04	M0	(DEMAGNIFICATION FACTOR OF FINE REGION 3 - 10)
015	IBOUND	(RADIAL INTEGER MESH # OF FINE REGION)
1	KFIELD	(FLAG, 0=FIELD, 1=TRAJ, 2=SPACE CHARGE)
3.E0	HC	(ANGULAR MESH SIZE IN DEGREES)
0	BATCH	(LOGICAL, 0=INTERACTIVE, 1=BATCH)
0	AUTOT	(LOGICAL, 1=AUTO TRAJECTORIES, 0=MANUAL TRAJ.)

Figure A-5.

**V ELECTRON TRAJECTORIES**  
**20 TRAJECTORIES WITH INITIAL LAUNCH ANGLE = 90 DEG.**

1	TY	(0=COLD AND ALPHA, 1=V ELECTRON)
1.880E0	AF	(ACCELERATION FACTOR ITERATIONS)
0.E0	AF10	(INITIAL ACCELERATION FACTOR)
1.0E0	EVINIT	(INITIAL K.E. IN ELECTRON VOLTS)
1.0E-08	EPS	(CONTROL ACCURACY OF TRAJECTORY CALCULATIONS)
019	KA	(NUMBER OF MINOR ITERATIONS)
1	KB	(FLAG, ACCELERATING FACTOR, 1=CONSTANT, 0=CHANGING)
0	KV	(FLAG, 0=AUTO EQUIPOTENTIALS, 1=MANUAL EQUIPOTENTIALS)
020	LT	(NUMBER OF TRAJECTORIES FROM TIP)
1	KREADY	(FLAG =1:USE PREVIOUS POTENTIALS, =0:CALC. POTENTIALS)
1900.E0	T	(TIP TEMPERATURE IN DEGREES KELVIN)
2.8E0	WF	(WORK FUNCTION FOR TIP)
1.E0	DMASS	(RELATIVE MASS OF PARTICLE, ELECTRON=1)
04	M0	(DEMAGNIFICATION FACTOR OF FINE REGION 3 - 10)
015	IBOUND	(RADIAL INTEGER MESH # OF FINE REGION)
1	KFIELD	(FLAG, 0=FIELD, 1=TRAJ, 2=SPACE CHARGE)
3.E0	HC	(ANGULAR MESH SIZE IN DEGREES)
0	BATCH	(LOGICAL, 0=INTERACTIVE, 1=BATCH)
0	AUTOT	(LOGICAL, 1=AUTO TRAJECTORIES, 0=MANUAL TRAJ.)

Figure A-6.

= 1 then this input is ignored.

EPS - Two calculations are made of each trajectory step, one using a  $\Delta t$  step to calculate a new position and velocity and one using two  $\Delta t/2$  steps to do the same thing.  $\Delta t$  is then increased, decreased or left unchanged depending on the relative errors in position and velocity between the two calculations. EPS is the relative error nominal value.

KA - number of iterations of overrelaxation calculation performed between successive estimates of AF.

KB - Equipotential control: If 0,  $V_{eq}(i) = V_{suppressor} + V_{ANODE}/i$  for  $i = 1$  through 20; if 1,  $V_{eq}$  is input from the terminal by a FORTRAN free-form read statement.

LT - Number of trajectories, subject to limits (see explanation of TY)

KREADY - Potential calculation bypass control, if 0 calculate potentials, if 1, use potentials calculated on TAPE 10. Saves time when doing different trajectories with same geometry and voltages. Note that the samples of TAPE 6 show KREADY = 0 only for cold electrons, since the order of calculation was cold, alpha, and V electron trajectories.

T - Emitter temperature in Kelvin

WF - Work function of emitting surface in eV

DMASS - Relative mass of the particle. Electron = 1.

MO - Demagnification factor of fine mesh relative to coarse mesh.

IBOUND - The fine mesh region extends out radially to the spherical surface associated with the integer IBOUND in the coarse mesh.

KFIELD - Controls extent of overall calculation:

- 0 -- Calculate Laplace field and cathode current density.
- 1 -- Calculate trajectories also.
- 2 -- Iterate space charge calculations to convergence.

HC - Coarse mesh angular mesh increment in degrees.

BATCH - Controls output back to terminal.

- 0 -- Various output is written to terminal during program execution.
- 1 -- Output to terminal is suppressed.

AUTOT - Auto trajectory control.

- 0 -- Trajectories start from emitter apex.
- 1 -- Trajectories are spaced at equal intervals from apex to edge of facet (or first breakpoint in geometry listed on TAPE 7).

ii) TAPE 7

This file contains the geometry and the applied voltages for the emitter and gun. Figures A-7 and A-8 are typical TAPE 7 input files. The geometry

SPHERICAL-END EMITTER  
 1 UM EMITTER WITH -300, 6000V APPLIED  
 5  
 5,7,11,15,17  
 0.E0                    0.E0                    0.E0  
 -.0460608E0            .3E0                    1.E0  
 -1.E0                    1.E0                    1.E0  
 -254.E0                  63.5E0                  0.E0  
 -762.E0                  63.5E0                  0.E0  
 3000.E0                  0.E0                    0.E0  
 3000.E0                  940.E0                  0.E0  
 1016.E0                  940.E0                  0.E0  
 584.2E0                  190.5E0                0.E0  
 500.E0                    190.5E0                0.E0  
 500.E0                    940.E0                  0.E0  
 -254.E0                  940.E0                  0.E0  
 -254.E0                  190.5E0                0.E0  
 -330.2E0                190.5E0                0.E0  
 -660.4E0                762.E0                  0.E0  
 -660.4E0                762.E0                  0.E0  
 -762.E0                  762.E0                  0.E0  
 0.E0    6000.E0    6000.E0    -300.E0    -300.E0

Figure A-7.

ZRWGUN STRUCTURE WITH 3000 UM MAX Z COORD.  
 1UM FACETED-END EMITTER

5  
 5,7,11,15,17

0.E0	0.E0	0.E0
0.E0	.3E0	0.E0
-0.9539E0	1.E0	1.E0
-254.E0	63.5E0	0.E0
-762.E0	63.5E0	0.E0
3000.E0	0.E0	0.E0
3000.E0	940.E0	0.E0
1016.E0	940.E0	0.E0
584.2E0	190.5E0	0.E0
508.E0	190.5E0	0.E0
508.E0	940.E0	0.E0
-254.E0	940.E0	0.E0
-254.E0	190.5E0	0.E0
-330.2E0	190.5E0	0.E0
-660.4E0	762.E0	0.E0
-660.4E0	762.E0	0.E0
-762.E0	762.E0	0.E0
0.E0	6000.E0	6000.E0
		-300.E0
		-300.E0

Figure A-8.



associated with these two files is shown in Figure A-9.

The rules of writing this file are as follows:

First two lines - character strings which are written into the output file, TAPE 14.

Total number of electrodes (KO) - Note that the number of intersections between each radial mesh line and each electrode must be  $\leq 2$ , otherwise divide the electrode into two electrodes.

Accumulating mode numbers (KK(K)) - In Figure A-9 the nodes or breakpoints between the geometrical lines and curves are numbered. The numbers corresponding to the last point on each electrode are listed here in sequence, separated by commas.

List of coordinates (Z, R,  $\rho$ ) of each node number in Figure A-9. All segments consist of straight lines except for the emitter which can be either faceted or spherical. The apex is always the first point where the coordinates are (0,0,0). The sequence of electrodes is always cathode, anode and Wehnelt. All axial dimensions (Z) are relative to the cathode apex. All radial dimensions (R) are relative to the axis. The third column,  $\rho$ , is zero for a straight line segment and  $\rho = R_0$ , the tip-end radius, for the

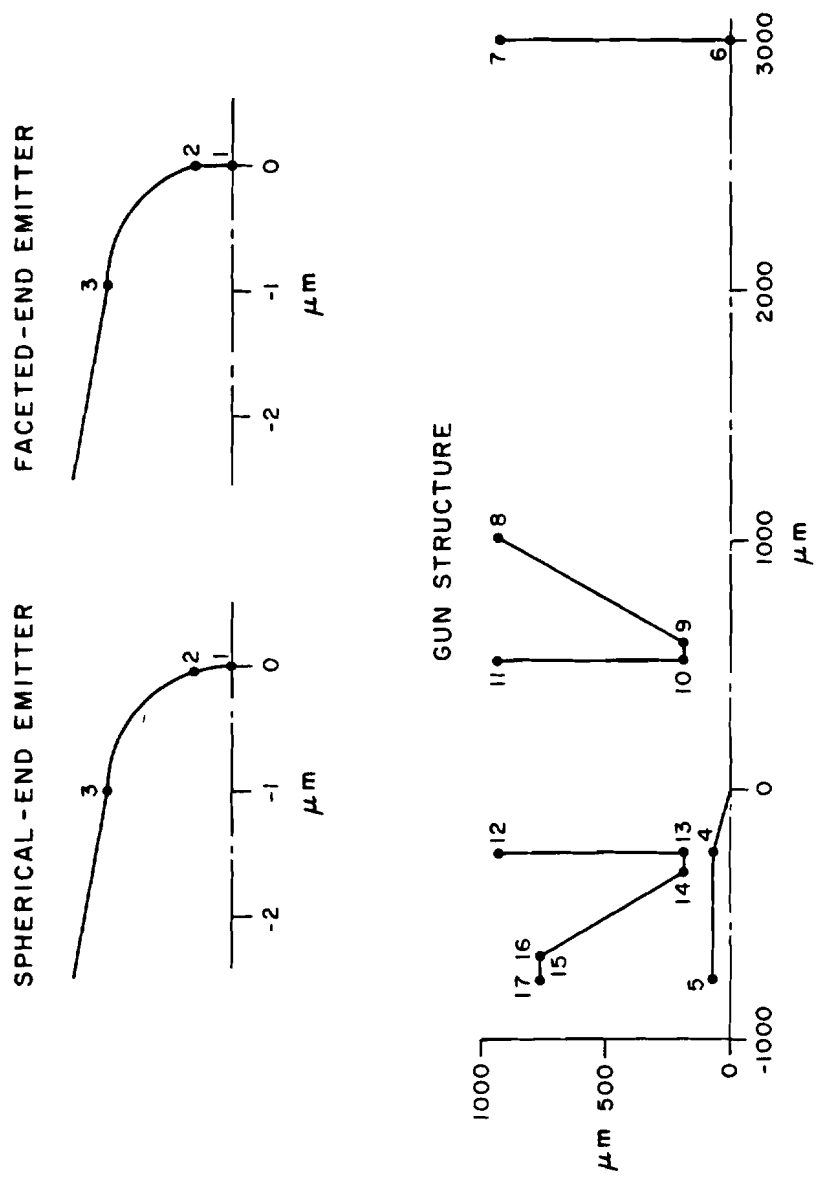


Figure A-9. Gun geometry for ZRWGUN program data input.

spherical portion of the emitter. All dimensions are in micrometers. In the TAPE 7 for the spherical-end emitter, note that even though the geometry is not faceted, a break point or node is included on the spherical surface. The reason for this is that the trajectory launching points for cold electrons and the angular extent of the fine mesh are determined by the location of the first node in the geometry after the apex. Other items to note are: a) the Z coordinates of the last nodes of the first and last electrode must be equal; b) the R coordinates of two points constituting an open boundary must be equal; c) the right hand side of the coordinate space must be closed (i.e. must start at  $R = 0$ ). Voltages of the electrodes are in sequence corresponding to the accumulating node numbers.

#### J. Output Data Files

There are 7 output data files as follows:

##### i. TAPE 8

This is a file for general check-up. It includes boundary data, radial mesh coordinates, data of boundary procedure, potential convergency, cathode density (both space charge limited and temperature limited) etc.

---

ii. TAPE 9

Current density at all mesh points (space charge density multiplied by velocity corresponding to mesh potential energy).

iii. TAPE 10

Laplace potential map for the mesh. This file can be used either for check-up purposes or for the next run (when KREADY = 1).

iv. TAPE 11

Boundary coordinates for graphic use.

v. TAPE 12

Trajectory coordinates for graphic use.

vi. TAPE 13

Equipotential coordinates for graphic use.

vii. TAPE 14

This file contains the major results of the run and is reproduced for a typical case in Figure A-10.

---

The following pages comprise Figure A-10. Tape 14 Output  
Data Files.

ZRNGUN PROGRAM STARTED EXECUTION: DEC. 7 1964 10:40 P.M.  
 COLD ELECTRON TRAJECTORIES  
 16 TRAJECTORIES FROM APEX TO EDGE OF FACET

SPH-END EMITTER WITH 45 & 10 DEG CONES  
 0.07 UM EMITTER WITH -3EV, 6800V APPLIED

INPUT DATA --- GEOMETRY AND VOLTAGES OF GUN

Z=	0.0000	R=	0.0000	P=	0.0000
Z=	-0.0032	R=	.0210	P=	.0700
Z=	-0.0208	R=	.0495	P=	.0700
Z=	-.3246	R=	.3536	P=	0.0000
Z=	-.5913	R=	.4924	P=	.5000
Z=	-357.9500	R=	63.5000	P=	0.0000
Z=	-762.0000	R=	63.5000	P=	0.0000
Z=	300.0000	R=	0.0000	P=	0.0000
Z=	300.0000	R=	940.0000	P=	0.0000
Z=	1016.0000	R=	940.0000	P=	0.0000
Z=	584.2000	R=	190.5000	P=	0.0000
Z=	509.0000	R=	190.5000	P=	0.0000
Z=	560.0000	R=	940.0000	P=	0.0000
Z=	-254.0000	R=	940.0000	P=	0.0000
Z=	-254.0000	R=	190.5000	P=	0.0000
Z=	-330.2000	R=	190.5000	P=	0.0000
Z=	-560.0000	R=	762.0000	P=	0.0000
Z=	-660.0000	R=	762.0000	P=	0.0000
Z=	-762.0000	R=	762.0000	P=	0.0000

VOLTAGES OF ELECTRODES (VOLTS) = 0.000 6800.000 6800.000 -300.000  
 -300.000

ACCELERATION FACTOR= .1280E+01  
 INITIAL ACCELERATION FACTOR= 0.  
 CONTROL ACCURACY= .1000E-07  
 # OF MAJOR ITERATIONS= 16  
 # OF TRAJECTORIES FROM TIP= 16  
 TIP TEMPERATURE= 2800.0  
 TIP WORK FUNCTION= .4500E+01  
 RELATIVE PARTICLE MASS= .1000E+01  
 DEMAGNIFICATION FACTOR= 4  
 RADIAL INTEGER MESH # OF FINE REGION= 15  
 ANGULAR MESH SIZE IN DEGREES= 3.000

ACCELERATING FACTOR IS CONSTANT  
 MANUAL EQUIPOTENTIALS  
 POTENTIALS CALCULATED FROM INPUT DATA  
 LAPLACE FIELD AND LAPLACE TRAJECTORIES  
 INTERACTIVE PROCESSING MODE  
 AUTOMATIC TRAJECTORY STARTING POINTS

I0 = 201 J0 = 61  
 I00 = 59 J00 = 33  
 MESH SETUP TIME (SEC) = .48  
 POTENTIAL COMPUTATION TIME (SEC) = 294.63

FIELD ON THE SURFACE IN V/A

TRAJ. NORMAL FIELD (V/A)

1	.533829E+00
2	.539669E+00
3	.539417E+00
4	.538994E+00
5	.538398E+00
6	.537625E+00
7	.536688E+00
8	.535520E+00
9	.534168E+00
10	.532597E+00
11	.531786E+00
12	.529705E+00
13	.526319E+00
14	.523538E+00
15	.520290E+00
16	.516409E+00

CATHODE CURRENT DENSITY IN A/CM2	
TRAJ.	CURRENT DENSITY
1	.242769E+07
2	.241962E+07
3	.240689E+07
4	.238570E+07
5	.235610E+07
6	.231815E+07
7	.227191E+07
8	.221743E+07
9	.215475E+07
10	.208381E+07
11	.200453E+07
12	.191660E+07
13	.181954E+07
14	.171247E+07
15	.159387E+07
16	.146149E+07
CATHODE FIELD & CURRENT CALC. (SEC) = .15	
TRAJECTORY CALCULATION TIME (SEC) = 342.33	

TRAJECTORY ENDPOINT PARAMETERS REGRESSION & AVERAGES FOR LAST 10 Z,R VALUES				
TRAJ	SLOPE (DR/DZ)	ENDPOINT R	ENDPOINT Z	AXIS INTERCEPT
2	.70825063E-02	.17501995E+02	.24448573E+04	-.30299753E+02
3	.14178031E-01	.35033734E+02	.24406812E+04	-.30306104E+02
4	.21222066E-01	.52433061E+02	.24403695E+04	-.30317387E+02
5	.26298573E-01	.69903060E+02	.24398636E+04	-.30333519E+02
6	.35368131E-01	.87347557E+02	.24393152E+04	-.30353256E+02
7	.42370197E-01	.10460128E+03	.24383655E+04	-.30381133E+02
8	.49402313E-01	.12192243E+03	.24375585E+04	-.30391209E+02
9	.56389291E-01	.13902954E+03	.24350749E+04	-.30456035E+02
10	.63326588E-01	.15617427E+03	.24340343E+04	-.30495503E+02
11	.70263124E-01	.17426800E+03	.24496915E+04	-.30497067E+02
12	.77114360E-01	.19116066E+03	.24483823E+04	-.30544595E+02
13	.83942486E-01	.20797608E+03	.24470048E+04	-.30597241E+02
14	.90726693E-01	.22466763E+03	.24456100E+04	-.30658190E+02
15	.99096281E-01	.24695447E+03	.24613849E+04	-.30681073E+02
16	.10402431E+00	.25910285E+03	.24600575E+04	-.30733870E+02

INTERPOLATED VALUES AT TARGET PLANE Z = 2400.000 UM.

TRAJ	DR	EV0 R (UM)	SLOPE (MR)	K.E. (EV)	AXIS INTCP(UM)	MAG.
1	.00001	0.0000	0.0000	6781.5	0.0000000	0.000000
2	.00002	17.2126	7.0817	6781.5	-30.5209999	0.000000
3	.00004	34.4569	14.1758	6781.5	-30.5264957	0.000000
4	.00008	51.5763	21.2170	6781.5	-30.5362550	0.000000
5	.00016	68.7749	28.2835	6781.5	-30.5498921	0.000000
6	.00032	85.9570	35.3513	6781.6	-30.5669385	0.000000
7	.00064	102.9756	42.3412	6781.6	-30.5900564	0.000000
8	.00128	120.0668	49.3530	6781.7	-30.5961340	0.000000
9	.00256	137.0515	56.3253	6781.7	-30.6418534	0.000000
10	.00512	153.9148	63.2374	6781.8	-30.6761130	0.000000
11	.01024	170.7742	70.1415	6781.9	-30.7138790	0.000000
12	.02048	187.4297	76.9553	6782.0	-30.7549531	0.000000
13	.04096	204.0302	83.7391	6782.0	-30.8007777	0.000000
14	.08192	220.5254	90.4716	6782.1	-30.8547928	0.000000
15	.16384	240.8713	98.7638	6781.8	-30.9261796	0.000000
16	.32768	252.8552	103.6413	6781.3	-30.9730606	0.000000

INITIAL K.E. (EV) = 0.000000

ANGULAR INTENSITY DISTRIBUTION			
TRAJ	THETA <sub>0</sub> (DEG)	ALPHA (DEG)	I <sub>PRIME</sub> (MA/SR)
1	0.00000	3.00000	.986575
2	1.16667	.45791	.977850
3	2.33333	.81227	.976538
4	3.50000	1.21572	.970097
5	4.66667	1.62096	.954981
6	5.83333	2.02560	.945678
7	7.00000	2.42612	.929559
8	8.16667	2.82825	.907551
9	9.33333	3.22745	.889143
10	10.50000	3.62358	.862933
11	11.66667	4.01917	.835836
12	12.83333	4.41960	.806508
13	14.00000	4.79831	.781778
14	15.16667	5.18464	.667857
15	16.33333	5.65932	.460932
16	17.50000	6.31461	.319492
TOTAL EXECUTION TIME (SEC) = 637.52			



ZRNGUN PROGRAM STARTED EXECUTION! DEC. 7 1984 11:30 P.M.  
 ALPHA ELECTRON TRAJECTORIES  
 18 TRAJECTORIES WITH INITIAL KE = 1EV

SPH-END EMITTER WITH +5 & 10 DEG CGNES  
 0.07 UM EMITTER WITH -300, 6000V APPLIED

INPUT DATA --- GEOMETRY AND VOLTAGES OF GUN

Z=	0.0000	R=	0.0000	P=	0.0000
Z=	-0.0032	R=	.0210	P=	.0700
Z=	-0.0205	R=	.0495	P=	.0700
Z=	-.3246	R=	.3536	P=	0.0000
Z=	-.5913	R=	.4924	P=	.5000
Z=	-357.9500	R=	63.5000	P=	0.0000
Z=	-762.0000	R=	63.5000	P=	0.0000
Z=	3000.0000	R=	0.0000	P=	0.0000
Z=	3000.0000	R=	940.0000	P=	0.0000
Z=	1016.0000	R=	940.0000	P=	0.0000
Z=	584.2000	R=	190.5000	P=	0.0000
Z=	508.0000	R=	190.5000	P=	0.0000
Z=	508.0000	R=	940.0000	P=	0.0000
Z=	-254.0000	R=	940.0000	P=	0.0000
Z=	-254.0000	R=	190.5000	P=	0.0000
Z=	-330.2000	R=	190.5000	P=	0.0000
Z=	-660.4000	R=	762.0000	P=	0.0000
Z=	-660.4000	R=	762.0000	P=	0.0000
Z=	-762.0000	R=	762.0000	P=	0.0000

VOLTAGES OF ELECTRODES VS (K)= 0.000 6000.000 6000.000 -300.000  
 -300.000

ACCELERATION FACTOR= .1880E+01

INITIAL ACCELERATION FACTOR= 0.

CONTROL ACCURACY= .1000E-07

# OF MAJOR ITERATIONS= 19

# OF TRAJECTORIES FROM TIP= 18

TIP TEMPERATURE= 1800.00

TIP WORK FUNCTION= .4500E+01

RELATIVE PARTICLE MASS= .1000E+01

DEMAGNIFICATION FACTOR= 4

RADIAL INTEGER MESH # OF FINE REGION= 15

ANGULAR MESH SIZE IN DEGREES= 3.000

ACCELERATING FACTOR IS CONSTANT

MANUAL EQUIPOTENTIALS

POTENTIALS TAKEN FROM TAPE10

LAPLACE FIELD AND LAPLACE TRAJECTORIES

INTERACTIVE PROCESSING MODE

MANUAL TRAJECTORY STARTING POINTS

I0= 201 J0= 61

I00= 59 J00= 33

MESH SETUP TIME (SEC) = .50

POTENTIAL COMPUTATION TIME (SEC) = 2.54

FIELD ON THE SURFACE IN V/A	
TRAJ.	NORMAL FIELD (V/A)
1	.539829E+00
2	.539688E+00
3	.539491E+00
4	.539163E+00
5	.538761E+00
6	.538102E+00
7	.537363E+00
8	.536480E+00
9	.535446E+00
10	.534253E+00
11	.532891E+00
12	.531345E+00
13	.529597E+00
14	.527620E+00
15	.525379E+00
16	.522822E+00
17	.519869E+00
18	.516409E+00

CATHODE CURRENT DENSITY IN A/CM2	
TRAJ.	CURRENT DENSITY
1	.242769E+07
2	.242256E+07
3	.241004E+07
4	.239414E+07
5	.237107E+07
6	.234148E+07
7	.230541E+07
8	.226289E+07
9	.221397E+07
10	.215866E+07
11	.209694E+07
12	.202873E+07
13	.195388E+07
14	.187210E+07
15	.178296E+07
16	.168567E+07
17	.157903E+07
18	.146149E+07

CATHODE FIELD & CURRENT CALC. (SEC) = .16  
 TRAJECTORY CALCULATION TIME (SEC) = 372.93

TRAJECTORY ENDPOINT PARAMETERS  
REGRESSION & AVERAGES FOR LAST 10 Z,R VALUES

TRAJ	SLOPE (DR/DZ)	ENDPOINT R	ENDPOINT Z	AXIS INTERCEPT
1	.35801674E-06	.87950789E-03	.24263372E+04	-.30273926E+02
2	.71603348E-06	.17590158E-02	.24263372E+04	-.30273926E+02
3	.14320670E-05	.35180316E-02	.24263372E+04	-.30273926E+02
4	.28641339E-05	.70360631E-02	.24263372E+04	-.30273926E+02
5	.57282678E-05	.14072126E-01	.24263372E+04	-.30273926E+02
6	.11456535E-04	.28144252E-01	.24263372E+04	-.30273926E+02
7	.22913070E-04	.56288503E-01	.24263372E+04	-.30273926E+02
8	.45826134E-04	.11257899E+00	.24263372E+04	-.30273926E+02
9	.91652221E-04	.22515386E+00	.24263372E+04	-.30273927E+02
10	.18330406E-03	.45330877E+00	.24263371E+04	-.30273925E+02
11	.36660503E-03	.90360592E+00	.24263370E+04	-.30273933E+02
12	.73318538E-03	.18011508E+01	.24263364E+04	-.30273954E+02
13	.14661733E-02	.36018132E+01	.24263340E+04	-.30274037E+02
14	.29307664E-02	.71997173E+01	.24263245E+04	-.30274367E+02
15	.58488632E-02	.14368110E+02	.24262873E+04	-.31275649E+02
16	.11592103E-01	.28639275E+02	.24377261E+04	-.30270889E+02
17	.22125790E-01	.54595653E+02	.24372249E+04	-.30287144E+02
18	.35914051E-01	.88685794E+02	.24391136E+04	-.30276275E+02

ZRMGUN PROGRAM STARTED EXECUTION: DEC. 9 1954 4:16 P.M.  
 V ELECTRON TRAJECTORIES  
 20 TRAJECTORIES WITH INITIAL LAUNCH ANGLE = 90 DEG.

SPH-END EMITTER WITH 45 & 10 DEG CONES  
 0.07 UM EMITTER WITH -300, 8900V APPLIED

INPUT DATA --- GEOMETRY AND VOLTAGES OF GUN

Z=	0.0000	R=	0.0000	P=	0.0000
Z=	-0.0032	R=	.0210	P=	.0700
Z=	-0.0205	R=	.0495	P=	.0700
Z=	-.3246	R=	.3536	P=	0.0000
Z=	-.5913	R=	.4924	P=	.5000
Z=	-357.9500	R=	63.5000	P=	0.0000
Z=	-762.0000	R=	63.5000	P=	0.0000
Z=	3000.0000	F=	0.0000	P=	0.0000
Z=	3000.0000	R=	940.0000	F=	0.0000
Z=	1270.0000	R=	940.0000	P=	0.0000
Z=	838.2000	R=	190.5000	P=	0.0000
Z=	762.0000	R=	190.5000	P=	0.0000
Z=	762.0000	R=	940.0000	P=	0.0000
Z=	-254.0000	R=	940.0000	P=	0.0000
Z=	-254.0000	R=	190.5000	P=	0.0000
Z=	-330.2000	R=	190.5000	P=	0.0000
Z=	-660.4000	R=	762.0000	P=	0.0000
Z=	-660.4000	R=	762.0000	P=	0.0000
Z=	-762.0000	R=	762.0000	P=	0.0000
VOLTAGES OF ELECTRODES V0(K) =					
	0.000		8900.000		8900.000
	-300.000				-300.000

ACCELERATION FACTOR= .1880E+01  
 INITIAL ACCELERATION FACTOR= 0.  
 CONTRL ACCURACY= .1000E-07  
 # OF MINOR ITERATIONS= 19  
 # OF TRAJECTORIES FROM TIP= 20  
 TIP TEMPERATURE= 1800.0  
 TIP WORK FUNCTION= .4500E+01  
 RELATIVE PARTICLE MASS= .1000E+01  
 DEMAGNIFICATION FACTOR= 4  
 RADIAL INTEGER MESH # OF FINE REGION= 15  
 ANGULAR MESH SIZE IN DEGREES= 3.000

ACCELERATING FACTOR IS CONSTANT  
 MANUAL EQUIPOTENTIALS  
 POTENTIALS TAKEN FROM TAPE10  
 LAPLACE FIELD AND LAPLACE TRAJECTORIES  
 INTERACTIVE PROCESSING MODE  
 MANUAL TRAJECTORY STARTING POINTS

I0= 201 J0= 61  
 I00 = 59 J00 = 33  
 MESH SETUP TIME (SEC) = .48  
 POTENTIAL COMPUTATION TIME (SEC) = 2.52

FIELD ON THE SURFACE IN V/A	
TRAJ.	NORMAL FIELD (V/A)
1	.524674E+00
2	.524550E+00
3	.524397E+00
4	.524141E+00
5	.523783E+00
6	.523318E+00
7	.522747E+00
8	.522066E+00
9	.521270E+00
10	.520357E+00
11	.519320E+00
12	.518151E+00
13	.516842E+00
14	.515379E+00
15	.513743E+00
16	.511925E+00
17	.509891E+00
18	.507574E+00
19	.504947E+00
20	.501911E+00

## CATHODE CURRENT DENSITY IN A/CM2

TRAJ.	CURRENT DENSITY
1	.175565E+07
2	.175022E+07
3	.174503E+07
4	.173529E+07
5	.172167E+07
6	.170420E+07
7	.168290E+07
8	.165779E+07
9	.162891E+07
10	.159626E+07
11	.155966E+07
12	.151971E+07
13	.147578E+07
14	.142800E+07
15	.137623E+07
16	.132041E+07
17	.126008E+07
18	.119497E+07
19	.112413E+07
20	.104695E+07

CATHODE FIELD & CURRENT CALC. (SEC) = .18  
 TRAJECTORY CALCULATION TIME (SEC) = 410.02

TRAJECTORY ENDPOINT PARAMETERS  
REGRESSION & AVERAGES FOR LAST 10 Z,R VALUES

TRAJ	SLOPE (DR/DZ)	ENDPOINT R	ENDPOINT Z	AXIS INTERCEPT
1	.10686462E-03	.26426236E+00	.24154819E+04	-.53925725E+02
2	.15115775E-03	.37372357E+00	.24164819E+04	-.53925726E+02
3	.21376953E-03	.52852541E+00	.24184819E+04	-.53925729E+02
4	.30231631E-03	.74744911E+00	.24194818E+04	-.53925734E+02
5	.42754134E-03	.10570564E+01	.24194817E+04	-.53925735E+02
6	.60463906E-03	.14949140E+01	.24184814E+04	-.53925767E+02
7	.85510093E-03	.21141573E+01	.24184809E+04	-.53925811E+02
8	.12093297E-02	.29899538E+01	.24184798E+04	-.53925896E+02
9	.17103478E-02	.42236706E+01	.24184778E+04	-.53926072E+02
10	.24190704E-02	.59379263E+01	.24255061E+04	-.53928279E+02
11	.34216614E-02	.84842550E+01	.24254979E+04	-.53926970E+02
12	.48414535E-02	.11969901E+02	.24184490E+04	-.53928474E+02
13	.66641522E-02	.17016932E+02	.24254605E+04	-.53932657E+02
14	.97090573E-02	.24003749E+02	.24183629E+04	-.53935933E+02
15	.13738843E-01	.34061818E+02	.24252862E+04	-.53947854E+02
16	.19433864E-01	.47917218E+02	.24116834E+04	-.53967324E+02
17	.27429362E-01	.67984221E+02	.24245118E+04	-.54008142E+02
18	.38781377E-01	.95573860E+02	.24103340E+04	-.54092662E+02
19	.54740569E-01	.13481552E+03	.24085637E+04	-.54244404E+02
20	.77168238E-01	.19082712E+03	.24182835E+04	-.54587779E+02

INTERPOLATED VALUES AT TARGET PLANE Z = 2400.000 UM.

TRAJ	AD OR EVO R (UM)	SLOPE (MR)	K.E. (EV)	AXIS INTCP(UM)	MAG.	
1	.00001	.2623	.1069	8888.6	-53.9305240	.002272
2	.00002	.3709	.1512	8888.6	-53.9305254	.003213
3	.00004	.5246	.2138	8888.6	-53.9305280	.004544
4	.00008	.7419	.3023	8888.6	-53.9305334	.006427
5	.00016	1.0492	.4275	8888.6	-53.9305443	.009089
6	.00032	1.4837	.6046	8888.6	-53.9305661	.012854
7	.00064	2.0984	.8551	8888.6	-53.9306097	.018177
8	.00128	2.9676	1.2093	8888.6	-53.9306967	.025706
9	.00256	4.1971	1.7103	8888.6	-53.9308703	.036352
10	.00512	5.9362	2.4191	8888.6	-53.9308157	.051403
11	.01024	8.3970	3.4218	8888.6	-53.9315042	.072678
12	.02048	11.8806	4.8414	8888.6	-53.9332663	.102730
13	.04096	16.8442	6.8640	8888.6	-53.9351833	.144887
14	.08192	23.8254	9.7887	8888.6	-53.9407090	.204699
15	.16384	33.7144	13.7380	8888.7	-53.9503435	.288358
16	.32768	47.6980	19.4314	8888.9	-53.9714019	.402236
17	.65536	67.3119	27.4225	8889.2	-54.0104676	.539883
18	1.31072	95.1730	38.7619	8889.9	-54.0964801	.605598
19	2.62144	134.3467	54.6859	8891.2	-54.2478654	.820607
20	5.24288	189.4162	77.0156	8893.9	-54.5888063	1.272194

INITIAL K.E. (EV) = 5.242880

TOTAL EXECUTION TIME (SEC) = 413.23

**K. List of Program Variables****i. Arrays**

V (168,65)	Coarse mesh voltages.
R (168)	Radial distances from origin to coarse mesh points.
VV (90,50)	Fine mesh voltages.
RR (90)	Radial distances from origin to fine mesh points.
UU (50)	Radial coordinates of emitter surface.
P (168,65)	Space charge density.
VOLUM (168,10)	Space charge cell volume.
HS (168)	Radial coarse mesh increments.
CJ (25)	Cathode current density for each trajectory.
CI (25)	Current associated with each trajectory.
* RM (25)	Radial coordinates of planar-diode anode (used in LABGUN only)
RS (20)	Radial coordinate of each trajectory on cathode.
CS (20)	Angular coordinate of each trajectory on cathode.
* ITRAJ (20)	Valid data indicator for trajectory regression analysis.

VINTC (4)	}	Intermediate interpolated potential values used in 16 point interpolation.
VINTR (4)		
* CM (25)		Angular coordinate of planar-diode anode (used in LABGUN only).
SI (25)		Cathode area corresponding to each trajectory.
RB (25)		Beginning radial coordinate of trajectory.
		$R, \theta, R', \theta'$ (Runge-Kutta Coordinates)
Y (4)		Next step values.
YT1 (4)	}	Auto step size.
YT2 (4)		
YE (4)		Relative error.
Y0 (4)		Initial values.
CB (25)		Beginning angular coordinate of trajectory.
* VM (25)		Potential of planar-diode anode (for LABGUN program only).

See Fig. A-11 for clarification of U and U1.

U (65,10)	Radial distance from origin to electrode boundary (outward side).
U1 (65,10)	Radial distance from origin to electrode boundary (inward side).



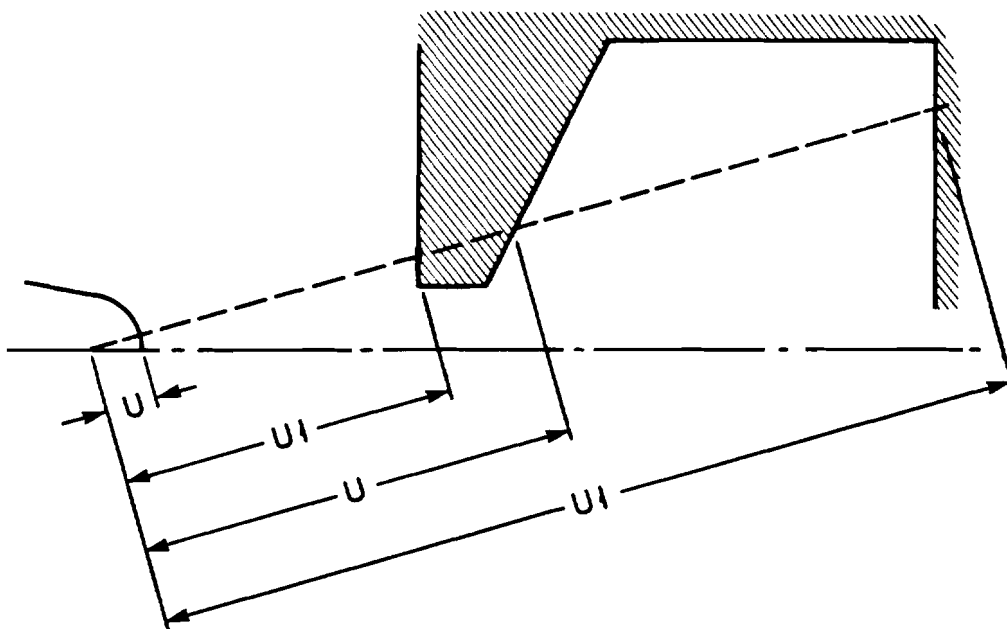


Figure A-11. Clarification of U and U1 arrays.

IU (65,10)	Integer corresponding to U.
IU1 (65,10)	Integer corresponding to U1.
KK (10)	Accumulating node point numbers of each electrode.
ZR (100,3)	Z, R, $\rho$ values from boundary data.
VO (10)	Voltages for each electrode.
IK (65)	Starting point of iteration
IG (65)	Ending point of iteration
	} Radial I No's.
JC (100)	Angular position for each boundary nodal point.
VEQ (20)	Values of equipotentials.
UB (65)	Radial distance to open boundaries.
VB (65)	Potentials on open vertical boundary (log interpolation).
IB (65)	Last iteration point for open boundary.
IB1 (65)	Irregular point on open boundary.
IC0 (65,10)	Radial I no. leaving boundary electrode.
DELTAC (168,65)	$\Delta\theta$ for irregular boundary points (mesh point not on boundary).
IC1 (65,10)	Radial I no. entering boundary electrode.
VB1 (65)	Potentials on open horizontal boundary (linear interpolation).

RX (100,65)	Approximate radial coordinate of nodal point.
RPOINT (100)	Exact radial coordinate of nodal point (permits distinguishing entrance and exit of radial lines).
HHS (90)	Radial fine mesh increments.
IIK (50)	Starting point of iteration (fine mesh).
EQJ (11)	Values of equi-current density.
PP (90,50)	Space charge density in fine mesh.
VVOLUM (90,50)	Space charge cell volume (fine mesh).

#### Trajectory Endpoint Calculation Parameters

The following arrays are associated with a maximum of 25 trajectories, the last 10 points of which are used for calculation.

POINTX (10,25)	REND (25)
POINTY (10,25)	POINTVR (10,25)
YI (25)	POINTVR (10,25)
XI (25)	SLOPE (25)
SLOPE1 (25)	VFINAL (25)
ANGI (25)	

\*Probably can be removed from ZRWGUN program.

## ii. Variables (not explained elsewhere)

IM	Maximum coarse mesh I no. (radial direction).
JM	Maximum coarse mesh J no. (angular direction).
IMM	Maximum fine mesh I no.
JMM	Maximum fine mesh J no.
EO	$8.854 \cdot 10^{-12} = \epsilon_0$
E	Small number $\approx 0$ ( $1 \cdot 10^{-10}$ )
KD	Major iteration no.
KE	Convergency indicator
JBOUND	Angular integer mesh no. of fine region. The fine mesh extends to JBOUND + 2 in the angular direction.

## L. References

1. N. K. Kang, J. Orloff, L. W. Swanson and D. Tuggle, J. Vac. Sci. Technol. 19, 1077 (1981).
2. A. El-Kareh, J. C. Wolfe and J. E. Wolfe, J. Appl. Phys. 48, 4749 (1977).
3. N. K. Kang, D. Tuggle and L. W. Swanson, Optik 33, 313 (1983).

## APPENDIX E

## EXPERIMENTAL TECHNIQUES

The data in this dissertation were collected with relatively simple experimental setups. Figure 1-2 shows the electron gun structure. Two different configurations of this structure were built. Figure 1-3 shows the emitter/suppressor/anode test structure used for angular distribution and some noise measurements. The other configuration is shown in Figure A-12. This is an apertured electron gun used for forming a microprobe in a dual magnetic lens system.<sup>1</sup> Data from the apertured gun is primarily given in the current fluctuation and electron optical chapters. The particular experimental apparatus used for a given figure can be determined by the identifying letter code in the upper right corner of the figure: A denotes the Figure 1-3 gun and G denotes the Figure A-12 gun. Because of poor pumping of the G type gun in the glass tube, a tip protection circuit was built to decouple the emitter from the large stored charge in the high voltage power supply and connecting cable. This device improved emitter life by preventing minor arcs from destroying the emitter. A schematic is shown in Figure A-13.

Angular distributions and I-V data were taken in UHV ion pumped chamber with the A type electron gun suspended over an x-y stage which had a Faraday cup mounted on it. A Keithley 600A

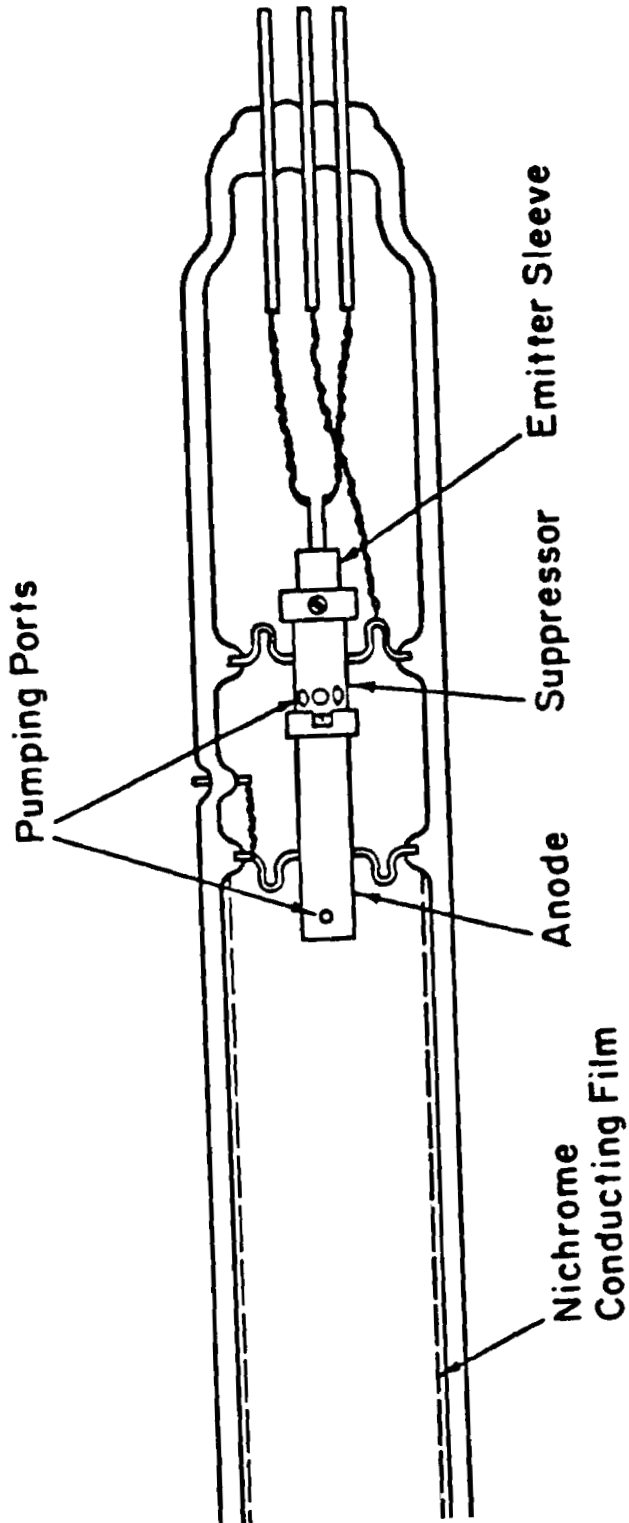


Figure A-12. Electron gun.

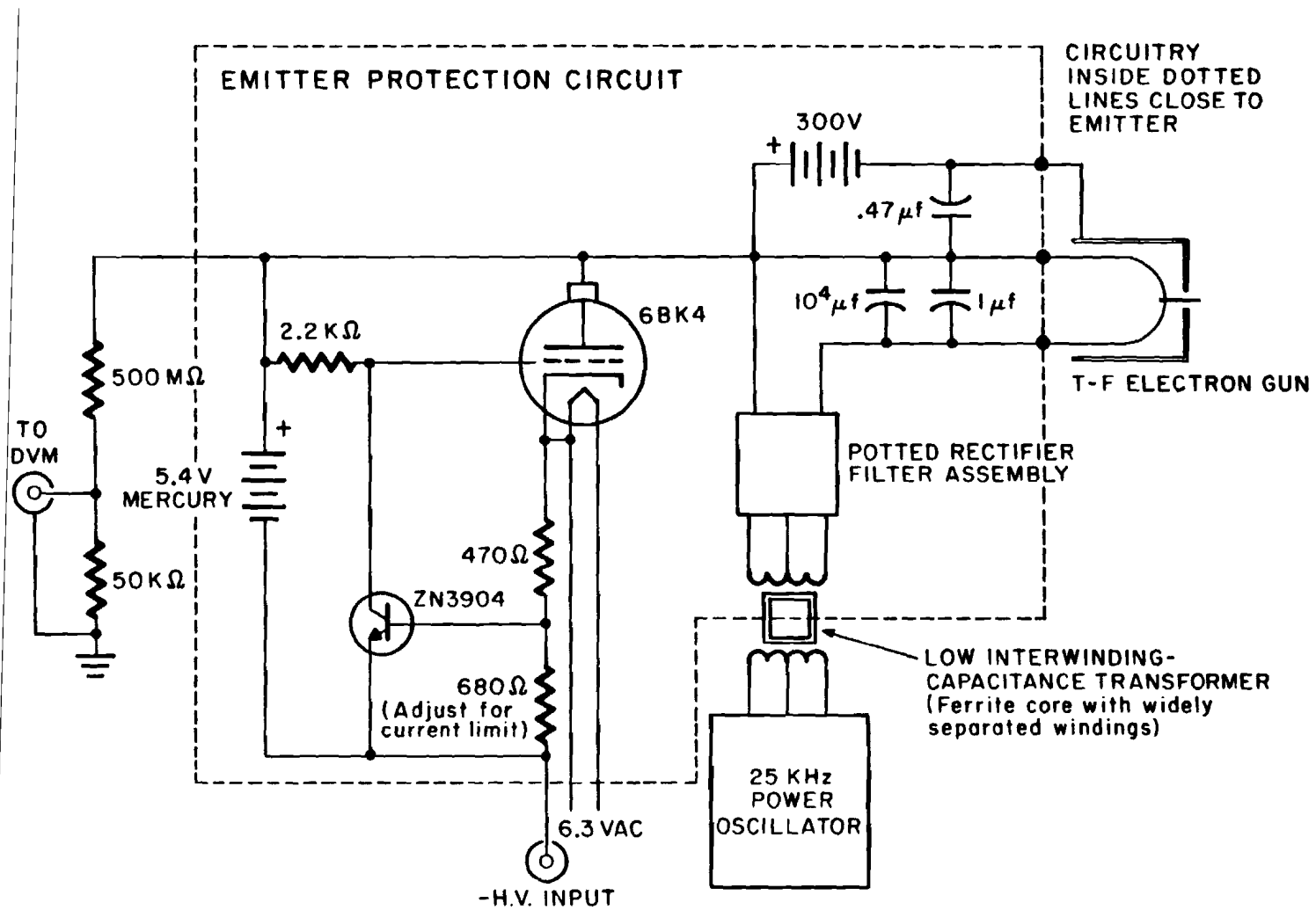


Figure A-13. Diagram of the emitter protection circuit used in this study.



electrometer was used to measure the cup current and was connected to an x-y recorder for obtaining plots of angular distributions. The stage position was transmitted to the x-y recorder via a 10 turn potentiometer coupled to the x-y stage motion control.

Noise spectra in Chapter 4 were taken using two different spectrum analyzers, an analog type (Quantech model 304) and a dual channel digital signal analyzer (Hewlett-Packard 5420A). The Faraday cup current was amplified with a PAR 181 current sensitive preamplifier in both cases. The experimental setup for dual channel coherence function measurements is shown in Figure A-14.

---

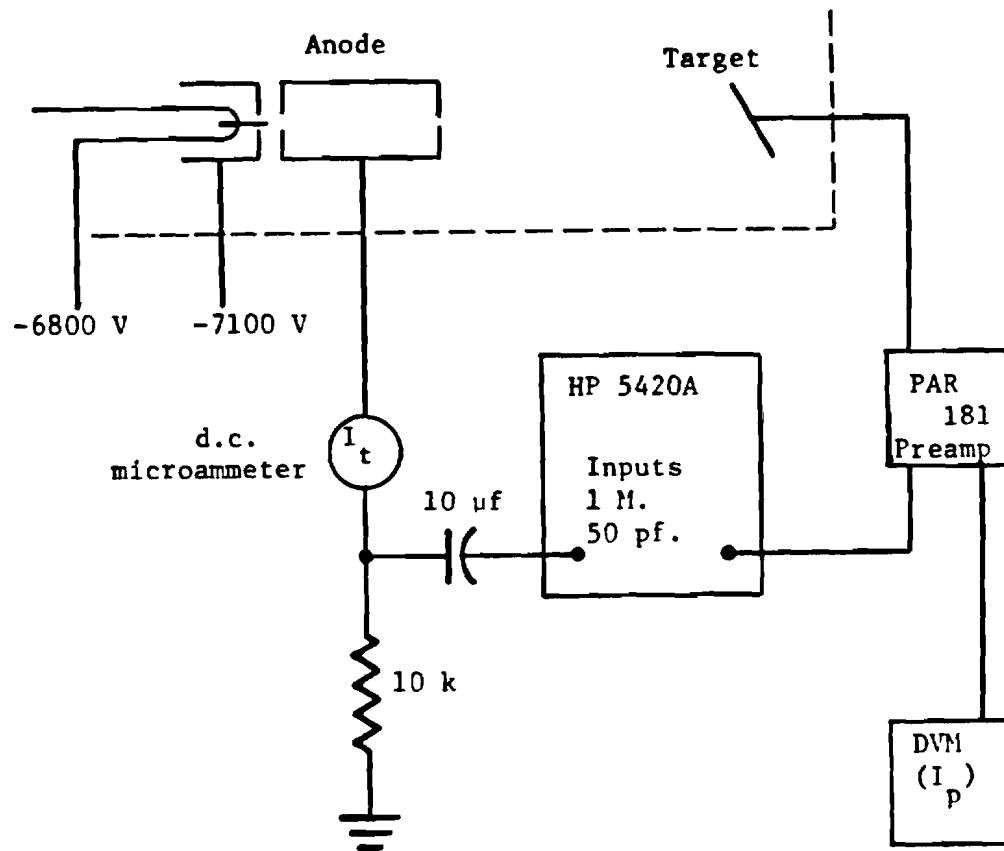


Figure A-14. Coherence function experimental apparatus.

## REFERENCES

1. D. Tuggle, L. W. Swanson and J. Orloff, *J. Vac. Sci. Technol.* 16, 1699 (1979).

## VITA

The author was born in Portland, Oregon on October 30, 1946. His public school education was completed in Portland schools where he graduated from Benson High School in 1964. After a year at Portland State University, the author was in the Navy for six years. The author completed his undergraduate education at Oregon State University, receiving a B.S. in Physics in 1974. The author worked at Tektronix until starting his graduate education in 1976 at the Oregon Graduate Center.

The author received his M.S. in Applied Physics from OGC in 1981 and continued work towards his Ph.D. In February, 1983 he became an independent consultant.

Publications

1. D. Tuggle, L. W. Swanson and J. Orloff, "Application of a Thermal Field Emission Source for High Resolution, High Current e-Beam Microprobes," J. Vac. Sci. Technol. 16, 1699 (1979).
2. L. W. Swanson and D. Tuggle, "Recent Progress in Thermal Field Electron Source Performance," Appl. Surf. Sci. 8, 185 (1981).
3. N. Kang, J. Orloff, L. W. Swanson and D. Tuggle, "An Improved Method for Numerical Analysis of Point Electron and Ion Source Optics," J. Vac. Sci. Technol. 19, 1077 (1981).

4. N. K. Kang, D. Tuggle and L. W. Swanson, "A Numerical Analysis of the Electric Field and Trajectories With and Without the Effect of Space Charge for a Field Electron Source," *Optik* 33, 313 (1983).
5. L. W. Swanson, D. Tuggle and Jia-Zheng Li, "The Role of Field Emission in Sub-micron Electron Beam Testing," *Thin Solid Films* 106, 241 (1983).
6. D. W. Tuggle and S. G. Watson, "A Low-Voltage Field-Emission Column With a Schottky Emitter," *Proc. 42nd Ann. Mtg. of the Electron Microscopy Soc. of America* 454 (1984).
7. D. W. Tuggle and L. W. Swanson, "Emission Characteristics of the ZrO/W Thermal Field Electron Source," *J. Vac. Sci. Technol.* B3(1), 220 (1985).
8. D. W. Tuggle, L. W. Swanson and M. A. Gesley, "Current Density Distribution in a Chromatically Limited Electron Microprobe," *J. Vac. Sci. Technol.* (submitted July 1985).
9. D. W. Tuggle, J.-Z. Li, and L. W. Swanson, "Point Cathodes for Use in Virtual Source Electron Optics," *J. Microscopy* (submitted June 1985).

#### Unpublished Work

1. D. Tuggle, "Application of a Thermal Field Emission Source for Scanning Auger Microscopy," M.S. Thesis, Oregon Graduate Center, January 1981.

2. D. Tuggle, N. Kang and L. Swanson, "Effect of Emitter Faceting on Electron Emission Properties," The 28th International Field Emission Symposium, Portland, OR, July 1981.
3. L. W. Swanson, D. W. Tuggle, J. H. Orloff and G. A. Schwind, TFE Electron Source Section of "VHSIC 3: Electron Beam Lithography Components for Directly Writing Very High-Speed Integrated Circuits," Interim Report No. 1, ERADCOM Report No. DELET-TR-80-0262-1, March 1982.
4. L. W. Swanson, D. Tuggle and N. Kang, "Emission Characteristics for a Zirconium/Tungsten Thermal Field Cathode," presented at The 1982 Tri-Service Cathode Workshop, U.S. Army ERADCOM, Hexagon Building, Fort Monmouth, NJ 07703.
5. D. W. Tuggle, "Emission Characteristics and Electron Optical Properties of the ZrO/W Point Cathode," Ph.D. Dissertation, Oregon Graduate Center, June 1984.